INTEGRATED COMPUTATIONAL MATERIALS ENGINEERING WORKFLOWS FOR MICROSTRUCTURE-SENSITIVE FATIGUE OF ADVANCED ALLOYS

A Dissertation
Presented to
The Academic Faculty

by

Krzysztof S. Stopka

In Partial Fulfillment
of the Requirements for the Degree
Doctor of Philosophy in the
George W. Woodruff School of Mechanical Engineering

Georgia Institute of Technology
May 2021

INTEGRATED COMPUTATIONAL MATERIALS ENGINEERING WORKFLOWS FOR MICROSTRUCTURE-SENSITIVE FATIGUE OF ADVANCED ALLOYS

Approved by:

Dr. David L. McDowell, Advisor
George W. Woodruff School of
Mechanical Engineering
Georgia Institute of Technology

Dr. Richard W. Neu
George W. Woodruff School of
Mechanical Engineering
Georgia Institute of Technology

Dr. Surya R. Kalidindi
George W. Woodruff School of
Mechanical Engineering
Georgia Institute of Technology

Dr. Hamid Garmestani
School of Materials Science and
Engineering
Georgia Institute of Technology

Dr. Olivier Pierron
George W. Woodruff School of
Mechanical Engineering
Georgia Institute of Technology

Date Approved: March 31, 2021

To my parents, family, friends, and loved ones.

"The purpose of life is finding the largest burden that you can bear and bearing it."

-Dr. Jordan B. Peterson

ACKNOWLEDGEMENTS

There are several individuals without whose support I would not be the person I am today. I would first like to thank Dr. David L. McDowell for his guidance, mentorship, availability, and kindness during this doctoral program. It is difficult to overstate how the last four and a half years have shaped me both as an individual and a researcher. Dr. McDowell's constant guidance and support was fundamental in my development as a scholar. I would like to recognize my committee members as their insight helped guide my research direction. I would like to thank Dr. Surya Kalidindi for his guidance and mentorship on several side projects and during several classes. I have had the pleasure to work closely with Dr. Richard Neu during the Mechanical Engineering Department's Teaching Practicum. I also give thanks to Dr. Hamid Garmestani and Dr. Olivier Pierron for joining my research committee and providing valuable guidance.

To the other faculty and staff members in the Woodruff School of Mechanical Engineering at Georgia Tech, thank you for always being available for students. I would like to thank Dr. Wayne Whiteman, Dr. Jeffrey A. Donnell, Dr. Andrei G. Fedorov, Dr. Shuman Xia and the entire team of academic advisors.

To my current and former lab mates in MRDC 3338, thank you for the countless hours of mentorship and discussions. I wish to thank Dr. Gary Whelan, Adrienne Muth, Dr. Aaron Tallman, Thomas Payne, Dr. Luke Costello, Theodore Zirkle, Alex Selimov, Kevin Chu, Dr. Tang Gu, Dr. Dengke Chen, and Dr. Shuozhi Xu. I have had the privilege to work closely with a few of you on sponsored projects or classwork. To the long list of

my other colleagues and friends that I met during my time in Atlanta, thank you for the company and I wish you the best.

I would like to thank everyone in the Georgia Tech Center for Teaching and Learning (CETL), especially Dr. Kate Williams, Dr. Tammy McCoy, and Dr. David Lawrence. I completed the "Tech to Teaching" program during the Fall 2019 – Fall 2020 semesters, which prepares future faculty in pedagogy and course design, and features a capstone teaching experience. The entire program was extremely rewarding, well-organized, and reinforced my desire to enter academia as a professional career.

I would like to thank the Leadership Education and Development (LEAD) program for allowing me to participate as a Coach. I enjoyed hearing Stacey Doremus, Wes Wynens, and other members speak passionately about the coaching process. I enjoyed meeting with undergraduate and graduate students during my time as a Leadership Coach and strongly benefitted from the program.

During the Summer of 2020, I was very fortunate to work as an intern at the Advanced Photon Source (APS) of Argonne National Laboratory (ANL). I worked closely with Jonathan Almer and the Material Physics and Engineering group on cutting-edge high-energy x-ray diffraction microscopy (HEDM) data. The experience was extremely rewarding, challenging, and vital to my development as a researcher and materials scientist.

During the last 1.5 years of my graduate studies, I worked closely with Dr. Mohammadreza (Reza) Yaghoobi and Dr. John Allison of the PRISMS Center at the University of Michigan, a DOE funded (Award# DE-SC0008637) effort. This collaboration has been extremely fruitful, and I hope we continue to work together. The

latter half of this thesis would not be possible without Reza's mentorship, guidance, and patience. Collaborators like this are truly hard to find.

My alma mater, the Rose-Hulman Institute of Technology (RHIT), will always have a special place in my heart. The lifelong friendships I developed there helped to shape me as the individual I am today. The faculty and staff at RHIT are unimaginatively selfless in their roles as educators. Dr. Simon Jones and Dr. Andrew Mech were instrumental to my positive experience at RHIT. To Christopher Repa, my fellow RHIT alumnus and high school physics teacher, thank you for consistently going above and beyond the role of an educator, for me and the entire Oak Lawn community. It does not go unnoticed.

I would like to thank my parents for their unwavering support and commitment to my sisters and me. My parents grew up in southern Poland during communist control of the government and persevered through unimaginable hardship. Somehow, they managed to bring my sisters and me to the United States for the opportunity of a better life, and it still astounds me how far one can go with proper encouragement and support. My outlook on life would not be the same without them, and for that I am immensely grateful. To my sisters, Joanna and Beata, thank you for putting up with me over the years, and I am hopeful your net experience with me has been and will continue to be positive.

This work was supported in part by the Office of Naval Research (ONR), under grant numbers N00014-17-1-2036 and N00014-18-1-2784. The views and conclusions contained herein are those of the author only and should not be interpreted as representing those of ONR, the U.S. Navy or the U.S. Government. I am also thankful for the support of the Carter N. Paden, Jr. Distinguished Chair in Metals Processing at Georgia Tech.

TABLE OF CONTENTS

LIST OF TABLES

LIST OF FIGURES

LIST OF SYMBOLS AND ABBREVIATIONS

ANL	Argonne National Laboratory
APS	Advanced Photon Source
BCC	Body-centered cubic
BOR	Burgers orientation relationship
CLI	Command line tool
CNN	Convolutional neural networks
COV	Coefficient of variation
CPFEM	Crystal plasticity finite element method
CRSS	Critically resolved shear stress
DAXM	Differential-aperture x-ray microscopy
DFT	Density-functional theory
DIC	Digital image correlation
DOE	Department of Energy
DOF	Degrees of freedom
EBSD	Electron backscatter diffraction
EPFM	Elastic plastic fracture mechanics
EVD	Extreme value distribution
FCC	Face-centered cubic
FCF	Fatigue crack formation
FE	Finite element
FF	Far-field
FFT	Fast Fourier transform
FIP	Fatigue Indicator Parameter

FIP_{FS}	Fatemi-Socie Fatigue Indicator Parameter
FIP_{GBI}	Grain boundary impingement Fatigue Indicator Parameter
FIP_{α}	Crystallographic version of Fatemi-Socie Fatigue Indicator Parameter
GOI	Grain of interest
GPR	Gaussian process regression
HCF	High cycle fatigue
HCP	Hexagonal close packed
HEDM	High energy x-ray diffraction microscopy
ICME	Integrated computational materials engineering
IP	In-phase
LCF	Low cycle fatigue
LEFM	Linear elastic fracture mechanics
LSY	Large scale yielding
MCAPI	Materials Commons Python Application Programming Interface
MDF	Misorientation distribution function
MGSE	Modified generalized strain energy
MKS	Materials knowledge system
MPI	Message Passing Interface
MSC	Microstructurally small crack
NF	Near-field
NN	Nearest neighbor
ODF	Orientation distribution function
OFHC	Oxygen Free High Conductivity
ONR	Office of Naval Research
OP	Out-of-phase

PACE	Partnership for an Advanced Computing Environment
PBC	Periodic boundary conditions
PHCM	Parametrically homogenized constitutive model
PRISMS	Predictive Integrated Structural Materials Science
PSSR	Plastic shear strain range
RVE	Representative volume element
SBA	Sub-band averaged
SF	Schmid factor
SP	Structure-property
SSY	Small scale yielding
SVE	Statistical volume element
UMAT	User material subroutine

a	Crack length
b	Fatigue strength exponent (Basquin's exponent)
c	Fatigue ductility exponent
C	Material constant
$\bar{C}$	Fourth-order elastic stiffness tensor
d	Mean slip distance
D^{α}	Drag stress on slip system α
E	Young's Modulus
$\mathbf{E}^{\mathbf{e}}$	Elastic Green strain tensor
$\mathbf{F}$	Deformation gradient
$\mathbf{F}^{\mathbf{e}}$	Elastic part of the deformation gradient

$\mathbf{F^p}$	Plastic part of the deformation gradient
g^{α}	Drag stress on slip system α
G	Constant for a given fatigue life
h	Direct hardening coefficient
h_D	Dynamic recovery coefficient
h_i	Material constant for back stress model
$\mathbf{I}$	Second rank identity tensor
J	Jacobian (determinant of deformation gradient)
k	Constant to control influence of normal stress
K	Constant to control influence of normal stress
K_{SIF}	Stress intensity factor
ΔK	Stress intensity range
$K_{\max}$	Maximum stress intensity
$K_{\min}$	Minimum stress intensity
K_s	Strength coefficient
$\mathbf{L}$	Velocity gradient in the current configuration
$\mathbf{L}_0^p$	Plastic velocity gradient in the intermediate configuration
m_i	Material constants for back stress model
m_c	Material constant
M	Scalar multiplier that controls the influence of the normal stress
M_s	Strain rate sensitivity exponent
n	Hardening exponent
n_0^{α}	Slip plane normal unit vector
N_i	Crack initiation life

N_f	Cycles to failure
r_i	Material constant for back stress model
s_0^α	Slip direction unit vector
u_n	Characteristic largest value of sampled population in Gumbel distribution
α_n	Inverse measure of dispersion for the Gumbel distribution
$\dot{\gamma}^\alpha$	Shearing rate on slip system α
$\dot{\gamma}_0$	Reference shearing rate
ΔCTD	Crack tip displacement range
$\Delta\sigma$	Stress range
$\Delta\sigma_n$	Stress normal to plane of maximum shear strain amplitude
$\Delta\varepsilon$	Strain range
$\Delta\varepsilon_e$	Elastic strain range
$\Delta\varepsilon_p$	Plastic strain range
$\Delta\tau_{\max}$	Maximum shear strain amplitude
$\Delta\gamma^p_{\max}$	Maximum plastic shear strain range
$\Delta\gamma^\alpha_p$	Plastic shear strain range on slip system α
ε_{eff}	Effective plastic strain
ε^p	Plastic strain tensor
$\varepsilon_f^{'}$	Fatigue ductility coefficient
η	Asymmetry strength coefficient
κ^α	Threshold stress on slip system α

κ_y	Hall-Petch slope
κ_s^α	Softening parameter
μ	Softening rate coefficient
σ_{ij}	Stress tensor
$\sigma_f^{'}$	Fatigue strength coefficient
$\sigma_n^{\max}$	Maximum stress normal to plane of maximum plastic shear strain range
σ_y	Yield strength
σ_n	Peak stress normal to slip plane of slip system α
σ_n^α	Peak stress normal to slip plane of slip system α for FIP_α calculation
$\boldsymbol{\sigma}$	Cauchy stress tensor
$\boldsymbol{\sigma}^{PK2}$	Symmetric second Piola-Kirchhoff stress tensor
τ^α	Resolved shear stress for slip system α
τ_{CRSS}^α	Critically resolved shear stress on slip system α
χ^α	Back stress on slip system α

SUMMARY

The high cost and data scatter of physical fatigue experiments, particularly in the High Cycle Fatigue (HCF) regime, requires a paradigm shift to efficiently assess the fatigue criticality of metallic components. Integrated Computational Materials Engineering (ICME) presents an attractive additional pathway that employs microstructure-sensitive simulations given accessible process paths and resulting microstructures to assist and augment decision-support from experiments. In this research, multilevel scripted workflows are implemented into the open-source Python programming language to study the effects of intrinsic (e.g., crystallographic orientation distribution, grain shape, and grain size distribution) microstructure attributes, boundary conditions (e.g., fully periodic vs. traction free), strain states (e.g., uniaxial, shear, biaxial), and model sample sizes. Digital microstructure instantiations of Duplex Ti-6Al-4V and Al 7075-T6 are generated for simulation with Crystal Plasticity Finite Element Method constitutive models using the open-source Dream.3D software, with extreme value fatigue response as the primary performance requirement. Fatigue Indicator Parameters (FIPs) are used as surrogate measures of the driving force for fatigue crack formation and are volume averaged over regions within grains representative of fatigue damage process zones. These FIPs are fit to known extreme value distributions so that the effects of different microstructure attributes and boundary/strain states may be assessed. Other extreme FIP characteristics (e.g., proximity to free surface, elastic strain normal to slip plane) are examined. A major contribution of this thesis to the research community is the open-source PRISMS-Fatigue framework pursued in collaboration with researchers at the University of Michigan, which is a highly efficient, scalable, flexible, and easy-to-use community ICME platform.

CHAPTER 1. INTRODUCTION

This chapter motivates the research topic and reviews fatigue in polycrystalline metals and alloys. Thesis objectives are discussed, and the structure of the thesis is presented.

1.1 Motivation

Fatigue failure is of utmost concern in the design of industrial components, and its annual cost is estimated to account for as much as 4% of the gross national product [1]. While extensive experimental testing has been performed to gain insight into the mechanisms of fatigue crack formation and growth, modern testing and characterization techniques have outpaced the ability to fully understand information gathered from such experiments [2]. Massive experimental datasets contain stress- and strain-life information that ostensibly support the design of components but understanding of the underlying physical mechanisms driving fatigue failures is deficient, relations to microstructure are tenuous, and the translation of fatigue concepts and test data to design engineering is incomplete. Design engineers and failure analysts still often rely on empirical correlations to deal with surface roughness, residual and mean stresses, combined stress state effects, and corrosion. Additionally, the high degree of data scatter in the High Cycle Fatigue (HCF) regime often requires high safety factors, resulting in excess weight.

While standard fatigue experiments are essential to validate and calibrate numerical models, they are inherently limited; the complex cause-and-effect interactions between grains/phases, secondary particles and other long-range interactions often remain elusive. Synchrotron diffraction and tomography experiments may assist in this regard but are of

high cost and limited sample size. Fatigue experiments are time-intensive and often require several samples due to the high degree of variability. Different specimen, loading, and environment conditions quickly exacerbate cost. Integrated Computational Materials Engineering (ICME) leverages the growing capability of computational resources to augment experiments with numerical simulations of response of material microstructures to provide additional decision support in materials selection and design processes [3]. These numerical studies leverage 3D digital microstructures that attempt to mimic actual microstructures, facilitating detailed analysis of stress, strain and other parameters that are related to fatigue mechanisms at the scale of microstructure. In this research, digital workflows to generate and explore the material response of the digital microstructures are scripted in the Python open-source software and utilize crystal plasticity finite element method (CPFEM) models with the commercial finite element solver ABAQUS [4] and the open-source finite element solver PRISMS-Plasticity [5]. A brief review of fatigue in metals and alloys is discussed next.

1.2 Fatigue in metals and alloys

Several historic methods of fatigue analysis are reviewed: the stress-life approach, strain-life approach, and the fracture mechanics approach [6]. More recent and state-of-the-art approaches are then discussed.

1.2.1 Stress-life approach

The basis for the stress-life approach is the *S*-*N* or Wöhler diagram, which plots the alternating stress, *S*, as a function of cycles to failure, *N*. A common method of generating this type of data is through rotating bending tests, one of which is called the “R. R. Moore”

test. It is a special case of a mirror-polished 0.25 in diameter specimen loaded under completely or fully reversed bending. There are undoubtedly many other factors that further contribute to fatigue failure and so it is common to apply so-called "modifying factors" that account for this knockdown in fatigue life. Some of these include the size of the specimen, the type of applied loading, the surface finish, surface treatments, temperature, and the environment. The mean applied stress during cyclic loading also affects fatigue life and can be taken into consideration using one of many relationships, e.g., Soderberg, Goodman, Gerber, or Morrow [6].

Basquin [7] observed that *S*-*N* data can be plotted linearly on a log-log scale as

$$\frac{\Delta\sigma}{2} = \sigma_f^{'}\left(2N_f\right)^b \tag{1.1}$$

where $\frac{\Delta\sigma}{2}$ is the stress amplitude, $\sigma_f^{'}$ is the fatigue strength coefficient, b is the fatigue strength exponent (Basquin's exponent), and $2N_f$ is the reversals to failure. The major limitation of the stress-life approach is the assumption that plastic strains are small and so it is only applicable in the HCF regime.

1.2.2 Strain-life approach

The strain-life approach is based on the observation that the response at critical locations such as notches is strain or deformation dependent. Coffin [8] and Manson [9] independently formulated that strain-life data (i.e., fatigue experiments performed at high applied strains) can also be linearly plotted in log-log coordinates as

$$\frac{\Delta\varepsilon_p}{2} = \varepsilon_f^{'}\left(2N_f\right)^c \tag{1.2}$$

where $\frac{\Delta\varepsilon_p}{2}$ is the plastic strain amplitude, $\varepsilon_f^{'}$ is the fatigue ductility coefficient, and c is the fatigue ductility exponent.

The total strain amplitude is the sum of the elastic and plastic strain ranges and can be expressed in terms of amplitudes as

$$\frac{\Delta\varepsilon}{2} = \frac{\Delta\varepsilon_e}{2} + \frac{\Delta\varepsilon_p}{2} \tag{1.3}$$

Thus, the total strain can be rewritten using Equations (1.1), (1.2), and (1.3) as

$$\frac{\Delta\varepsilon}{2} = \frac{\sigma_f^{'}}{E}\left(2N_f\right)^b + \varepsilon_f^{'}\left(2N_f\right)^c \tag{1.4}$$

where E is the Young's Modulus. Equation (1.4) is termed the strain-life relation. In the strain-life approach, crack growth is not explicitly modeled and failure is assumed when the "equally stressed volume of material" fails [6]. This approach is thus often used as a life estimate for fatigue crack "initiation," pertaining to a crack with specified length which can be measured experimentally, typically on the order of hundreds of microns. This approach requires a stress-strain model that reflects plastic deformation, one of which is expressed as

$$\varepsilon = \frac{\sigma}{E} + \left(\frac{\sigma}{K_s} \right)^{\frac{1}{n}} \tag{1.5}$$

where K_s is the strength coefficient and n is the hardening exponent [6].

1.2.3 Fracture mechanics

The fatigue life of a component can be decomposed into initiation and propagation stages. The crack size and associated number of cycles at the transition from initiation and propagation stages is typically unknown and often depends on the specimen size [6]. This is an important distinction because at low strain amplitudes in the HCF, up to 90% of the fatigue life is spent initiating the crack, while at high strain amplitudes in the Low Cycle Fatigue (LCF) regime, the majority of the fatigue life is spent propagating the crack [6]. The initiation life can be estimated using the stress- or strain-life approach. The fracture mechanics approach deals with crack propagation and requires an initial crack or flaw size be estimated or assumed. This approach can assign initial crack size based on porosity, inclusions, or casting defects.

In the 1920s, Griffith [10] formulated that for brittle materials, a crack will propagate if the total potential energy of the system is lowered by virtue of crack propagation [6], balanced by creation of new crack surfaces. In the 1940s, Irwin [11] extended the theory for ductile materials and hypothesised that the energy associated with plastic deformation must be included in the energy balance for crack propagation. Irwin [12] later showed that for Linear Elastic Fracture Mechanics (LEFM), the local stresses near the crack tip can be expressed in the general singular form of

$$\sigma_{ij} = \frac{K_{SIF}}{\sqrt{2\pi r}} f_{ij}(\theta) + \ldots \tag{1.6}$$

where r and θ are cylindrical coordinates of a point with respect to the crack tip and K_{SIF} is the stress intensity factor. K_{SIF} defines the amplitude of local stresses around the crack tip and depends on the type of loading, crack size and shape, and geometric boundaries. LEFM employs this concept under small scale yielding (SSY) to study the driving force for crack growth. Elasticity assumptions are inherent in LEFM, such as the general linearity between stresses and strains and small displacements [6]. LEFM is commonly used to correlate fatigue crack growth, most notably using the Paris [13] equation defined as

$$\frac{da}{dN} = C(\Delta K)^{m_c} \tag{1.7}$$

where $\frac{da}{dN}$ is the crack growth rate, C and m_c are material constants, and ΔK is the stress intensity range calculated as $K_{\max} - K_{\min}$ during cyclic loading. At higher applied loads with larger strains near the crack tip (i.e., large scale yielding (LSY)) that induce yielding even in the enclave around the crack tip, Elastic Plastic Fracture Mechanics (EPFM) is employed, in which the ΔJ -integral can be used in place of ΔK to study crack growth. Various forms of Equation (1.7) have been introduced to incorporate combined effects of $K_{\max}$ and $K_{\min}$ (i.e., both range and mean value of K), as well as threshold effects on ΔK.

Forsyth [14] classified two regimes of crack formation and early growth as Stage I and Stage II, respectively. Stage I corresponds to the initial phase of plastic deformation

along well-defined crystallographic slip planes, typically in grains favourably oriented for slip. Stage II is characterized by slip and crack growth along multiple slip planes, tending towards Mode I, maximum principal stress-dominated conditions. Neither LEFM (governed by ΔK) or EPFM (governed by the ΔJ-integral) can be considered to be accurate for microstructurally small cracks (MSC), the length of which is on the order of the nucleant grain/phase [2], owing to the LSY conditions combined with strong microstructure heterogeneity at the scale of the crack size and elastic and plastic crystalline anisotropies. However, at crack lengths of 3-10 grain diameters, experimental data for $\frac{da}{dN}$ vs. ΔK or ΔJ tend to merge with that of long cracks, and statistical fluctuations associated with microstructure diminish. For MSCs, these growth rates oscillate due to the microstructural barriers such as grain boundaries [2].

1.2.4 Critical plane approach

Findley [15] was one of the first to propose a critical-plane approach which considered the effect of maximum shear stress amplitude acting on a plane to form and growth fatigue cracks influenced by the stress normal to that plane as

$$\frac{\Delta\tau_{\max}}{2} + M\frac{\Delta\sigma_n}{2} = G \tag{1.8}$$

where $\Delta\tau_{\max}$ is the maximum shear stress amplitude, $\Delta\sigma_n$ is the stress normal to the associated plane on which it acts, M is a scalar multiplier that controls the influence of the normal stress, and G is a constant for a given fatigue life [2]. Brown and Miller [16] built on this approach with a stronger emphasis on the LCF regime to introduce the Gamma (Γ)

Plane, which considered a series of strain states and amplitudes and related them to fatigue life. Fatemi and colleagues [17, 18] introduced a similar two parameter approach which considered the maximum plastic shear strain range on a plane and the peak stress normal to this plane, i.e.,

$$\frac{\Delta\gamma_{\max}^{p}}{2}+\left[1+K\frac{\sigma_{n}^{\max}}{\sigma_{y}}\right]=F\left(N_{i}\right) \tag{1.9}$$

where $\Delta\gamma_{\max}^{p}$ is the maximum plastic shear strain range, $\sigma_{n}^{\max}$ is the maximum stress normal to this plane, K is a constant that controls the influence of the normal stress and σ_{y} is the yield strength. This parameter relates to crack initiation life N_{i} for a given constant amplitude loading condition. This approach is based on the assumption that the stress normal to the plane of maximum shear strain will directly influence the Stage I shear-dominated small crack propagation [2]. McDowell and Berard [19] formulated a ΔJ-integral-inspired approach for small fatigue cracks under multiaxial loading that included relevant critical plane concepts for Stage I fatigue crack growth. Equation (1.9) provides a foundational basis for the surrogate driving force employed in many of the computational fatigue studies that will be discussed in the next chapter.

1.2.5 Recent computational microstructure-sensitive fatigue strategies

Early crystal plasticity microstructure-sensitive computational studies by Bennett and McDowell [20-23] employed the Fatemi-Socie critical plane parameter in Equation (1.9) and crack tip opening and sliding displacements in a 2D fcc material. Key early contributions outlining the methodology of microstructure-sensitive computational fatigue

assessment that followed this early work and served as a precursor to this thesis include those of McDowell et al. [24], Goh et al. [25], McDowell [26-28], and McDowell and Dunne [29]. McDowell et al. [24] developed an early multi-stage fatigue framework for cast aluminum alloy A356-T6 that factored in multiscale hierarchy of material structure and defects, quantitative metallography, fractography, and computational micromechanics. They considered various microstructure features such as dendrite cell size, maximum pore size and average porosity, maximum Si particle size, and proximity to the free surface. Goh et al. [25] investigated how crystallographic orientation affects the micromechanical response under fretting fatigue loading, and compared crystal plasticity simulations to an isotropic J_2 model with nonlinear kinematic hardening. Crystal plasticity finite element method simulations have subsequently been employed to study the effects of numerous intrinsic (e.g., grain size [30, 31], phase volume fraction [30]) and extrinsic (e.g., surface roughness [32-35], porosity [36], annealing twins [37], inclusions [38-40], and residual stresses [41]) microstructure or microstructure-scale attributes on fatigue performance.

Owolabi and colleagues developed a microstructure-sensitive probabilistic framework to study fatigue notch sensitivity in Oxygen Free High Conductivity (OFHC) Cu [42, 43], Duplex Ti-6Al-4V [44], and Ni base superalloy IN 100 [45, 46]. Musinski and McDowell later extended this framework to effects of inclusions on fatigue crack formation and early growth in IN 100 [38, 40, 47]. Bozek, Hochhalter, and colleagues [48-50] established a framework to investigate fatigue crack incubation at constituent particles and subsequent nucleation to the surrounding matrix in aluminum alloy 7075-T651. They demonstrated that slip-based metrics computed over appropriate spatial domains correlated well with location or site of crack formation and early growth. Particular attention has been

paid to investigate characteristics of dwell fatigue [51-56] and also creep [57-59] in high-strength titanium alloys using crystal plasticity constitutive models. Wilson et al. [60] examined microstructure-sensitive fatigue crack growth in hcp, bcc, and fcc polycrystalline specimens and compared experimentally observed crack paths to crystal plasticity simulations for Ti-6Al-4V, ferritic steel, zirconium alloy (zircaloy 4), and a Ni-base superalloy. Zhang, Bridier, and colleagues investigated slip activity and the evolution of slip bands in Ti-6Al-4V under high cycle fatigue loading [61, 62]. Comparison of experimental and computational fatigue crack nucleation in Ni microbeams by Kakandar et al. [63] demonstrated comparable scatter and fatigue life.

Przybyla and McDowell outlined the earliest comprehensive extreme value probability algorithmic framework for microstructure-sensitive HCF modeling of Duplex Ti-6Al-4V [30, 64] and Ni-base superalloy IN 100 [65]. In this approach, many statistical volume elements (SVEs) were simulated to build up the extreme value fatigue response. Smith et al. [66] used a similar framework to investigate fatigue in two distinct titanium microstructures. A mesoscale fatigue crack formation and early growth model for Ni-base superalloy RR1000 was developed by Castelluccio and McDowell [31, 67]. The reviews by McDowell [27], McDowell and Dunne [29], Dunne [68], Przybyla et al. [69, 70], and Castelluccio et al. [71, 72] discuss in detail these particular microstructure-sensitive approaches developed over the last few decades.

Other unique techniques, in combination with crystal plasticity simulations, have substantially advanced fatigue modeling. A parametrically homogenized constitutive model (PHCM) crystal plasticity framework with uncertainty quantification [73] and two-way multi-scale coupling [74] was developed by Ozturk, Kotha, and colleagues. This

framework has been extensively used to investigate fatigue crack nucleation in titanium alloys [74-76]. Paulson, Priddy, and colleagues [77-80] employed the Materials Knowledge System (MKS) to created reduced-order structure-property (SP) linkages for fatigue-critical Ti-6Al-4V applications. High energy x-ray diffraction microscopy (HEDM) has recently provided revolutionary insight into fatigue of polycrystalline metals and alloys, especially during *in situ* fatigue cycling [81-83] but also for calibration of crystal plasticity constitutive model parameters [84-86]. In particular, Bandyopadhyay et al. [87] compared the performance of different back stress models using HEDM and CPFEM simulations of additively manufactured Ni-base superalloy "718Plus". A very recent study by Ravi et al. [88] used HEDM to characterize crack closure during microstructurally small crack (MSC) growth in Ni-base superalloy IN718, which may prove useful in further advancing capabilities of crystal plasticity models aimed at modeling MSC growth. Micropillar compression of advanced titanium alloys has also proved useful in the calibration of such parameters [89-91]. Jun et al. [92] investigated local strain rate sensitivity of single α phase in a dual-phase titanium alloy using micropillar compression. They found that the local strain rate sensitivity (i.e., m value) of prismatic slip systems is remarkably larger than that of basal slip systems, which has important implications for dwell fatigue applications.

1.3 Thesis objectives

The objectives of this thesis are to build onto the state-of-the-art microstructure-sensitive fatigue modeling techniques reviewed in the previous section to extend capabilities and to develop digital ICME workflows to assess the fatigue resistance of polycrystalline metals and alloys to augment decision-support from experiments. The two

alloys of interest that are investigated in this thesis are Al 7075-T6 and Ti-6Al-4V. Al 7075-T6 is a high strength, relatively low-density Al-Zn-Mg-Cu alloy designed for structural aerospace applications. The T6 designation indicates peak aging to optimize precipitation hardening. Duplex (or bimodal) Ti-6Al-4V is a common morphology for high cycle fatigue resistance, consisting of an hcp primary α-phase and a lamellar α+β colony phase of alternating layers of secondary α-phase and bcc β-phase. Ti-6Al-4V is used in applications that demand high specific strength, elevated operating temperature, and sufficient corrosion resistance (such as inlet regions of gas-turbine engines). These alloys are exemplars for the digital workflows developed and exercised in this thesis, and their assessment is key to improving the rate at which these and other alloys are implemented into service.

Although there are many microstructure-sensitive studies published in the literature, each one typically employs a "homemade" or standalone code that is not made available to the broader research community, either for numerical simulations and for pre- (generation or instantiation of digital microstructure realizations) and post-processing (e.g., analysis of local metrics to evaluate fatigue performance). Therefore, the objectives of this thesis are to further develop and exploit the microstructure-sensitive computational fatigue assessment technology for comparison of extreme value fatigue response among microstructures, and:

1) to develop digital workflows to generate microstructures and evaluate the extreme value fatigue response,

2) to exercise these workflows for a variety of microstructure attributes, boundary conditions, strain states and magnitudes, and sample sizes, and

3) to make these workflows available to the fatigue research community.

The tools developed in this work are intended to increase the rate at which decisions can be made regarding development of new and improved materials for fatigue critical applications. As will be demonstrated in Chapter 5, beyond scientific advances, a key goal of this work is to share tools and methods with the broader fatigue research community to encourage collaborative development of new and improved methods or workflows. Critical considerations in crystal plasticity simulations in fatigue simulations of realistic microstructures are therefore evaluated using the open-source PRISMS-Fatigue framework developed in this work jointly with the University of Michigan PRISMS center [93], a DOE funded (Award# DE-SC0008637) effort. In addition, the PRISMS-Fatigue platform is the most powerful finite element framework known to the author to date for simulation of very large microstructure volume elements. Additionally, the tools developed here are exercised for a variety of applications to further understanding of the extreme value fatigue response of polycrystalline metals and alloys.

1.4 Thesis structure

Chapter 2 describes the computational and theoretical methods and tools underlying this research. It discusses kinematics of crystal plasticity, constitutive models and their implementation, modeling of fatigue using damage parameters, digital microstructure workflows, and extreme value statistics. In Chapter 3, these methods and tools are used to investigate the surface versus bulk fatigue response of the two alloys of interest. Distinction

between surface and bulk boundary conditions and detailed studies for different alloy systems is vital since fatigue cracks in practice most often form at free surfaces. Lack of constraint on slip at free surfaces, combined with other microstructure attributes (e.g., crystal symmetry and available slip systems, crystallographic texture, grain shape, and grain size distribution), have important and surprisingly little understood influences on the driving force for fatigue crack formation. The fatigue response under different multiaxial states of strain (e.g., uniaxial, shear, and biaxial) and strain magnitudes is subsequently explored in Chapter 4 for both alloys of interest. The methodology outlined establishes protocols for assessing the fatigue resistance of different microstructures at the same maximum shear strain amplitude, which is considered as the measure of equivalent strain for purposes of imposing target loading levels in simulations with different applied strain states. Additionally, a framework to generate computational Γ Planes that span all possible strain states for a range of strain amplitudes is presented. This framework may aid designers in tailoring or supporting multiaxial fatigue criteria to use in the design of complex engineering components, since they often encounter complex states of strain. In Chapter 5, a novel open-source framework entitled PRISMS-Fatigue is introduced. This framework is a significant contribution of this thesis to the research community and provides a highly efficient, scalable, flexible, and easy-to-use ICME platform to explore the fatigue response of polycrystalline metals and alloys. The implementation of a previously developed crystal plasticity constitutive model into PRISMS-Fatigue is benchmarked against the commercial finite element solver ABAQUS, and the versatility of the framework is demonstrated. Chapter 6 demonstrates the effects of various boundary conditions available for simulation in PRISMS-Fatigue. A detailed study of the influence of periodic boundary conditions on

microstructure statistical volume elements or SVEs is presented, as well as the effects of different applied boundary conditions on distinct mechanical responses such as the macroscopic stress-strain response, local measures of plastic slip, and corresponding fatigue damage parameters. Chapter 7 examines the extreme value fatigue response of progressively larger microstructures and compares the response of ensembles of SVEs to a single massive microstructure. The structural mechanisms of the fatigue "hot spot" grains that manifest the largest extreme value fatigue response are then examined. Afterwards, the sensitivity of local micromechanical response at these hot spot grains is quantitatively investigated by systematically altering the orientations of first and higher nearest neighbor grains. Chapter 8 closes with conclusions and recommendations for future work.

CHAPTER 2. BACKGROUND AND METHODOLOGY

This chapter describes the theory, methods, and tools used in this thesis. The kinematics of crystal plasticity are briefly reviewed along with the constitutive models for Al 7075-T6 and Ti-6Al-4V. These models have previously been developed with advisement of David L. McDowell at Georgia Tech. Different methods of generating digital polycrystalline microstructures for simulation are reviewed next. Fatigue Indicator Parameters (FIPs) used to model fatigue and their volume averaging schemes are then reviewed. FIPs are fit to Extreme Value Distributions (EVDs) that facilitate relative rank-ordering of fatigue resistance. Attempts to simulate a single large microstructure with enough material grain/phase heterogeneity to fully characterize some material property (i.e., a representative volume element), which in this case is the extreme value fatigue response, are still very much in their infancy, and so the more traditional method of simulating large ensembles of SVEs is described and employed in this thesis. Finally, the digital workflows that link the different tools described here are summarized.

2.1 Crystal Plasticity Finite Element Method (CPFEM) models

Constitutive model forms and parameters for both materials considered in this work reflect a cyclically stable hysteresis response and are implemented for use with ABAQUS [4] as User MATerial (UMAT) subroutines with C3D8R (reduced integration) elements. In Chapter 5, the Al 7075-T6 constitutive model is implemented into the PRISMS-Fatigue framework as part of a collaboration with the PRISMS Center at the University of Michigan [5, 93, 94]. A current limitation is that the models do not explicitly account for

slip transfer between grains; grain boundaries are treated as impenetrable to slip. Models that consider details of slip transfer are quite challenging and are yet to be fully developed.

2.1.1 Kinematics of Crystal Plasticity

The kinematics framework of crystal plasticity considers the typical multiplicative decomposition of the deformation gradient $\mathbf{F}$ [95, 96] into elastic and plastic deformation gradients as

$$\mathbf{F} = \mathbf{F^e} \cdot \mathbf{F^p} \tag{2.1}$$

where $\mathbf{F^e}$ describes rigid body rotation and elastic stretching of the lattice and $\mathbf{F^p}$ captures deformation associated with dislocation motion through the lattice along the various slip systems. Note that $\det\left(\mathrm{F^p}\right) = 1$ due to plastic incompressibility associated with dislocation glide. Note that all deformation modes occur simultaneously. A schematic representation of the multiplicative decomposition is shown in Figure 2.1, where n_0^α and s_0^α represent the slip plane normal unit vector and slip direction unit vector, respectively, in both the reference and intermediate isoclinic configurations of the α^{th} slip system. The slip plane normal unit vector and slip direction unit vector in the current configuration are represented by n^α and s^α, respectively.

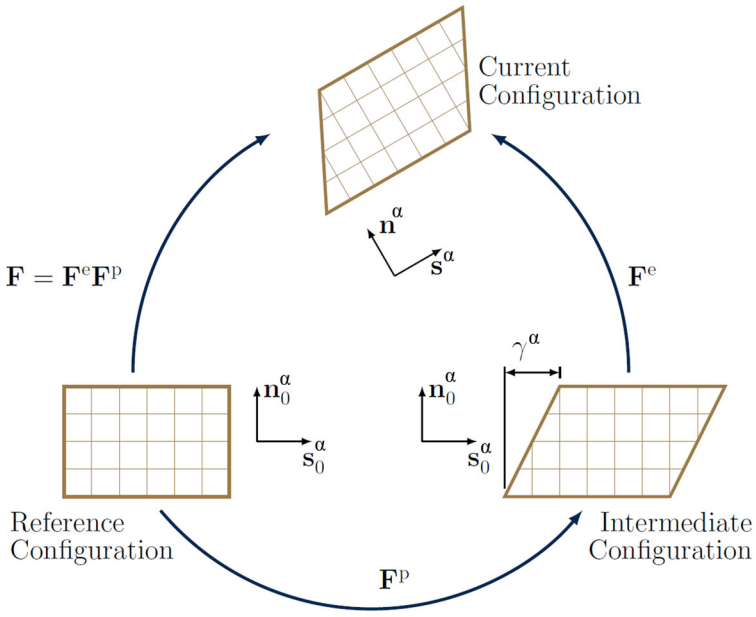

Figure 2.1. Schematic representation of the multiplicative decomposition of the deformation gradient $\mathbf{F}$ into elastic and plastic contributions (adapted from [97]).

The velocity gradient in the current configuration, $\mathbf{L}$, is defined as

$$\mathbf{L} = \dot{\mathbf{F}} \cdot \left(\mathbf{F}^{-1}\right) \tag{2.2}$$

The shearing rate, $\dot{\gamma}^{\alpha}$, is related to the plastic velocity gradient $\mathbf{L}_0^p$ in the intermediate isoclinic configuration through the expression

$$\mathbf{L}_0^p = \sum_{\alpha=1}^{\mathbf{N}} \dot{\gamma}^{\alpha} \left(s_0^{\alpha} \otimes n_0^{\alpha}\right) = \dot{\mathbf{F}}^{p} \cdot \left(\mathbf{F}^{p}\right)^{-1} \tag{2.3}$$

where N is the number of slip systems. The elastic Green strain Tensor, $\mathbf{E}^{e}$, in the intermediate configuration is defined as

$$\mathbf{E}^{\mathbf{e}} = \frac{1}{2}\left[\left(\mathbf{F}^{\mathbf{e}}\right)^{\mathbf{T}} \cdot \mathbf{F}^{\mathbf{e}} - \mathbf{I}\right] \tag{2.4}$$

Here, $\mathbf{I}$ is the second rank identity tensor. The symmetric second Piola-Kirchhoff stress tensor defined in the intermediate configuration is related to the Green St. Venant strain tensor in the intermediate configuration as

$$\boldsymbol{\sigma}^{PK2} = \bar{C} : \mathbf{E}^{\mathbf{e}} \tag{2.5}$$

where $\bar{C}$ is the fourth-order elastic stiffness tensor in the intermediate configuration. The Cauchy stress, $\boldsymbol{\sigma}$, is obtained by pushing the second Piola-Kirchhoff stress tensor forward to the current configuration, i.e.,

$$\boldsymbol{\sigma} = \frac{1}{\det\left(\mathbf{F}^{\mathbf{e}}\right)}\left[\mathbf{F}^{\mathbf{e}} \cdot \boldsymbol{\sigma}^{PK2} \cdot \left(\mathbf{F}^{\mathbf{e}}\right)^{\mathbf{T}}\right] \tag{2.6}$$

Finally, the resolved shear stress acting on slip system α is defined in the intermediate configuration and calculated from the second Piola- Kirchhoff stress tensor as

$$\tau^{\alpha} = \boldsymbol{\sigma}^{PK2} : \left(s_0^{\alpha} \otimes n_0^{\alpha}\right) \tag{2.7}$$

2.1.2 Al 7075-T6 Model

Hennessey et al. [98] developed the Al 7075-T6 crystal plasticity model (flow and hardening rules). They considered two different constitutive models for slip system kinematic hardening with nonlinear dynamic recovery, which was essential to match experimentally measured plastic strain at low levels of applied stress. Experimental peak

stress vs. plastic strain data were leveraged from Renard et al. [99], who used a special recording device to amplify the strain signal. The model includes the 12 fcc slip systems (three slip directions on the four octahedral slip planes). A two-term Ohno-Wang type hardening law with nonlinear dynamic recovery decouples the back-stress response into short- and long-range components, that quickly and slowly respond to smaller and larger applied cyclic strains, respectively.

The power law crystal plasticity modeling framework of McGinty [100], original applied to OFHC Cu, serves as the basis of the flow rule for the Al 7075-T6 model, written as

$$\dot{\gamma}^{\alpha} = \dot{\gamma}_0 \left| \frac{\tau^{\alpha} - \chi^{\alpha}}{g^{\alpha}} \right|^{M_s} \operatorname{sgn}\left(\tau^{\alpha} - \chi^{\alpha}\right) \tag{2.8}$$

where $\dot{\gamma}^{\alpha}$ is the shearing rate for slip system α, $\dot{\gamma}_0$ is the reference shearing rate, and τ^{α}, χ^{α}, g^{α} correspond to the slip system resolved shear stress, back stress, and drag stress, respectively, for the α^{th} slip system. Here, M_s is the strain rate sensitivity exponent. The two-term Ohno-Wang type back stress evolution law is defined as

$$\dot{\chi}_i^{\alpha} = h_i \dot{\gamma}^{\alpha} - r_i \left(\frac{\left|\chi_i^{\alpha}\right|}{b_i} \right)^{m_i} \chi_i^{\alpha} \left|\dot{\gamma}^{\alpha}\right|, \qquad \dot{\chi}^{\alpha} = \sum_{i=1}^{2} \dot{\chi}_i^{\alpha} \tag{2.9}$$

where r_i and h_i are material constants and $b_i = \frac{h_i}{r_i}$. The crystal plasticity parameters used are similar to the ones calibrated by Hennessey et al. [98] for the cyclic response of Al

7075-T6. The only difference are the values of m_1 and m_2 which are set to 70 instead of 200 [101]. The cubic crystal elastic constants are $C_{11} = 107.3$ GPa, $C_{12} = 60.9$ GPa, and $C_{44} = 28.3$ GPa. A reference shearing rate of 0.001 s^{-1} and inverse strain rate sensitivity of M_S = 75 were used for all simulations. The calibrated crystal plasticity parameters of Al 7075-T6 alloy are shown in Table 2.1. Model parameters were calibrated to fully reversed cyclic stress-strain data at strain amplitudes of 1.0% and 1.8% and at room temperature. Multiple strain ranges with both symmetric and asymmetric strain-controlled cycling were then used to investigate model performance.

Table 2.1. Crystal plasticity parameters for the Al 7075-T6 model calibrated to fully reversed cyclic stress-strain data at strain amplitudes of 1.0% and 1.8% and at room temperature.

M_S	g	h_1 (MPa)	r_1	h_2 (MPa)	r_2	$m_1 = m_2$
75	35	2×10^6	2.4×10^4	1.35×10^5	1421	70

2.1.3 Duplex Ti-6Al-4V Model

The CPFEM model used here as an exemplar for duplex Ti-6Al-4V was initially developed by Mayeur and McDowell [102] as an extension of the works by Goh et al. [25] and Morrissey et al. [103]. The model accounts for active slip systems and related Critical Resolved Shear Stress (CRSS), assignment of crystallographic texture in addition to grain size and shape, and length scale dependent yield criteria. Zhang et al. [104] calibrated the model using complex cyclic loading histories, and investigated the effects of various strain rates, grain sizes and volume fractions of primary α phase on both monotonic and cyclic

loading. Smith et al. [105] further calibrated model parameters, including elastic constants, CRSS values for various slip systems, and others.

Duplex Ti-6Al-4V consists of primary α grains and lamellar colony grains that contain alternating layers of secondary α and β phase. The hcp primary α grains include 24 active slip systems: three basal $\langle 11\bar{2}0\rangle(0001)$, three prismatic $\langle 11\bar{2}0\rangle\{10\bar{1}0\}$, six <a> first-order pyramidal $\langle 11\bar{2}0\rangle\{10\bar{1}1\}$, and 12 <c+a> $\langle 11\bar{2}3\rangle\{10\bar{1}1\}$ second-order pyramidal. Although in reality the lamellar colony grains consist of alternating layers of secondary α and β phase, the colony grains are homogenized in the model due to compute-time constraints and lack of certainty with regard to understanding and modeling more detailed responses [106]. The 24 active slip systems of the colony grains include: three basal $\langle 11\bar{2}0\rangle(0001)$, three prismatic $\langle 11\bar{2}0\rangle\{10\bar{1}0\}$, six <a> first-order pyramidal $\langle 11\bar{2}0\rangle\{10\bar{1}1\}$, and 12 $\langle 111\rangle\{110\}$ body-centered cubic (bcc) slip systems. The Burgers Orientation Relationship (BOR) maintains the proper crystallographic relationship between the secondary α and β, and is given as $(0001)_\alpha // \{101\}_\beta$ and $\langle 11\bar{2}0\rangle_\alpha // \langle 111\rangle_\beta$.

The flow rule for Ti-6Al-4V employed here is unchanged from the works of Mayeur and McDowell [102], Zhang et al. [104] and Smith et al. [105], i.e.,

$$\dot{\gamma}^\alpha = \dot{\gamma}_0 \left\langle \frac{\left|\tau^\alpha - \chi^\alpha\right| - \kappa^\alpha}{D^\alpha} \right\rangle^{M_S} \operatorname{sgn}\left(\tau^\alpha - \chi^\alpha\right) \tag{2.10}$$

where κ^{α} is the threshold stress and D^{α} is the drag stress. The back stress is represented by a self-hardening form of the Armstrong-Frederick direct hardening/dynamic recovery relation as

$$\dot{\chi}^{\alpha} = h_i \dot{\gamma}^{\alpha} - h_D \chi^{\alpha} \left| \dot{\gamma}^{\alpha} \right| \tag{2.11}$$

where h and h_D are the direct hardening and dynamic recovery coefficients, respectively. The threshold stress represents isotropic hardening of the α^{th} slip system, which grows the yield surface in all directions as the material deforms plastically. It consists of a Hall-Petch strengthening term and a softening term due to break of short-range order and is defined as

$$\kappa^{\alpha} = \frac{\kappa_y}{\sqrt{d}} + \kappa_s^{\alpha} \tag{2.12}$$

where κ_y is the Hall-Petch slope, d is the mean slip distance, and κ_s^{α} is the softening parameter. The value of d is set to the grain diameter for alpha phase grains and to the width of the alpha-beta laths for the colony phase grains. The evolution of the threshold stress is governed solely by the softening term as

$$\dot{\kappa}^{\alpha} = \dot{\kappa}_s^{\alpha} = -\mu \kappa_s^{\alpha} \left| \dot{\gamma}^{\alpha} \right| \tag{2.13}$$

where μ is the softening rate coefficient. The drag stress does not evolve and is simply the critical resolved shear stress (CRSS) for each type of slip system, i.e.,

$$D^{\alpha} = \tau_{CRSS}^{\alpha} \tag{2.14}$$

To account for the experimentally observed tension-compression asymmetry in Ti-6Al-4V, the CRSS of the prismatic slip systems is increased in compression by the addition of a non-planar dislocation core strength term [105]. Compressive dilatation is first determined using $\det(\mathbf{F}) < 1$ and the strength contribution is described as

$$\begin{aligned} \tau_{CRSS}^{prism} &= \tau_{CRSS}^{prism}\big|_0 + \eta\left(\left|\tau_{RSS}^{pyr1,1}\right| + \left|\tau_{RSS}^{pyr1,2}\right|\right), J = \det(\mathbf{F}) < 1 \\ \tau_{CRSS}^{prism} &= \tau_{CRSS}^{prism}\big|_0, J \geq 1 \end{aligned} \tag{2.15}$$

where $\tau_{RSS}^{pyr1,1}$ and $\tau_{RSS}^{pyr1,2}$ denote the resolved shear stress of the two first order pyramidal slip systems that share the same slip direction as the prismatic plane, $\tau_{CRSS}^{prism}\big|_0$ is the CRSS for the prismatic slip systems, and η controls the sensitivity of the asymmetry strength in relation to the resolved shear stress of the pyramidal plane slip systems [105].

The difference between the CPFEM model used in this thesis and that of Smith et al. [105] is that the drag stress here is comprised of only the CRSS value and not the initial threshold stress (see equation 6 in [105]). Subsequently, certain flow rule parameters have since been calibrated to the same experimental data used by Smith et al. [105] and the updated parameters are listed in Table 2.2 [107, 108]. The calibrations were performed using fully reversed cyclic stress-strain data at strain amplitudes of 1.0% and 0.8% with strain rates of $5\times10^{-4}s^{-1}$ and $10^{-3}s^{-1}$, respectively, at room temperature.

Table 2.2. Updated Ti-6Al-4V flow rule parameters compared to the previous calibration of Smith et al. [105]. Calibrations were performed using fully reversed cyclic stress-strain data at strain amplitudes of 1.0% and 0.8% with strain rates of $5\times10^{-4}s^{-1}$ and $10^{-3}s^{-1}$, respectively, at room temperature.

Flow Rule parameter	Value from Smith et al. [105]	Updated calibration
$CRSS_{Basal}$	350 MPa	339 MPa
$CRSS_{Prismatic}$	275 MPa	266 MPa
$CRSS_{Pyramidal\ <a>}$	450 MPa	450 MPa
$CRSS_{Pyramidal\ <a+c>}$	550 MPa	551 MPa
Softening term, $\left(\kappa_S^{\alpha}\right)_{t=0}$	50 MPa	42 MPa
Asymmetry Sensitivity, η	15	22

Elastic properties are identical between the alpha primary and lamellar colony grains. To reflect the experimentally observed stronger nature of the colony phase, the CRSS values of the basal slip systems and the prismatic slip system that is oriented parallel to the lamellar laths are increased by 25% as

$$\tau_{CRSS}^{\alpha}\left(\alpha+\beta\right)=1.25\tau_{CRSS}^{\alpha}\left(\alpha\right) \tag{2.16}$$

The remaining model parameters for the Ti-6Al-4V model are shown in Table 2.3.

Table 2.3. Remaining Ti-6Al-4V model parameters as calibrated by Smith et al. [105] using fully reversed cyclic stress-strain data at strain amplitudes of 1.0% and 0.8% with strain rates of $5\times10^{-4}s^{-1}$ and $10^{-3}s^{-1}$, respectively, at room temperature.

Parameter	Value	Parameter	Value	Parameter	Value (MPa)
$\dot{\gamma}_0$	0.001 s^{-1}	h	8,000 MPa	C_{11}	172,832
M_S	15	h_d	8,000	C_{12}	97,910
κ_y	12.7 MPa $mm^{0.5}$	μ	2	C_{13}	73,432
		$\chi_{t=0}$	0 MPa	C_{33}	192,308
				C_{44}	49,700

2.1.4 CPFEM Model Calibration

The issue of non-uniqueness of CPFEM model parameters often arises. However, the focus of this thesis is to develop and exercise digital workflows to assess the fatigue resistance of different microstructures. Accordingly, the two CPFEM models are utilized without attempts to improve either their form or calibration. That being said, there exist several modes of input in calibrating these types of models in addition to the use of macroscopic stress-strain responses. Some of these modes include microindentation and nanoindentation [109, 110], x-ray diffraction [84, 85], and *in situ* micro-compression [89]. Tallman et al. [111, 112] describe the calibration of a CPFEM model using a combined top-down (physical experiments of single crystal yield strength at multiple temperatures and orientations) and bottom-up (atomistic simulations) approach.

2.2 Microstructure generation/instantiation

This section first reviews previous methods of generating synthetic microstructures or reconstructing microstructures from experimental data. The open-source DREAM.3D [113] software is then described, which is used throughout this thesis to instantiate microstructures.

2.2.1 Previous microstructure reconstruction or generation

Voronoi tessellation is one of the simplest methods to create a polycrystalline microstructure [65], but has certain limitations in accurate representation of realistic 3D microstructures. Przybyla and McDowell [30, 64, 114] developed an ellipsoidal packing algorithm to instantiate polycrystalline microstructures based on distributions of the aspect ratios b/a and b/c. These were determined by randomly sampling experimentally characterized distributions of aspect ratios to serve as targets for an optimization process. Unlike Voronoi tessellation, an equivalent ellipsoidal packing algorithm allows construction of more complex grain morphologies such as elongated grains common in rolled metals. Musinski and McDowell [47] used a random sequential adsorption algorithm for finer control over grain size as compared to a traditional random seed Voronoi tessellation. Grain size typically follows a lognormal distribution. Using the peaks-over-threshold approach, Donegan et al. [115] examined how the extreme value grain size departs from log-normality in Al thin film, Ni-based superalloy IN100, and a synthetic data set obtained from a large-scale Potts model simulation. Fullwood et al. [116] used phase-recovery algorithms from the image processing field to reconstruct 2D and 3D

microstructures using their 2-point statistics. Turner and Kalidindi [117] developed a framework to construct statistically equivalent 3D microstructures using 2D sections.

Zhang et al. [118] combined electron backscatter diffraction (EBSD) and differential-aperture x-ray microscopy (DAXM) data collected at Beamline 34-ID-E of the Advanced Photon Source (APS) at Argonne National Laboratory (ANL) to reconstruct a Ti-5Al-2.5Sn sample for CPFEM simulation. Near-field (NF) and far-field (FF) HEDM data collected at Beamline 1-ID-E of the APS was used to compare the experimental and CPFEM simulated micromechanical response of a reconstructed Ti-7Al specimen [86, 119]. In a similar study on Ni-based superalloy RR1000 [83], absorption contrast tomography supplemented the microstructure reconstruction to characterize the 3D crack morphology and advancing crack front. Lamellar TiAl micropillars were digitally reconstructed for CPFEM simulation by Chen et al. [89] based on EBSD scans of frontal surfaces. Similarly, Chen et al. [120] used high resolution EBSD to create a model for Ni alloy FGH96 containing a non-metallic inclusion. Recently published advanced workflows demonstrate the generation of material specific microstructures, e.g., Aluminum alloy 7075-T651 with non-equiaxed grain morphology and precipitates [121], Inconel 718 aircraft engine disks [122], and convolutional neural networks (CNN) to generate realistic solid oxide fuel cell electrodes [123]. The comprehensive review by Bargmann et al. [124] systematically classifies the 3D RVE generation of these and other heterogeneous engineering materials of interest.

2.2.2 Open-source Digital Microstructure Generators

Groeber et al. [125, 126] developed a framework to first statistically characterize polycrystalline materials using serial-sectioning and EBSD, and then to digitally reconstruct the sample for simulation. This eventually led to the development of the open-source DREAM.3D [113] software that is widely used by the materials science community to generate synthetic [52, 63, 108, 127-137] and reconstruct experimental (e.g., EBSD with serial sectioning [138, 139], Laguerre tessellations using grain centroids and relative volumes from HEDM experiments [36, 82]) microstructures, largely for subsequent numerical simulation. NEPER [140, 141] is another powerful open-source software capable of generating complex microstructures. It can also reconstruct 3D microstructures using HEDM determined grain centroids and relative volumes [141]. Kasemer et al. [142] generated and simulated single and dual phase microstructures of Ti-6Al-4V using NEPER to investigate yield strength and ductility. Chatterjee et al. [139] used DREAM.3D to first reconstruct and statistically characterize a Ti-6Al-4V sample with an equiaxed grain structure, after which NEPER was used to instantiate and mesh sets of statistically equivalent microstructures. PRISMS-Plasticity [5], an open-source CPFEM solver described further in Chapter 5, is compatible with input files from both DREAM.3D and NEPER. The recently developed open-source Python package entitled MicroStructPy [143, 144] can generate microstructures with arbitrary numbers of phases, volume fractions, and associated distributions.

2.2.3 Microstructures Generated for Simulations

DREAM.3D can generate both periodic and non-periodic microstructures (see Figure 2.2a) and is executed by the *generate_microstructures.py* module in the PRISMS-Fatigue framework (described in detail in Chapter 5). A synthetic volume is created into which grains are packed and tessellated. Grain tessellations that reach the boundary in a periodic microstructure begin to grow from the opposite face. Sample periodic microstructures with 29^3 elements and ~250 grains are shown in Figure 2.3 with equiaxed and elongated grain morphology.

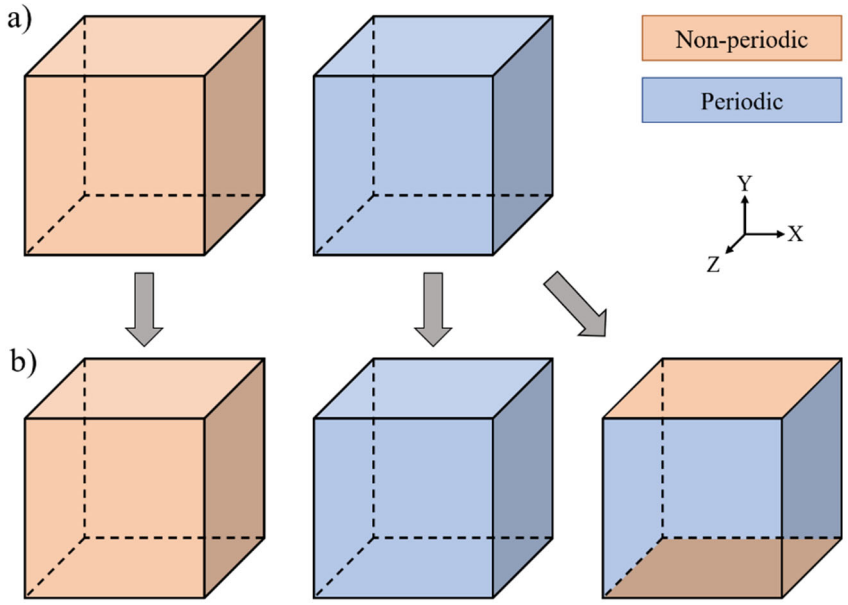

Figure 2.2. Options for a) microstructure generation in DREAM.3D [113] and b) CPFEM simulation in terms of periodicity. DREAM.3D instantiates synthetic microstructures by packing a volume with either non-periodic or periodic options. In the latter, grain tessellations that reach the boundary of a microstructure begin to grow from the opposite face. In b), the third option represents a "thin film" condition where one set of parallel faces (in this case, those perpendicular to the Y direction) can deform freely. The Python pre-processing module *generate_microstructures.py* in PRISMS-Fatigue detects and modifies the grains split by the non-periodic direction and indexes them as new grains for appropriate Fatigue Indicator Parameter (FIP, described in Section 2.4) volume averaging.

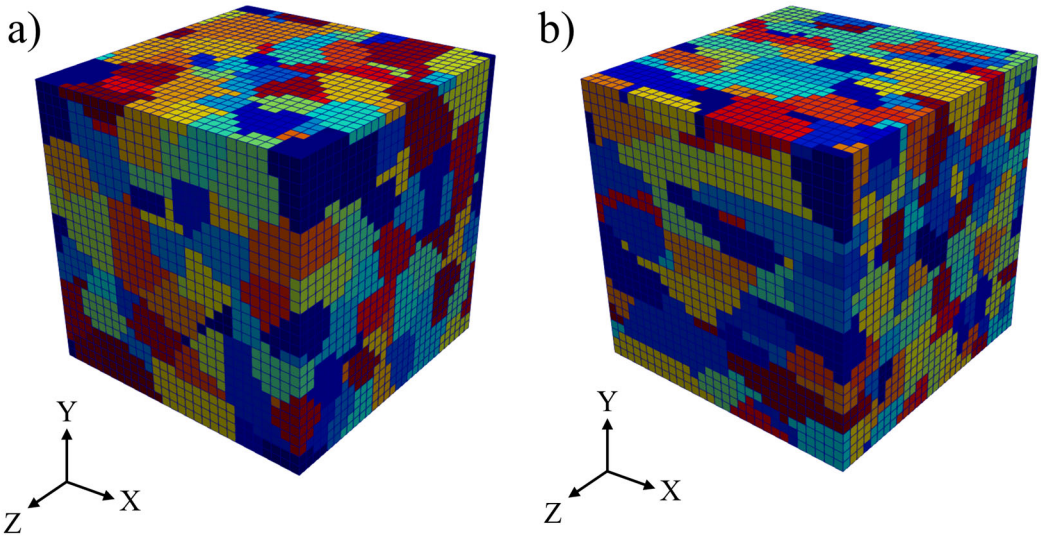

Figure 2.3. Sample statistical volume element (SVE) instantiation with a) equiaxed and b) elongated grain morphology (elongation ratio of 5:1:1) generated using DREAM.3D [113].

The target grain size for all microstructures in this work follows a lognormal distribution with a mean and standard deviation of 14 µm and 2 µm, respectively, for Al 7075-T6 and a mean and standard deviation of 60 µm and 15 µm, respectively, for Ti-6Al-4V. The response of three Al 7075-T6 crystallographic textures is explored throughout this thesis. Their orientation distribution function (ODF) pole figures are shown in Figure 2.4 and include cubic (observed after recrystallization or homogenization heat treatment [145]), random, and rolled (observed after cold rolling [146]). The X, Y and Z directions correspond to the rolling, transverse, and normal directions, respectively. In addition to ODFs, Dream.3D also incorporates Misorientation Distribution Functions (MDF) to consider target grain disorientation distributions.

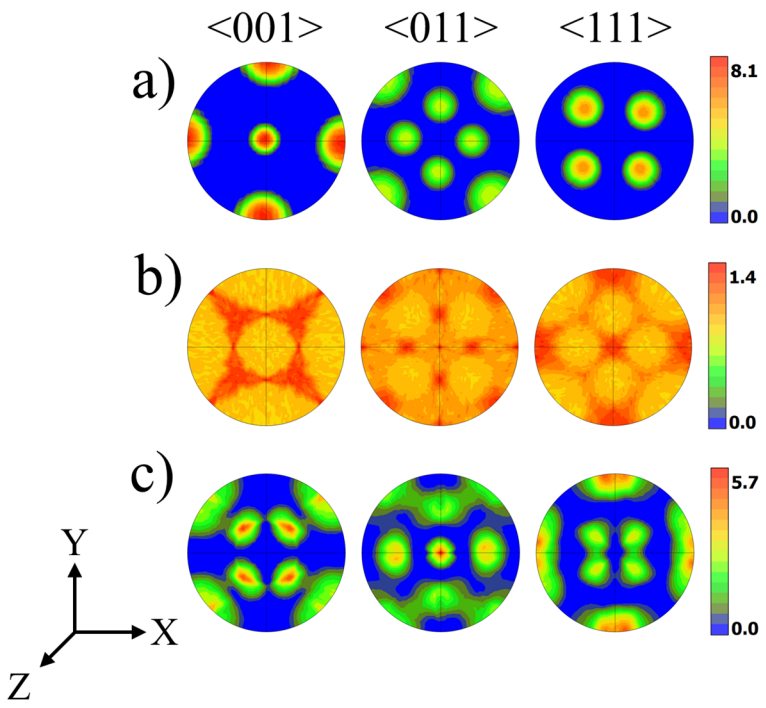

Figure 2.4. Orientation distribution function (ODF) pole figures for the a) cubic (observed after recrystallization or homogenization heat treatment [145]), b) random, and c) rolled (observed after cold rolling [146]) crystallographic textures used in DREAM.3D [113] to instantiate Al 7075-T6 microstructures.

Chapter 3 explores the fatigue response of different Ti-6Al-4V crystallographic textures that include β-annealed (determined by EBSD and achieved by annealing above the α-β transus temperature and cooling at an appropriate rate [66, 105]), random (typical of powder metallurgy components), basal-transverse and transverse (due to unidirectional rolling at 800°C and 960°C, respectively [147, 148]). The corresponding four ODF pole figures are shown in Figure 2.5. The Y direction corresponds to the rolling direction. All Ti-6Al-4V microstructures are generated with 50% alpha phase grains and 50% lamellar colony phase grains.

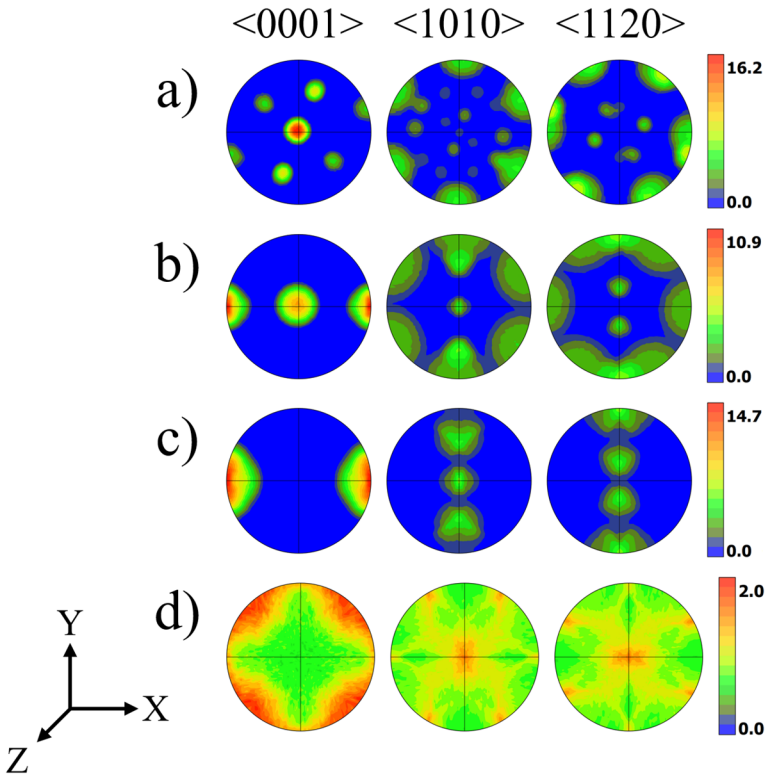

Figure 2.5. Orientation distribution function (ODF) pole figures for the a) β-annealed (determined by EBSD and achieved by annealing above the α-β transus temperature and cooling at an appropriate rate [66, 105]), b,c) basal-transverse and transverse (due to unidirectional rolling at 800°C and 960°C, respectively [147, 148]), and d) random (typical of powder metallurgy components) crystallographic textures used in DREAM.3D [113] to instantiate Ti-6Al-4V microstructures. Input values for DREAM.3D were taken from Appendix B of Priddy [97].

The fatigue crack formation process is influenced by the presence of a free surface and some materials are more sensitive in this regard than others. For instance, fatigue cracks in 7000 series Al alloys were found to form either at or within 10 μm of the free surface for various surface conditions and stress amplitudes [149, 150]. Alternatively, the location of fatigue crack formation in high strength titanium alloys such as Ti-6Al-4V is more sensitive to the surface condition and fatigue regime [151-153]. It is therefore crucial to both appropriately constrain the polycrystalline microstructure and enforce

microstructure periodicity in fatigue critical computational studies. The next section describes the available boundary conditions, one of which is non-periodic in a single direction and has a high surface area-to-volume ratio (akin to a "thin film" boundary condition, see third cube in Figure 2.2b).

Once the CPFEM simulations are complete, local field quantities necessary to assess nonlocal FIPs are computed for each element and volume averaged, as outlined in the next sections. CPFEM simulations that employ the third "thin film" boundary condition must be further processed beforehand. In the third diagram of Figure 2.2b, boundary and microstructure periodicities are enforced in two directions, in this case the X and Z directions. The CPFEM simulation appropriately constrains the micromechanical response in these directions. Although the voxel grain ID map technically specifies the same grain present at the top and bottom Y face (which is non-periodic in the simulation), this has no effect on the micromechanical response. When FIPs undergo volume averaging, however, microstructure periodicity in the Y direction must be manipulated accordingly. The Python digital workflows index grains at one non-periodic microstructure boundary with new grain IDs. The workflows allow any combination of two periodic and one non-periodic direction for this "thin film" boundary condition. This is especially useful when microstructures with different grain morphologies are instantiated in DREAM.3D. In summary, non-periodic microstructures generated in DREAM.3D require no further manipulation and are simulated with the prescribed loadings described in the next section. On the other hand, periodic microstructures can undergo fully periodic or "thin film" boundary conditions, the latter of which requires additional preprocessing for appropriate FIP volume averaging.

2.3 Boundary conditions

Periodic boundary conditions for polycrystalline crystal plasticity simulations were described in detail by Przybyla [114]. The fine details of the multi-point constraint implementation will not be reproduced here and readers are instead encouraged to examine Tables 5.1 thru 5.5 and Figure 5.9 in [114]. There are three main components of the multi-point constraints to implement with a structured, uniform mesh as generated by DREAM.3D. These include constraints on opposing faces, parallel edges, and vertices. An additional constraint prevents rigid body motion. First, displacements of nodes on opposing faces are constrained to be identical in the direction perpendicular to those faces. Displacements of nodes on each set of four parallel edges are constrained to be identical in the two directions perpendicular to the edges. Lastly, the displacement of vertices in all directions is constrained to be the same. These constraints account for any expansion or contraction of the microstructure due to applied load/strain. To enforce periodicity in only two directions for the "thin film" boundary condition, the constraints on one set of parallel faces are removed. All microstructures generated in this thesis undergo fully reversed (R_ε = -1) cyclic straining. Temperature is assigned as 300K. Straining is initiated in compression with zero initial back stress and zero initial strain.

2.4 Fatigue Indicator Parameters

FIPs serve as surrogate measures of the driving force to form and grow microstructurally small cracks within grains, and correlate with the number of cycles to form a fatigue crack with length on the order of the damage process zone over which the FIPs are averaged. FIPs can capture the influence on fatigue variability of intrinsic and

extrinsic microstructure attributes (e.g., grain size [30, 31], phase volume fraction [30], surface roughness [34, 35], porosity [154], presence of inclusions [39, 155], etc.) and loading conditions (e.g., applied strain state and magnitude [129, 156]). McDowell and Dunne [29], McDowell [27], and Przybyla et al. [69] detail the framework for the use of FIPs as surrogate measures of driving force for fatigue crack formation and early growth. Fatemi and Socie [18] modified the critical plane approach by Brown and Miller [16] to predict fatigue lives under both IP and OP loading and proposed what we refer to in this work as the Fatemi-Socie FIP, i.e.,

$$FIP_{FS} = \frac{\Delta\gamma_p^{\max}}{2}\left[1 + k\frac{\sigma_n^{\max}}{\sigma_y}\right] \tag{2.17}$$

where $\Delta\gamma_p^{\max}$ is the maximum cyclic plastic shear strain range, $\sigma_n^{\max}$ is the maximum normal stress acting on the plane of $\Delta\gamma_p^{\max}$, σ_y is the macroscopic yield strength of the material, and k is a constant that controls the influence of the normal stress. The value of k depends on material system. Various FIPs have been defined and used for fatigue correlations/predictions. FIP_{FS} is well suited to capture fatigue crack formation and early growth driving forces along slip bands, whereas a grain boundary impingement FIP (FIP_{GBI}) can be used to model fatigue crack formation on grain boundaries. FIP_{GBI} considers the accumulated plastic shear strain and peak stress normal to a grain boundary, which leads to intergranular fracture [69].

Chen et al. [120] evaluated various FIPs, including FIP_{FS}, and found good correlation between experimentally observed crack locations and measures of the local stored energy density. Zhu et al. [157] evaluated three critical plane approaches (Fatemi-Socie, Wang-Brown, and modified Smith-Watson-Topper) against a proposed modified generalized strain energy (MGSE) criteria for multiaxial fatigue of both ductile and brittle metals. The MGSE model requires additional material constants to capture the effects of the normal stress on the critical plane but displayed superior prediction of fatigue life in the materials studied by the authors. Hor et al. [158] evaluated HCF response of pure copper using three different FIPs (Crossland, Matake and Dang Van). Their approach was based on the work of Przybyla et al. [70] which is similar to the methodology of this thesis (simulation of SVE ensembles, from which data is extracted and fit to an extreme value distribution). The grain-scale FIPs they employed showed non-conservative results as compared to macroscopic criteria. Subsequently, Robert et al. [159] further refined their model and investigated four distinct material property characteristics or responses of pure copper (namely isotropic elasticity, cubic elasticity, isotropic elasticity with crystal plasticity, and cubic elasticity with crystal plasticity), which showed strong effects on the same three FIPs they investigated earlier. Although macroscopic effects may be small, they showed the local response is highly dependent on model parameters. Poncelet et al. [160] used two models based on "self-heating tests" to predict high cycle fatigue properties of C45 (SAE 45) steel. While the only difference between the two models is their description of microplasticity, both were able to relate thermal effects due to microplasticity under multiaxial loading to fatigue properties, and accounted for hydrostatic stress, the volume effect, and the influence of stress heterogeneity. Sahadi et al. [161] investigated the

multiaxial fatigue response of Waspaloy, a Ni-base superalloy used in the fabrication of aero engine disks, with several measures based on combined peak loads (von Mises equivalent stress and elastic strain energy density), stress based multiaxial criteria (Crossland [162]), and stress-based critical plane criteria (Findley and Matake [15, 163]). They concluded that the elastic strain energy and Crossland criteria resulted in good predictions but recognized the utility in multiplicative criteria such as the Smith-Watson-Topper and Fatemi-Socie. Kallmeyer et al. [164] evaluated 14 multiaxial fatigue models and found that two critical plane models (Findley and Fatemi-Socie-Kurath) best correlated both uniaxial and biaxial fatigue data. In addition, several researchers meta-analyzed multiaxial fatigue data to better assess the capability of various damage parameters and FIPs. Skibicki and Pejkowski [165] collected proportional/in-phase (IP) vs. non-proportional/OP data from literature on 25 materials and performed their own fatigue experiments on five other materials. They expressed a view that additional hardening due to non-proportional loading should not be a basis for informing multiaxial fatigue models.

Castelluccio and McDowell [166] investigated a transgranular version of the FIP_{FS} defined by

$$FIP_{\alpha} = \frac{\Delta\gamma_p^{\alpha}}{2}\left[1 + k\frac{\sigma_n^{\alpha}}{\sigma_y}\right] \tag{2.18}$$

where $\Delta\gamma_p^{\alpha}$ is the range of cyclic plastic shear strain on the α^{th} slip system, σ_n^{α} is the peak stress normal to this slip plane [27], and parameters k and σ_y retain their meaning from

Equation (2.17). They showed close correlation between FIP_α and the crack tip displacement range (ΔCTD), which is often used as a the driving force for fatigue crack growth [166]), for cracks in homogeneous single crystals and for cracks lying at the interface of a slip band in a single crystal. Direct computation of ΔCTD in CPFEM simulations requires extensive mesh refinement, and this close correlation advocates the use of FIP_α as a surrogate measure of driving force for fatigue crack formation without excessive computational demands. Musinski and McDowell [167] used FIP_α to calculate the microstructurally small crack (MSC) growth rate in Ni-base superalloy IN100. In the content of these simulations, FIP_{FS} is typically calculated using elemental plastic strain and stress tensors, whereas FIP_α is calculated on individual slip systems. The plastic strain and stress tensor at an integration point is an amalgam of response among all the slip systems, which consequently smears out extreme slip system behavior that drives transgranular fatigue crack formation. Therefore, the focus of this work is on FIP_α, calculated during the last loading cycle with $k=1$ for Ti-6Al-4V and $k=10$ for Al 7075-T6. This higher value of k was found to better correlate to fatigue experiments for Al 7075-T6 [168, 169]. Chapter 3 demonstrates that the value of k does not affect results of rank-ordering between different microstructures. However, absolute values of FIPs become more significant when used to correlate to absolute experimental fatigue lives, as was done by Castelluccio and McDowell [31, 156] for Ni-base superalloy RR1000 or by Kern [169] and Hennessey [168] for Al 7075-T6. The Python module entitled *calculate_FIPs.py* in PRISMS-Fatigue performs these tasks and allows the user to choose from a library of FIPs.

2.5 FIP Volume Averaging Schemes

Fatigue crack formation occurs over some fatigue damage process zone with scale on the order of microns typically, and therefore the FIP_α must be appropriately volume averaged. This volume averaging also serves to regularize and alleviate mesh sensitivity in computations, as shown by Castelluccio and McDowell [170]. Additionally, they showed that although mesh refinement had a notable influence on the frequency distribution of FIP_α at individual integration points, it had a negligible influence on the band-averaged and grain-averaged frequency distributions of FIP_α, with grain refinement on the same order as the SVEs used throughout this research (~100 elements per grain). The simplest approach is to volume average FIPs over entire grains, but this too intensely smears the FIP values; a high driving force for fatigue crack formation over a sub-region of the grain will be averaged out. Also, the lognormal grain size distribution would then result in different averaging volumes. Transgranular fatigue crack formation occurs within a finite damage process zone within the nucleant grain at a scale below the grain size. Consequently, FIPs in this work are averaged over regions within the grain, each corresponding to nearly the same damage process zone size.

This thesis aims to assess the driving force to form and grow sub-grain scale, microstructurally small fatigue cracks. Castelluccio and McDowell [166] introduced the notion of grain "banding," in which the elements of a grain are assigned to volume sub-domains that are defined along material's crystallographic slip planes; Figure 2.6a shows a single grain banded along one crystallographic slip system. The width of each band is typically one or two elements. Each slip system FIP_α is averaged over the band corresponding to that slip plane, i.e., FIP_α for the first three slip systems in Al 7075-T6

(which correspond to the same slip plane) are averaged over the same elements. In this work, each element has a single integration point (because C3D8R elements are used) and has as many FIP_α values as it does slip systems (12 for Al 7075-T6 and 24 for Ti-6Al-4V). At any given element, slip activity will vary between the available slip systems, and so averaging FIPs over bands more appropriately captures the driving force for fatigue crack formation. The limitation with the band-averaging scheme, however, is that bands themselves vary in volume; the first and last band of the grain contains the least number of elements whereas the center band contains the most (which is the result of cutting a sphere into slices of identical thickness). In this work, the grains are banded but are further designated to "sub-bands." Each band is analyzed so that all unique combinations of some number of adjacent elements (in this work, eight) are identified (depicted in Figure 2.6b). These sub-bands are then used as the FIP_α volume averaging domains. The effect of different sub-band volumes on FIP EVDs was previously studied [130].

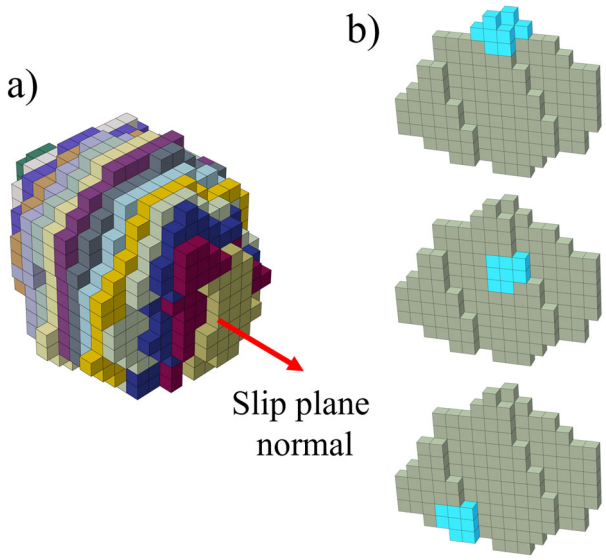

Figure 2.6. (a) A single grain partitioned into a slip band that is parallel to one crystallographic slip plane. (b) A single slip band from (a) in which different sub-band regions are highlighted for FIP volume averaging.

The 12 octahedral slip systems of Al 7075-T6 have identical initial resistance to slip, and so Al 7075-T6 grains are banded in accordance with the four octahedral slip planes. In contrast, Ti-6Al-4V grains have different types of slip systems that vary in terms of the initial CRSS. The basal and prismatic slip systems have a much lower CRSS than the pyramidal and accommodate a majority of the deformation via slip [105]. Experiments show that fatigue cracks predominately form on these two slip systems [171, 172]. Therefore, the Ti-6Al-4V grains are only banded along the single basal and three prismatic slip planes, whose sub-bands serve as the averaging domain for FIP_{α} calculated on the three basal and three distinct prismatic slip systems, respectively. The Python module entitled *volume_average_FIPs.py* in PRISMS-Fatigue performs these tasks and allows the user to average FIPs over grains, bands, or sub-bands.

2.6 Representative Volume Elements

Comparison of FIPs from different microstructures to rank order relative fatigue resistance requires a sufficiently large simulated volume to encompass a very large number of grains [29]. This is often computationally prohibitive and instead smaller, statistically equivalent samples of microstructure (so called statistical volume elements, SVEs) are simulated to build up a reliable distribution of grain-to-grain or phase-to-phase interactions that affect the variability of a computed response of interest [30, 64, 65, 69, 70, 108, 127-130, 173]. In contrast, a representative volume element (RVE) is sufficiently large to contain all moments of spatial interactions of grain/phase heterogeneity to achieve convergence of some material property independent of boundary conditions [174, 175]. Elastic properties typically require the least amount of material volume simulated to achieve convergence (e.g., elastic stiffness), whereas properties that invoke plastic flow response (e.g., yield strength, extreme value fatigue response) require larger volumes. It is challenging to determine the RVE size for local extreme value fields at fatigue hot spot grains. In this case, the RVE must be large enough to sufficiently sample all possible grain orientation space and interactions amongst neighboring grains, which can be inordinately large. From a practical perspective, the very existence of a RVE for fatigue is a challenging issue to address, since laboratory fatigue experiments invariably exhibit scatter at all specimen sizes considered, as do engineering components that fail via fatigue. Even if the RVE size issue is challenging to resolve, some sense of the rate of convergence of the extreme value driving forces to form and grow fatigue cracks with increase of highly stressed volume of microstructure is quite relevant to fatigue modeling. This is a primary

thrust of Chapter 7, whereas the first half of this thesis (Chapters 3 and 4) employs SVE ensembles to build up the extreme value fatigue response.

Several researchers have previously explored RVE size for certain behaviors of polycrystalline materials. Qayyum et al. [176] simulated the global and local stress-strain response in progressively larger 2D and 3D RVE microstructures of single- and dual-phase steels. They concluded that 3D RVEs for this response must be at least five times larger than the average grain size. They later incorporated an isotropic ductile damage model based on the total accumulated plastic slip to assess differences in damage initiation for 2D and 3D RVEs [177]. Bong et al. [178] investigated a bottom-up method to generate a RVE for dual phase steel DP980 using measured microstructural properties. Mechanical behavior was then determined using a standard continuum model, a CPFEM model, and a CPFEM model that included elastic interactions of discrete dislocations in the martensite and ferrite phases. The latter model better predicted strain hardening behavior and matched loading-unloading and compression-tension experiments. Bouchedjra et al. [179] estimated the RVE size for convergence of macroscopic elastoplastic behavior in Al alloy 5083 with several microstructure realizations ranging from 10 to 250 grains. The elastoplastic and local response of different FCC RVE single crystals and polycrystalline microstructures was examined by Lim et al. [180] using various mesh resolutions, boundary conditions, and hardening models. Tu et al. [121] developed a workflow to generate statistically equivalent representative volume elements (SERVE) of Al alloy 7075-T651 that considered morphological and crystallographic distribution of grains and the presence of precipitates. They determined the minimum number of grains for microstructure-based and property-based SERVEs. The former corresponds to the minimum size at which the

statistics of any crystallographic or morphological feature in the digital microstructure converges to that of the experimental data, whereas the latter corresponds to the minimum size that should be analyzed to predict some effective material property of interest. Sangid et al. [181] combined HEDM and digital image correlation (DIC) coupled with EBSD to examine the stress-strain response of individual grains in Ni-base superalloy Haynes 282 and Ti alloy Ti-7Al. The number of sampled grains necessary to constitute a RVE was determined using grain-level variability and was higher for Haynes 282 because of its larger grain size distribution, underlying precipitate structure, and the presence of annealing twins.

Interactions between nearest neighbor (NN) grains critically affect the local fatigue response and directly influence the RVE size for fatigue related applications. Boyle and Curtin [182] investigated how the strain in a central grain of interest deviates from the global applied strain in an FCC material when i) the orientation of the grain of interest (GOI) is changed, ii) the orientations of the first NN grains are changed, and iii) the orientations of the second NN grains are changed. The microstructure was composed of cubic geometry grains with 343 grains in a 7 x 7 x 7 array. Each grain was then discretized with 1, 8, or 27 elements. They showed that for most of the tested configurations, deviations from the applied strain are primarily influenced by interactions with the surrounding grain environment, and not by grain self-orientation. Castelluccio and McDowell [170] similarly investigated FIP variability in a surface grain by altering the orientations of NN grains in Ni-base superalloy RR1000. They also held the orientation of the GOI and orientations of the first NN grains constant and changed all other grain orientations (second NN grains and beyond). Grain interactions in the first NN grain layer affected variability of the

maximum FIP by a factor of 2-3, while the orientations of second NN grains and beyond accounted for ~30% of the variability. In a recent work on dual-phase steels, Diehl et al. [183] compared the local stress-strain response at free surface grains after varying grain orientation, grain morphology, and volume fraction of two hard and soft phases in subsurface grains. Structural changes farther than about three average grain sizes were considered negligible for stress and strain partitioning. Variations in grain morphology and an increase in microstructure heterogeneity more strongly affected the local stress-strain response at the surface grains than changes in grain orientations. They also found that the assumption of a columnar grain structure introduces a strong simplification that may be misleading in 2.5D simulations of damage in 3D microstructures.

2.7 Extreme Value Statistics

After FIPs are computed and volume averaged, the highest values are fit to the Gumbel EVD. Distributions of a single variable with a sufficiently large sample size n will converge to one of three non-degenerate distributions: 1) Gumbel, 2) Fréchet, and 3) Weibull [184]. The latter requires an upper bound on the data and is therefore not considered. FIPs have previously been characterized well by both former distributions with subtle difference depending on whether fully periodic or "thin film" boundary conditions were prescribed [64]. FIPs are fit to the Gumbel EVD in this work which is expressed as

$$F_{Y_n}\left(y_n\right) = \exp\left[-e^{-\alpha_n\left(y_n - u_n\right)}\right] \tag{2.19}$$

where $F_{Y_n}(y_n)$ is the probability that the value Y_n will be less than or equal to y_n, u_n is the characteristic largest value of the sampled population, and α_n is an inverse measure of

dispersion of the largest value of the population [184]. FIPs are sorted in ascending order with their probabilities estimated by

$$F_{Y_j}\left(y_j\right)=\frac{j-0.3}{n+0.4} \tag{2.20}$$

where *j* is the rank order of the corresponding FIP and *n* is the number of FIPs from a single or multiple microstructures. Equation (2.19) is written as a linear function of *y* in the form

$$\ln\left[\ln\left(\frac{1}{F_{Y_n}\left(y_n\right)}\right)\right]^{-1}=\alpha_n y_n-\alpha_n u_n \tag{2.21}$$

where α_n is the slope and $-\alpha_n u_n$ is the y-intercept. In this form, data that are well characterized by a Gumbel distribution appear as a straight line. Only a single sub-band averaged FIP is considered per grain. Gu et al. [108] examined the convergence behavior of FIPs fit to the Gumbel EVD and devised a strategy to predict the maximum FIPs in larger volumes using extreme value theory. This requires a rigorous consideration of a FIP threshold in the fitting process. In this thesis, some number of the highest FIPs (e.g., top 50 FIPs) from each microstructure or SVE ensemble are fit to the Gumbel EVD for the sole purpose of rank ordering relative fatigue resistance, i.e., only the highest FIPs are of interest since these are associated with the highest driving forces for fatigue crack formation. The Python module entitled *compile_and_plot_FIPs.py* in PRISMS-Fatigue performs these tasks and allows the user to fit FIPs to either the Gumbel or Fréchet EVD.

2.8 Digital Workflows

The digital workflows to generate microstructures, execute CPFEM simulations, and post-process results were initially enabled by the Python pipeline created by Kern [169]. Chapter 5 details the open-source PRISMS-Fatigue framework that has since been released for the public to replicate the studies performed in this thesis. All pre- and post-processing in PRISMS-Fatigue is performed using a series of Python modules with PRISMS-Plasticity [5] as the CPFEM solver.

CHAPTER 3. SURFACE VERSUS BULK EFFECTS ON FIPS

3.1 Introduction

As mentioned in Section 2.2.3, the presence of a free surface exerts additional influence beyond that of bulk interactions that may significantly affect driving forces for fatigue crack formation [152, 185]. This chapter builds on a previous study by Przybyla and McDowell [64], in which driving forces for surface vs. subsurface fatigue crack formation were examined for different Ti-6Al-4V microstructures. Microstructure-sensitive CPFEM simulations are used to assess the surface and bulk responses of the two alloys of interest.

The effect of certain microstructure attributes on fatigue life is clear: a finer grain size leads to improved fatigue resistance due to shorter mean free paths for slip, and grain boundaries promote retardation of crack growth [186]. However, the effects of other key attributes (crystallographic texture, grain shape, and grain size distribution) are not obvious or intuitive, particularly regarding how neighboring grains/phases affect slip near the free surface. This chapter explores interactions between these key microstructure attributes, comparing the effects of bulk and free surface cases on driving forces for fatigue crack formation in Ti-6Al-4V and Al 7075-T6.

3.2 Methodology

This chapter employs the CPFEM models, DREAM.3D microstructure generator, and FIPs as described in the previous chapter. The details of the microstructures and loading conditions specific to this chapter are described in the following.

3.2.1 Microstructure generation

Each SVE ensemble contains 30 SVEs and unique SVE instantiations are employed for both fully periodic (representative of bulk material response) and traction-free (i.e., free surface on one set of parallel faces) simulations. The latter condition is representative of a sheet of material with a relatively high surface area-to-volume ratio. It is therefore important to establish that the sheet thickness is large enough to capture near-bulk conditions at the center. SVE instantiations for both material systems are cubic with 30^3 elements.

The Ti-6Al-4V SVEs vary in both texture and grain size distribution, whereas composition is held constant at 50% α phase and 50% α+β colony phase. An ensemble of 30 SVEs is generated for each of the four textures in Figure 2.5 and each grain size distribution described below. The lognormal grain size is set to 60 ± 15 μm for simulations comparing the effects of different textures and straining directions, whereas simulations aimed at comparing the effects of grain size distributions employ an average lognormal grain size of 60 μm with standard deviations of 10 μm, 20 μm and 30 μm using the random and transverse textures. These two textures are chosen to study the effects of grain size distribution because they represent the extremes of the Ti-6Al-4V textures simulated. Regarding the effects of grain size distribution, the random texture is uniaxially strained only in the X direction, whereas the transverse texture is uniaxially strained in the X and Z directions relative to the ODF pole figures in Figure 2.5; this convention is retained throughout this chapter. The cubic SVE volume is set to $(300\ \mu m)^3$, with an average of 264 grains per SVE.

The three crystallographic textures of Al 7075-T6 shown in Figure 2.4 are investigated. The lognormal grain size is set to 14 ± 2 μm for simulations comparing the effects of different textures and grain elongation. An average lognormal grain size of 14 μm with standard deviations of 2 μm, 4 μm and 6 μm is used to study the effects of grain size distributions for the three Al 7075-T6 textures with equiaxed grains. Zhao and Jiang [187] found the Al 7075-T6 grain elongation ratio after cold working to be as severe as 7:1:1, and so a range of grain elongation ratios were chosen to study their effect on fatigue response, which include 1:1:1 (equiaxed), 3:1:1, 5:1:1 and the experimentally observed 7:1:1. The cubic SVE volume is set to $(75\ \mu m)^3$, with an average of 278 grains per SVE.

3.2.2 Loading parameters

Simulation parameters are held constant for both alloys. Three fully reversed $\left(R_\varepsilon = -1\right)$ uniaxial straining cycles are applied at a strain rate of 0.001 s^{-1} to a maximum strain of 0.8% with zero initial strain and zero initial back stress to promote elastic-plastic shakedown. Preliminary analysis has shown that volume averaged FIPs vary by less than 1% after additional straining cycles, and so three cycles suffice for elastic-plastic shakedown (and FIP saturation). Loading is quasi-static, and the strain rate is used to determine the time step for the simulations. Temperature is assigned as 300K and straining is initiated in compression. The traction-free surfaces for Al 7075-T6 are normal to the Z-axis, so that the free surface is representative of the normal direction relative to the rolling process, while straining is performed in the X-axis, representative of the rolling direction. The traction-free surfaces for Ti-6Al-4V are set normal to the Y-axis, and uniaxial straining is performed in the X- and Z-axes. These straining directions are studied in Ti-6Al-4V

because the strong anisotropy of the hcp crystal structure is expected to cause pronounced effects of load orientation.

3.3 Results and Discussion

3.3.1 Stress and plastic strain in the presence of a free surface

To quantify possible effects of the traction-free surface on cyclic slip intensity, the relative difference between stress and plastic strain is computed for 30 Ti-6Al-4V and Al 7075-T6 SVEs representing the same microstructures with random crystallographic texture, i.e., 30 SVEs are subjected to uniaxial cyclic straining with both fully periodic and traction-free boundary conditions [64]. Stress and plastic strain are then averaged across planes one element thick and oriented normal to the traction-free boundaries and compared between the two sets of simulations. The relative difference of the stress component in the direction of applied straining σ_{11} and effective plastic strain (i.e., $\varepsilon_{eff} = \sqrt{(2/3)\varepsilon^p : \varepsilon^p}$ where ε^p is the plastic strain tensor) is defined as

$$E_r = \frac{|x_f - x_p|}{x_f} \tag{3.1}$$

where x_f and x_p represent either the stress or plastic strain defined above for traction-free and fully periodic boundary conditions, respectively. The maximum relative difference at the free surface for σ_{11} and ε_{eff} reaches 0.78% and 22.0% and is as low as 0.05% and 1.3% in the center of the SVE, respectively, for Ti-6Al-4V. While there appears to be some influence of the free surface at the center of the SVEs, this effect is minimal and compares

favorably with previous work [64], in which the relative difference of the effective plastic strain remained as high as 13% at the center of the SVEs. For Al 7075-T6, the maximum relative difference at the free surface for σ_{11} and ε_{eff} reaches 8.0% and 15.3% and is as low as 6.7% and 6.9% in the center of the SVE, respectively. The high symmetry of the fcc Al 7075-T6 crystal structure results in stronger interactions between the microstructure and free surface as compared to Ti-6Al-4V. This suggests that further studies with larger thicknesses might be pursued for Al 7075-T6, thereby allowing for an improved consideration of the change of constraint from the free surface to the bulk of the material.

3.3.2 Free surface effects in Al 7075-T6

Figure 3.1a and Figure 3.1c present the highest 50 non-local, sub-band averaged FIPs (hereby referred to simply as FIPs) compiled from distinct grains for surface and bulk simulation SVE ensembles of equiaxed Al 7075-T6 that vary solely in texture, for $k=10$ and $k=1$, respectively. The parameter k (which controls the influence of the normal stress component in Equation (2.18)) affects the resulting FIP magnitudes, but not the rank ordering of the FIPs. The differences in FIP magnitudes and importance of the parameter k are critical when using FIPs to determine crack growth rates or absolute fatigue lives, as was done by Castelluccio and McDowell [31, 156]. However, this work solely considers the relative rank ordering of different types of microstructures.

The cubic and rolled textures exhibit the lowest and highest FIPs, respectively, indicating the rolled texture's higher propensity to form fatigue cracks (for the specific case of uniaxial straining in the rolled direction). The random texture exhibits moderate FIPs. Free surface effects intensify FIP response; traction-free boundary conditions increase FIPs

significantly for the random and rolled textures, but only slightly for the cubic texture. Additionally, cubic textured FIPs at low cumulative probabilities tend to merge, whereas they remain separate at all probabilities for the Random and Rolled textures. The 10 highest FIPs from each SVE ensemble are plotted as a function of their distance from the SVE boundary (i.e., the centroid of the eight element sub-band region over which the FIPs are averaged) to examine possible interactions between the free surface and crystallographic texture (shown in Figure 3.1b and Figure 3.1d). FIPs from the fully periodic simulations (with labels "P") and their locations are included to show their tendency to form throughout the SVE, whereas the traction-free surface FIPs (with labels "NP") have a much stronger propensity to lie closer to the free surface.

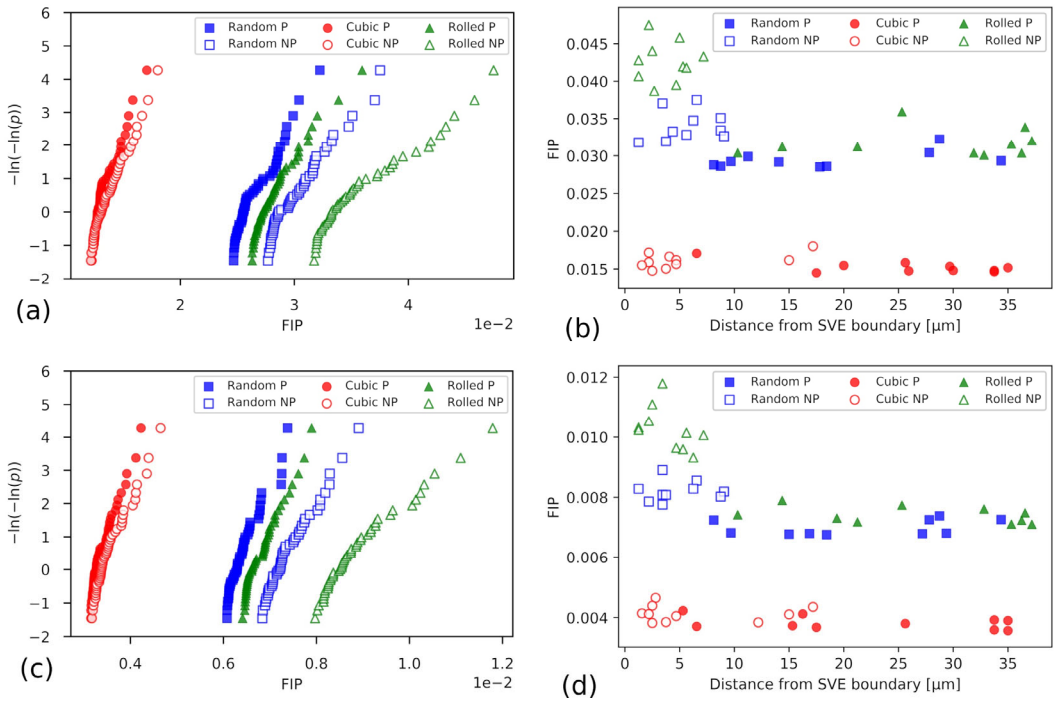

Figure 3.1. Gumbel EVD of the highest 50 Al 7075-T6 FIPs (equiaxed grains) with varying texture for surface (NP) and bulk (P) boundary conditions using (a) $k = 10$ and (c) $k = 1$ in Equation (2.18). Location of the 10 highest FIPs using (b) $k = 10$ and (d) $k = 1$ in Equation (2.18) with respect to the free surface (i.e., SVE boundary).

Elongation of grains in Al 7075-T6 due to rolling may have significant effects on fatigue behavior [187]. Figure 3.2a and Figure 3.2b present the highest 50 FIPs compiled from unique grains for surface and bulk simulation SVE ensembles of Al 7075-T6 with rolled and random texture, respectively, and varying grain elongation. FIPs for equiaxed grains (grain elongation ratio of 1:1:1) are highest in magnitude and steadily decrease, with the most severe elongation (7:1:1) exhibiting the lowest FIPs. The random texture is simulated with only equiaxed and 7:1:1 grain elongation ensembles to verify that the observed effects are due to grain morphology and are independent of texture. Recall that uniaxial straining is applied in the direction of the elongated grains. The potency of this morphological effect rivals crystallographic texture effects for this alloy system. SVEs and grains with different grain elongation ratios maintain a constant number of grains and consistent grain volume statistics, respectively, as shown in Figure 3.3. Therefore, an equivalent number of grains is sampled for all elongation ratios.

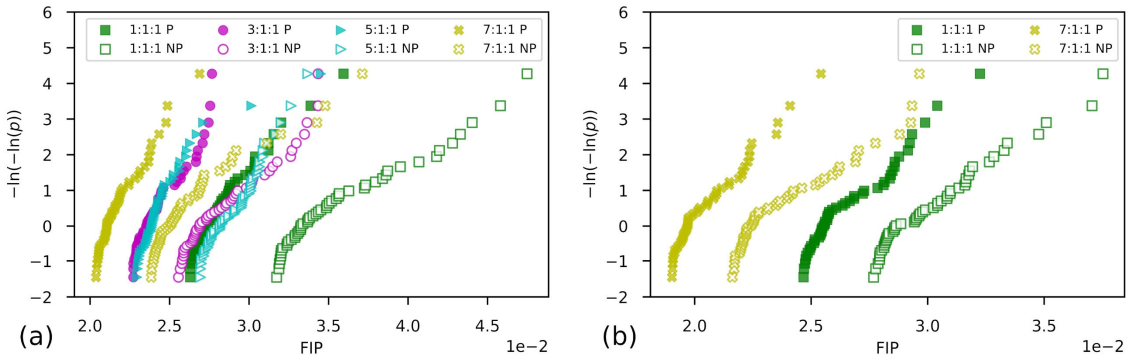

Figure 3.2. Gumbel EVD of the highest 50 Al 7075-T6 FIPs for (a) rolled and (b) random texture with varying grain elongation for surface (NP) and bulk (P) boundary conditions.

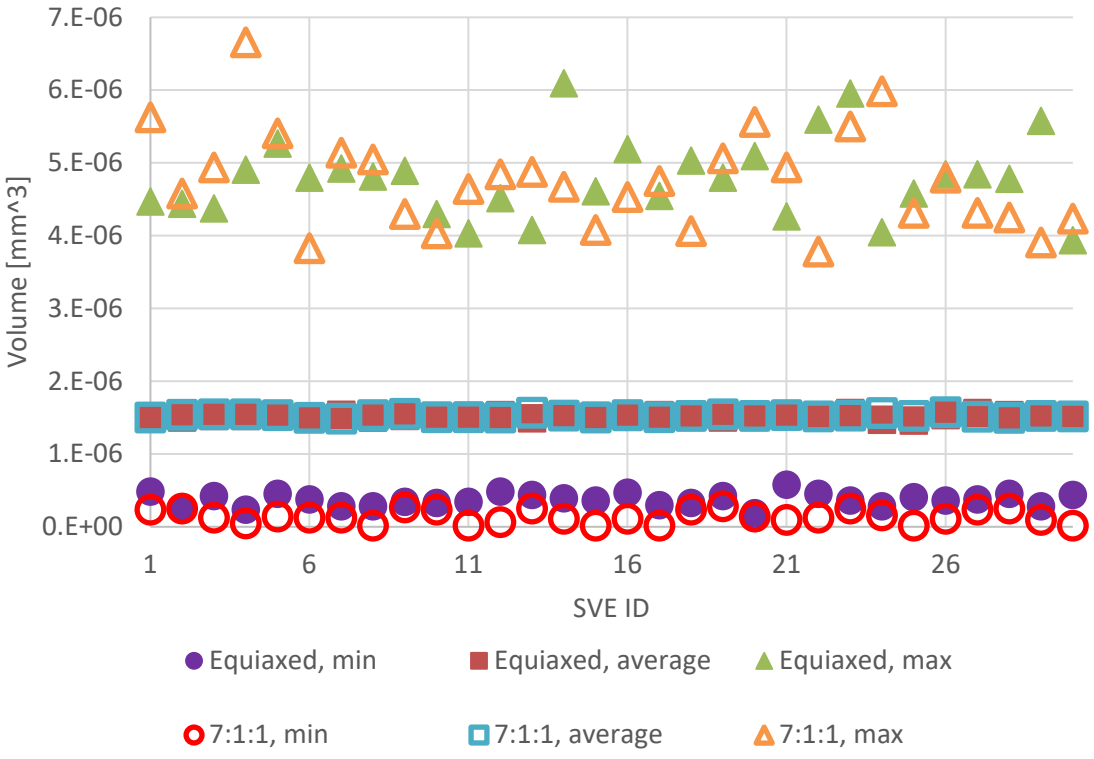

Figure 3.3. Grain volume (units in mm^3) statistics for equiaxed and 7:1:1 grain elongation ratios of Al 7075-T6 SVEs.

3.3.3 Free surface effects in Ti-6Al-4V

Ti-6Al-4V SVE ensembles are subjected to uniaxial cyclic straining in both X and Z directions to examine the combined effects of a free surface, crystallographic texture, and uniaxial straining direction. The highest 50 FIPs for the four Ti-6Al-4V textures strained in the two directions are shown in Figure 3.4. The random texture is loaded only in the X direction because no difference is expected in FIP response between different straining directions. In contrast to Al 7075-T6, there is only a slight increase in FIP magnitude between surface and bulk loading conditions; the transverse texture strained in

the Z direction (T-Z) shows little, if any, increase, like the cubic Al 7075-T6 texture. This same texture strained in the X direction (T-X), however, results in the highest FIPs observed and correlates with experimental findings by Peters et al. [147], who found that this combination of texture and loading direction resulted in the lowest fatigue strength out of the five they considered. This same experimental study, however, did not exhibit the superior performance of the T-Z texture shown here, which may indicate that FIPs below a certain threshold may not serve as adequate surrogate measures of driving force for fatigue crack formation (many of the T-Z FIPs are close to zero). Conversely, the β-annealed texture exhibits little difference with regard to straining direction, whereas the basal-transverse texture shows intermediate sensitivity. Although the transverse texture strained in the Z direction manifests the lowest FIPs, other factors must be considered in the process of material selection and component design. This texture's high sensitivity to straining direction may create issues for fatigue design of components if not accounted for. Additionally, performance requirements such as elastic stiffness and yield strength must be considered; the transverse texture loaded in the Z direction exhibits the lowest stiffness and strength [147].

To ensure enough grains are sampled during FIP compilation, Al 7075-T6 and Ti-6Al-4V FIPs are fit to the Gumbel EVD using 10, 20 and 30 SVEs per ensemble. While minor differences are observed when comparing EVDs of FIPs from 10 and 20 SVEs per ensemble, there is little difference in FIP position and no difference in the rank ordering observed in the figures when comparing EVDs of FIPs from 20 and 30 SVEs per ensemble. Therefore, we conclude that ensembles of 30 SVEs are sufficient for the rank ordering of textures, grain morphologies and straining directions (with the specified number of grains

per SVE used in this study). However, the different number of slip systems in these two materials may affect this number, as well as the fact that Ti-6Al-4V contain two phases, which may affect the total volume occupied by the most detrimental phase with regard to fatigue resistance.

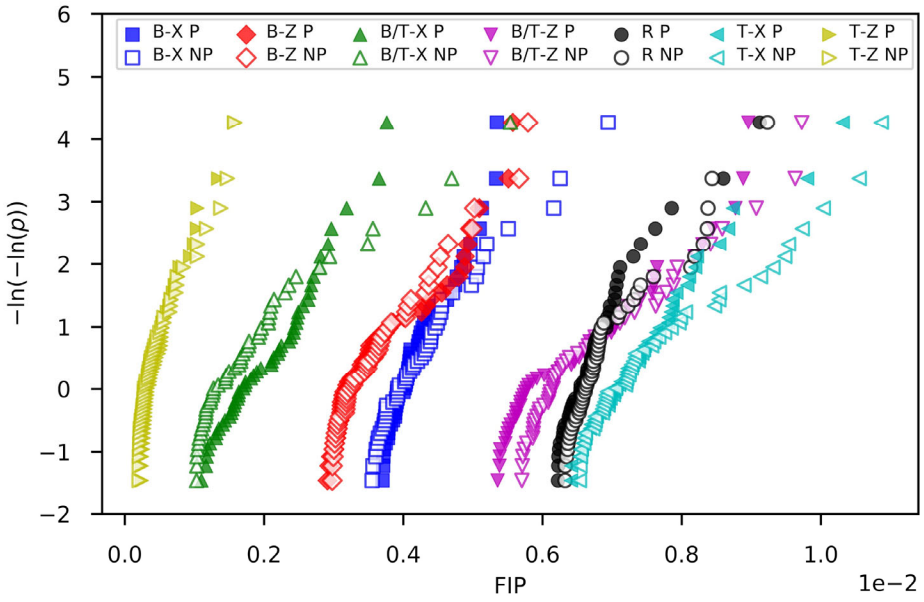

Figure 3.4. Gumbel EVD of the highest 50 Ti-6Al-4V FIPs with varying texture (β-annealed: B, basal-transverse: B/T, random: R, transverse: T) and straining direction (X or Z directions relative to $\langle 0001 \rangle$ ODF pole figure in Figure 2.5 for surface (NP) and bulk (P) boundary conditions.

3.3.4 Effects of grain size variation

The effects of grain size variation in Al 7075-T6 for the cubic, random and rolled texture are shown in Figure 3.5a, Figure 3.5b, Figure 3.5c, respectively. The intent of these simulations is to determine how nearest neighbor grains affect FIP response; a wider grain size variation will increase the probability that the FIP value for a grain will be influenced

by an increased number of neighboring grains. The cubic textured FIPs in Figure 3.5a vary at high cumulative probabilities but tend to merge at low to mid cumulative probabilities; an increase in grain size variation for traction-free conditions significantly increases FIP magnitude. In contrast, the FIPs for the traction-free random texture (Figure 3.5b) display a uniform increase in FIP magnitude at all cumulative probabilities. Lastly, the rolled texture (Figure 3.5c) displays a similar uniform increase in magnitude, which is exacerbated at the highest cumulative probabilities. The rank ordering of FIP magnitudes as a function of grain size variation is non-intuitive and changes for each texture, indicating non-trivial interactions between texture, grain size variation and the influence of a free surface in Al 7075-T6.

Less extreme effects of grain size variation are observed for Ti-6Al-4V. Little effect of the free surface is observed in comparing the random and T-X simulations (Figure 3.5d and Figure 3.5e, respectively), but the rank ordering of FIP magnitudes is flipped: the largest grain size variation in random textured SVEs results in FIPs of highest magnitude, whereas they are lowest for T-X. FIPs calculated for the T-Z straining condition (Figure 3.5f) only vary at the highest cumulative probabilities and merge at low cumulative probabilities, as the FIPs quickly tend to zero. The non-trivial effects observed for Al 7075-T6 hold true for Ti-6Al-4V and may require advanced probabilistic frameworks (such as use of extreme value marked correlation functions) for further elucidation [30, 65].

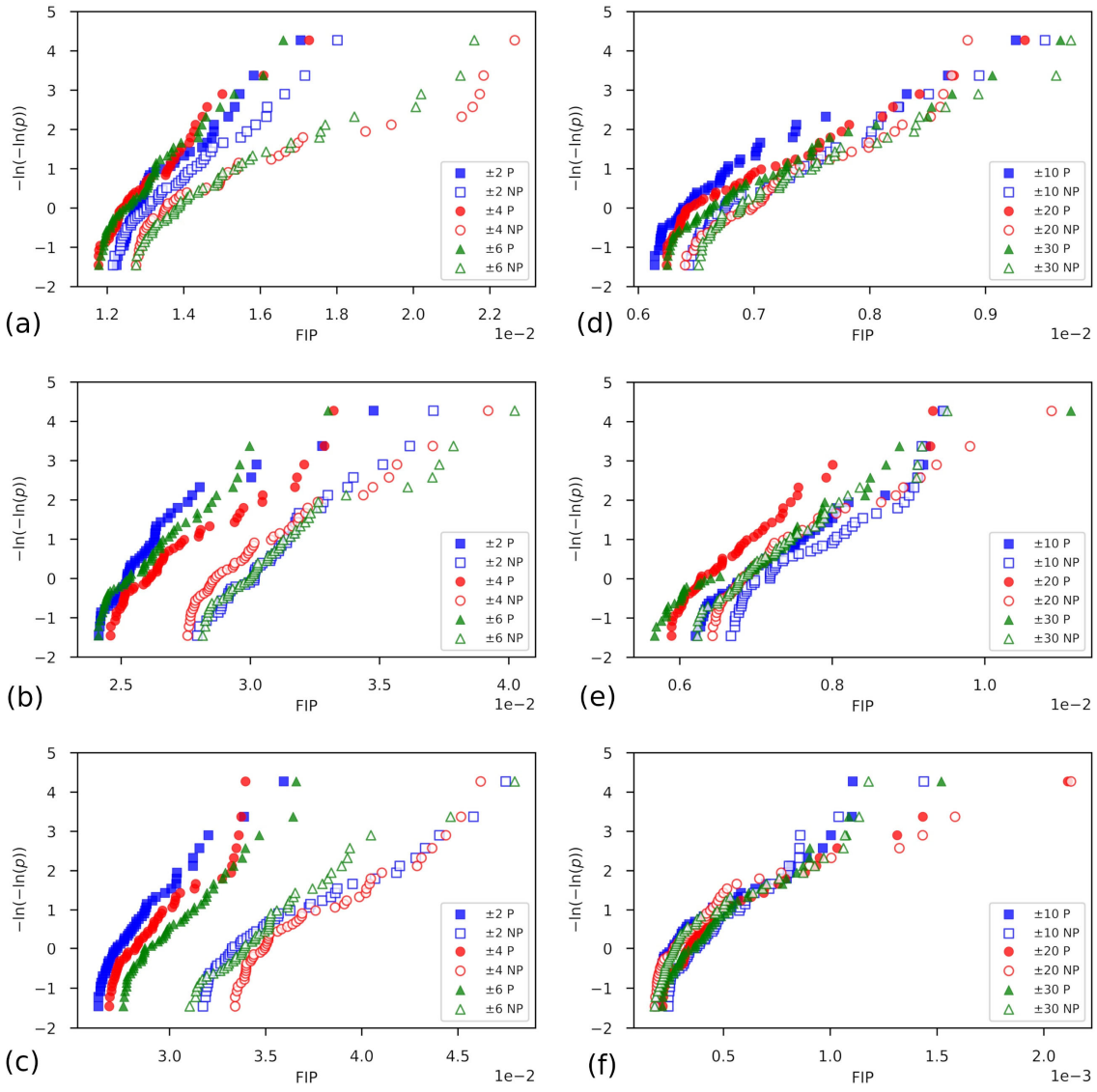

Figure 3.5. Gumbel EVD with varying grain size variation for the highest 50 Al 7075-T6 FIPs of (a) cubic, (b) random, and (c) rolled texture, and the highest 50 Ti-6Al-4V FIPs of (d) random, (e) T-X, and (f) T-Z texture, for surface (NP) and bulk (P) boundary conditions. All grains are equiaxed.

3.3.5 FIP Distance to the free surface

FIPs are further examined by considering their surface proximity in the traction-free simulations. The average distance from the traction-free boundary of the 10 highest Al 7075-T6 FIPs from ensembles varying in texture with equiaxed grains (Figure 3.1a) and grain elongation with rolled grains (Figure 3.2a) is computed. The minimum and maximum average distances are 3.77 μm and 9.19 μm, respectively, indicating a strong propensity for these FIPs to occur near the surface. If the FIPs had no propensity to occur near the free surface, the average values would be around 18.75 μm (half of 37.5 μm, which is the maximum distance from the free surface to the center of the Al 7075-T6 SVEs). FIPs with rolled texture and equiaxed grains are highest in magnitude, with the lowest average distance to the free surface (3.77 μm). However, this rank ordering between FIP magnitude and average distance to the free surface does not hold true for the remaining FIPs. There may be a threshold on Al 7075-T6 FIPs, above which the propensity to occur very close to the free surface is strongest.

For Ti-6Al-4V, the minimum and maximum average distances are 29.9 μm and 73.4 μm, respectively. Since the Ti-6Al-4V SVEs are larger, an average distance from the surface of 75 μm would indicate negligible preference for the highest FIPs to occur near the traction-free boundary (half of 150 μm, which is the maximum distance from the free surface to the center of the Ti-6Al-4V SVEs). Therefore, the Ti-6Al-4V FIPs have a much weaker propensity to occur near the free surface as compared to Al 7075-T6 FIPs. This suggests that the increased crystallographic slip and elastic symmetry of fcc Al 7075-T6 results in stronger interactions between individual grains and the free surface. In contrast, the low symmetry of hcp Ti-6Al-4V appears to result in much stronger interactions

between neighboring grains, which dominates free surface effects. Additionally, the Ti-6Al-4V SVEs are multiphase (50% α phase and 50% α+β colony phase), whereas Al 7075-T6 is single phase. Rank ordering between FIP magnitude and average distance from the free surface mimics that of Al 7075-T6, except for the β-annealed texture loaded in the Z-direction; FIPs of higher magnitude appear to occur closer to the free surface, whereas the lowest FIPs tend to occur throughout the SVE.

3.3.6 Distribution of slip in Al 7075-T6

Ti-6Al-4V FIPs vary mainly at high cumulative probabilities and tend to merge at mid to low cumulative probabilities (in most textures and straining directions considered). In contrast, Al 7075-T6 FIPs display clear separation at all cumulative probabilities (excluding the cubic texture, which varies the least between free surface and bulk boundary conditions). To investigate these EVD FIP tendencies, the number of activated slip systems in different Al 7075-T6 textures is analyzed.

For the three Al 7075-T6 textures with equiaxed grains, the plastic shear strain range during the last loading cycle is extracted for each integration point and for each of the 12 slip systems. Figure 3.6 shows the number of integration points with a select number of slip systems active (defined as having a plastic shear strain range above 0.00001). While there is minor difference between surface and bulk slip system activation, slip activity is more homogeneously distributed in the cubic texture (Figure 3.6a and Figure 3.6d), with the greatest number of integration points having eight active slip systems; four, six and eight active slip systems are most prevalent. Slip is much more homogeneously distributed

in cubic textured microstructures, thereby reducing FIPs since the probability of grains favorably oriented for significant slip is reduced.

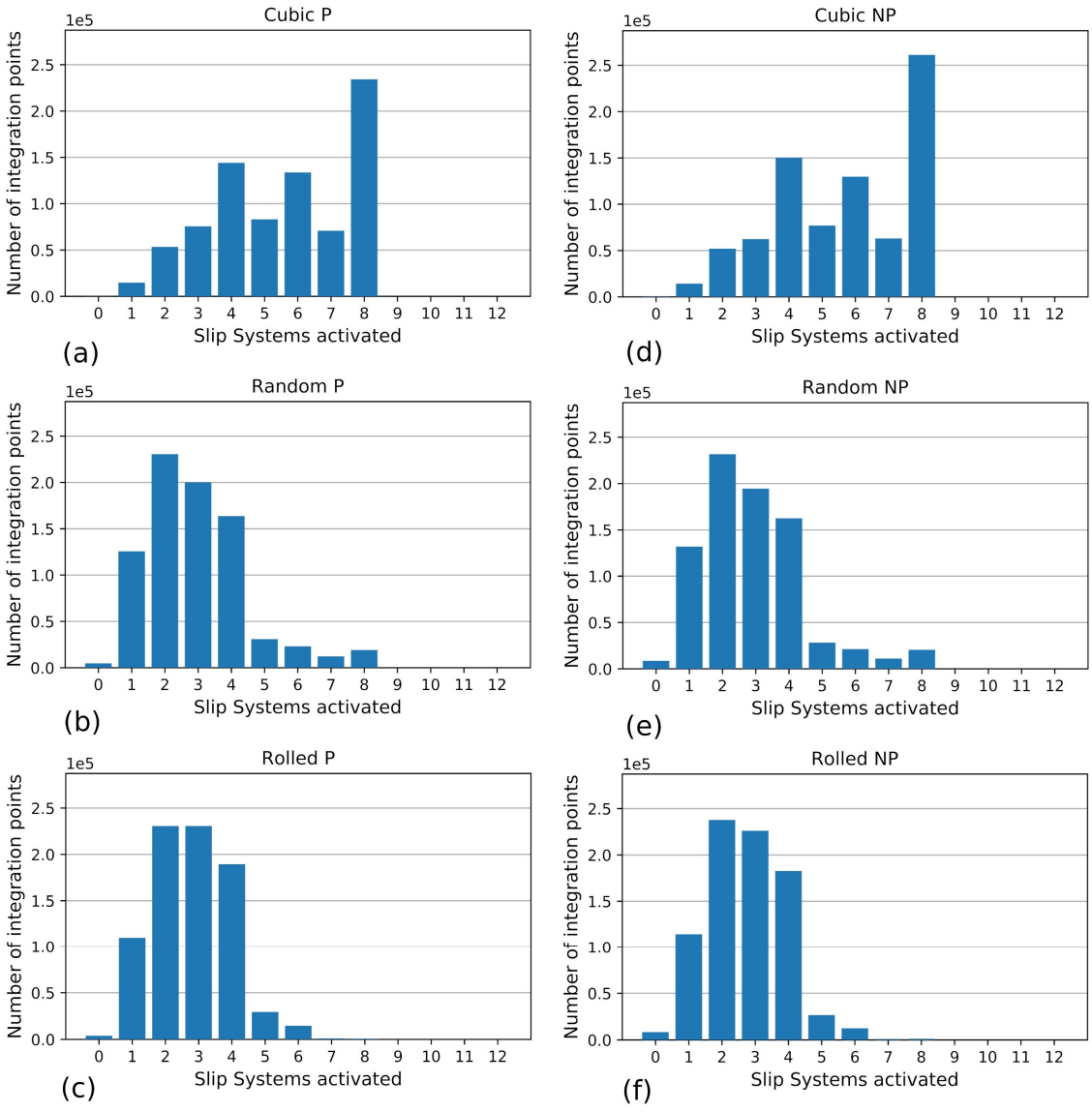

Figure 3.6. Number of integration points with a select number of slip systems active (criteria: plastic shear strange range above 0.00001) for (a,d) Cubic, (b,e) Random, and (c,f) Rolled texture of equiaxed Al 7075-T6 for surface (NP) and bulk (P) simulations. Crystallographic slip is more homogeneously distributed in the Cubic texture as compared to the Random and Rolled textures.

3.4 Conclusions

This chapter explores differences in EVDs of driving forces for fatigue crack formation in Al 7075-T6 and Ti-6Al-4V for a range of microstructure variants for several uniaxial cyclic straining directions, comparing cases representative of bulk and free surface. The main conclusions are as follows:

- Different combinations of textures, straining directions, and surface versus bulk boundary conditions for the two alloys results in different rank ordering of fatigue resistance as reflected by EVDs of FIPs.
- Due to differences in crystal structure and symmetry, the fcc Al 7075-T6 grains interact much more strongly with the free surface in producing high FIP values than is observed for hcp Ti-6Al-4V, in which individual grain/phase interactions dominate and no preference is indicated for surface-correlated activity. This aligns with the experimental trends discussed in Section 2.2.3: fatigue cracks in 7000 series Al alloys were found to form either at or within 10 μm of the free surface for various surface conditions and stress amplitudes [149, 150]. Alternatively, the location of fatigue crack formation in high strength titanium alloys such as Ti-6Al-4V is more sensitive to the surface condition and fatigue regime [151-153].
- FIPs of highest magnitude have strong propensity to occur much closer to the free surface for Al 7075-T6 than for Ti-6Al-4V.
- For uniaxial cyclic straining along the rolling direction, an increase in grain elongation in Al 7075-T6 results in a corresponding reduction of FIP magnitudes.

- More homogeneous slip system activation may alleviate both FIP magnitude and the effect of a free surface in Al 7075-T6, as observed with the cubic texture.

This computational study points to a clear role for *in situ* 3-D and 4-D experimental studies to further focus on quantitative correlations of microstructure with proximity to the free surface in producing extreme values of lattice distortion and cyclic plastic deformation in fatigue. In particular, the new finding of this chapter regarding apparent fundamental and non-intuitive differences in this regard between the propensity for a high symmetry fcc Al alloy and a low symmetry hcp Ti alloy to promote elevated driving forces for fatigue crack formation near the free surface should be explored experimentally. The gist of material in this chapter has been published as a standalone journal article [128].

CHAPTER 4. THE EFFECT OF MULTIAXIAL STRAIN STATES ON THE DRIVING FORCE FOR FATIGUE CRACK FORMATION

Multiaxial fatigue experiments are expensive and typically require specialized equipment and specimens, but they are essential to support fatigue design of components that experience multiaxial stress states. This represents a major practical limitation of fatigue design based on simple fatigue models or correlations based on uniaxial test data, for example. To leverage limited experimental data, this chapter pursues digital workflows and parametric simulations regarding the influence of multiaxial strain state on EVDs of the driving force for fatigue crack formation in realistic microstructures. Ensembles of SVEs for both Al 7075-T6 and Ti-6Al-4V polycrystalline microstructures are subjected to multiaxial cyclic straining to compute EVDs of FIPs that serve as computable surrogate measures of the driving force for fatigue crack formation.

4.1 Introduction

Fatigue experiments are crucial to quantify the mechanisms of fatigue crack formation. On one hand, modern testing and characterization techniques have outpaced the ability to fully understand the implications of measured data [2]. On the other hand, engineers must design structures subjected to multiaxial cyclic stress and strain states, based on calibration of life prediction methods to fatigue datasets that are often limited to a relatively small set of uniaxial experiments, sometimes with a bit of additional information regarding other stress states (e.g., cyclic torsion). Even if available, the interpretation of fatigue crack formation data corresponding to different stress states and specimen geometries is complicated by uncertainties arising from specimen design,

influence of strain gradients and stress concentrations, load frames, test configuration, test controllers, strain measurement, inference of damage, access to the surface, and definition of an initiated crack (shape, length relative to microstructure, etc.). Given the lack of multiaxial fatigue data and uncertainties listed above, the significant scatter of data in the transition and HCF regimes invites use of conservative forms of multiaxial fatigue criteria, often coupled with excessive safety factors. The ICME initiative seeks methods and algorithms to augment results from physical experiments with computational simulations based on digital microstructures subjected to complex stress/states with various models (e.g. crystal plasticity) [3]. These simulations facilitate more rapid assessment of the relative fatigue resistance of various microstructures subjected to complex loading conditions, including scatter or variability arising from randomness of microstructure. To replicate these strain states, complex test systems and specimen geometries capable of both biaxial and torsional loading are required (typically with hollow/tubular [187-195], or cruciform [196] specimens).

The early work of Brown and Miller [16] sought to quantify a relationship between fatigue life and complex multiaxial stress-strain states, considering the role of the imposed cyclic strain state relative to a free surface. Their review of metallurgical experiments revealed several key characteristics of fatigue crack formation and propagation processes. First, transgranular fatigue crack formation is controlled by cyclic shear (e.g., the plane of maximum shear), and the crack propagates due to slip irreversibility ahead of the crack tip. Early Stage I single slip dominates growth [197]. The crack growth transitions to Stage II, growing more or less perpendicular to the local peak tensile stress amplitude once the crack tip field samples enough grains ahead of the advancing crack. Second, the relative

orientation of the primary cyclic slip planes with respect to the free surface plays an important role in distinguishing regimes of observe fatigue crack formation and growth in favorably oriented surface grains. Third, Brown and Miller introduced dependence on the peak tensile strain normal to the plane of maximum shear strain range, considering that this normal strain influences mobility of dislocations and decohesion associated with irreversible slip activity.

Brown and Miller accordingly introduced the Gamma (Γ) Plane representing fatigue iso-life contours for all possible surface strain states [16]. They distinguished two cases of multiaxial loading, termed Case A and Case B. In Case A loading, the maximum shear strain range acts on a plane that intersects the free surface at 90 degrees, and cyclic shear does not produce substantial surface slip offset. In contrast, for Case B the maximum shear strain range intersects the free surface, resulting in a pronounced cyclic slip offset, and is considered as more likely to drive cracks into the bulk of the material, resulting in reduction of fatigue life corresponding to a formation and growth to a specified formation crack size for a given applied cyclic shear strain. These Cases have associated distinct crack shapes and aspect ratios for cracks with all dimensions on the order of microstructure, e.g., grain size. Fatemi and Socie [18] introduced a modified dependence on the peak tensile stress to the plane of maximum shear strain range, ostensibly to account for additional hardening due to out-of-phase (OP) multiaxial loading (caused by rotation of principal axes). They explored effects of mean stress in biaxial fatigue testing of Inconel 718, and considered extensions to variable amplitude loading. McDowell and Berard [19] applied a ΔJ-based correlation to multiaxial fatigue, considering both axial-torsional and tension-tension experimental results, to show correlations of iso-life contours in the Γ plane based

on principal plastic strains, which they labeled as the Γ^p plane. In addition, the formulation was consistent with experimentally-based forms of Γ Plane iso-life contours [16]. McDowell and Bennett [198] later built on this concept and considered multiple regimes, including fatigue crack formation and early growth within a nucleant grain, Stage II growth within the first few grains/phases, and the transition to Stage II growth. Microcrack growth behavior of 1045 steel and IN 718 was qualitatively predicted using the Fatemi-Socie parameter as a surrogate driving force parameter.

The two alloys investigated in this chapter are Al 7075-T6 and Ti-6Al-4V. The multiaxial fatigue responses of these two alloys have been extensively studied experimentally. Zhao and Jiang [187] performed uniaxial, torsional, and axial-torsional loading experiments on aluminum alloy 7075-T651, and found that the mean stress has a significant effect on fatigue life. For aerospace alloy 2024-T3, Gates and Fatemi [195] found that for the same equivalent nominal stress, experimental fatigue lives in pure torsional loading exceeded those for the uniaxial case. They correlated specimen fatigue life using the Fatemi-Socie parameter within a factor of three, and later used this same parameter to correlate fatigue lives of 7075-T651 [199]. Lee and Taylor [196] studied the fatigue crack growth behavior of aluminum alloys 7075-T651 and 1100-H14 with cruciform specimens. Fatemi, Shamsaei and colleagues investigated multiaxial fatigue behavior affected by surface roughness [200], and load path alteration/sequence effects [192] in Ti-6Al-4V and another titanium alloy similar to Ti-6Al-4V (Ti-6.5Al-3.4Mo). Hoshide et al. [190] revealed different crack growth behavior for two different microstructures of Ti-6Al-4V under low cycle fatigue (LCF) multiaxial loading conditions. Wu et al. [191] performed multiaxial fatigue experiments on TC4 (which is the titanium

equivalent of Ti-6Al-4V in China) and correlated fatigue lives to a new critical-plane parameter based on the Fatemi-Socie parameter. Berto et al. [193] studied Ti-6Al-4V multiaxial behavior under a variety of loading conditions, including Mode I and Mode III, various load ratios, and both smooth and notched specimens. A study of mean strain effects on the LCF multiaxial behavior of Ti-6Al-4V was carried out by Itoh et al. [188]. Meneghetti et al. [194] performed both physical and numerical experiments on Ti-6Al-4V and studied the effects of different notch root radii.

In this chapter, the completely reversed fatigue response of the two alloys of interest is examined under different strain states (uniaxial, shear, biaxial) and strain amplitudes. Several important factors that further complicate the fatigue response of components under multiaxial loading conditions are not considered here (mean stress/strain effects [187, 188, 199, 201], notches [193-196], IP vs. OP loading [165, 187-189, 191-196, 199], variable amplitude loading, and load sequence effects [192]). Instead, the focus is on multiaxial response of near surface grains under various strain states for completely reversed, constant amplitude room temperature fatigue. The computational tools employed here have been previously applied to study the fatigue response of the two materials of interest [30, 64, 127], as well as Ni-base superalloys IN100 [47, 65, 202] and RR1000 [31, 156, 170], and martensitic gear steels [155, 203]. Castelluccio and McDowell [156] performed numerical simulations of Ni-base superalloy RR1000 to study the effects of different strain ratios, multiaxial strain states, and geometric discontinues. The work replicated experimental trends: fatigue life under torsional loading exceeds that of axial tension-compression for both smooth and notched members. In addition, Kern [169] used models for both fatigue crack formation and microstructurally small fatigue crack growth to generate a first

generation set of iso-life contours in the Γ Plane for Al 7075-T6 that served as proof of concept for the present work.

The outline of this chapter is as follows. Section 4.2 describes the tools unique to this chapter that are used alongside the CPFEM models and FIPs described in Chapter 2. Results are discussed in Section 4.3 with conclusions in Section 4.4.

4.2 Methodology

The multiaxial strain states and strain magnitudes that are unique to this chapter are discussed first. The microstructures and textured explored are then described. Finally, the process of generating a computational Γ plane is presented.

4.2.1 Boundary and Loading Conditions

The simulated strain states include uniaxial tension-compression, equibiaxial tension-compression, simple shear, and pure shear. These are shown in Figure 4.1, where the red, dashed prisms represent the deformed state in each case. Both pure and simple shear are investigated to study the differences between these two methods of shear deformation. Segal [204] presents a thorough overview of these two deformation modes, and discusses both theoretical and experimental analyses. Pure shear involves no rotation; principal strain directions coincide with principal stress directions [204]. In contrast, simple shear involves a rotation, and for relatively small strains, simple shear may be expressed as pure shear with an additional rotation. The differences in these two modes of shear have important implications on processing characteristics of metals (texture evolution, hardening, etc.) [204]. In this chapter the possible effects of these two modes of cyclic

shear on fatigue response are evaluated since experiments typically lie between these two conditions.

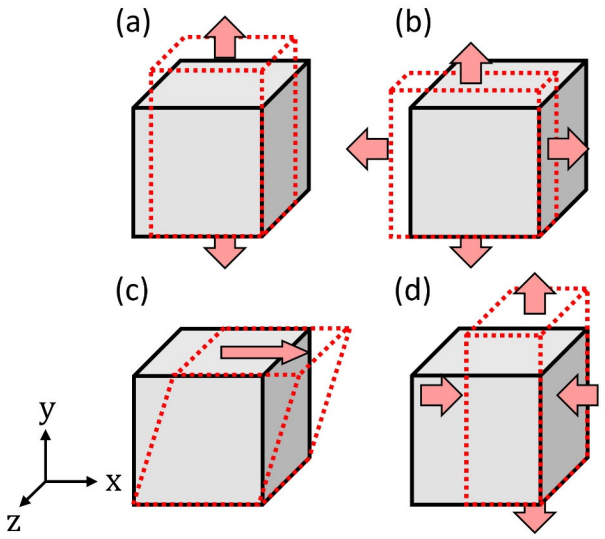

Figure 4.1. Diagrams of deformation and corresponding strain states that span the entire range of the Γ plane for (a) uniaxial tension-compression, (b) equibiaxial tension-compression, (c) simple shear, and (d) pure shear. The red, dashed prisms indicate the deformed state.

The maximum shear strain is considered as the measure of equivalent strain for purposes of imposing target loading levels in the simulations. The applied strain amplitudes are such that the maximum shear strain amplitude is the same for all strain states imposed. Of course, this is not assumed as the fatigue criterion, since that emerges naturally from the simulations; rather, it allows to populate simulations with target levels of loading across strain states. The maximum shear strain amplitude is first determined for uniaxial tension-compression (Figure 4.2a) at some initial desired fully-reversed strain amplitude (this is chosen as 0.705% to reflect loading conditions near HCF). Strain is applied in the Y axis and contracts the material in the X and Z axes due to the Poisson effect. This corresponds to an equivalent shear strain of approximately 0.965% (verified in simulations by calculating macroscopic stress-strain response). Thus, for target equivalency between

uniaxial and simple shear simulations, the chosen applied strain amplitudes are 0.705% and 0.965% for Al 7075-T6, respectively. With this information, the required strain amplitudes for the other two deformation modes may be determined; these values are shown in Table 4.1. In equibiaxial straining, normal strains are applied in the X and Y axis directions simultaneously, with contraction in the Z axis Figure 4.1b and Figure 4.2b). For pure shear, the strains in the X and Y axes are equal and opposite in magnitude and result in near zero strain in the Z axis (Figure 4.1d and Figure 4.2c). Two maximum shear strain amplitudes are explored for both alloys (termed "low" and "high" as shown in Table 4.1). For each strain state, the corresponding strain amplitude is determined via numerical simulation of polycrystals to ensure that the comparison between different deformation modes pertains to the same maximum shear strain amplitude. Note that this comparison could also have been made based on the same maximum plastic shear strain. The surrogate driving forces (i.e., FIPs) to form fatigue cracks will be assessed within each grain in the polycrystalline ensembles and as described later, curves will be interpolated in the Γ plane given the computational data based on Table 4.1. Such interpolation would be necessary even if equivalent strains were employed based on plastic strain.

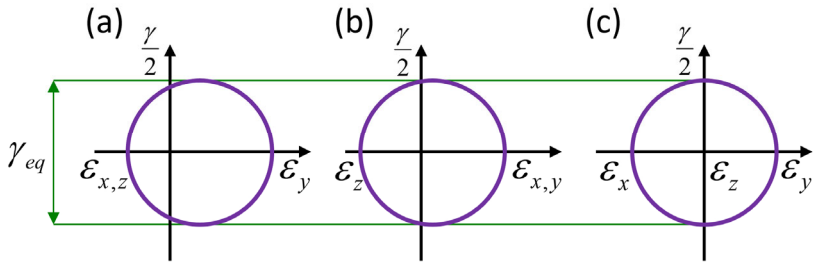

Figure 4.2. Mohr's circle of strain for (a) uniaxial, (b) equibiaxial and (c) pure shear deformation, with strain applied in the Y, X/Y, and X/Y directions, respectively. The maximum shear strain is equal to the diameter of each circle.

Table 4.1. Fully-reversed applied strain amplitudes for various strain states for both materials at two maximum shear strain amplitudes (termed "low" and "high"). The associated Mohr's circles of strain are shown in Figure 4.2.

Material	Strain level	Uniaxial (%)	Equibiaxial (%)	Simple shear (%)	Pure shear (%)	Maximum shear strain (%)
Al 7075-T6	Low	0.705	0.455	0.955	0.478	0.955
	High	1.000	0.615	1.391	0.695	1.391
Ti-6Al-4V	Low	0.705	0.478	0.931	0.466	0.931
	High	1.000	0.663	-	-	1.340

The faces of the SVEs parallel to the X-Y plane (i.e., perpendicular to the Z-direction) are non-periodic and traction-free to assess the influence of the free surface on the maximum local cyclic plastic shear response under the four different deformation modes. For all simulations, three fully reversed ($R_\varepsilon = -1$) strain-controlled cycles at a quasistatic strain rate of 0.001 s^{-1} are applied to promote elastic-plastic shakedown and correspond to proportional straining (in-phase). Preliminary analysis shows that after three cycles, FIPs saturate (increase by less than 1%) and additional loading cycles are not warranted. Temperature is assigned as 300K, with zero initial back stress and zero initial strain and plastic strain.

The Ti-6Al-4V basal and prismatic slip systems are easiest to activate (due to the relatively low CRSS values compared to the pyramidal slip systems) and therefore accommodate most of the deformation. However, the pyramidal slip systems accommodate deformation along the c-axis of the hcp crystal structure. At the higher strain level, Ti-6Al-4V is strained solely in uniaxial and equibiaxial fatigue; under shear strain, the anisotropy

in deformation and available slip systems results in poor numerical convergence within three fully-reversed straining cycles.

4.2.2 Microstructure generation

DREAM.3D [113] is used to generate all microstructures for the multiaxial simulations. SVE ensembles are generated to compile the statistical distribution of FIPs pertinent to large volumes of microstructure. The SVE instantiations in this chapter are cubic with 30^3 elements for both material systems.

SVE ensembles of two crystallographic textures are explored for equiaxed Al7075: random and cubic with the ODF pole figures shown in Figure 2.4. Each ensemble contains 30 SVEs with one set of parallel faces normal to the Z direction being non-periodic and traction-free. This boundary condition is representative of a thin sheet of material with a relatively high surface area-to-volume ratio, which still allows for near-bulk conditions at the center of the SVE. These conditions are identical to the CPFEM simulations in the previous chapter which evaluated the effects of a free surface on the driving force for fatigue crack formation for Al 7075-T6 and Ti-6Al-4V with different crystallographic textures under different uniaxial straining directions. As a reminder, it was concluded there that ensembles of 30 SVEs suffice for the rank ordering of different microstructure attributes. Each SVE ensemble undergoes the four strain states described in the previous section. Grains are equiaxed and follow a lognormal grain size distribution with an average grain size of 14 ± 2 μm. The volume of each cubic SVE is to $(75\ \mu m)^3$ and results in an average of 278 grains per SVE. Although two different textures of Al7075 are simulated,

the difference in required strain amplitude to reach the same equivalent shear strain for the different deformation modes (described in Section 4.2.1) is less than 1%.

The Al 7075-T6 cubic texture has strong cubic symmetry (as shown in Figure 2.4a). Under fully periodic boundary conditions, the direction of applied strain for any of the four strain states shown in Figure 4.1 is expected to result in the same material response (i.e., uniaxial straining in the X, Y, and Z directions, or equibiaxial straining in the X-Y vs. X-Z vs. Y-Z, will produce equivalent results). In the case of free surface simulations, displacements are applied in the X and Y directions, but result in no expected difference in material response. Furthermore, under pure shear loading, whether tension and compression are initiated in the X and Y directions, respectively, or vice-versa, makes no difference in the expected material response. For Ti-6Al-4V, the simplest texture (not including the random texture) is the basal-transverse (B/T) texture, which forms after unidirectional rolling at relatively low temperatures [148] (the ODF pole figure is shown in Figure 2.5b). The reduced symmetry of the hcp crystal structure as compared to fcc means that for any of the four strain states shown in Figure 4.1, multiple straining directions must be performed with the B/T texture due to the difference in expected response [79]. For instance, uniaxial straining in the X and Y directions is expected to result in drastically different material responses, as demonstrated in the previous chapter. The same is true for the other three strain states, and so to reduce the total number of simulations performed, only the random texture for Ti-6Al-4V is examined (ODF pole figure shown in Figure 2.5d). Composition is set to 50% α phase and 50% α+β colony phase, with a lognormal grain size of 60 ± 15 μm which results an average of 264 grains per SVE.

4.2.3 Generation of Γ plane Iso-FIP Contours

Experimentally-based construction of iso-life contours on the Γ Plane for all possible surface strain states is challenging and expensive for many reasons. To examine the possible deformation modes (uniaxial, equibiaxial, shear, and everything in-between) for an array of strain amplitudes, access to special test equipment is required. Microstructure variability (which causes fatigue life scatter, particularly in the HCF regime) requires multiple experiments for each strain state and amplitude. Moreover, imposition of strain conditions to achieve the same target lifetime for various strain states has a great deal of uncertainty. In this chapter, a micromechanical, microstructure-sensitive computational approach is developed to estimate iso-FIP contours in the Γ Plane for both materials with random texture. Kern [169] was the first to produce a similar Γ Plane with iso-life contours for Al 7075-T6 (by correlating FIPs/damage parameters to experimental fatigue lives). Several improvements are introduced in this section: a) the SVE mesh is heavily refined to represent more realistic microstructures, b) more SVEs are included in the ensemble to better capture inherent fatigue variability, and c) FIPs are volume averaged over sub-band regions, which provides a regularized averaging scheme without excessive smearing of individual element FIPs. A Gaussian Process Regression (GPR) model (also referred to as Kriging) is used to generate the iso-FIP contours by sampling the fatigue response, which we defined here as the average of the 10 highest FIP per grain of the ensemble at each response coordinate.

A new ensemble of 10 SVEs is subjected to cyclic straining to populate the Γ Plane response surface, as depicted in Figure 4.3 and Figure 4.4 for Al 7075-T6 and Ti-6Al-4V,

respectively. Table 4.2 lists the fully-reversed strain amplitudes used to populate the response surface. The abscissa and ordinate represent the maximum shear strain and the tensile strain normal to the plane of maximum shear, respectively, for completely reversed straining in the form

$$\frac{\varepsilon_1 - \varepsilon_3}{2} = f\left(\frac{\varepsilon_1 + \varepsilon_3}{2}\right) \tag{4.1}$$

where $\varepsilon_1 \geq \varepsilon_2 \geq \varepsilon_3$ are the ordered principal strains used to describe the macroscopic strain state [16]. To avoid distortion of the bounds of the FIP contours in the Γ Plane due to the Poisson effect, the principal plastic strains are used instead of the total principal strains, i.e., $\varepsilon_1^p \geq \varepsilon_2^p \geq \varepsilon_3^p$. The resultant plot is referred to as the Γ^p plane. Different markers represent different macroscopic strain states: in Figure 4.3, squares and triangles represent Case A and Case B loading, respectively, whereas the circles represent uniaxial loading, which is Case A and B simultaneously. For Ti-6Al-4V, only Case B contours are simulated due to the difficulties with model convergence at the higher shear strain amplitudes required for reasonable macroscopic plastic strains (as described in Section 4.2.1). To determine the response coordinate of the ensemble under various strain states/amplitudes, the macroscopic plastic strain tensor for each SVE is calculated with each element's plastic strain tensor. The plastic strain tensor for each SVE is then averaged and used to determine the principal plastic strains of the ensemble at a particular strain state/magnitude, which locate the ensemble in Figure 4.3 and Figure 4.4. Kern [169] recognized that the use of a coarser mesh and a limited number of SVEs in the ensemble introduces variation in both the response coordinate (principal plastic strains) and response value (in the case of Kern's

work, crack growth). The improved ensemble fidelity in this work (heavily refined SVEs and more SVEs per ensemble) results in negligible differences in macroscopic plastic strain tensors between the SVEs at any given strain state/amplitude, and so variation in the response coordinate may be neglected.

Table 4.2. Fully-reversed applied strain amplitudes (lowest to highest) used to populate the Γ^p Plane response surface.

Material	Uniaxial (%)	Equibiaxial (%)	Pure Shear (%)
Al 7075-T6	0.72 to 1.12	0.49 to 0.73	0.52 to 0.86
Ti-6Al-4V	0.85 to 1.01	0.53 to 0.69	-

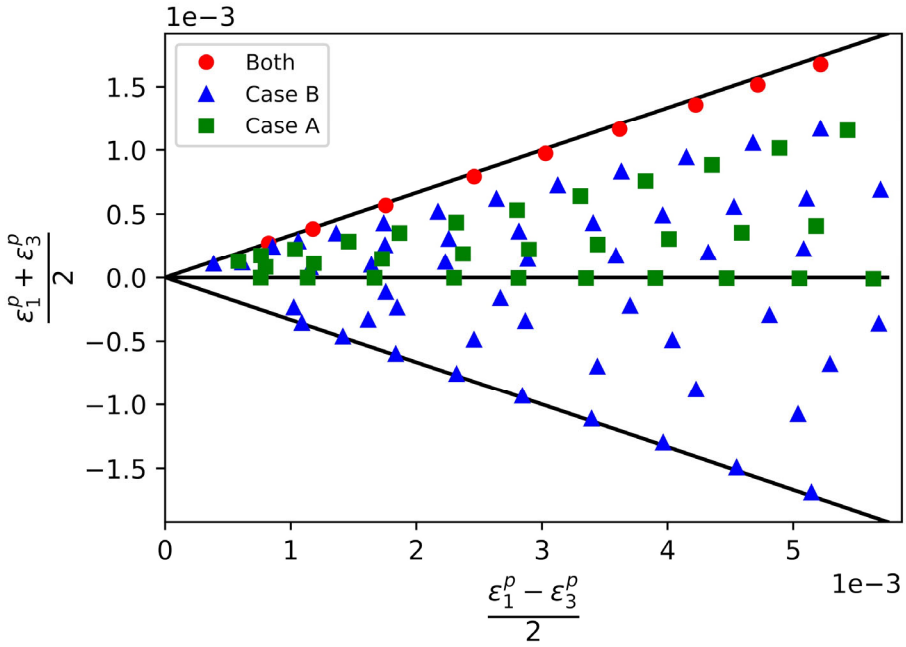

Figure 4.3. Response coordinates of Al 7075-T6 (10 SVE ensemble with random texture) on the Γ^p Plane framed in terms of polycrystal (macroscopic) principal plastic strains. The upper and lower limits represent the uniaxial and equibiaxial strain state, respectively, and the abscissa corresponds to pure shear.

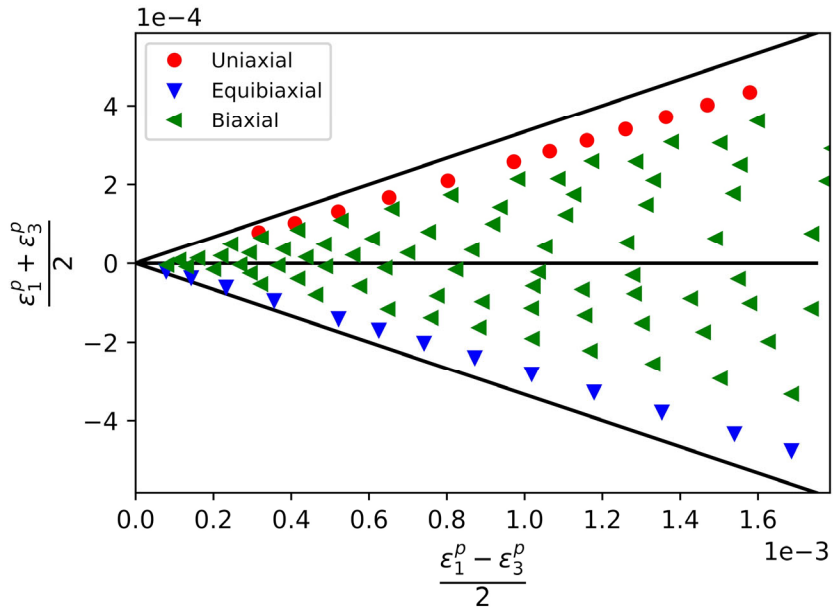

Figure 4.4. Response coordinates of Ti-6Al-4V (10 SVE ensemble with random texture) on the Γ^p Plane framed in terms of polycrystal (macroscopic) principal plastic strains. In contrast to the Al 7075-T6, only Case B contours are calculated due to the difficulty in convergence under high shear strain amplitudes).

Three fully-reversed straining cycles are applied, and in accordance with Section 2.7, the single highest sub-band-averaged FIP of each grain is identified and compiled for the entire ensemble. Each response coordinate's averaged FIP constitutes the response surface. The GPR model then interpolates the space between the response coordinates with the response surface as the input, and in general can also provide empirical confidence intervals. Predetermined values for the iso-FIP contours are used with the GPR-generated response surface to then create the iso-FIP contours [205]. For Al 7075-T6, separate contours are generated for both Case A and Case B. FIPs from uniaxial straining (red circles in Figure 4.3) are lumped with the Case A dataset. To ensure continuity in the contours at the upper uniaxial limit of the Γ^p Plane, the GPR predicted iso-FIP data from Case A is fed into the Case B data. For both Γ^p Planes, the noise parameter is adjusted appropriately to aid with numerical stability and convergence of the GPR model. Lastly, the uniaxial and

equibiaxial response coordinates in Figure 4.4 do not lie exactly on the Γ^p Plane bounds due to the increase anisotropy of Ti-6Al-4V.

4.3 Results and Discussion

4.3.1 Al 7075-T6 FIPs

Random textured Al 7075-T6 FIPs are fit to the Gumbel EVD and shown in Figure 4.5a and Figure 4.5b for low and high strain levels, respectively, in reference to Table 4.1. Figure 4.5a shows nearly equal FIP distributions under uniaxial and equibiaxial straining to the same equivalent shear strain (0.955%), and also under both types of shear. At a higher equivalent shear strain (1.391%), equibiaxial and simple shear FIPs surpass uniaxial and pure shear FIPs, respectively (Figure 4.5b).

The previous chapter investigated the surface proximity of the 10 highest FIPs of each ensemble and showed that under uniaxial straining, the highest FIPs appeared close to the free surface, especially for the random and rolled textures. Figure 4.5c shows the surface proximity of the 10 highest FIPs in Figure 4.5a. In accordance with the previous chapter, the highest Al 7075-T6 FIPs under all deformation modes appear close to the free surface. The average distance to the free surface of the FIPs in Figure 4.5c ranges from 4.25 μm to 12.53 μm, and ranges from 6.19 μm to 9.84 μm in Figure 4.5d (strained to the higher equivalent shear strain). The average distance to the free surface of the top 10 FIPs from all simulations is shown in Table 4.3. The previous chapter concluded that the differences in crystal structure and symmetry between fcc Al 7075-T6 and hcp Ti-6Al-4V results in Al 7075-T6 grains interacting more strongly with the free surface to produce high FIPs, whereas Ti-6Al-4V grain interactions dominate and show weak free surface influence

(under fully-reversed uniaxial straining to a strain amplitude of 0.8%). Overall, the numerical results reflect experimental observations by Gates and Fatemi [195]: under an equivalent strain condition, fatigue lives under shear straining exceed those under uniaxial straining, as reflected by the decreased FIP magnitudes shown in Figure 4.5. Lee and Taylor [196] performed biaxial fatigue experiments with notched Al 7075-T6 cruciform specimens and found that equibiaxial loading with applied stresses below one-third of the yield strength resulted in the longest fatigue lives. However, specimen failure was defined once the crack length grew from 1 mm to 140 mm, and so their experiments pertain more to fatigue crack growth rather than fatigue crack formation, which is relevant to this study.

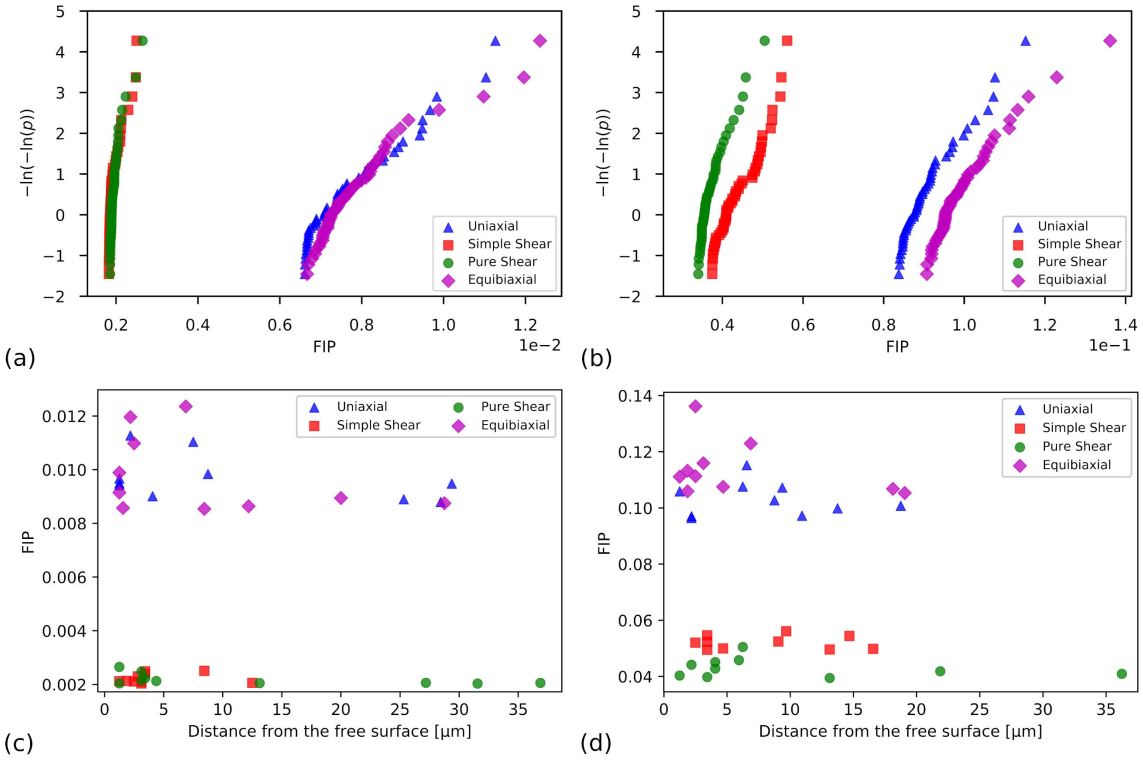

Figure 4.5. Al 7075-T6 FIPs with random texture fit to the Gumbel EVD under the (a) low and (b) high strain level (in reference to Table 4.1). The distance from the free surface of the top 10 FIPs is shown in (c) and (d) for the low and high strain levels, respectively. The maximum distance from the free surface is 37.5 μm because SVE volume is $(75\ \mu m)^3$.

Table 4.3. Fully-reversed applied strain amplitudes for various strain states for both materials at two maximum shear strain amplitudes (termed "low" and "high"). The associated Mohr's circles of strain are shown in Figure 4.2.

Material	Strain level	Uniaxial	Equibiaxial	Simple shear	Pure shear
Al 7075-T6 Random	Low	10.94	8.50	4.25	12.53
	High	8.00	6.19	8.06	9.84
Al 7075-T6 Cubic	Low	12.63	13.75	16.28	21.20
	High	4.31	4.19	13.69	19.38
Ti-6Al-4V	Low	74.00	80.00	81.63	71.75
	High	22.63	16.63	-	-

Cubic textured Al 7075-T6 FIPs are shown in Figure 4.6a and Figure 4.6b for low and high strain levels, respectively, in reference to Table 4.1. There is now a significant increase in FIPs under simple shear straining as compared to pure shear. As a matter of fact, at the lower strain level under simple shear straining, cubic textured FIPs exceed random textured FIPs. Aside from this one instance, random textured FIPs are higher in magnitude at either strain level or any strain state. The reason for this is the anisotropy of the fcc crystal structure. Uniaxial straining along the fcc <001> direction results in an equal probability for slip on eight of the 12 slip systems, and in a cubic textured Al 7075-T6 polycrystal, uniaxial straining in any one of these global direction distributes slip much more homogeneously as compared to other textures, as shown in Section 3.3.6. Pure shear, uniaxial and equibiaxial straining of the cubic textured Al 7075-T6 SVEs are all along the <001> directions, which homogeneously distributes slip across the 12 slip systems.

Extreme FIP values are due to intense slip activity on any particular slip system (in addition to the stress normal to the respective slip plane), which is characteristic of heterogeneous slip distribution. Additionally, simple shear no longer distributes slip homogeneously and results in the increased FIP magnitudes observed in Figure 4.6a and Figure 4.6b. Pure shear, uniaxial and equibiaxial straining along directions other than <001> would therefore also be expected to result in an increase in FIP magnitude. In contrast to the random textured Al 7075-T6 FIPs, the cubic textured FIPs under all deformation modes at the lower strain level and both types of shear straining at the higher strain level show weak propensity to manifest near the free surface. Cyclic uniaxial and equibiaxial straining at the higher strain amplitude, however, results in the lowest distances to the free surface out of any set of 10 Al 7075-T6 FIPs; detailed values are shown in Table 4.3. The orientations of the sub-bands with the highest FIPs are expected to be nearly identical in the cubic textured SVEs relative to the global straining directions. In contrast, the random textured SVEs contain sub-bands that span all possible orientations, but the highest FIPs reside on sub-band planes most favorably oriented for slip.

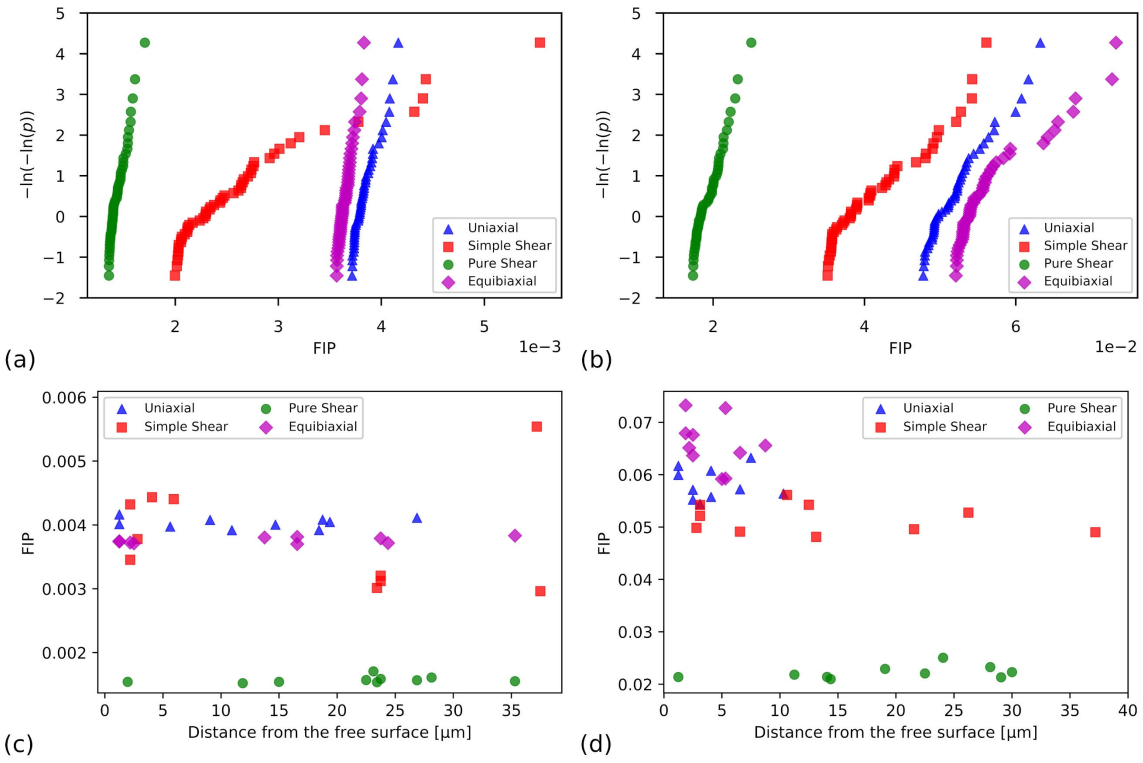

Figure 4.6. Al 7075-T6 FIPs with cubic texture fit to the Gumbel EVD under the (a) low and (b) high strain level (in reference to Table 4.1). The distance from the free surface of the top 10 FIPs is shown in (c) and (d) for the low and high strain levels, respectively. The maximum distance from the free surface is 37.5 μm because SVE volume is $(75\ \mu m)^3$.

4.3.2 Al 7075-T6 Γ^p Plane

Computed iso-FIP contours in the Γ^p Plane for Al 7075-T6 with random texture and equiaxed grains are shown in Figure 4.7. The iso-FIP contours bear striking resemblance to experimental trends observed by Brown and Miller (cf. Fig. 6 and Fig. 7 in [16]). Although the contours here represent FIPs and not fatigue lives, a calibration may be performed to transform the Γ^p plane into one with fatigue life. The Case A and Case B contours are generated separately, and as a result display a slight discontinuity at the top of Figure 4.7. Iso-FIP contours for Al 7075-T6 with cubic texture are not expected to be

identical to the Random textured contours shown here. Creating a similar gamma plane for a textured SVE ensemble is complicated by virtue of loading direction. As mentioned previously, the FIP response of a cubic textured SVE will depend heavily on the global loading direction. Therefore, a cubic textured SVE ensemble would result in multiple Γ^p Planes because uniaxial, biaxial and shear can be applied in various direction with respect to the ODF pole figure shown in Figure 2.4a.

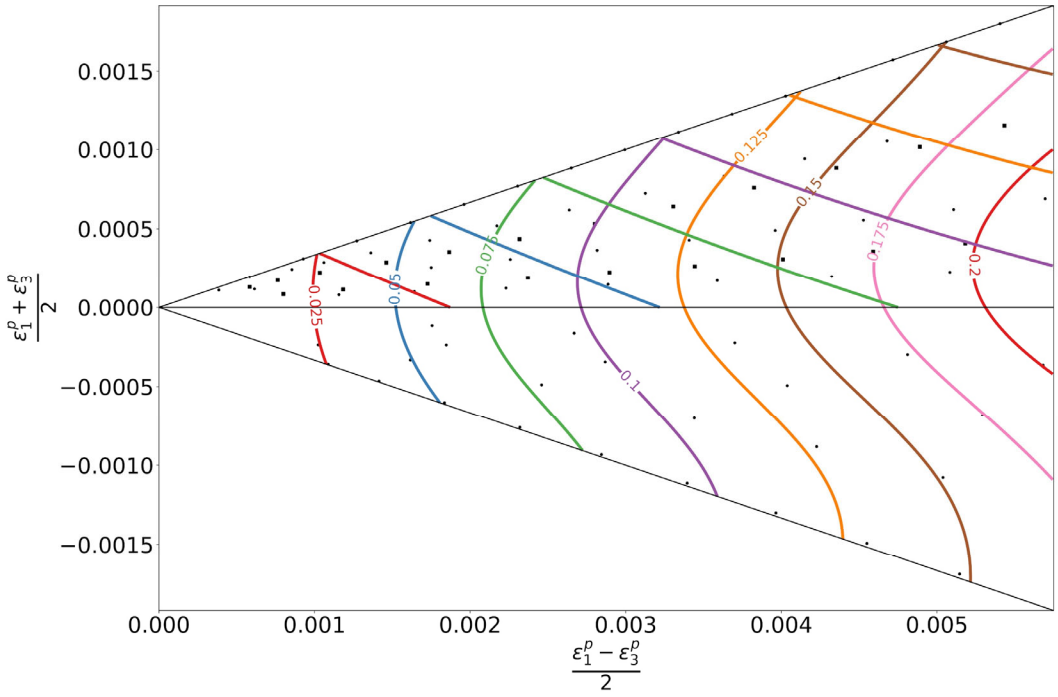

Figure 4.7. Computed iso-FIP contours in the Γ^p Plane for Al 7075-T6 (equiaxed grains with random texture).

4.3.3 Ti-6Al-4V FIPs

Ti-6Al-4V random textured FIPs are shown in Figure 4.8a and Figure 4.8b for low and high strain levels, respectively, in reference to Table 4.1. Interestingly, simple shear straining results in a notable increase in FIPs as compared to pure shear. Ti-6Al-4V fatigue

experiments show that fatigue lives are longer in shear than uniaxial straining/loading [189-192, 206]. In contrast to random textured Al 7075-T6 FIPs at the higher strain level, Ti-6Al-4V uniaxial FIPs exceed those of equibiaxial straining. This coincides with experimental results by Wang et al. [207] and Doquet and De Greef [208], which showed a positive influence on fatigue life with an increase in stress ratio (biaxiality) for pure titanium and Ti-6Al-4V, respectively.

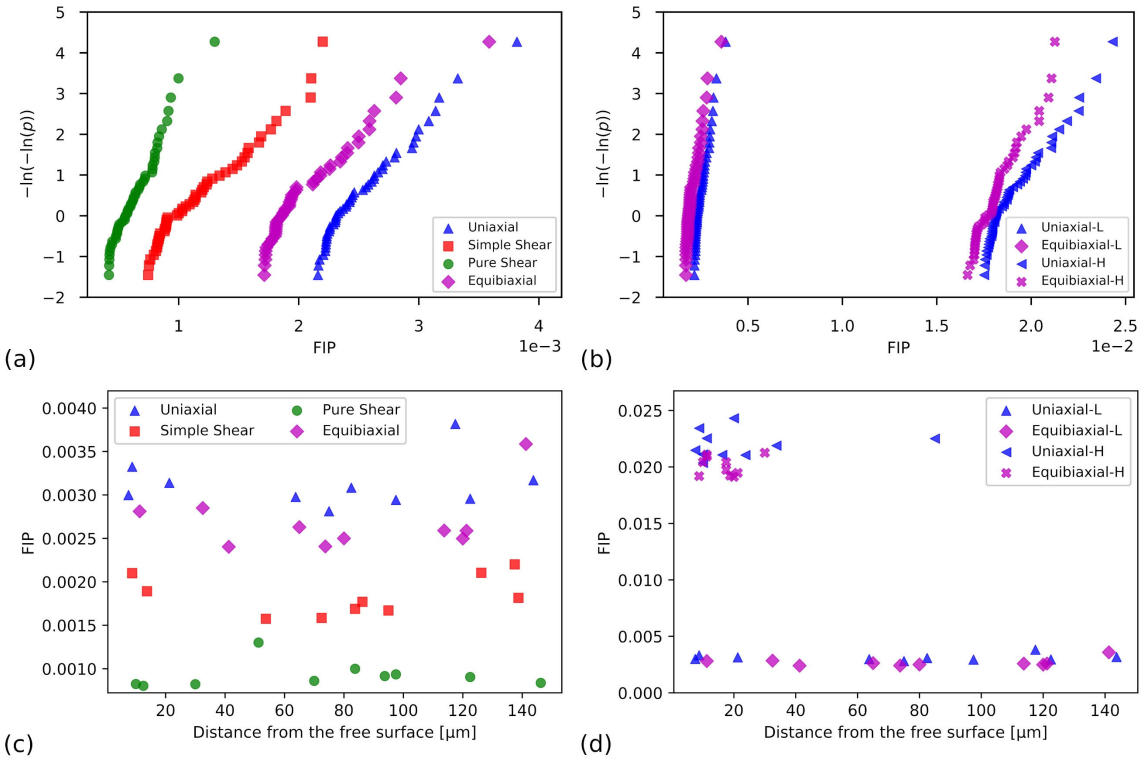

Figure 4.8. Ti-6Al-4V FIPs with random texture fit to the Gumbel EVD under the (a) low and (b) high strain level (in reference to Table 4.1). In (b), the uniaxial and equibiaxial FIPs from (a) are reproduced with legend suffix "-L" indicating lower strain level, whereas the uniaxial and equibiaxial FIPs strained to the high strain level are indicated with suffix "-H." The distance from the free surface of the top 10 FIPs is shown in (c) and (d) for the low and high strain levels, respectively. Uniaxial and equibiaxial surface distances in (c) are also shown in (d). The maximum distance from the free surface is 150 μm because SVE volume is $(300\ \mu m)^3$.

Uniaxial and equibiaxial FIPs under the lower strain level are shown alongside the high strain level FIPs in Figure 4.8b. Under a sufficiently large equivalent shear strain, the free surface begins to have a profound effect on FIP magnitudes. The surface proximity of the Ti-6Al-4V FIPs are shown in Figure 4.8c and Figure 4.8d. At the lower strain level, the average distances of the 10 highest FIPs to the free surface is between 71.75 μm and 81.63 μm. An average value of 75 μm would indicate insignificant free surface effects (half of 150 μm, which is the maximum distance from the free surface for the Ti-6Al-4V SVEs). At the higher strain level, the average distances for uniaxial and equibiaxial straining are 22.63 μm and 16.63 μm (shown in Figure 4.8d with detailed values given in Table 4.3).

4.3.4 Ti-6Al-4V Γ^p Plane

Computed iso-FIP contours in the Γ^p plane for Ti-6Al-4V are shown in Figure 4.9. As mentioned in Section 4.2.1, only the Case B contours are shown. It is expected that the Case A contours would resemble those for Al 7075-T6 in Figure 4.7. Additionally, Section 4.3.3 shows the reduced driving forces for fatigue crack formation under shear loading (characteristic of Case A). The iso-FIP contours are only extended to the limits of the response coordinates used in the GPR model. The characteristically different shapes of the contours in Figure 4.9 may be due to the more anisotropic crystal structure of hcp Ti-6Al-4V. The previous chapter demonstrated complex interactions between the presence of a free surface and crystal structure under uniaxial straining. Therefore, it is not entirely unexpected that the presence of a free surface and different strain states would result in complex material response, leading to the distinct contours shown here.

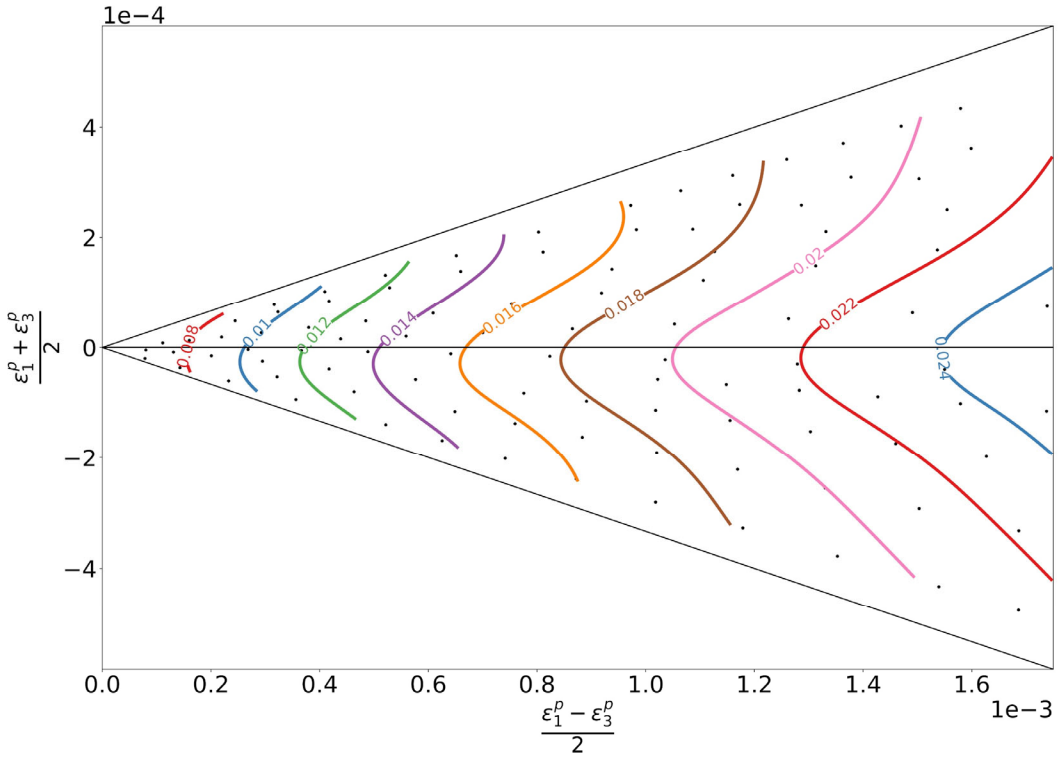

Figure 4.9. Computed Case B iso-FIP contours in the Γ^p Plane for Ti-6Al-4V (equiaxed grains with Random texture).

4.3.5 Lattice Strain

In this section, the elastic strain normal to the sub-band regions of the highest FIPs is examined. The elastic Green strain tensor for each element is exported from the CPFEM simulations. Elements that correspond to the sub-bands of the highest FIPs are identified, and the elastic strain tensors are rotated to determine the elastic strain normal to the respective slip planes. FIP_α calculated with Equation (2.18) incorporates the tensile stress normal to the slip plane, as justified by Brown and Miller [16], but a measure of the elastic strain normal to the slip plane (equivalent to the lattice strain) is more useful for experimental comparison. The values reported here can serve as a comparison between lattice strains measured in synchrotron experiments under cyclic loading, some of which

have already been performed on the two alloys of interest. Turkmen et al. [209] measured lattice strains for Al 7075-T6 in both loaded and unloaded states (after one and 1,000 cycles, but also intermittently) and observed a decrease in average stress and the average number of active slip systems at the peak load. The macroscopic stress relaxation was well predicted by their Finite Element Method simulations. Bernier et al. [210] examined Ti-6Al-4V loaded in uniaxial tension to 540 MPa and calculated lattice strain pole figures which were used to calculate the local stress using Hooke's law and single-crystal elastic moduli. They confirmed multiaxial stress conditions within individual grains under a uniaxial macroscopic load.

Figure 4.10a and Figure 4.10b depict the 10 highest Al 7075-T6 random textured FIPs as a function of the lattice strain on the corresponding sub-band slip plane for the low and high strain level, respectively. An immediate observation is that although FIP magnitudes vary for pure shear, simple shear and equibiaxial straining, all three have similar lattice strains. Some of these lattice strains are negative, but this is entirely expected as FIP_α is a strain-based damage parameter. If the peak stress normal to the slip plane happens to be negative, the second term in the parenthesis in Equation (2.18), $k\frac{\sigma_n^\alpha}{\sigma_y}$, is treated as 0, and a high value of FIP_α may still manifest. The highest 10 equibiaxial and uniaxial FIPs are of similar magnitude but the latter always occur with a positive lattice strain. Minimal difference between the low and high strain levels is observed. The 10 highest Al 7075-T6 cubic textured FIPs for the low and high strain level are shown in Figure 4.10c and Figure 4.10d. Only simple shear FIPs display a notable increase in lattice strain for the cubic texture.

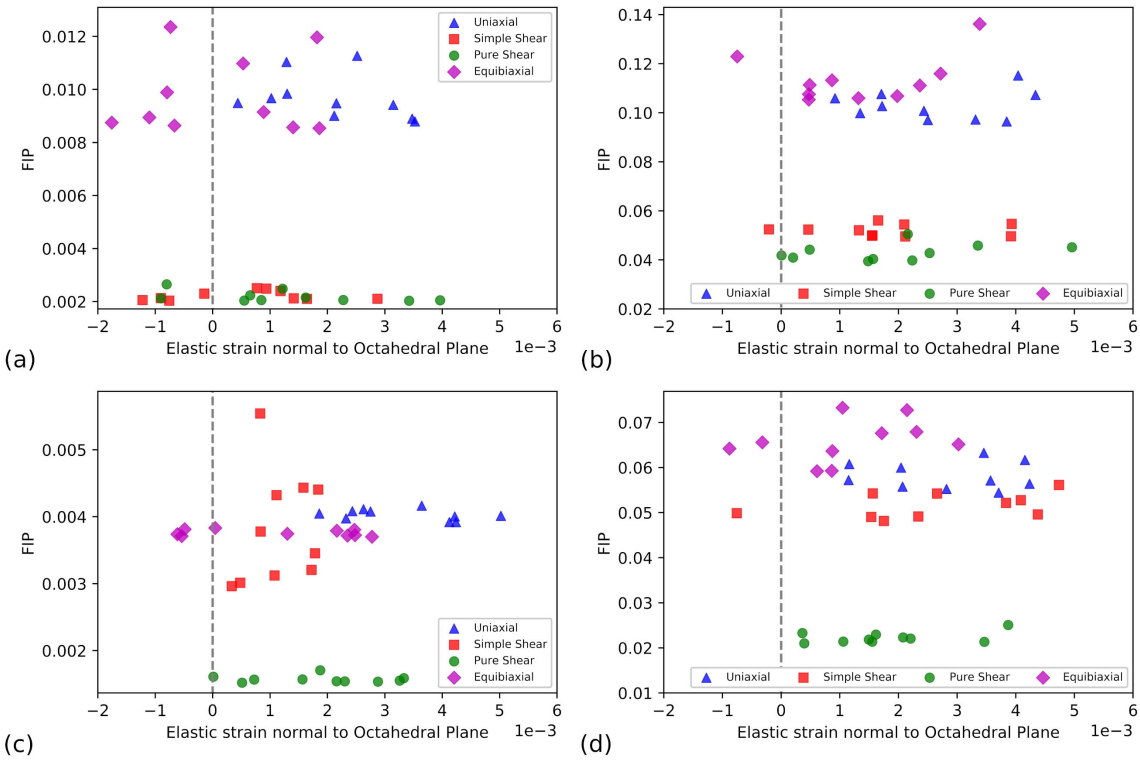

Figure 4.10. The 10 highest FIPs for Al 7075-T6 as a function of the elastic strain normal to the octahedral slip plane for random texture under the (a) low and (b) high strain level, and for cubic texture under the (c) low and (d) high strain level (in reference to Table 4.1).

The 10 highest Ti-6Al-4V FIPs as a function of the lattice strain on the corresponding sub-band slip plane for the low and high strain levels are shown in Figure 4.11a and Figure 4.11b, respectively. Similar to Al 7075-T6 , uniaxial straining results in the highest lattice strains. Since Ti-6Al-4V grains are banded along two types of slip planes (basal and prismatic), the FIPs are analyzed to determine which of these two slip planes manifest the highest FIPs. The majority of the highest FIPs reside on the basal plane, and only under pure shear and simple shear straining do some of the 10 highest FIPs occur on the prismatic plane. These instances are shown in Figure 4.11a as black star markers. This is unique to shear loading: even when the highest 50 FIPs are considered from each

compiled EVD, the maximum FIPs always occur on the basal plane for uniaxial and equibiaxial straining, whereas they occur at the same ratio as seen in Figure 4.11a for the two types of shear straining. Figure 4.12 depicts the 50 highest Ti-6Al-4V FIPs as a function of lattice strain. At the higher strain level, uniaxial and equibiaxial lattice strains both increase, but the former displays a larger increase.

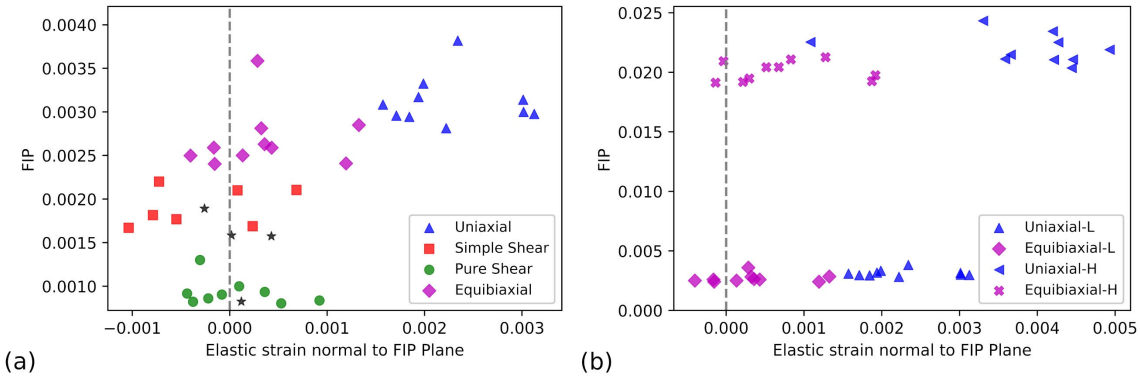

Figure 4.11. The 10 highest FIPs for Ti-6Al-4V as a function of the elastic strain normal to the corresponding sub-band region slip plane (basal or prismatic) for the (a) low and (b) high strain level (in reference to Table 4.1). In (b), the uniaxial and equibiaxial FIPs from (a) are reproduced with legend suffix "-L" indicating lower strain level, whereas the uniaxial and equibiaxial FIPs strained to the high strain level are indicated with suffix "-H." All FIPs occur on the basal plane with the exception of a few under shear loading, which are shown as black star markers in (a).

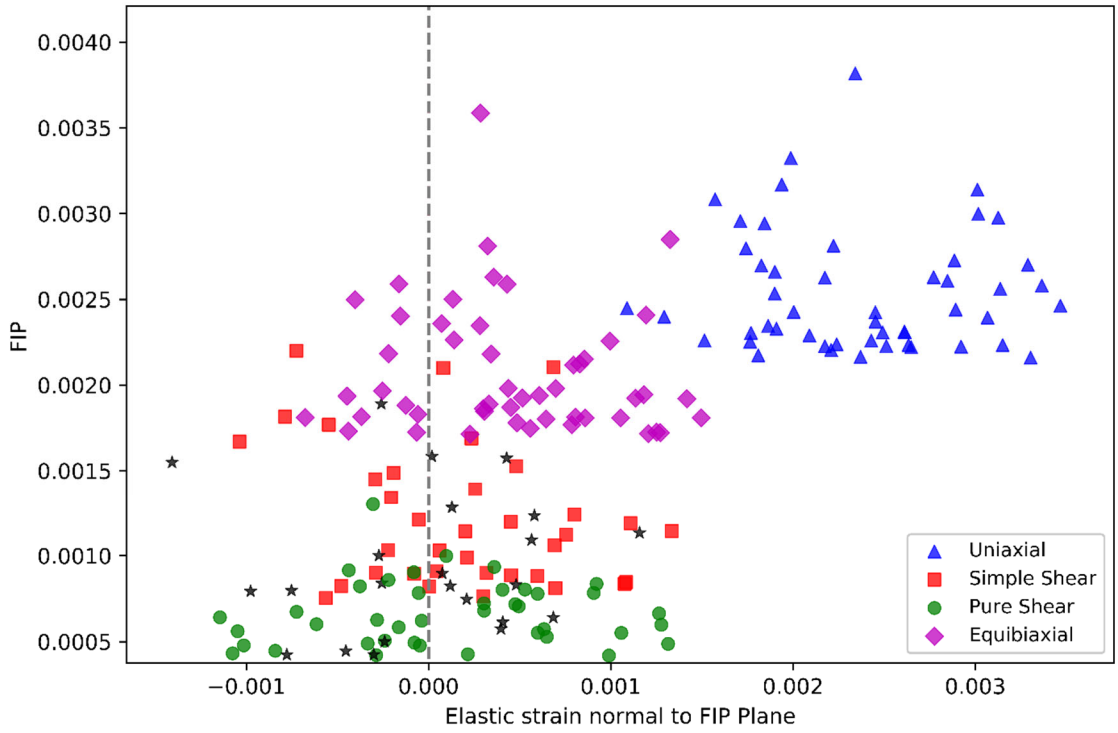

Figure 4.12. The 50 highest FIPs for Ti-6Al-4V as a function of the elastic strain normal to the corresponding sub-band region slip plane (basal or prismatic) for the low strain level (in reference to Table 4.1). All FIPs occur on the basal plane except where black star markers are shown, which occur on the prismatic plane solely for pure shear and simple shear straining.

4.4 Conclusions

In this chapter, the effects of different multiaxial strain states and strain magnitudes on the two alloys of interest are examined. A methodology to impose the same target equivalent strain for the uniaxial, equibiaxial, and shear strain states is developed. Fatigue resistance is assessed with FIPs, which are fit to a Gumbel EVD to rank order different strain states and magnitudes. Additionally, any correlation of proximity to the free surface with FIPs and the lattice strains of the most extreme FIPs is assessed. A computational framework to estimate iso-FIP contours that may aid in the design of engineering

components is presented and the generated contours accord with experimental trends. The digital workflows developed in this chapter thus builds on the previous chapter to allow for rapid assessment of polycrystalline microstructures under progressively complex strain states and magnitudes. The gist of material in this chapter has been published as a standalone journal article [129]. The conclusions are as follows:

- Under the same equivalent cyclic maximum shear strain amplitude, pure and simple shear straining result in lower FIP magnitudes as compared to uniaxial straining, in agreement with experimental trends.
- Under the same, relatively lower equivalent shear strain, the highest driving forces for fatigue crack formation in Ti-6Al-4V under all four strain states considered experience negligible influence of the free surface. However, at a higher equivalent shear strain, the extreme FIPs have a strong propensity to occur near the free surface.
- The computational Γ^p Planes match experimental trends compiled by Brown and Miller [16], particularly for Al 7075-T6.
- Although uniaxial and equibiaxial cyclic straining at the same equivalent shear strain amplitude may manifest similar FIP magnitudes, the lattice strains in the vicinity of these highest FIPs vary greatly for both alloys.
- Pure shear, simple shear, and equibiaxial straining results in similar lattice strains but significant differences in FIP magnitude.
- Shear straining shifts the highest magnitude FIPs from the basal plane to the prismatic plane in Ti-6Al-4V.

CHAPTER 5. PRISMS-FATIGUE: AN OPEN-SOURCE CRYSTAL PLASTICITY FATIGUE ANALYSIS TOOL

The digital workflows developed thus far examine important fatigue characteristics and accord with experimental observations. These types of studies and publications in the literature often employ homemade codes and workflows unavailable to the broader research community, potentially imposing barriers to future research progress. Additionally, prior chapters employed a strategy of simulating SVE ensembles as opposed to exploring very large ensembles that might approach that of the RVE, due to computational constraints. It is assumed that the same volume of material simulated with either approach results in equivalent material response, or at least the ability to consistently and properly rank order fatigue response of various distinct microstructures regardless of the adopted SVE size, but these assumptions can only be tested using larger scale SVEs, even massive SVEs compared to prior research. Computational crystal plasticity has long been the "bottleneck" for doing this.

In response to these concerns, this chapter presents an open-source framework entitled PRISMS-Fatigue that enables simulation-based comparison of microstructures with regard to fatigue resistance for polycrystalline metals and alloys, taking advantage of a highly parallelized, scalable platform. The framework uses the CPFEM as its microstructure-sensitive fatigue analysis tool and provides a highly efficient, scalable, flexible, and easy-to-use ICME community platform. The PRISMS-Fatigue framework is linked to different open-source software to instantiate microstructures, compute material response, assess volume averaged FIPs, and visualize the data. A FIP library is available which enables users to investigate fatigue resistance based on damage mechanisms specific

to different metals and alloys, and the framework is flexible in that user-defined FIPs can be easily added. The performance of PRISMS-Fatigue is benchmarked against a similar framework implemented using the commercial software ABAQUS. Results indicate that the multilevel parallelism scheme of PRISMS-Fatigue is more efficient and scalable than ABAQUS for large scale fatigue simulations. The performance and flexibility of this framework is demonstrated with various examples from prior chapters that assess the driving force for fatigue crack formation of microstructures with different crystallographic textures (cubic, random, and rolled), grain morphologies (equiaxed and elongated), and sizes, and under different multiaxial strain states (uniaxial, shear, and biaxial), strain magnitudes, and boundary conditions (bulk vs. surface effects). PRISMS-Fatigue is linked to the Materials Commons, an information repository to store and share inputs and results.

5.1 Introduction

Numerous fatigue studies and corresponding modeling frameworks have been developed as stand-alone codes or subroutines used with commercial software. Thus far, there has been little emphasis within the fatigue community on open-source toolboxes for simulation and relative assessment of microstructures with regard to resistance to fatigue crack formation. The main challenges are tracking with standard testing protocols, reproducibility of the results, and model and code documentation. Clearly, “reinventing” common codes and methods routinely is inefficient and leads to difficulty in verification and validation. An alternative paradigm more commonly pursued in modern digital materials science is based on developing a verified and validated open-source framework which can be used and/or modified by the fatigue community. In this regard examples in related materials research communities include Density-functional theory (DFT)

calculations (NWChem [211], DFT-FE [212]), first-principles statistical mechanics (CASM [93, 213]), atomistic simulation (LAMMPS [214] and NAMD [215]), crystal plasticity finite element method (CPFEM) codes (PRISMS-Plasticity [5]), and phase-field codes (PRISMS-PF [94], MOOSE [216], OpenPhase [217]). Developing an open-source fatigue framework for microstructure-scale comparisons broadens the community of research to investigate complex fatigue-related problems, with a focus on developing new features rather than reimplementing basic elements of the framework in limited-use, ”homegrown” codes and subroutines. Finally, the PRISMS-Fatigue framework is linked to the Materials Commons [218] to keep a record of simulations and workflows, share with collaborators, and publish data, which is key to data reproducibility in the scientific community. More importantly, it increases the rate at which materials and microstructures can be evaluated for fatigue-critical applications, with a corresponding acceleration of the pace of materials discovery and development.

The open-source PRISMS-Fatigue platform allows the material science and mechanics community to use its tools, contribute to fatigue-related research and applications, and potentially update or create modules with their own constitutive laws and tools. The framework is linked to the open-source software DREAM.3D [113], PRISMS-Plasticity [5], Python, and ParaView to respectively generate microstructure instantiations, calculate material response, execute scripted workflows to compute volume averaged FIPs, and to visualize data. PRISMS-Plasticity [5] serves as the CPFE engine for PRISMS-Fatigue. PRISMS-Plasticity [5] is an open-source parallel 3-D CPFEM software, that can handle both rate-dependent and rate-independent formulation along different hardening models. The PRISMS-Plasticity software is modular, flexible, and scales well with large

scale simulations. Furthermore, the model can handle address twinning mechanisms [219, 220] and multi-phase simulations.

Parallel performance of the framework is critical since most microstructure-sensitive fatigue applications require detailed and expensive CPFEM simulations. The performance of PRISMS-Fatigue is tested against a similar framework implemented using the popular commercial software ABAQUS [4] with an identical simulation setup. A set of applications are then presented to demonstrate the performance and flexibility of the framework in assessing the driving force for fatigue crack formation. These include different crystallographic textures (cubic, random, and rolled), grain morphologies (equiaxed and elongated), multiaxial strain states (uniaxial, shear, and biaxial), strain magnitudes, and boundary conditions (bulk vs. surface effects). As a last application, the effect of sample size on the driving force for fatigue crack formation is investigated. The largest simulation is a ~160,000 grain sample discretized with 250^3 elements. A detailed discussion of the methods mentioned above and their implementation in the framework, including the code structure, constitutive material model library, integration with DREAM.3D [113], implicit time stepping, inputs and outputs, periodic boundary conditions, parallelization, and integration of PRISMS-Fatigue and Materials Commons are elaborated in the next section. Other parts of the framework (e.g., microstructure generation, FIPs, extreme value statistics) were discussed earlier in Chapter 2. A flowchart of the framework is presented in Figure 5.1.

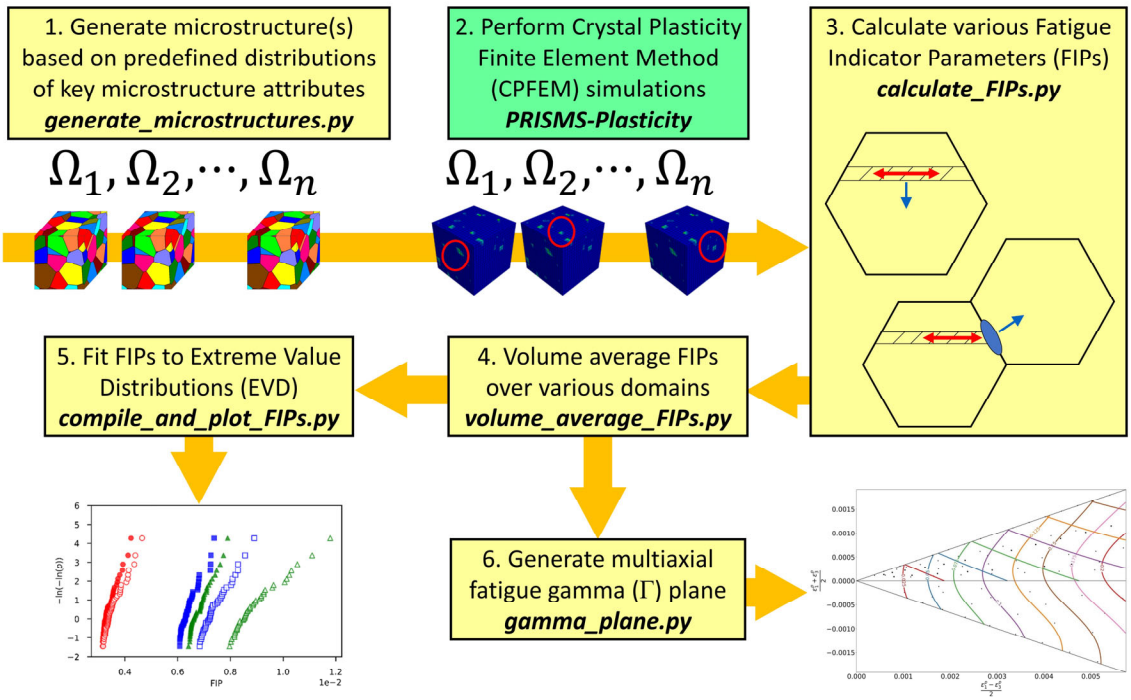

Figure 5.1. Flowchart of the PRISMS-Fatigue framework for the simulated fatigue applications.

5.2 Methods

PRISMS-Fatigue serves as a foundation for the establishment of a fatigue research community by providing an open-source fatigue framework which implements advanced numerical schemes to achieve high performance, flexibility, and scalability. Since microstructure-sensitive CPFEM fatigue simulations are very demanding computationally, it is crucial that the framework can scale well with the size of problems and number of processors. The research community can use this framework at three different levels: (1) as a simple user of the predeveloped applications without any required programming skills (2) adding new applications including the modification or addition of new FIPs or constitutive models that require intermediate programming skills, and (3) contributing to

the core library which requires advanced programming skills. This chapter describes PRISMS-Fatigue version 1.0 which uses PRISMS-Plasticity version 1.2.0 as its CPFEM engine.

5.2.1 Code Structure

PRISMS-Fatigue is developed in two separate parts written in the programming languages of C++ and Python. The C++ portion includes the core CPFEM simulations built upon PRISMS-Plasticity [5] and the deal.ii finite element library [221], while the Python portion instantiates microstructures using DREAM.3D, calculates and volume averaged FIPs, and performs the statistical analysis with plot/visualization features. This combination provides efficient CPFEM computational performance with great data science flexibility for FIP analysis and post-processing.

5.2.2 Constitutive material library

An essential part of PRISMS-Fatigue is the core CPFEM engine, PRISMS-Plasticity. The material constitutive models for fatigue applications should be able to model cyclic material response. For the PRISMS-Fatigue applications, both rate-independent [222-224] and rate-dependent [98, 225, 226] models are implemented in the library to represent the cyclic response of polycrystals. An important part of these implementations is the calculation of the algorithmic tangent modulus which strongly affects the simulation wall time and number of required steps to obtain the converged solution. The implemented models employ finite deformation continuum kinematics based on a multiplicative decomposition of the deformation gradient tensor [95, 227, 228]. A new multiscale cyclic model is developed within the PRISMS Center to include twinning-detwinning

mechanisms as a part of constitutive model [219]. This is especially important for many applications and particularly for HCP polycrystals. Development and implementation of the crystal plasticity models requires tremendous experience and time. An open-source constitutive model library will thus considerably aid the research community and diminish time spent in reimplementing models. A user-defined constitutive model feature is designed to make the PRISMS-Fatigue framework as flexible as possible. Accordingly, one can integrate their constitutive model into the framework with modifications to the *calculatePlasticity.cc* file. The CPFEM model employed in the simulations presented here was developed initially by Hennessey et al. [98] as an ABAQUS User MATerial subroutine (UMAT). It was adapted for use in PRISMS-Plasticity.

5.2.3 Integration with DREAM.3D

DREAM.3D [113] is used to instantiate synthetic microstructures, as described in Section 2.2.3. In this application, a Python wrapper in the *generate_microstructures.py* module calls DREAM.3D to generate either single, large microstructures or ensembles of SVEs. This consists of two main DREAM.3D files: a *.dream3d* file with the "StatsGenerator" filter, which specifies the statistics of the microstructure(s) to be instantiated (grain size distribution, crystallographic textures, grain morphology, phase, etc.), and the *.json* pipeline that contains the filters to create the synthetic volume, pack the phase(s), iteratively swap grains to achieve the desired crystallographic or morphological statistics, and to finally write out the required input files for PRISMS-Fatigue. DREAM.3D is executed entirely from within Python, but the user can instantiate microstructures using the DREAM.3D GUI if more precisely controlled microstructures are desired. However,

the Python wrapper enables the generation of SVE ensembles with proper numbering, followed by automated grain banding and sub-banding as described in Section 2.5.

5.2.4 Implicit time stepping

The weak form of the equilibrium equation, as the governing equation for PRISMS-Fatigue displacement-based FE application, is solved using the Newton-Raphson iterative scheme. To do so, the loading history is divided into small increments. Each increment is then solved using the Newton-Raphson iterative scheme involving a linearized set of equations. An algorithmic tangent modulus derived for each constitutive model is employed to form the sparse stiffness matrix. In the standard Newton-Raphson scheme, the sparse stiffness matrix is updated in every iteration within an increment, which can be computationally expensive. A modified Newton-Raphson scheme is also implemented in the framework in which the sparse stiffness matrix is updated only at the start of each increment, which is effective for mildly nonlinear problems. This decreases the computational time of sparse stiffness matrix formation which is considerable in large scale simulations. The solution to the linear equation is obtained using the PETSc library [229, 230] included in deal.ii [221]. Preconditioning of the sparse stiffness matrix improves convergence of the iterative scheme. The values of degrees of freedom (DOFs) are updated using the solution from the previous iteration, which are then used to compute the external forces which are residuals for this iteration. The iterative process continues until the residuals meet certain criteria.

5.2.5 Inputs and Outputs

The Fatigue framework has two families of inputs including: (I) microstructure generation and FIP calculation inputs and (II) CPFEM inputs for PRISMS-Plasticity. The CPFEM simulation inputs can be summarized as: (1) Microstructure, including two files of *orientation.txt* which defines the grain orientations in the Rodrigues space and phases (for multiphase simulations) and *grainID.txt* which define the grain ID map inside the sample (2) Boundary conditions, including a file *BCinfo.txt* which defines the type of applied boundary conditions (3) Latent hardening matrix which can accommodate complex cases of latent hardening ratios in a matrix format (4) Crystallographic information for slip (twin) directions and normal to the slip (twin) planes (5) main input files including the geometry, discretization, numerical integration, crystal plasticity simulation parameters, and convergence parameters. The FIP calculation input includes modifications to the input file that specifies what PRISMS-Plasticity should export (e.g., cyclic range of plastic shear strain on slip systems, peak stress normal to slip plane, etc.) in a *.csv* format. These are then read by the *calculate_FIPs.py* module to compute FIPs. Users can define their own FIP equation or select an option from the existing library.

The *generate_microstructures.py* module requires a single *.dream3d* input file (as described in the *Integration with DREAM.3D* section above) and generates the *orientation.txt* and *grainID.txt* files. It also stores the elements that belong to the desired volume averaging domain (e.g., grains, bands, or sub-bands) as an efficient *.p* pickle file. The *calculate_FIPs.py* module computes and stores FIPs for every element in pickle files as well. Both pickle files are then read by *volume_average_FIPs.py* to volume average FIPs over one of the available domains. The volume averaged FIPs are stored in the same

pickle format for efficient access by the plotting modules (*compile_and_plot_FIPs.py* and *gamma_plane.py*) but also to a .csv file for rapid user assessment. These last two modules can generate all the figures in the applications section of this work.

The PRISMS-Fatigue YouTube video tutorials and written tutorial describe each file input and output file in detail. Please see the *Code Availability* section for the direct link to the content.

5.2.6 Periodic boundary conditions

Included in PRISMS-Fatigue is the capability to perform CPFEM simulations with fully periodic boundary conditions (PBCs). This is crucial in calculations of fatigue resistance when smaller microstructure instantiations are employed that represent bulk, i.e., subsurface, material response. Przybyla [114] presented the details of the PBCs required to mimic the subsurface microstructure response during fatigue simulations. In PRISMS-Fatigue, PBCs are implemented using a set of linear constraints. These constraints are defined on three components of opposing faces, parallel edges, and vertices. Rigid body motion is also excluded by assigning additional constraints. Three sets of constraints are applied on nodes on opposing faces (in the direction perpendicular to those faces), nodes on each set of four parallel edges (in the two directions perpendicular to the direction in which the edges are parallel), and vertices (in all directions). Contraction or expansion of the dimensions of the actual microstructure volume are considered. One should note that an efficient parallel implementation of the PBCs is nontrivial, as will be discussed later.

5.2.7 Parallelization

Efficient parallelization plays a key role in the PRISMS-Fatigue framework since the size of the microstructure-sensitive CPFEM simulations can grow considerably. A Message Passing Interface (MPI) framework is implemented as proposed by deal.ii [221]. The initial discretization is divided among the processors and each processor handles a part of DOFs. In addition, each processor will have access to a neighboring processor's layer of DOFs which requires their values during the simulation, termed as ghost DOFs. During assembly of the sparse stiffness matrix to solve the linear equation, each processor requires access to its own DOFs and the ghost DOFs. The ordinary MPI parallelization scheme makes the PBCs nontrivial to implement because certain processors may not have access to the required DOFs. Consequently, the parallelization scheme may change depending on the type of boundary conditions. The file *periodicBCs.cc* handles these tasks to appropriately implement PBCs. One should note that the conventional PBCs, which are different from the one used in PRISMS-Fatigue, are already implemented in deal.ii [221]. However, in the current PBCs used to model the subsurface effect, some constraints are defined between the DOFs of vertices and edges with the DOFs of the faces. These constraints are captured by efficiently modifying the ghost layer of each processor, which is handled by the file *periodicBCs.cc*. Another bottleneck in large-scale simulations is data-output. A serial data-output scheme can create an inefficient bottleneck as the simulation size increases. Thus, a parallel scheme is employed in which each processor is responsible for writing the outputs of its own DOFs.

5.2.8 Integration of PRISMS-Fatigue and Materials Commons

An important step towards ensuring the reproducibility and reusability of simulation data is taken here by linking PRISMS-Fatigue to Materials Common; such reproducibility and reusability has rarely been addressed in fatigue-related research and applications. The Materials Commons is a collaboration platform and information repository for the materials community [218]. It provides a common site for researchers to store, share, curate, publish, and reuse experimental and computational data, with a data model designed for the needs of the materials community. The Materials Commons Python Application Programming Interfaces (MCAPI) wrapper is used to automate the integration of PRISMS-Fatigue results into Materials Commons. Using MCAPI, the command line tool (CLI) automatically parses the software input file and the corresponding simulation results to Materials Commons. The applications presented in this chapter are uploaded into Materials Common and published, which can be accessed using the link provided in the "Data Availability" section.

Materials Commons can also be used to establish a Community of Practice, which can share information for reuse, establish protocols, standards and best practices and, ultimately, curate information. This can include results of PRISMS-Fatigue simulations as well as experimental information for model calibration and validation. In order to expedite the rate at which materials are developed and implemented, the fatigue community is encouraged to transition to open-source simulations and software development as is already the case for other materials science software (DFT-FE, LAMMPS, etc.). The framework presented here will enable researchers to focus on critical microstructure-sensitive fatigue-

related problems (e.g., assessing new FIPs, more complex microstructure heterogeneity, as is the case with additively manufactured microstructures).

5.2.9 Data availability

The microstructures, CPFEM input files, and PRISMS-Plasticity raw simulation results are available on Materials Commons at https://doi.org/10.13011/m3-rcyy-gx13.

5.2.10 Code availability

PRISMS-Fatigue is an open-source computer code available for download at https://github.com/prisms-center/Fatigue. In addition to a written tutorial available in the GitHub repository, a series of video tutorials totaling nearly three hours of content are available at https://www.youtube.com/playlist?list=PL4yBCojM4Swo3CvlA57syFrzk3p1mugP5 which entirely replicate the results and figures presented in the Applications section of this chapter.

5.3 Results and discussion

The scaling performance of the PRISMS-Fatigue framework is investigated first for a large-scale fatigue simulation of Al 7075-T6. Volume averaged FIPs are fit to the Gumbel EVD which permits comparison of fatigue resistance between different microstructures [128, 129], or fatigue life prediction with a proper calibration [31]. In the following step, a slightly smaller simulation is used as a benchmark to compare the FIP EVD response and performance scalability of an identical Al 7075-T6 microstructure instantiation simulated in both PRISMS-Fatigue and a similar framework implemented

using ABAQUS. Lastly, several fatigue applications including the effects of crystallographic textures, grain morphologies, boundary conditions, multiaxial strain states, strain magnitudes, and sample sizes are presented to demonstrate the capabilities of PRISMS-Fatigue.

5.3.1 Parallel scaling

One of the important aspects of a parallel code is the capability to scale to a large number of degrees of freedom using multiple processors while solving problems in a reasonable amount of time. Microstructure-sensitive fatigue analysis through CPFEM simulations frequently includes problems with millions of degrees of freedom. Accordingly, the scalability of the PRISMS-Fatigue framework is key to its performance. The strong scaling of PRISMS-Fatigue is investigated here by studying the extreme value fatigue response of an Al 7075-T6 microstructure instantiation with ~41,000 equiaxed grains and random initial crystallographic texture. The 160^3 voxelized microstructure was generated using DREAM.3D [113] (Figure 5.2a). Each microstructure voxel is modeled with reduced integration linear hexahedral elements, resulting in an FE mesh with 4,096,000 elements; each grain is represented by multiple elements. A phenomenological viscoplastic flow rule and associated hardening rules with OW kinematic hardening [98, 231-233] were implemented in the PRISMS-Plasticity [5] material library. Three fully reversed uniaxial straining cycles are applied to a strain amplitude of 0.7% and at a strain rate of 10^{-3} s^{-1} to facilitate elastic–plastic shakedown. Periodic boundary conditions were incorporated to represent bulk, subsurface material response [30, 64, 65, 114]. All simulations performed in this chapter were conducted on Georgia Institute of Technology's Partnership for an Advanced Computing Environment (PACE) "Hive" supercomputing

cluster equipped with Intel Xeon 6226 CPU processors and 8 GB memory per processor. Figure 5.2b shows the cyclic response of the sample during three straining cycles. The variation of elemental FIPs throughout the sample is shown in Figure 5.2c. Microplasticity is heterogeneously distributed throughout the microstructure and fatigue crack formation is most probable at "hot spots" corresponding to high FIP values. Accordingly, the Gumbel EVD of the highest 50 sub-band averaged FIPs is illustrated in Figure 5.2d. Furthermore, the grains with the highest 50 sub-band averaged FIPs are presented in Figure 5.2e. The simulation was conducted with different number of processors (between 6 to 480) and the strong scaling results are presented in Figure 5.2f, which demonstrate excellent scalability. The required wall times to reach the point of initial maximum compressive strain for the 160^3 voxelized microstructure are 250 hours using 6 processors or 8.4 hours using 480 processors.

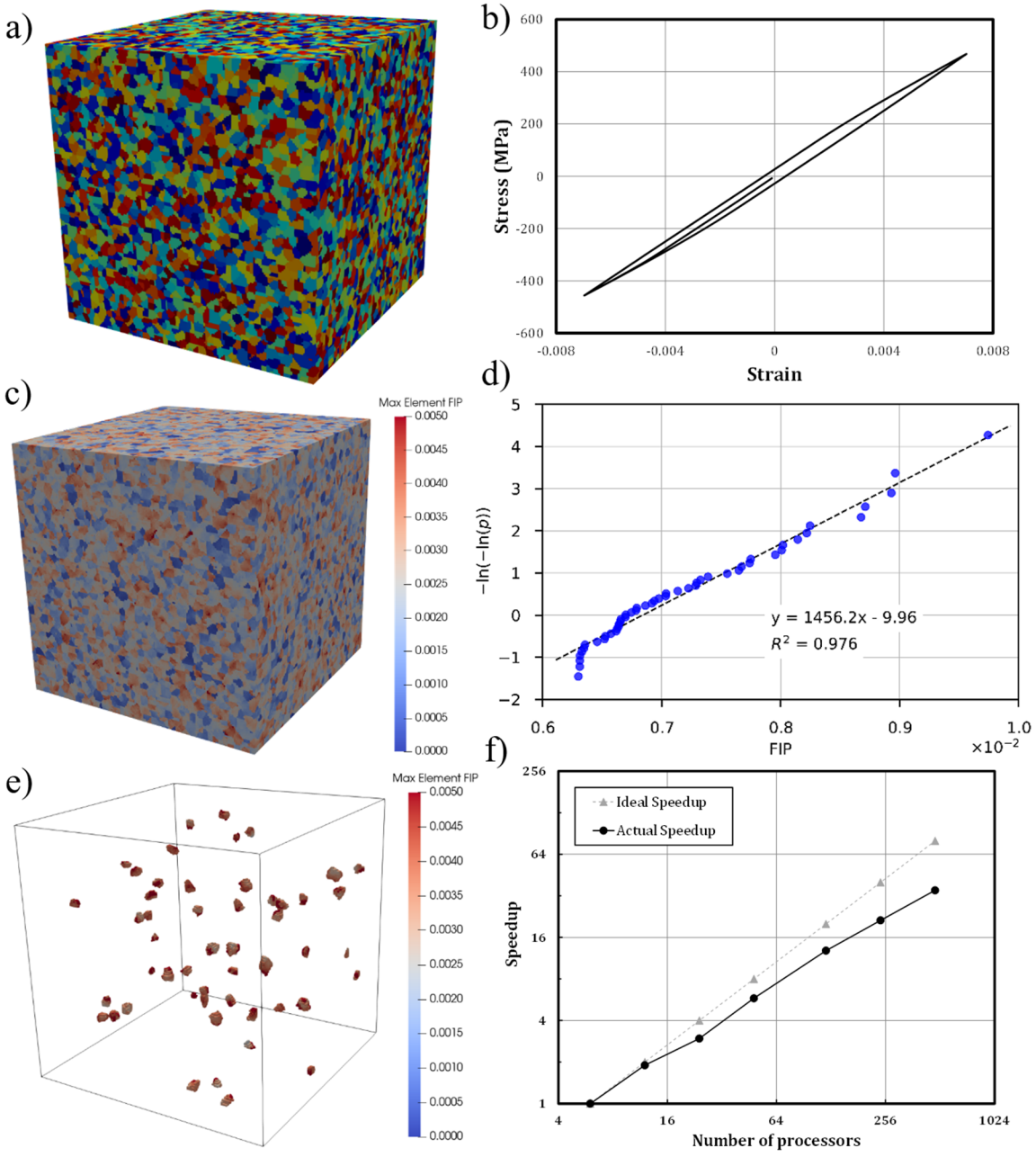

Figure 5.2. A large-scale microstructure used to investigate the parallel scalability of PRISMS-Fatigue. (a) The microstructure with distinct grains shown in different colors. (b) Macroscopic stress-strain cyclic response. (c) Variation of elemental Fatigue Indicator Parameters (FIPs) throughout the sample. Although some elemental FIPs are larger than the legend maximum of 0.005, the purpose is to emphasize the heterogeneity of FIPs throughout the sample. (d) The highest 50 sub-band averaged (SBA) FIPs fit to the Gumbel Extreme Value Distribution (EVD). (e) The grains with the highest 50 SBA FIPs. (f) Strong-scaling CPU performance.

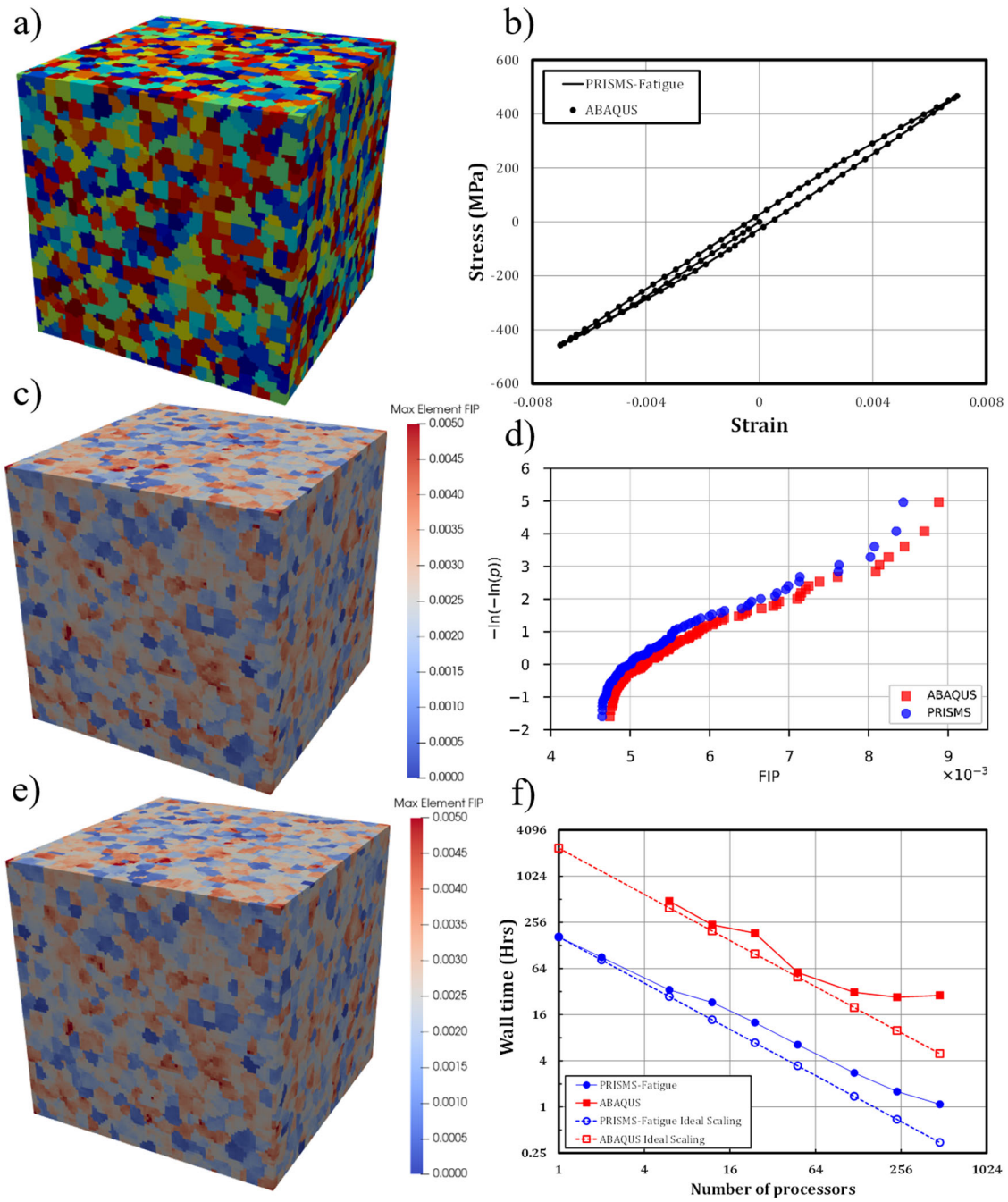

Figure 5.3. Comparison between PRISMS-Fatigue and a similar framework implemented in ABAQUS. (a) Microstructure instantiated with DREAM.3D. (b) Macroscopic cyclic stress-strain response in both simulation suites. (c,e) Variation of elemental FIPs in ABAQUS and PRISMS-Fatigue, respectively. Although some elemental FIPs are larger than the legend maximum of 0.005, the purpose is to emphasize the heterogeneity of FIPs throughout the sample. (d) Comparison of sub-band-averaged (SBA) FIP Extreme Value Distributions (EVDs). (f) Strong-scaling CPU performance.

5.3.2 PRISMS-Fatigue benchmarking versus ABAQUS

The performance and scalability of the PRISM-Fatigue framework is compared to a similar framework implemented in the commercial software ABAQUS using a smaller microstructure instantiation and the same material model. An Al 7075-T6 microstructure with ~7,500 grains, random initial crystallographic texture, and 90^3 voxels was instantiated using DREAM.3D (Figure 5.3a). The same loading and boundary conditions were implemented as those of the parallel scaling investigation in the previous section. Figure 5.3b compares the cyclic response obtained using ABAQUS versus PRISMS-Fatigue across three loading cycles, and Figure 5.3c and Figure 5.3e illustrate the variation of FIPs in the microstructure. The highest 100 FIPs from each simulation are fit to the Gumbel EVD and compared in Figure 5.3d. Additionally, these highest FIPs occur in the same grains as simulated using the two frameworks. The maximum difference between EVD FIPs from ABAQUS and PRISMS-Fatigue is ~5%. It is emphasized that a comparison of extreme value FIP response is arguably the strictest criteria that can be used to compare the simulation frameworks given the highly nonlinear constitutive model and different numerical implementations. Accordingly, a ~5% difference in the highest FIPs demonstrates that the results of PRISMS-Fatigue agree well with those of ABAQUS. The average absolute difference between the FIPs obtained by ABAQUS and PRISMS-Fatigue for all grains, not just the highest 50 FIPs, is 1.1 %. Additionally, the cyclic responses presented in Figure 5.3b are precisely the same for ABAQUS and PRISMS-Fatigue. Although the constitutive model is similar for both fatigue frameworks implemented in ABAQUS and PRISMS-Fatigue (see Section 2.1.2) the model implementations are slightly different in ABAQUS and PRISMS-Fatigue (see Supplementary Note 5 of [101]). In the

ABAQUS implementation, the slip (i.e., plastic shear strain) for each slip system is selected as the Newton-Raphson scheme variable. In the PRISMS-Plasticity implementation, however, the stress tensor and back stress for each slip system are selected as the Newton-Raphson variables. In a highly nonlinear model and large-scale simulation, a very small difference among the calculated FIPs is inevitable by these two fatigue frameworks.

The fatigue simulation was conducted using a different number of processors, which are 1−480 for PRISMS-Fatigue and 6−480 for ABAQUS. ABAQUS was not able to finish the simulation in less than 720 hours using less than six processors. The strong scaling results shown in Figure 5.3f demonstrate significantly reduced simulation times using PRISMS-Fatigue. In the case of total simulation time, PRISMS-Fatigue requires much smaller wall time compared to ABAQUS for all numbers of processors. In addition to the simulation wall time, the ideal scaling of each framework is plotted in Figure 5.3f. To plot the ideal scaling of ABAQUS, the simulation time of a single processor is estimated by assuming a similar scaling efficiency for PRISMS-Fatigue and ABAQUS in the case of using six processors, i.e., minimum number of processors in which ABAQUS was able to finish the simulation within 720 hours. While ABAQUS demonstrates better scalability for a smaller number of processors, the trend is not consistent as 24 processors has a weaker scalability compared to 48 processors. Furthermore, ABAQUS scaling performance saturates at 240 processors, and cannot reduce the simulation time by further increasing the number of processors, which is not the case for PRISMS-Fatigue. In the case of massive fatigue simulations, the PRISMS-Fatigue framework becomes a more suitable tool compared to the similar framework implemented in ABAQUS. Figure 5.3f shows that

PRISMS-Fatigue can simulate the sample in 1.08 hours using 480 processors, while ABAQUS requires 28.5 hours using the same number of processors.

5.3.3 Applications

Five different fatigue-related applications are investigated to demonstrate the flexibility of the PRISMS-Fatigue framework. The applications include the effects of different crystallographic textures, grain morphologies, boundary conditions, multiaxial strain states and strain magnitudes, and sample sizes on the FIP EVDs [127-129]. The first four applications employ the more traditional strategy of simulating SVE ensembles to build up the extreme value response. The fatigue simulations of microstructure instantiations with 90^3 and 160^3 voxels are computationally intractable for researchers without access to a very powerful supercomputing cluster and an advanced parallel code such as PRISMS-Fatigue. The alternative method is to simulate multiple smaller microstructure instantiation (i.e., SVEs) which facilitates a near equivalent study of material fatigue response with reduced computational demands. For the applications of crystallographic textures, grain morphologies, and boundary conditions, each SVE contains 29^3 voxels with an average of 250 grains per SVE, and there are 30 SVEs in each ensemble. The SVE instantiations used in the applications along with their grain morphologies and crystallographic ODF pole figures are Figure 2.3 and Figure 2.4, respectively. To investigate the effects of multiaxial strain states and different strain magnitudes, an ensemble of 10 SVEs with 30^3 voxels and an average of 278 grains per SVE undergoes 95 different combinations of strain state and amplitude. The total required wall time, number of required simulations, total DOFs, and number of processors are reported in Table 5.1. Figure 5.4 shows the results for each of these applications which

employ the same Al 7075-T6 crystal plasticity constitutive model as mentioned in the scaling study simulations.

Table 5.1. A summary of the simulation details and performance of the first four applications presented here including the effects of texture, grain morphology, and free surface on the driving force for fatigue crack formation along with the calculation of the Gamma (Γ) Plane iso-FIP contours. The wall time reported here was averaged over all the simulations of each Application.

Application	DOF	# of Processors	Wall time (s)	# of simulations
Texture effect	81,000	64	12,233	90
Grain Morphology effect	81,000	64	11,600	90
Free surface effect	81,000	64	28,100	90
Gamma (Γ) Plane	89,373	64	30,144	950

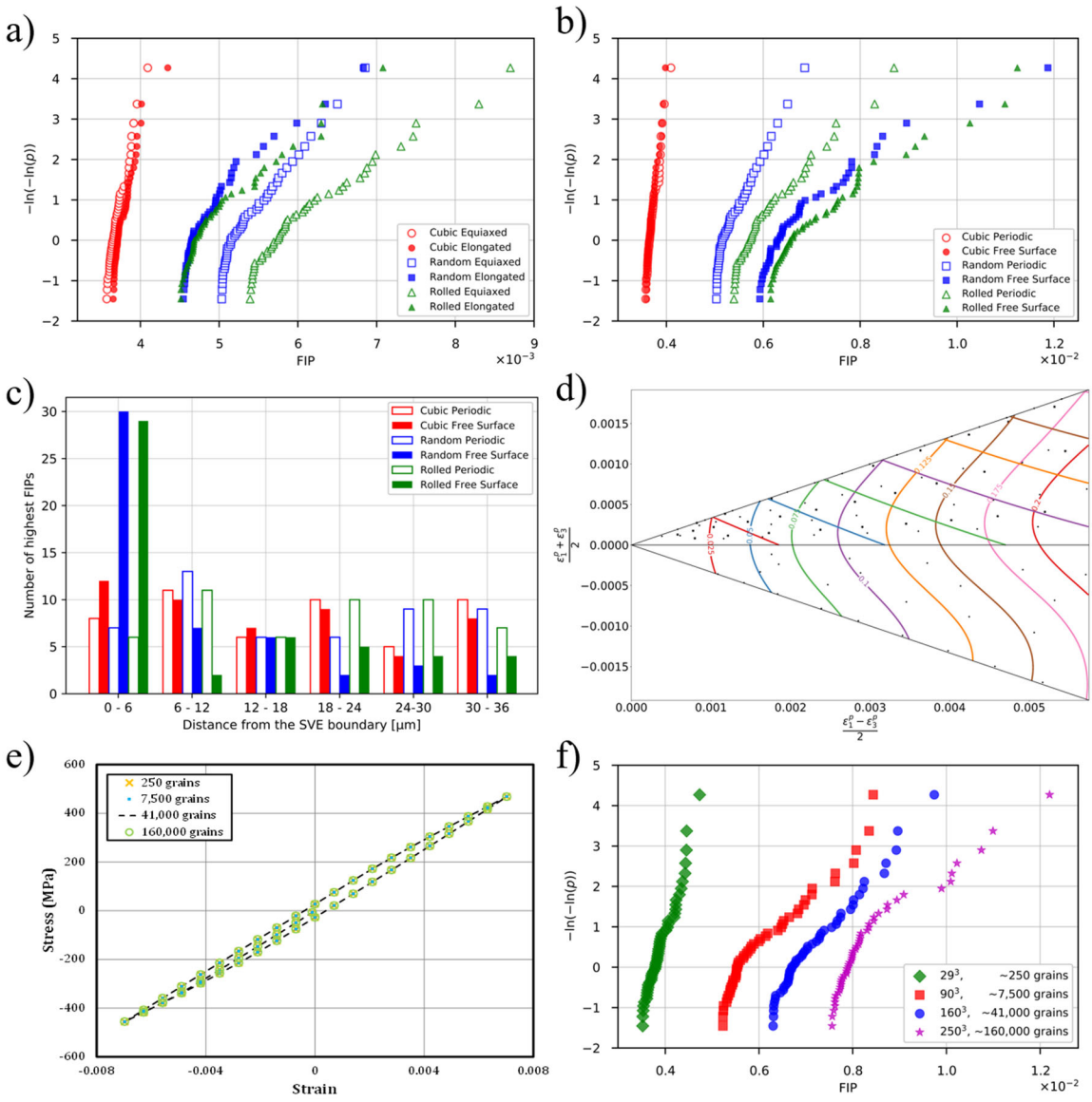

Figure 5.4. Five different applications of PRISMS-Fatigue. In (a,b), SBA FIPs are fit to the Gumbel EVD. In (a), FIP EVDs from microstructure ensembles with elongated grain morphology reduce FIP magnitudes. In (b), the combined effects of crystallographic texture and boundary conditions show an increase in FIP magnitudes in the presence of a free surface for the random and rolled textures. (c) The 50 highest sub-band averaged FIPs from (b) are plotted as a histogram of the distance to the edge of the sample, which indicates that the highest FIPs manifest close to the free surface for the random and rolled textures. However, there is no correlation between the grains with high FIPs and distance to the edge of the sample in the case of periodic boundary conditions. Iso-FIP contours in (d) are shown on a multiaxial gamma (Γ) plane. In (e), different size samples shows an indistinguishable stress-strain response. However, in (f), the FIP EVDs strongly depend on the sample size such that FIPs from the larger microstructures progressively increase and shift to the right.

As was examined in the two previous chapters, initial crystallographic texture plays a potentially important role in the micromechanical response of polycrystalline materials, including the microstructure-sensitive driving force for fatigue crack formation [147, 234]. Moreover, morphological texture (e.g., shape of grains) and boundary conditions also play important roles, even for high symmetry fcc metals such as Al alloys [235]. Accordingly, SVE ensembles of three different crystallographic textures are instantiated using DREAM.3D and include cubic, random, and rolled textures [128]. For each of the three textures, three ensembles were instantiated, i.e., nine ensembles in total, as follows: (1) equiaxed grains with fully periodic boundary conditions, (2) elongated grains with fully periodic boundary conditions, and (3) equiaxed grains with one set of parallel faces in each SVE set as traction-free/free surfaces/non-periodic while the other two pairs of faces are set as periodic. The latter instantiations are analogous to a material with a high area-to-volume ratio. Each SVE was subjected to fully reversed cyclic straining to a strain amplitude of 0.7% and at a strain rate of 10^{-3} s^{-1}. FIPs were calculated and volume averaged across the third straining cycle. Compressive straining was initiated in the X direction relative to the ODF pole figures. These applications mimic the results of the two previous chapters to demonstrate that the novel open-source PRISMS-Fatigue framework can capture the same material response as the previous ABAQUS implementation.

The effects of crystallographic texture and grain morphology are investigated first, more specifically to ensure PRISMS-Fatigue can produce the same results as the two previous chapters in which the ABAQUS commercial solver was used. After FIPs are calculated, they are volume averaged over sub-bands [128]. Figure 5.4a shows the highest 50 SBA FIPs from each ensemble of 30 SVEs fit to the Gumbel EVD. The cubic texture

results in the lowest driving force for fatigue crack formation. Examination of the cubic ODF pole figure indicates that grains are predominantly oriented for slip on multiple slip systems (nominally 8 of the 12 slip systems). Fatigue is expected to occur in locations of substantial local cyclic plastic deformation for which the Fatemi-Socie transgranular FIP is intended to apply. It is therefore expected that the cubic texture should result in relatively lower FIP EVDs, as slip is more homogeneously distributed throughout the microstructure; this decreases the probability of a single slip system with substantial slip. Conversely, both random and rolled textures exhibit higher FIP EVDs. Grain morphology in the cubic-textured SVEs does not considerably change the FIP EVDs. However, in the random and rolled textures, grain elongation considerably decreases the FIP EVDs (Figure 5.4a). It is important to note that the equiaxed and elongated grain SVEs contain the same nominal number of grains (i.e., grain volumes are similar). Thus, the lower values of these FIPs may be a consequence of plastic shear strain constraints due to the reduced mean free slip path in the elongated grains. The applications entitled *Texture_Effect_Al7075T6* and *GrainMorphology_Effect_Al7075T6* on Materials Commons contain the required information to perform these or similar simulations in PRISMS-Fatigue.

As was investigated in Chapter 3, the fatigue response of certain alloys is more sensitive to local micromechanical response near a free surface. Elastic/plastic anisotropy, surface condition, and applied strain play a strong role. For instance, in the lower crystal symmetry hcp titanium alloy Ti-6Al-4V, fatigue crack formation (FCF) was observed more than 500 μm below the specimen surface in the HCF regime but occurred near the surface in LCF [151]. Comparable Ti-alloys exhibit similar behavior with FCF at the surface only under rough surface conditions [153, 236, 237]. Conversely, FCF in aluminum alloy 7010-

T7451 is observed near the specimen surface under various surface conditions [150]. In the LCF regime (below 10^5 cycles), FCF occurred within 10 μm of the surface in Al 7075-T6, whereas in the HCF regime (above 10^5 cycles) all cracks formed at the surface [149]. The simulations performed here aim to capture these differences in the driving force for fatigue crack formation in Al 7075-T6 using two sets SVE ensembles for the three crystallographic textures with equiaxed grains. In the first set, boundary conditions are set to fully periodic in all three directions to imitate bulk material response. In the other set, one pair of parallel SVE faces are set to non-periodic and traction-free to replicate free surface conditions. This second set is representative of a thin sheet of material with a high surface area-to-volume ratio. A comparison of the FIP EVDs for the three textures with surface vs. bulk boundary conditions is shown in Figure 5.4b. The random and rolled textures show a substantial increase in FIP EVDs (these data are shifted to the right), which indicates the framework can capture the complex effects of free surface interactions on local micromechanical response, in accordance with experimental observations [149]. In addition, Figure 5.4c shows the 50 highest SBA FIPs from each of the ensembles in Figure 5.4b plotted as a function of the distance from the SVE boundary, which indicates that the highest FIPs occur close to the free surface for the random and rolled textures. However, there is no correlation between the FIP and the distance from the SVE boundary in the case of periodic boundary conditions. The application entitled *FreeSurface_Effect_Al7075T6* on Materials Commons contains the required information to perform these or similar simulations in PRISMS-Fatigue.

The fourth application demonstrates the ability to capture the effects of multiaxial strain states and different strain amplitudes. PRISMS-Fatigue is used here to generate a

computational Γ Plane as outlined in Chapter 4. The same ensemble of 10 SVEs from Chapter 4 is simulated to the same strain amplitudes. SVEs contain 30^3 voxels, an average of 278 grains, and have one pair of faces set to traction-free/non-periodic since the concept of the Γ Plane involves macroscopic plastic strain with respect to the free surface. Each SVE in the ensemble undergoes 95 different combinations of strain state and amplitude to populate the Γ Plane response coordinates using the macroscopic plastic strain tensor. At each response coordinate, the average of the 10 highest SBA FIPs for the ensemble are used as the response surface. A GPR model is then used with the response coordinates and surface as an input to populate the Γ Plane (i.e., interpolate across the Plane). The computational Γ Plane is shown in Figure 5.4d. It closely resembles experimental trends observed by Brown and Miller [16] and closely matches the Γ plane in Figure 4.7 [129]. The upper and lower limits represent uniaxial and equiaxial strain states, respectively, and the abscissa corresponds to pure shear. The application entitled *MultiaxialFatigue_Al7075T6* on Materials Commons contains the required information to perform these or similar simulations in PRISMS-Fatigue.

The fifth and final application investigates the effect of sample size on the driving force for fatigue crack formation. This application demonstrates the remarkably large microstructures that PRISMS-Fatigue can generate, simulate, and post-process to assess the microstructure-sensitive fatigue response. Four progressively larger samples of the Al alloy are generated and undergo cyclic straining with a strain amplitude of 0.7% as before. The four samples contain approximately 250, 7 500, 41 000, and 160 000 grains discretized with 30^3, 90^3, 160^3, and 250^3 elements, respectively. Each sample is generated as fully periodic and contains equiaxed grains with random initial crystallographic texture. Mesh

density is unchanged so the absolute size between samples is different, but the constitutive model employed does not consider size effects. The 160,000-grain microstructure discretized by 15,625,000 elements is the largest microstructure-sensitive fatigue CPFEM simulation currently available in the literature, not considering other simulation schemes such as FFT crystal plasticity [238, 239], for example. The required wall time to reach the point of initial maximum compressive strain for the 250^3 voxelized microstructure is 12 hours using 1,200 processors.

Figure 5.4e shows the cyclic stress-strain response between the four samples. The results demonstrate that the macro response is identical across the four different sample sizes and show that even the microstructure with 250 grains and 29^3 elements is large enough to capture the macro response. FIPs are computed across the third and final straining cycle and are subsequently averaged over sub-bands. The highest 50 FIPs from each sample are then fit to the Gumbel EVD as shown in Figure 5.4f. Whereas the macroscopic response between these samples is identical, the extreme value fatigue response is radically different. FIPs from the larger microstructures progressively increase and shift to the right Figure 5.4f. This reflects the experimentally observed volume knock-down effect in fatigue, where larger specimens of the same material exhibit lower fatigue lives due to an increased probability of a critical "hot-spot" for fatigue crack nucleation [240]. Similarly, the larger samples contain more grains and therefore a higher probability of grains favorably oriented for significant slip.

Comparison of FIPs from different types of microstructures to rank order fatigue resistance requires a sufficiently large simulated volume. This is often computationally intractable and consequently, ensembles of SVEs are simulated to build up a reliable

extreme value distribution [29]. In contrast, an RVE (as described in Section 2.6) contains sufficient grain/phase heterogeneity to reach convergence of some material property independent of boundary conditions [174, 175]. The RVE size for macroscopic elasto-plastic properties (as shown in Figure 5.4e) is relatively small whereas the FIP EVDs Figure 5.4f increase and suggest convergence is within reach. Thus, studies of RVE fatigue characteristics previously thought intractable can now be investigated by researchers using the superior performance of PRISMS-Fatigue to generate, simulate, and post-process very large polycrystalline samples. The post-processing task is particularly challenging and requires efficient Python scripted digital workflows. The Al 7075-T6 material system modeled here follows a lognormal grain size distribution with a mean and standard deviation of 14 μm and 2 μm, respectively. However, for other material systems with a larger mean grain size such as duplex Ti-6Al-4V, the physical size of the microstructure approaches experimental laboratory specimen size. For example, a mean grain size of 60 μm with ~160 000 grains and with the same mesh density results in a cubic simulated volume with a side length of 2.625 mm. This approaches laboratory scale specimen dimensions and will be critical for future simulation of additively manufactured microstructures for example.

5.4 Conclusions

An open-source microstructure-sensitive computational fatigue framework is presented with a focus on performance and flexibility. The framework contributes to both research and educational purposes by providing the basic tools to model fatigue crack formation within nucleant grains/phases; this chapter demonstrates its capability to compare relative fatigue resistance of a range of microstructures distinguished by

differences of crystallographic and morphological texture. This framework introduces a new paradigm in which researchers can utilize the foundational tools developed to focus on new aspects of microstructure-sensitive fatigue without having to build their own tools from the "ground up". The open-source software PRISMS-Plasticity serves as the CPFEM engine of PRISMS-Fatigue to capture micromechanical response of polycrystals. Benchmark simulations of surrogate fatigue driving forces, i.e., FIPs, in a polycrystalline Al 7075-T6 sample with random crystallographic texture and equiaxed grains demonstrated that PRISMS-Fatigue is up to 26 times faster than a similar framework implemented in the ABAQUS (both using 480 processors) with minimal differences in extreme value FIP response. The simulation speed and scaling become particularly important with large-scale simulations (~tens of millions of DOFs) which should complete in a reasonable timeframe. PRISMS-Fatigue was developed around flexibility and modularity in a way that users can easily modify parts of the code to customize their investigation. Two important aspects are the material library in which users can define their own constitutive model, and the FIPs library in which they can introduce new fatigue criteria. Five applications demonstrated the performance and flexibility of PRISMS-Fatigue in capturing the driving force for fatigue crack formation: different crystallographic textures, grain morphologies, multiaxial strain states and magnitudes using a computational multiaxial Gamma (Γ) Plane, boundary conditions, and sample sizes. Maximizing the downstream value of PRISMS-Fatigue depends on contributions from the research community analogous to other material science and mechanics platforms (e.g., NWChem [211], DFT-FE [212], CASM [213], LAMMPS [214], and NAMD [215]). Thus, the link

between PRISMS-Fatigue and Materials Commons will focus on facilitating continuous improvement in the framework as an efficient, flexible, scalable, and modular tool.

5.5 Future work

The PRISMS-Fatigue framework is flexible in terms of adding new physics and mechanics, and to enhance performance, flexibility, and accessibility. After capturing the formation of a small fatigue crack within a grain, for example, its growth to a size over the first 5-10 grains [31, 67] can be added to PRISMS-Fatigue. This regime is still strongly influenced by the microstructure and is important in its contribution to fatigue crack formation lifetime in the transition from low cycle into high cycle fatigue as strain amplitude is decreased. As the fatigue crack continues to grow, eventually it can be modeled using fracture mechanics methods. Yet another aspect of the PRISMS-Fatigue framework is integration with phase field methodology to model the macroscopic fatigue crack propagation for which the crack length and cyclic plastic zone are suitably large compared to the scale of microstructure. Accordingly, fatigue crack formation and early growth can be modeled by PRISMS-Fatigue, with subsequent propagation of macrocracks addressed using a phase field framework, for example. This provides a simulation platform for various stages of fatigue crack formation and growth coupled with microstructure. In this context, it is important to acknowledge that the PRISMS software includes PRISMS-PF, a high performance phase field code [94] which is based on the same deal.ii subroutines and framework as PRISMS-Plasticity, and the two codes are well integrated [93]. Adding new constitutive models into the material library is envisioned as a means to explore microstructure-sensitive fatigue simulation for a diverse range of materials.

CHAPTER 6. EFFECTS OF BOUNDARY CONDITIONS ON MICROSTRUCTURE-SENSITIVE FATIGUE CRYSTAL PLASTICITY ANALYSIS

The previous chapters demonstrated the use of FIP EVDs to rank order the fatigue resistance of different microstructures. This required simulating many grains/phases to capture sufficient microstructure heterogeneity. A crucial consideration in these types of CPFEM simulations is the nature of applied boundary conditions. The previously described open-source PRISMS-Fatigue framework enables the simulation of very large microstructures that may be used to study fatigue RVE characteristics. The available multi-point constraints in PRISMS-Fatigue impose periodic boundary conditions that can appropriately distinguish between the bulk and surface driving forces for fatigue crack formation, as demonstrated in the previous chapter. This chapter demonstrates the efficacy of these multi-point constraints in microstructure-sensitive CPFEM simulations and compares the extreme value fatigue crack driving force response using various boundary conditions, microstructures, and crystallographic textures. The effects of applied boundary conditions on different mechanical responses such as the macroscopic stress-strain response, local measures of plastic slip, and corresponding FIPs are studied. The results provide guidance for future microstructure-sensitive crystal plasticity fatigue studies and demonstrate the advanced capabilities of PRISMS-Fatigue to model large volumes of material microstructure.

6.1 Introduction

To examine the fatigue response of a certain volume of material, PRISMS-Fatigue can simulate a single large microstructure or an ensemble of SVEs. The latter approach can

be less computationally demanding if a single SVE is simulated at a time. The high scalability of PRISMS-Fatigue allows for the simulation of very large microstructures that were previously considered computationally intractable [5]. In so doing, the advantages of a finite element-based approached are preserved, for example rendering of grain boundaries and large deformation conditions. Several simulation boundary conditions are available in PRISMS-Fatigue. One of these employs multi-point constraints to impose periodic boundary conditions and emulates bulk, subsurface response [114]. Any discrepancies in the extreme value FIP response between a single large microstructure and that of an SVE ensemble comprising the same combined volume must first be evaluated before very large-scale simulations can be employed to study fatigue response with confidence of its RVE character. Increases in computational resources and algorithm efficiency will eventually enable the simulation of massive microstructures at the scale of actual experimental laboratory specimens with simpler boundary conditions. However, even these simpler boundary conditions must be evaluated to prevent erroneous simulation constraints. Moreover, even well-controlled fatigue experiments exhibit substantial variability in fatigue response, and therefore sources of uncertainty and variability must be sorted out. Among these, the scale of microstructure considered in simulations is considered in this work.

The goal of this chapter is to examine the efficacy and characteristics of different finite element method boundary conditions and how these may affect the mechanical response (e.g., macroscopic stress-strain, plastic slip, and extreme value fatigue response) in polycrystalline crystal plasticity simulations conducted for various material volumes. Zhang et al. [118] studied the response of an experimentally reconstructed Ti-5Al-2.5Sn

sample. They determined that geometrically realistic grain morphologies and physically meaningful boundary conditions are more important than fine tuning constitutive model parameters to accurately simulate polycrystalline heterogeneous deformation. Lim et al. [180] demonstrated that relatively constrained boundary conditions may induce additional mesh sensitivity and error in single crystal simulations. A strategy to incorporate grain-level residual stresses into simulations of an experimentally reconstructed Ti-7Al sample by Kapoor and Sangid [241] demonstrated the importance of physically realistic boundary conditions. They also showed the importance of simulating an adequate amount of material surrounding the reconstructed region of interest. It is thus clear that the type of applied boundary condition in polycrystalline crystal plasticity simulations has important implications, particularly if the extreme value cyclic slip response is of interest.

Section 6.2 describes the unique non-periodic boundary conditions investigated in this chapter. Section 6.3 examines the effect of periodic boundary conditions using two comparisons. In the first comparison, an ensemble of five microstructure instantiations with 29^3 elements and ~250 grains are simulated with periodic boundary conditions. These five microstructures are then "padded" with themselves in every direction, creating a repeated microstructure with 87^3 elements. The mechanical response including the uniaxial cyclic stress-strain response, plastic slip, and extreme value FIPs are compared between the original 29^3 microstructures and the center 29^3 regions of the repeated 87^3 microstructures. For the second comparison, five microstructure instantiations are generated with 90^3 elements and ~7,500 grains. The entire 90^3 microstructures are simulated but only the 30^3 regions in the center are examined. Simultaneously, these center 30^3 regions are cropped and simulated with periodic boundary conditions. The mechanical responses of the 30^3

regions extracted from the 90^3 microstructures are compared to the cropped 30^3 regions with erroneously imposed PBCs.

To replicate laboratory experiments and to determine the extent to which surrounding microstructure affects the micromechanical response, Section 6.4 investigates a microstructure with 90^3 elements and ~7,500 grains that is progressively extended in one direction whilst retaining periodicity. In addition to fully periodic and periodic with one pair of free surfaces (i.e., "thin film") boundary conditions, three types of non-periodic boundary conditions are investigated: 1) "grip" boundary condition, in which one face is completely restrained and traction is applied to the opposite face, and 2) "symmetry" boundary condition, which mimics a sample subjected to pure uniaxial loading that has symmetry and only one-eight of the sample is modeled, and 3) "minimal" boundary condition, which is the least restricting and contains four free surfaces. In Section 6.5, the mechanical response including the uniaxial cyclic stress-strain curve, plastic slip, and extreme value fatigue (i.e., FIP) response of three crystallographic textures is examined with two different surface area-to-volume ratios simulated with the "thin film" and fully periodic boundary conditions.

6.2 Methodology

This chapter employs the same crystal plasticity constitutive model of Al 7075-T6, DREAM.3D microstructure generator, FIP calculations, and extreme value statistics as the previous chapter. The unique non-periodic boundary conditions that are the focus of this chapter are described below.

6.2.1 Boundary and loading conditions

The simulation boundary conditions available in PRISMS-Fatigue were previously shown Figure 2.2b and include non-periodic, periodic, and a "thin film" boundary condition in which two directions are periodic (in this case, the X and Z directions), and the Y direction is non-periodic and allowed to deform freely. The first case is perhaps most commonly employed in finite element method simulations with several options.

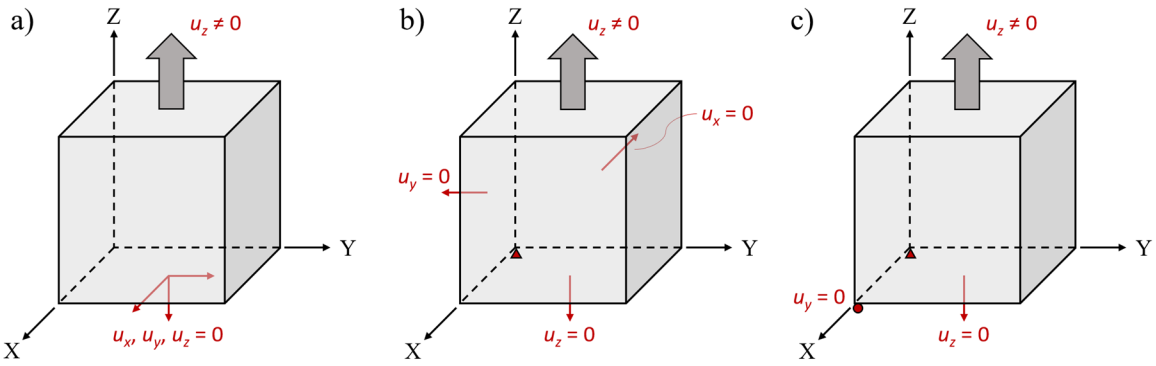

Figure 6.1. Schematic of the a) grip, b) symmetry, and c) minimal non-periodic boundary conditions.

The boundary conditions employed for the non-periodic simulations in this chapter are termed "grip", "symmetry", and "minimal", and are shown schematically in Figure 6.1. The same three options are available in the FEpX open-source finite element solver [242]. The "grip" boundary condition fully constrains one face with an applied traction or displacement applied to the opposite face. "Symmetry" boundary conditions mimic a sample subjected to uniaxial loading which has symmetry such that only one-eight of the sample is modeled. Accordingly, roller constraints are applied to three adjacent, mutually perpendicular faces with the common vertex fixed in all directions, while the uniaxial

displacement or traction is applied on one of the free surfaces associated with the loading direction. The "minimal" boundary condition constrains the node at the origin, the displacement of one face in the direction perpendicular to the face, and one node at the vertex of the same face. Traction or load is then applied to the opposite face. This final condition has four free surfaces like the "grip" condition but is less computationally restrictive.

Naturally, these simplest boundary conditions perturb the micromechanical response. They are applied to a progressively larger microstructure in Section 6.4 to characterize their effects on the mechanical response, including the macroscopic stress-strain response, local plastic slip, and extreme value FIP response. Zhang et al. [118] studied the response of a reconstructed Ti-5Al-2.5Sn sample with a "soft" (four unconstrained faces comparable to uniaxial tension and equivalent to the "minimal" boundary condition described above) and "hard" (only one unconstrained face representative of the free surface with the others forced to remain planar and similar to the "symmetry" boundary condition described above) boundary condition. They concluded that a geometrically realistic grain morphology along with a physically meaningful boundary condition is more important to accurately simulate polycrystalline heterogeneous deformation rather than fine-tuning constitutive model parameters for a given boundary condition type. Lim et al. [180] showed that relatively constrained boundary conditions (e.g., strain applied in one direction while constraining the other two directions) may induce additional mesh sensitivity and error in single crystal simulations. In contrast, the same applied strain in one direction without the extra constraints in the other two directions significantly reduced mesh sensitivity [180]. Some studies have focused on a single type

of boundary condition but with different loading conditions (e.g., “minimal” boundary conditions with “static” and “kinematic” loading, corresponding to an applied traction and displacement, respectively [179]).

Periodic boundary conditions for the polycrystalline crystal plasticity simulations in this chapter were described in detail in Section 2.3 as outlined by Przybyla [114]. All microstructures generated in this chapter undergo fully reversed ($R_\varepsilon = -1$) uniaxial cyclic straining to a strain amplitude of 0.7% to mimic HCF regime conditions. Straining is initiated in compression with zero initial back stress and zero initial strain. Temperature is assigned as 300 K. Only two fully reversed straining cycles are applied since computed FIPs rapidly saturate within a few cycles with the constitutive model employed here. This alleviates computational demands which are quite high in the largest simulations (e.g., 90 x 90 x 250 = 2,025,000 elements in Section 6.4). The microstructures simulated in Section 6.5 with different crystallographic textures are strained in the X direction relative to the ODF pole figures in Figure 2.4. In simulations where only a random crystallographic texture is considered, the macroscopic response of the sample is independent of loading direction, but the local (e.g., grain level) response varies.

6.3 Efficacy of periodic boundary conditions

PRISMS-Fatigue can perform CPFEM simulations of large microstructures previously thought intractable. To populate a reliable FIP EVD, one may simulate an ensemble of SVEs or a single large microstructure instantiation. The matter in question is whether FIPs from these two scenarios may be directly compared. Although the same volume of material is simulated, the former scenario contains more area and grains split by

the microstructure boundary. Thus, the efficacy of periodic boundary conditions is examined in this section using two microstructure sets, specifically whether the multi-point constraints impose periodic micromechanical deformation as intended.

6.3.1 Repeating microstructure with periodic boundary conditions

For the first microstructure set, five periodic microstructures with 29^3 elements and ~250 grains are generated using DREAM.3D. They are then padded in each direction to create five 87^3 microstructures that are repeating (see Figure 6.2a). The pairs of five microstructures undergo fully reversed cyclic straining to a strain amplitude of 0.7% as described in Section 6.2.1, with periodic boundary conditions in all three directions. The mechanical response of each 29^3 microstructure is then compared to the center 29^3 region of the associated repeating 87^3 microstructure. In other words, the response of identical microstructures, simulated in one scenario with periodic boundary conditions and in the other by placing them into periodic repeating microstructures, is directly compared.

The macroscopic cyclic stress-strain curves, histograms of cumulative effective plastic strain at each integration point, and largest sub-band volume averaged FIPs from each grain are shown in Figure 6.2b, Figure 6.2c, and Figure 6.2d, respectively, for the first of the five 29^3 and 87^3 microstructure pairs. In Figure 6.2c, the effective cumulative plastic strain is extracted from the final point of maximum tension in the simulations. The results indicate that the periodic boundary conditions imposed using multi-point constraints work remarkably well to emulate bulk, subsurface material response of periodic microstructures generated using DREAM.3D. The results are shown only for the first of the five 29^3 and 87^3 microstructure pairs, but the results are identical for the other four.

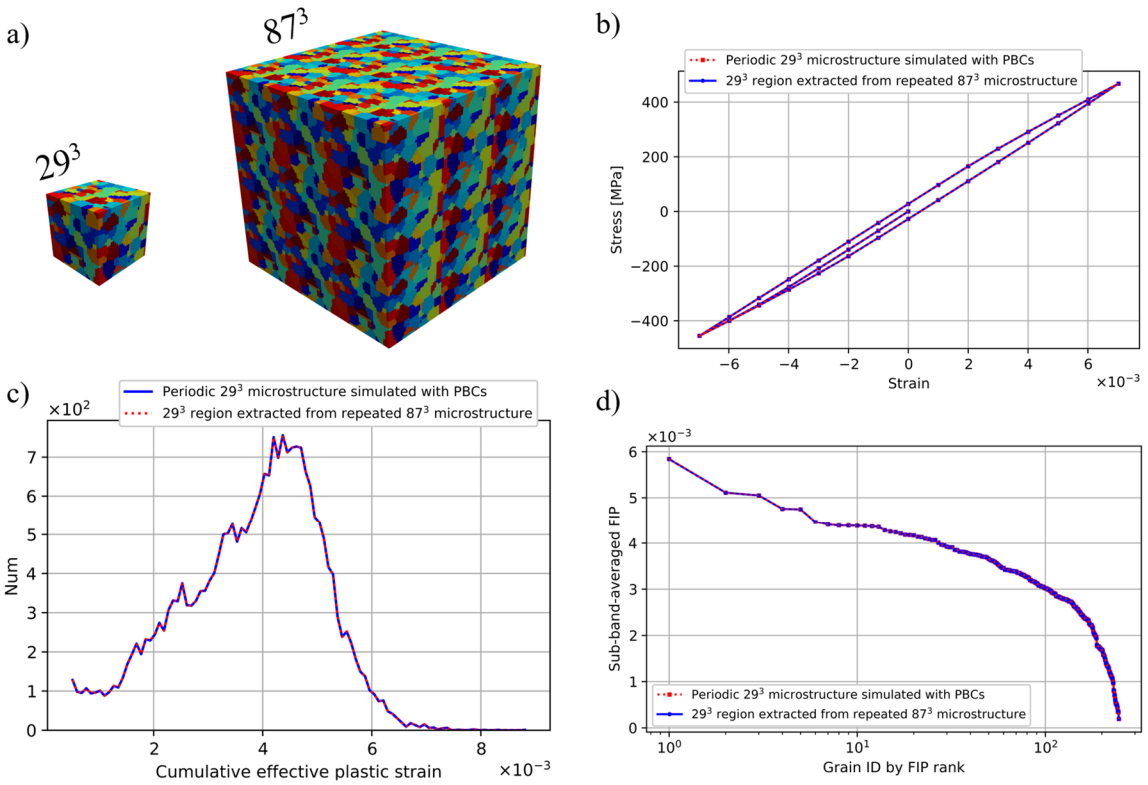

Figure 6.2. a) One of the five 29^3 microstructures that is padded in all directions to create a repeating 87^3 microstructure. Data in b) thru d) are shown for one of the five 29^3 and 87^3 microstructure pairs. b) Macroscopic cyclic stress-strain curves of the 29^3 microstructure and the center 29^3 region from the repeating 87^3 microstructure. c) Histograms of cumulative effective plastic strain at each integration point of both 29^3 regions. d) The largest sub-band volume averaged FIP per grain from both 29^3 regions in descending order.

6.3.2 Effects of erroneously applied periodic boundary conditions

This section demonstrates the necessity of generating a periodic microstructure along with periodic boundary conditions based on multi-point constraints. Numerous prior studies have enforced the former without the latter To this end, the consequences of imposing periodic boundary conditions on non-periodic microstructures are evaluated using the second microstructure set. Five microstructures with 90^3 elements and ~7,500 grains are generated using DREAM.3D. The center 30^3 region of each 90^3 microstructure

is then extracted (see Figure 6.3a), which is undoubtedly non-periodic. The five microstructure pairs undergo cyclic straining to a strain amplitude of 0.7% with periodic boundary conditions as described in Section 6.2.1.

The macroscopic stress-strain curves for the first pair of 30^3 and 90^3 microstructures are shown in Figure 6.3b, i.e., the center 30^3 region of the 90^3 microstructure and the nonperiodic 30^3-region simulated by itself with periodic boundary conditions. The macroscopic response is not expected to vary, and the curves are indistinguishable. Figure 6.3c shows the largest sub-band volume averaged FIP per grain from the 30^3 regions of all five microstructure pairs. Only the 400 largest FIPs are compared because the FIPs quickly converge. Although the 30^3 non-periodic microstructures simulated with periodic boundary conditions manifest a few FIPs that are larger in magnitude, the 30^3-region extracted from the 90^3 microstructures consistently displayer larger FIPs, until about 200 grains are considered.

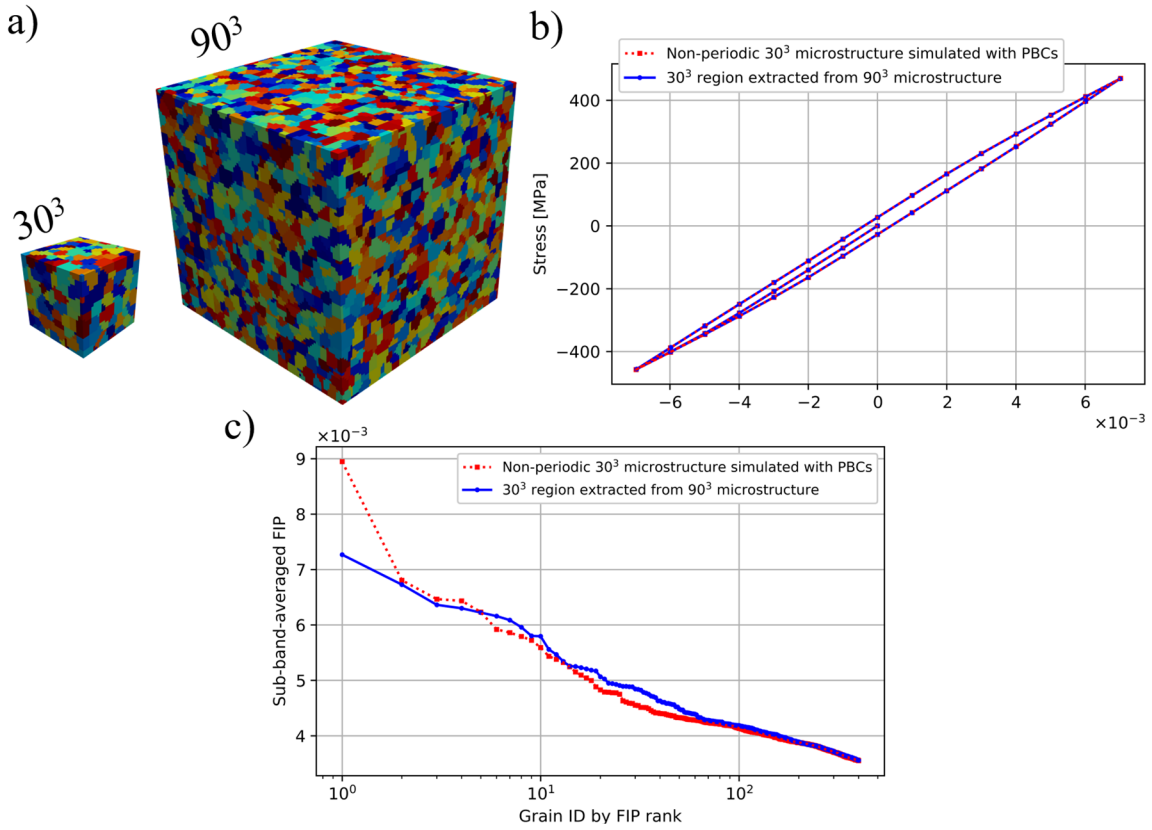

Figure 6.3. a) One of the five 90^3 microstructures from which the center 30^3 region is extracted. Although the 30^3 microstructures are no longer periodic, they are simulated with periodic boundary conditions to assess whether their micromechanical responses are comparable to the center 30^3 regions of the 90^3 microstructures. b) Macroscopic cyclic stress-strain curves from one pair of 30^3 microstructures and the center 30^3 region of the associated 90^3 microstructure. c) The largest sub-band volume averaged FIP per grain from both 30^3 regions in descending order. Although there are around 2,100 total grains in the five 30^3 regions, only the largest 400 are shown in c) because the FIPs converge.

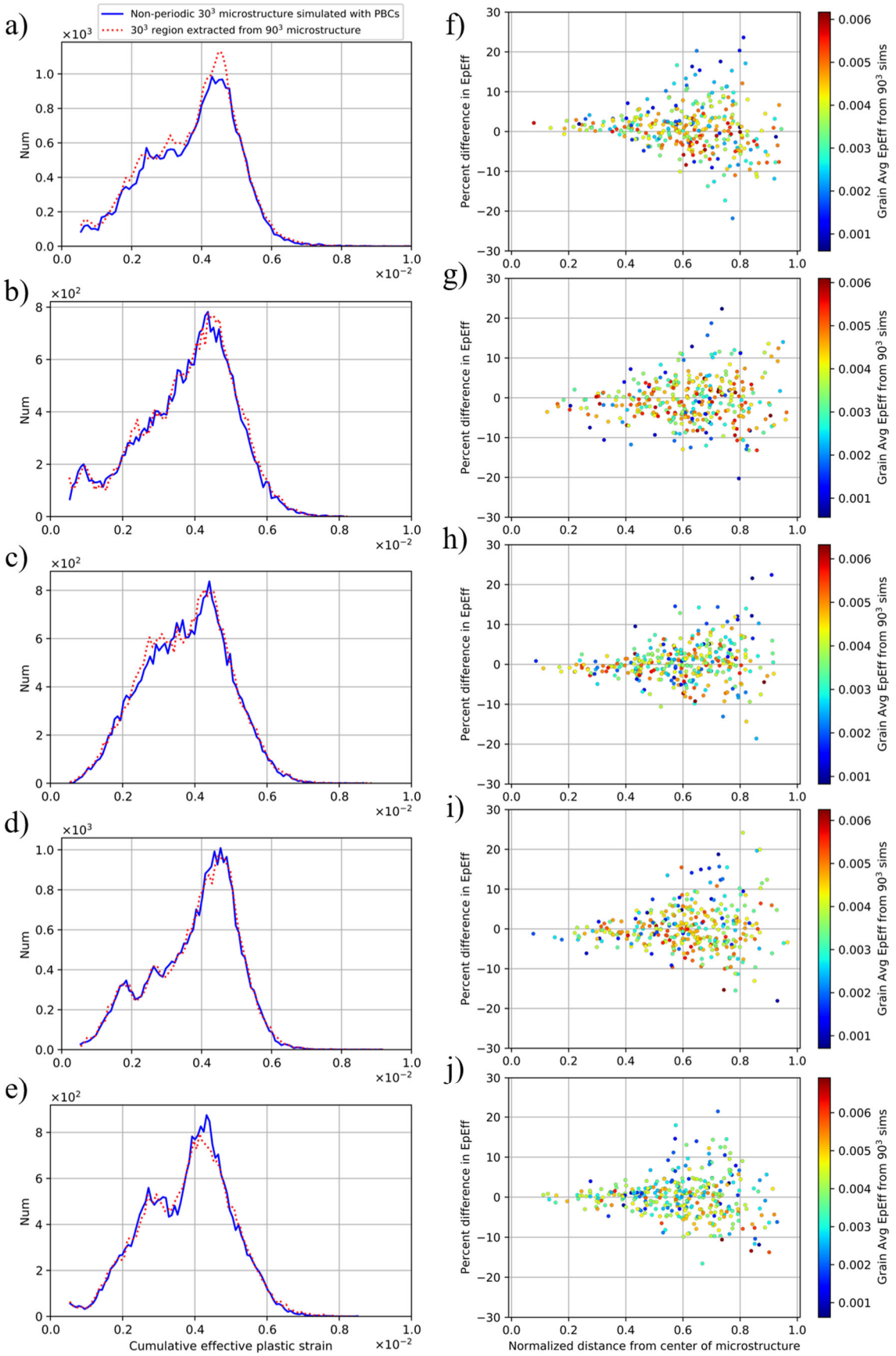
a)
b)
c)
d)
e)
f)
g)
h)
i)
j)
Non-periodic 30³ microstructure simulated with PBCs
30³ region extracted from 90³ microstructure
Num
Cumulative effective plastic strain
Percent difference in EpEff
Normalized distance from center of microstructure
Grain Avg EpEff from 90³ sims

Figure 6.4. (a-e) Histograms of cumulative effective plastic strain at each integration point for each of the five microstructure pairs. (f-j) Percentage difference in grain averaged cumulative effective plastic strain as a function of distance from the center of the microstructure. The responses of the 30^3 regions within the 90^3 microstructures are considered the original values, and the percentage indicates whether the plastic deformation averaged over that grain is promoted (positive percentage) or restricted (negative percentage) when the 30^3 region is simulated by itself with periodic boundary conditions. Furthermore, only grains with at least 20 elements are considered. The color bar indicates the grain averaged cumulative effective plastic strain from the 30^3 regions within the 90^3 microstructures.

The local response for each of the five microstructure pairs is shown in Figure 6.4. In the left column, Figure 6.4a-e show histograms of the cumulative effective plastic strain for each integration point and for each of the five microstructure pairs. The effective cumulative plastic strain is extracted from the final point of maximum tension in the simulations, and the data in each plot look comparable. The right column of Figure 6.4 shows the difference in grain averaged cumulative effective plastic strain. More specifically, the data represents the percentage difference in micromechanical response after the center 30^3 regions are extracted from the 90^3 microstructures and are simulated separately with periodic boundary conditions. Thus, a negative percentage indicates that the grain in question experiences less plastic deformation as compared to that same grain's response when imbedded and simulated in the original 90^3 microstructures, i.e., plastic deformation is restricted. The data is plotted as a function of the grain distance from the center of the microstructure to evaluate any spatial correlations. Furthermore, only grains with at least 20 elements are considered. The color bar indicates the grain averaged cumulative effective plastic strain from the 30^3 regions simulated within the 90^3 microstructures.

Grains near the microstructure boundary are strongly perturbed, whereas grains near the center of the microstructure show minimal change in grain averaged plastic deformation. Chapter 3 examined the micromechanical response of Al 7075-T6 microstructures using the same constitutive model and simulation sizes as employed here. The results likewise indicated that the influence of different boundary conditions decayed towards the center of the microstructures. The percentages of data below 0% (indicative of more restricted plastic deformation) in Figure 6.4f-j are 40.9%, 56.3%, 48.3%, 54.2%, and 46.4%, respectively. Thus, in some microstructures, the grain averaged response is in general suppressed, whereas it is promoted in others. An important implication of Figure 6.4f-j and the sub-band volume averaged FIPs in Figure 6.3c is that these effects are nontrivial. The efficacy of multi-point constraints as demonstrated in the previous section indicate that the results here are entirely influenced by the change in the microstructure neighborhood.

In general, the deformation of nodes as sets on the microstructure boundaries restricts deformation. This is because the multi-point constraints are not imposed on individual nodes but rather on faces, edges, and vertices. Constrains on individual nodes may be more physically realistic but are drastically more complicated to implemented into a finite element method framework. Nodes along a boundary of the extracted 30^3 regions are forced to deform as a plane in the smaller microstructures, whereas those same nodes are less constrained in the 90^3 microstructure simulations. However, the previous section demonstrated that even the extreme value local response is not affected when nodes are constrained to deform as sets, provided that the microstructure neighborhood is unaltered.

To conclude, both microstructure and simulation periodicity must be jointly enforced in these types of microstructure-structure fatigue simulations.

6.4 Non-periodic boundary conditions

As computational capabilities increase and more efficient simulation algorithms are developed, large microstructures approaching realistic laboratory test specimen dimensions may be simulated. This may remove the need for periodic microstructures and boundary conditions, but non-periodic boundary conditions must still be evaluated regarding their effects on the extreme value fatigue response, for example the influence of a free surface on modification of constraint on slip. In this section, a periodic microstructure with 90^3 elements, ~7,500 grains, and random crystallographic texture is simulated. It is progressively extended in the Z-direction as shown in Figure 6.5. Element layers from the opposing Z faces are used to extend the microstructure while retaining periodicity. The effects of boundary conditions applied farther from the center 90^3 region of interest are then investigated.

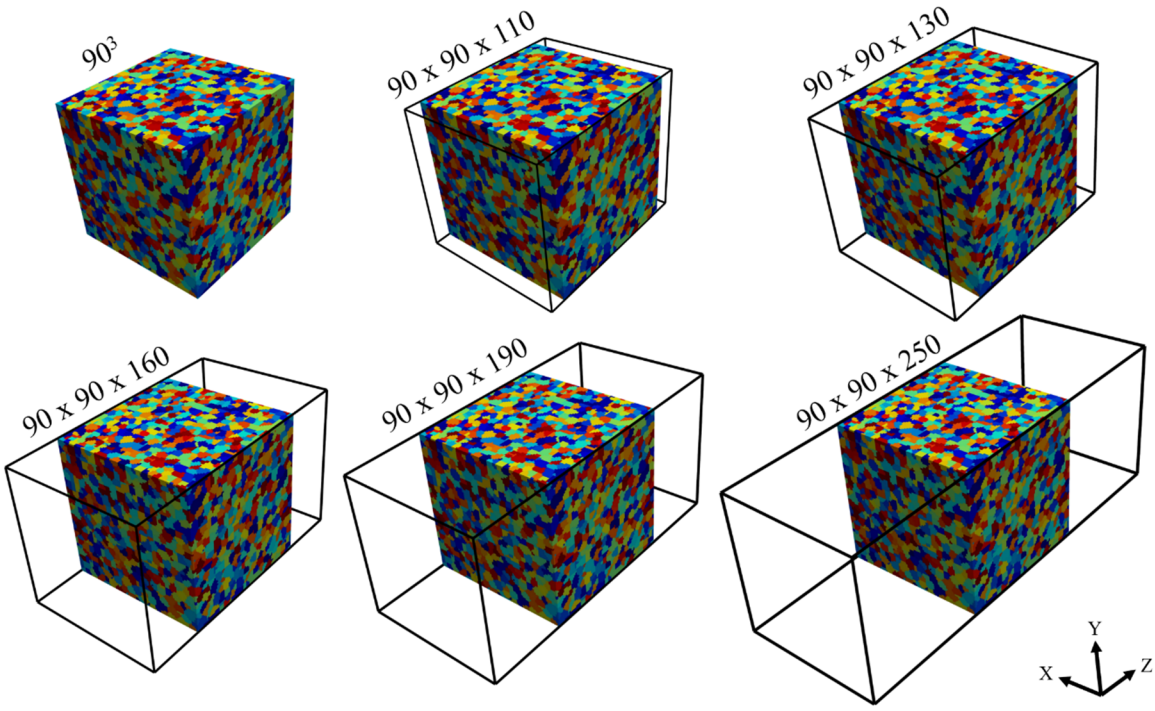

Figure 6.5. A periodic microstructure with 90^3 elements and ~7,500 grains that is progressively extended in the Z direction with element layers from the opposite Z face to retain periodicity. The response of each microstructure is only evaluated in the center 90^3 region.

The "grip" and "minimal" boundary conditions are applied to the top and bottom Z face for the microstructures shown in Figure 6.5. In both scenarios, the microstructure has four free surfaces. This microstructure is generated as periodic in DREAM.3D, and grains that are split by the microstructure boundary in the X and Y directions are located and indexed accordingly for proper FIP volume averaging. The "symmetry" boundary condition mimics a sample subjected to pure uniaxial loading which has symmetry and only one-eight of the sample is modeled. For the "symmetry" boundary condition, the origin is fixed, and the three mutual adjacent and orthogonal faces are constrained as "rollers" (i.e., deformation normal to the plane is restricted) with displacement applied to

a fourth face. Thus, the "symmetry" boundary condition renders only two faces as free. The original 90^3 microstructure is also simulated with fully periodic boundary conditions and under the "thin film" boundary condition with the Y direction set to a free surface/non-periodic. The latter case also results in two free surfaces, although these are now on opposites faces and not adjacent as is the case of the symmetry boundary condition. All microstructures undergo fully reversed cyclic straining to 0.7% strain and FIPs are calculated across the second straining cycle.

6.4.1 Macroscopic response

Macroscopic cyclic stress-strain curves for the grip, symmetry, and minimal boundary conditions are shown in Figure 6.6a, Figure 6.6b, Figure 6.6c, respectively. The legends indicate the microstructure in Figure 6.5 from which the response of the center 90^3 region was extracted. The macroscopic response of the fully periodic boundary condition is shown in each plot so that all curves may be relatively compared. The macroscopic response of the "thin film" boundary condition is shown in Figure 6.6b and Figure 6.6c. There are negligible differences between all curves expect for the point of maximum applied tension using the grip boundary condition. Figure 6.6a shows a relatively stiffer response that slowly approaches the response of the fully periodic boundary conditions with additional padding. The grip boundary condition is not considered for the original 90^3 microstructure due to an artificial stress concentration along the edges of the constrained bottom Z face which produced an unrealistic micromechanical response.

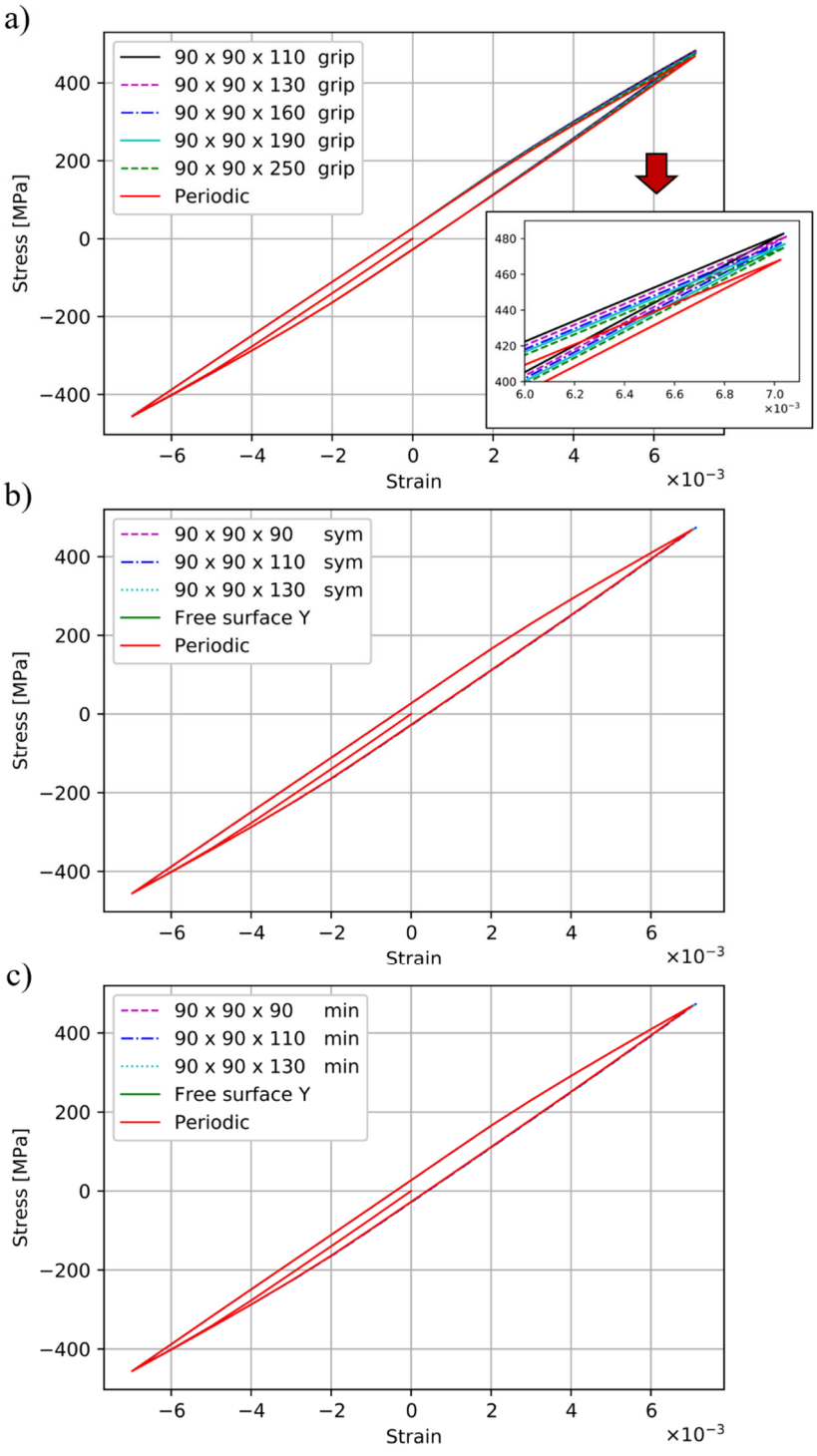

Figure 6.6. Macroscopic cyclic stress-strain response of the center 90^3 region of the microstructures in Figure 6.5 under different applied boundary conditions. All microstructures were cyclically strained to a fully reversed strain amplitude of 0.7% at room temperature.

6.4.2 Local response

Histograms of the cumulative effective plastic strain for the grip, symmetry, and minimal boundary conditions are shown in Figure 6.7a, Figure 6.7c, and Figure 6.7e, respectively, for each integration point. Data for the fully periodic boundary condition is shown in each of the three plots for comparison and displays the lowest values, which reflects the more restricted sub-surface material response. The grip boundary condition does not appear to converge even for the largest padding of 90 x 90 x 250. In contrast, the other two boundary conditions converge with only 10 element layers padded onto each side of the Z face, i.e., 90 x 90 x 110, because the response does not change with additional padding using the 90 x 90 x 130 microstructures. Finally, the "thin film" boundary conditions with the two faces perpendicular to the Y direction set to free surfaces displays slightly larger cumulative effective plastic strain values.

The sub-band volume averaged FIPs for the three boundary conditions are shown in Figure 6.7b, Figure 6.7d, and Figure 6.7f, respectively. A single FIP per grain is considered here and the 50 largest from each center 90^3 region are fit to the Gumbel EVD to facilitate fatigue resistance rank ordering. FIPs from the fully periodic simulation display the lowest FIPs (green square markers). In the presence of a free surface (blue circle markers in Figure 6.7b), FIPs slightly increase in magnitude, reflecting experimental observations for this material system [149, 150] and in line with previous simulations [128] and chapters. The extreme value micromechanical effect of different boundary conditions varies greatly. Figure 6.7b shows that progressively padding the original 90^3 microstructure using the grip boundary condition decreases FIP magnitude, but the values do not appear to converge for any practical simulation size. The grip boundary condition not only

perturbs the macroscopic response as shown in Figure 6.6a but also the extreme value response in a way that makes it ill-advised for these types of simulations. Its response is not shown for the original 90^3 microstructure because the artificial stress concentration mentioned earlier manifests FIPs an order of magnitude larger than those shown here.

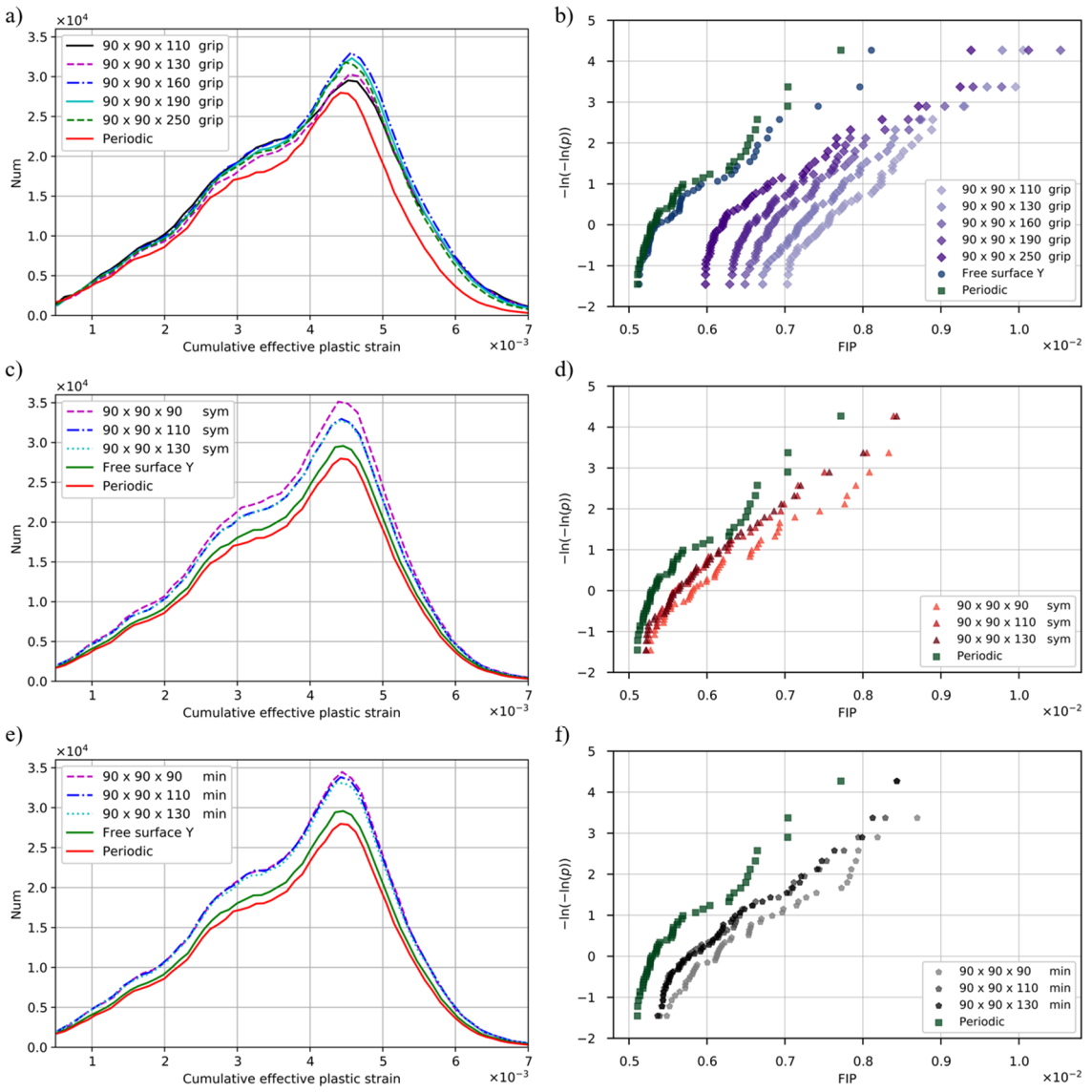

Figure 6.7. Histograms of cumulative effective plastic strain for the a) grip, c) symmetry, and e) minimal boundary conditions. The highest 50 sub-band volume averaged Fatigue Indicator Parameters (FIPs) from the center 90^3 region fit to the Gumbel Extreme Value Distribution (EVD) for the b) grip, d) symmetry, and f) minimal boundary conditions.

On the other hand, the symmetry and minimal boundary conditions converge for the extreme value FIP response using the 90 x 90 x 110 microstructure, i.e., padding with more than 10 element layers on each side of the Z face does not further influence the extreme value response (see Figure 6.7d and Figure 6.7f). This makes both boundary conditions desirable for non-periodic fatigue related applications. Furthermore, the distribution of converged FIPs varies slightly from those under the "thin film" boundary conditions shown in Figure 6.7b. Both "thin film" and symmetry boundary conditions contain two free surfaces, and as such their FIP EVDs display similar values. In the former, the X and Z directions are periodic in microstructure and in the simulation (using the multi-point constraints, which constrain the nodes on a microstructure face as a whole), whereas the Y is a free surface. In the latter, one of the two X and Y faces are free surfaces, while the other two are "rollers" and constrained from in-plane deformation, and both Z face are periodic in microstructure with padding. The minimal boundary condition contains four free surfaces and the converged FIP EVDs in Figure 6.7f are accordingly slightly larger in magnitude. This latter boundary condition is best suited to simulate large microstructures to replicate experimental fatigue tests. Finally, the local response of all boundary conditions is shown in Figure 6.8 using data extracted from the center 90^3 region of the 90 x 90 x 130 microstructure. The grip boundary condition produces a notably different response for both cumulative effective plastic strain and extreme value fatigue response. Importantly, the histogram distributions of cumulative effective plastic strain converge well for the symmetry and minimal boundary conditions, and their slight difference in extreme value fatigue response is due to an increased number of grains exposed to the free surface in the latter boundary condition. The next section investigates this effect further.

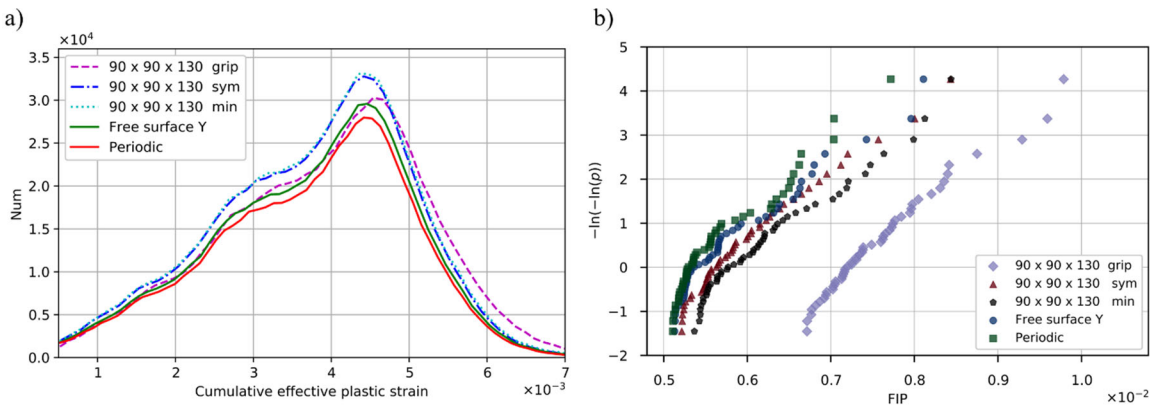

Figure 6.8. a) Histograms of cumulative effective plastic strain and b) the highest 50 sub-band volume averaged Fatigue Indicator Parameters (FIPs) fit to the Gumbel Extreme Value Distribution. The first three data sets were extracted from the center 90^3 region of the 90 x 90 x 130 microstructure in Figure 6.5, whereas the last two data sets were simulated using the original 90^3 microstructure.

6.5 SVE ensemble fatigue response

This section compares how fully periodic and "thin film" boundary conditions affect the driving forces for fatigue crack formation for microstructures with three crystallographic textures, using a single large microstructure and an SVE ensemble of smaller microstructures. The effect of two different surface area-to-volume ratios is also investigated. The macroscopic cyclic stress-strain curves for the three crystallographic textures are shown in Figure 6.9 using microstructures with ~7,500 grains discretized by 90^3 elements. Simulations were initiated in compression with straining in the X direction relative to the ODF pole figures in Figure 2.4 and fully periodic boundary conditions. The response of the random and rolled textures is similar whereas the cubic texture displays a softer response, due to more homogenous distribution of plastic deformation.

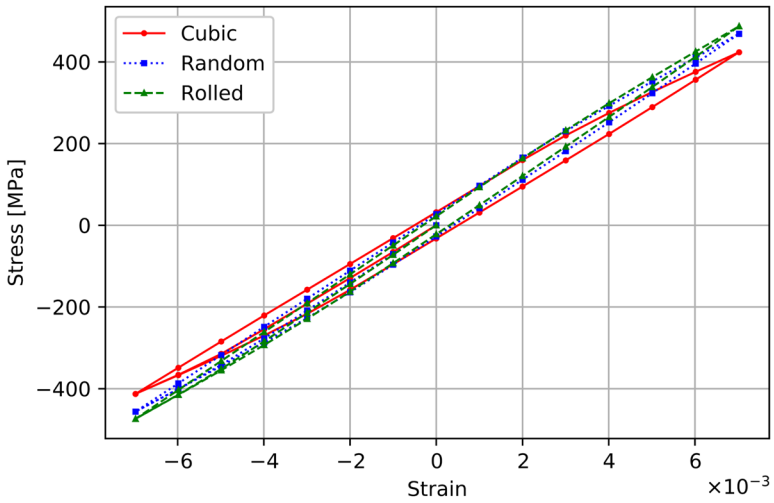

Figure 6.9. Macroscopic cyclic stress-strain curves for the three crystallographic textures simulated with ~7,500 grains, 90^3 elements, and fully periodic boundary conditions. Microstructures were loaded in the X direction relative to the ODF pole figures in Figure 2.4.

The three sets of simulations are shown in the left column of Figure 6.10 with approximately the same total number of grains. In the first set, 30 SVEs with 29^3 elements and ~250 grains are simulated with fully periodic and thin film boundary conditions (shown in Figure 6.10a). This can be equivalently compared to the second simulation shown in Figure 6.10b of a single large microstructure with 159 x 29 x 159 elements and approximately the same number of total grains. In the final simulation, a cubic volume of 90^3 elements and still the same number of grains is simulated. In each case, unique microstructure instantiations are generated and simulated with both boundary conditions under two fully reversed straining cycles to a strain amplitude of 0.7%. The first two simulation sets compare the difference in extreme value response from a single large microstructure and an SVE ensemble, while the last two sets compare the effect of a different surface area-to-volume ratio. All simulations and microstructures are periodic in

the X and Z directions, whereas the Y direction is non-periodic only under the “thin film” boundary conditions.

The FIP EVDs in Figure 6.10 show that the cubic crystallographic texture appears fully converged in all three scenarios and shows little difference between the bulk and surface response. This texture’s ODF pole figure in Figure 2.4 reveals that plastic slip, on average, is evenly distributed on 8 of the 12 available slip systems. This explains why these FIPs are the lowest: the likelihood of a single grain oriented favorably for significant slip is lower than the other two textures. For a sufficiently large microstructure, the response of the random crystallographic texture is expected to be identical in all possible straining directions [79]. It is interesting that the rolled crystallographic texture FIPs are the highest, which may not be the case if these microstructures are strained in another direction. As a reminder, all microstructures were strained in the X direction relative to the ODF pole figures in Figure 2.4, which for the rolled texture corresponds to the rolling direction after material processing. Random and rolled textured FIPs increase in magnitude in the presence of a free surface.

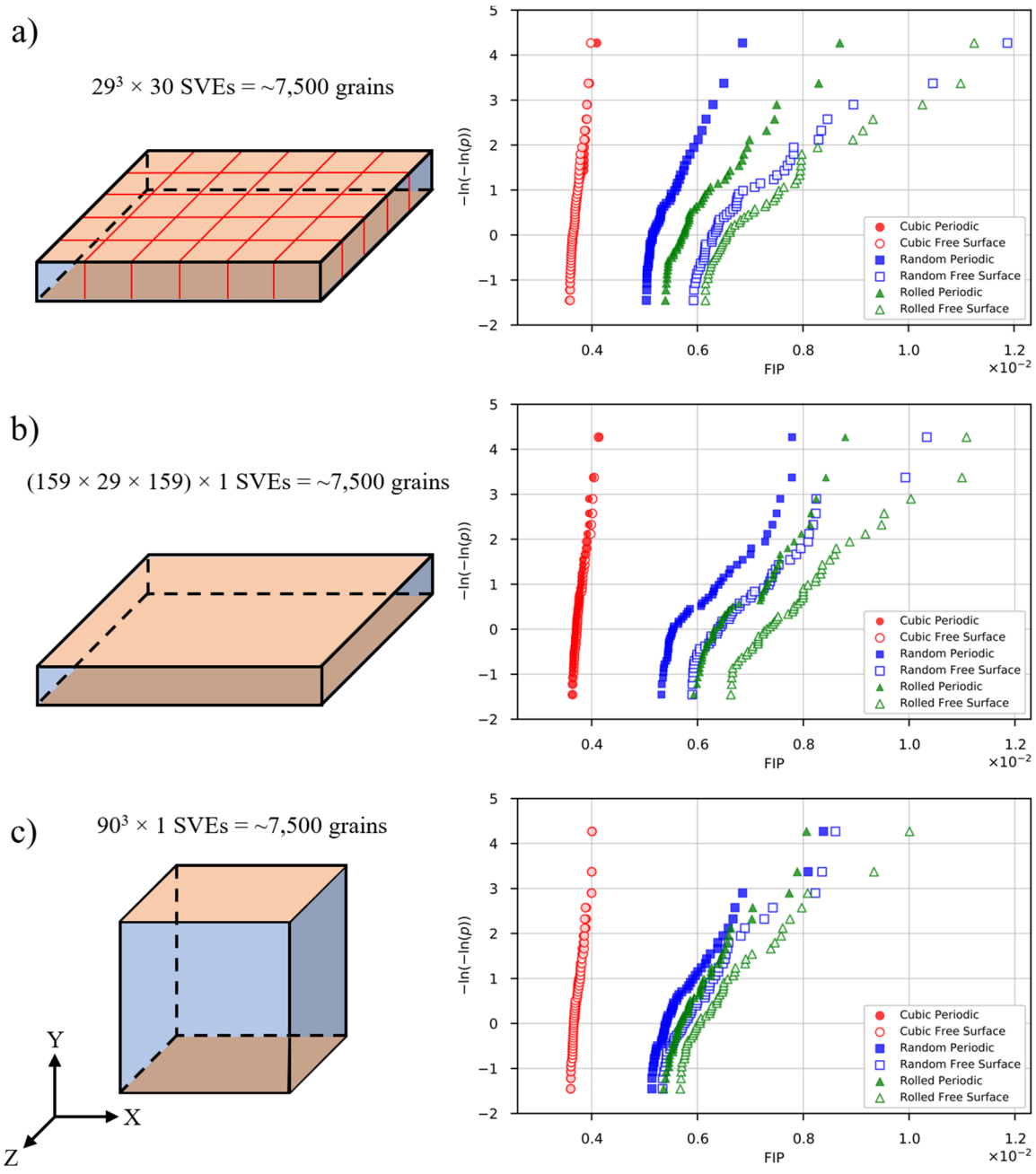

Figure 6.10. Comparison of FIPs fit to the Gumbel extreme value distribution (EVD) for three crystallographic textures with different surface-area-to-volume ratio microstructures and different periodic boundary conditions. a) FIP EVDs from ensembles of 30 SVEs. In b) the same number of grains are simulated using a single microstructure with the same surface-area-to-volume ratio as a). The microstructure in c) has the same total number of grains but with a reduced surface-area-to-volume ratio. In c) there is an expected decrease in FIP magnitudes as more grains are located further from the free surface. Microstructures were loaded in the X direction relative to the ODF pole figures in Figure 2.4.

The random and rolled textured FIPs in the first two simulations sets (with the same surface area-to-volume ratio) show a comparable increase in magnitude when a free surface is introduced. In contrast, FIPs from the last set of simulations (with a decreased surface area-to-volume ratio) shows a markedly lower increase in FIPs, although the limited number of grains exposed to the free surface still manifest larger FIPs. It is crucial to note that the FIP EVDs across the three plots in Figure 6.10 are not expected to be identical because it is unclear how many grains must be simulated to achieve convergence. This is investigated in the next chapter. However, one can evaluate the increase in FIPs when the same periodic microstructure is simulated with fully periodic and subsequently "thin film" boundary conditions to evaluate the increase in FIPs. The FIP EVDs in this section demonstrate that different simulation strategies lead to the same rank ordering regarding fatigue resistance of different microstructures.

Finally, histograms of cumulative effective plastic strain for the 90^3 microstructures in Figure 6.10c are shown in Figure 6.11a, under both fully periodic and "thin film" boundary conditions. As expected, the latter boundary condition slightly increases plastic deformation because it is less constraining. The random and rolled textures displays the broadest histogram distribution due to the most sampled grain orientations. The maximum plastic shear stress range for each integration point is displayed in Figure 6.11b. The cubic texture shows a markedly different response due to the homogeneous distribution of slip. The random and rolled textures display many integration points with large values that lead to the extreme value fatigue response observed in Figure 6.10c.

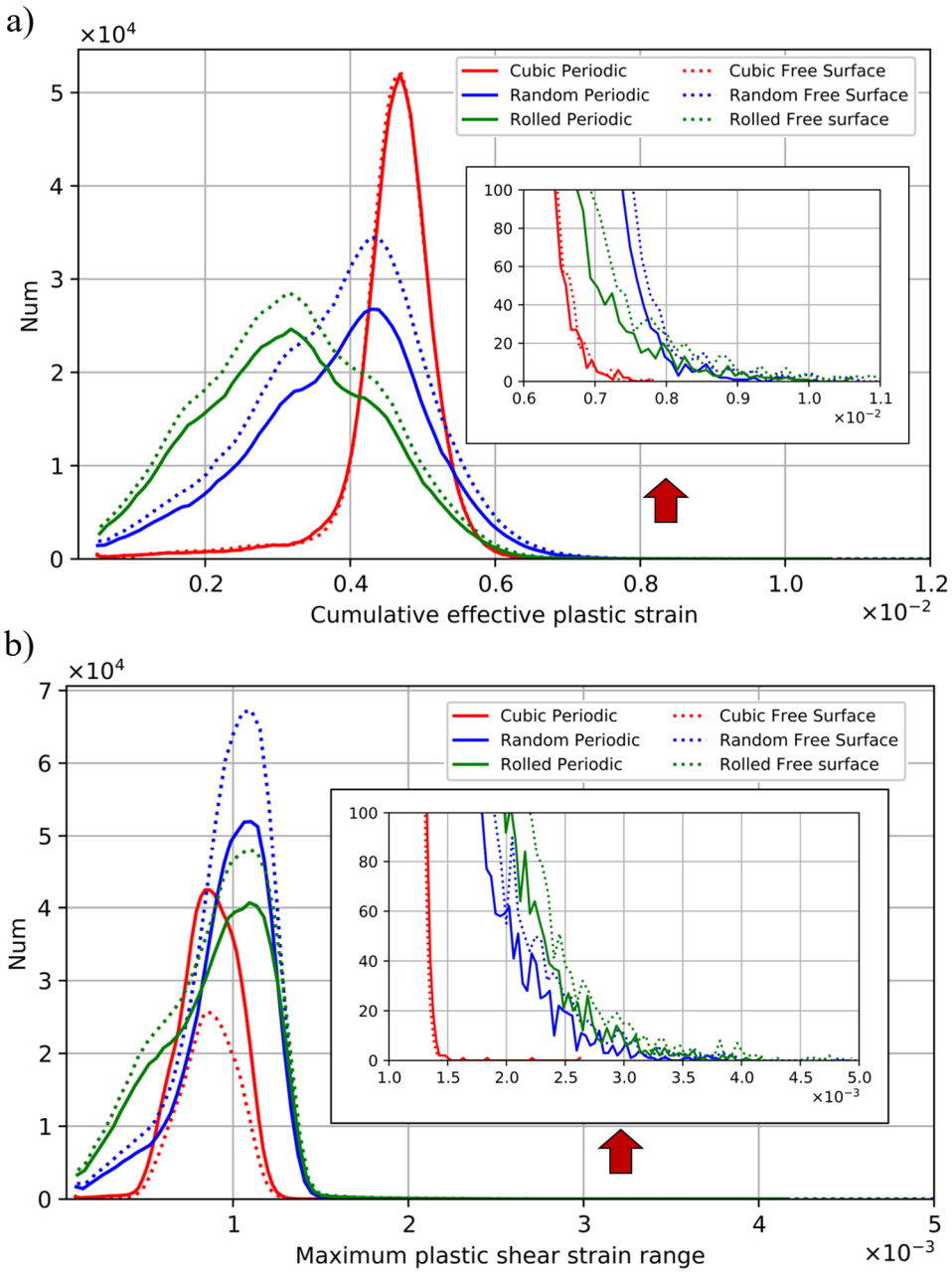

Figure 6.11. Histograms of a) cumulative effective plastic strain and b) maximum plastic shear strain range for each integration point. Data correspond to the cubic SVE in Figure 6.10c.

6.6 Conclusions

The nature of applied boundary conditions is a critical consideration in microstructure-sensitive crystal plasticity simulations targeting extreme value FIP responses. Periodic boundary conditions imposed using multi-point constraints can appropriately distinguish between the bulk and surface driving forces for fatigue crack formation. This chapter demonstrates the efficacy of these multi-point constrains to appropriately distinguish between the bulk and surface response in polycrystalline metals and alloys.

Three non-periodic boundary conditions were assessed: 1) "grip" boundary condition, in which one face is completely restrained and traction is applied to the opposite face, and 2) "symmetry" boundary condition, which mimics a sample subjected to pure uniaxial loading that has symmetry and only one-eighth of the sample is modeled, and 3) "minimal" boundary condition, which is the least restrictive and contains four free surfaces. The effect of each boundary condition was investigated and included analysis of cyclic stress-strain curves, distribution of local plastic deformation, and extreme value FIPs. The results show that the grip boundary condition needs a very large buffer layer and is too artificially constraining, whereas the symmetry and minimal boundary conditions quickly converged for all three of the mechanical metrics considered using a small layer of padding elements.

Lastly, the response of three crystallographic textures was assessed by considering macroscopic cyclic stress-strain curves, distributions of local plastic slip, and extreme value FIPs, under fully periodic and "thin film" boundary conditions. Two different

governing factors were examined and include 1) simulating one large microstructure versus an ensemble of statistical volume elements, and 2) two different surface area-to-volume ratios. Neither of these factors had a considerable effect on the computed FIPs in cubic textured microstructures. For random and rolled textures, however, a larger surface area-to-volume ratio was more detrimental to computed fatigue resistance. Furthermore, the results show that populating an extreme value distribution using a large, computed set of smaller SVEs can successfully mimic the results of a single very large microstructure for the purpose of rank-ordering fatigue resistance. This chapter provides vital guidance to future studies aimed at assessing the surrogate driving force for fatigue crack formation in polycrystalline metals and alloys. Furthermore, several advanced capabilities of the PRISMS-Fatigue framework were demonstrated.

CHAPTER 7. EFFECTS OF SVE SIZE AND GRAIN NEIGHBORHOOD ON THE EXTREME VALUE FATIGUE RESPONSE

Seeking to compute at the scale of the large size of RVEs for fatigue-related applications is challenging and impractical, as discussed earlier. A sufficient volume of material should be addressed to capture variations of FIPs induced by the grain/phase heterogeneity at "hot spot" grains. Consequently, single microstructure RVEs are largely computationally intractable and elusive. This chapter leverages the PRISMS-Fatigue framework to examine the convergence of EVD of FIPs in progressively larger polycrystalline microstructures of FCC Al alloy 7075-T6 using CPFEM simulations. The results are compared to the traditional method in which ensembles of SVEs are simulated to build up statistics intended to approximate those of a larger volume of material. The previous chapter demonstrated the efficacy of periodic boundary conditions enforced using multi-point constraints, which suggests that FIP EVDs for these two cases should converge given the same sufficiently large, simulated volume. The effects of different crystallographic textures are grain morphologies are also examined. The RVE size is closely related to the extent of nearest neighbor (NN) grain interactions. Accordingly, the sensitivity of local micromechanical response at fatigue hot spot grains is quantitatively investigated by systematically varying the orientations of NN grains.

7.1 Introduction

As discussed in Section 2.6, it is challenging to determine the RVE size for local extreme value fields at fatigue hot spot grains. Even if the RVE size cannot be resolved, however, some sense of the rate of convergence of FIPs with increase of highly stressed

volume of microstructure is important for fatigue modeling. Thus, the goal of this chapter is to leverage the advanced capabilities of PRISMS-Fatigue to employ CPFEM simulations to evaluate FIP characteristics in very large polycrystalline microstructures of Al alloy 7075-T6 and to consider how the associated EVDs of FIPs may or may not converge with increase of SVE size, as would point an approach to RVE response. More specifically, one of the goals is to determine whether progressively larger microstructures manifest gradually FIP EVDs with larger magnitude, and to investigate the structure characteristics or spatial correlations of hot spot grains that manifest the highest FIPs. Subsequently, a systematic study on the largest SVEs investigates the influence of NN grain interactions on the extreme value FIPs. Section 7.2 details the unique digital microstructures generated for this chapter and the CPFEM loading conditions. Section 7.3 then investigates the combined effects of crystallographic texture, grain morphology, and different sized microstructures on the extreme value fatigue response. Progressively larger microstructures with the same target number of grains are simulated in Section 7.4, the largest of which contains over 160,000 grains discretized by 250^3 elements. The microstructure characteristics of the ~5-10 highest FIPs in the ~160,000 grain microstructure are investigated in Section 7.5. Section 7.6 quantifies the effects of NN grains on the extreme value FIPs in the ~160,000 grain microstructure. The chapter draws conclusions in Section 7.

7.2 Methodology

This chapter employs the same crystal plasticity constitutive model of Al 7075-T6, DREAM.3D microstructure generator, FIP calculations, and extreme value statistics as the

previous chapter. The unique microstructures and loading conditions in this chapter are summarized below.

7.2.1 Microstructure generation

Fully periodic microstructures are generated using DREAM.3D in accordance with Section 2.2.3. This chapter explores the fatigue response of SVEs with both equiaxed and elongated grain morphology, the latter of which have a grain elongation ratio of 5:1:1 in the rolling direction (see Figure 2.3). The three FCC crystallographic textures with ODF pole figures shown in Figure 2.4 are also investigated. Section 7.3 explores the macroscopic and extreme value FIP response of all six combinations of grain morphologies and crystallographic textures. All microstructures are generated as fully periodic.

7.2.2 Loading conditions

The previous chapter demonstrated the efficacy of periodic boundary conditions. These are applied to all microstructures in this chapter. Microstructures undergo cyclic straining at a strain amplitude of 0.7% with zero initial strain, zero initial back stress at with temperature assigned as 300K. FIPs are computed and volume averaged after two fully reversed straining cycles, in accordance with the previous chapters. Microstructures are strained in the X direction relative to the coordinate axis shown in Figure 2.3 and relative to the ODF pole figures in Figure 2.4.

7.3 Crystallographic texture and grain morphology effects on FIP EVDs

The effects of crystallographic texture and grain morphology on the convergence of FIPs are investigated using two different scenarios:

- The FIP EVDs for an ensemble of SVEs is compared to the FIP EVDs of a single large microstructure with the same total number of grains
- FIP EVDs for progressively larger microstructures with many more grains are compared

Three microstructure sets are generated and simulated for each combination of texture and morphology. The first set is an ensemble of 30 SVEs each with 29^3 elements and ~250 grains, and therefore a total of ~7,500 grains. The second set is a single, larger microstructure with 90^3 elements and the same total of ~7,500 grains. The third set is also a single but much larger microstructure with 160^3 elements and ~41,000 grains, and therefore more than five times the volume and grains of the two previous microstructure sets. The first, second, and third sets contain (30 x 6) = 150, 6, and 6 microstructure instantiations, respectively, which are subjected to fully reversed cyclic straining at a strain amplitude of 0.7%, as described in Section 7.2.2.

The macroscopic cyclic stress-strain response of the six microstructures in the second and third set is shown in Figure 7.1a and Figure 7.1b, respectively, and does not vary with the number of grains simulated. The cubic texture manifests a slightly softer response since plastic deformation is, on average, more homogeneously distributed. The response is also unaffected by grain morphology, but it is important to note that the microstructures here are strained in the direction of grain elongation. The macroscale response of microstructures with as little as ~250 and many as ~160,000 grains were previously shown to be indistinguishable (see Figure 5.4e in Chapter 5). Thus, the RVE size for macroscale stress-strain response is readily achieved, but this is not the case for local FIP hot spots, as will be discussed next. FIPs are computed for each SVE in the first

set and compiled, after which only the highest 50 are considered. In the second and third sets, the highest 50 FIPs from each microstructure are considered.

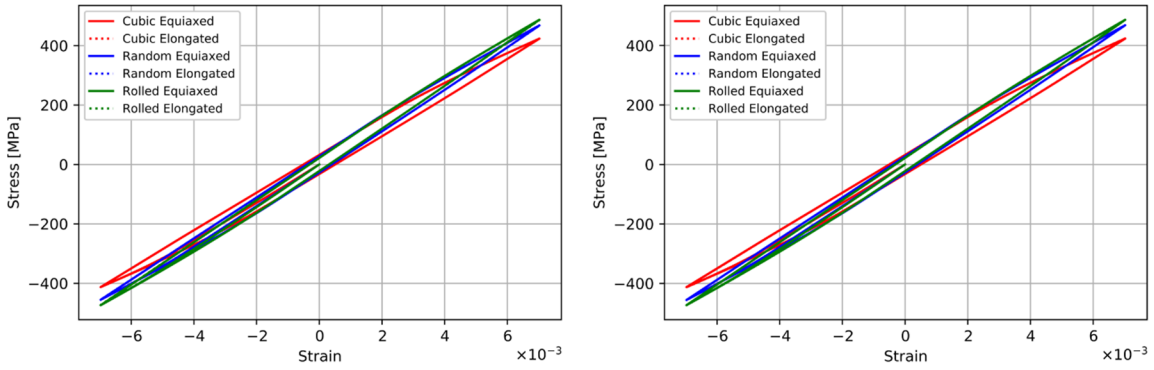

Figure 7.1. Macroscopic cyclic stress-strain curves for the three crystallographic textures and two grain morphologies extracted from microstructures with a) ~7,500 grains and 90^3 elements, and b) ~41,000 grains and 160^3 elements. Curves in a) and b) are indistinguishable.

7.3.1 SVE ensemble response versus a single large microstructure

The first comparison is made between FIP EVDs for the same nominal number of simulated grains from an SVE ensemble and a single large microstructure, as shown in Figure 7.2a and Figure 7.2b, respectively. This comparison permits the rank ordering of relative fatigue resistance between the six different combinations of crystallographic texture and grain morphology. The variability in the extreme value FIP response for multiple instantiations of the same target microstructure will be investigated later. The six data sets from both scenarios are comparable and FIP rank ordering is unchanged. The axis limits are identical in all figures to facilitate straightforward comparison. The cubic textured FIPs show the highest resistance to fatigue (i.e., the lowest FIPs) whereas the rolled texture with equiaxed grain morphology displays the highest FIPs and therefore least

resistance to fatigue. As will be demonstrated later, simulating a limited number of grains (e.g., ~7,500) is insufficient for volume simulated to constitute a RVE for fatigue-related properties. Different instantiations of a single large microstructure or SVE ensemble may result in substantial variability amongst FIP EVDs. However, a limited number of simulated grains may suffice for rank-ordering of fatigue resistance, as clearly indicated by comparing Figure 7.2a and Figure 7.2b to Figure 7.2c. An interesting observation is that the elongated grain morphology reduces extreme value FIPs, which is most likely a consequence of plastic shear strain constraints due to the reduced mean free slip path. It is expected that cyclic straining in another direction, perhaps perpendicular or at 45° to the elongated morphology, would produce the opposite effect and result in substantially higher FIPs.

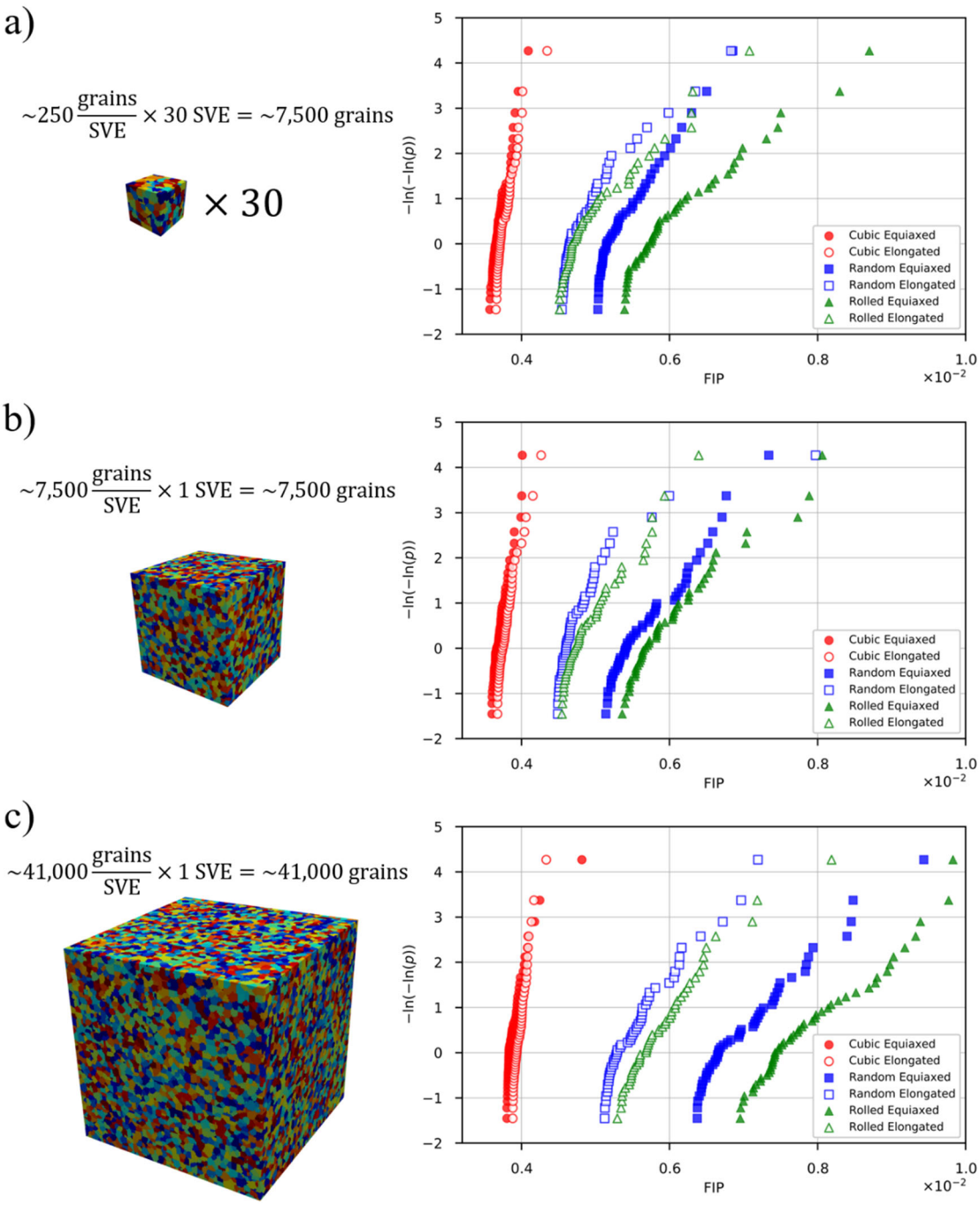

Figure 7.2. Comparison of FIPs from ensembles with different grain morphologies and crystallographic textures. As larger volumes are simulated, a greater number of critical grain orientations and neighborhood interactions that manifest high FIPs are captured. In a), ensembles of 30 SVEs are simulated. The same total number of grains are simulated for each combination of crystallographic texture and grain morphology in b) but with a single larger microstructure. In c), an even larger microstructure is simulated for each of the six data sets with more than five times as many grains.

7.3.2 Simulating larger volumes

As larger microstructures and more grains are simulated, the likelihood of capturing grains oriented favorably for significant slip increases. It will be shown later that grain orientation alone does not account for the highest FIPs, but it is nonetheless an important factor. FIPs from progressively larger microstructures are compared in Figure 7.2b and Figure 7.2c. The cubic textured FIPs show a minuscule increase, whereas the other textures and morphologies increase significantly. In particular, the equiaxed grain morphology for the random and rolled textures shows the largest increase in FIPs. The relatively smaller increase in cubic-textured FIPs, even though more than five times as many grains are simulated, is due to a reduced probability of grains oriented for significant slip. Analysis of the cubic ODF pole figure in Figure 2.4a shows that on average, eight of the 12 available slip systems are equally activated with an apparent Schmid Factor (SF) of 0.41 [243]. On the other hand, grains favorably oriented for significant slip are much more likely in the other two textures. Therefore, it may be concluded that cubic textured microstructures require on the order of tens of thousands of grains for FIP EVDs to begin to approach conditions of convergence to RVE size for this response.

7.4 FIP convergence and variability

The results presented in Figure 7.2 demonstrate that FIP convergence is primarily affected by the number of grains simulated. Here, four different microstructure sets are generated with random crystallographic texture and equiaxed grain morphology to examine following scenarios:

- Whether the FIP EVDs from some number of SVEs converge to that of a single massive microstructure comprising all the grains in the associated SVE ensemble
- Whether FIP EVDs tend to converge to some upper bound value as very large volumes of material are simulated.

Each set contains progressively larger microstructures. A sample microstructure from each of the four sets is shown in Figure 7.3. The largest microstructure contains over 160,000 grains discretized by a 250^3 = 15,625,000 finite element (FE) mesh. The microstructures generated and simulated here demonstrate the powerful capabilities of the PRISMS-Fatigue framework not only in terms of scalability for massive CPFEM simulations but also for pre- and post-processing of the associated data sets. Moreover, other material systems with a larger grain size can be generated with the same number of grains as the largest sample shown here but with a physical size approaching an actual laboratory specimen. For instance, at the same grain mesh resolution (~98 elements per grain), a material with a lognormal mean grain size of 60 μm yields a microstructure with a side length of 2.625 mm. Crystal plasticity simulations previously inaccessible in more conventional serial FE codes are made possible using PRISMS-Fatigue.

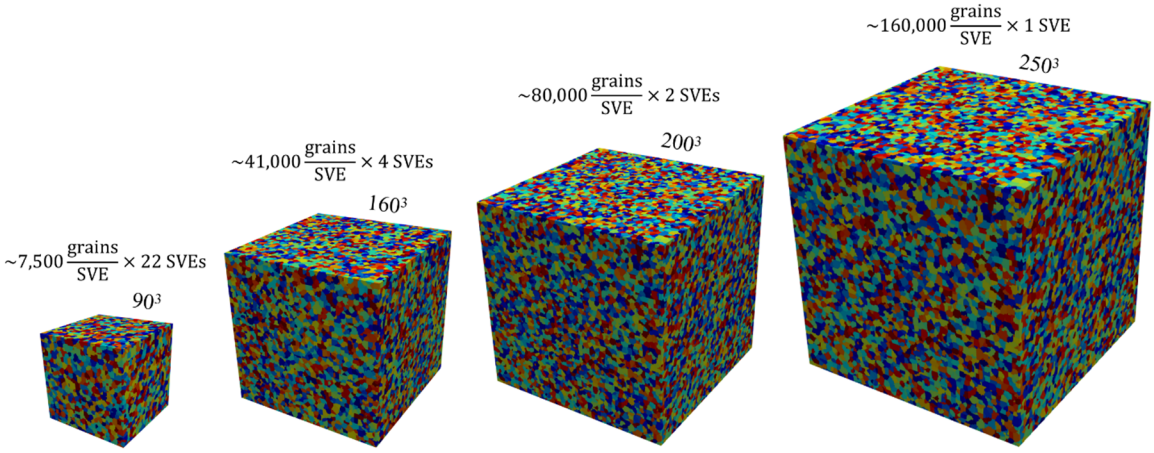

Figure 7.3. Microstructures with random crystallographic texture generated using DREAM.3D for the large scale FIP comparison. Each of the four data sets contains nearly ~160,000 – 165,000 grains.

The macroscopic cyclic stress-strain responses of the different sized microstructures in Figure 7.3 were previously shown to be expectedly indistinguishable (see Figure 5.4e in Chapter 5). Each microstructure set undergoes fully reversed cyclic straining to a strain amplitude of 0.7%. The highest 100 FIPs are then extracted from each microstructure individually and fit to the Gumbel EVD in Figure 7.4a, Figure 7.4b, and Figure 7.4c for the ~7 500, ~41 000, and ~80 000 grain microstructures, respectively. In Figure 7.4d, the highest 100 FIPs from the entire ensemble of the three previous microstructures are compiled and fit to the Gumbel EVD alongside the 100 highest FIPs from the ~160,000 grain microstructure. The variability between FIP EVDs is greatest across the 22 smallest ~7,500 grain microstructures. However, it is inappropriate to draw conclusions regarding FIP EVD variability between these figures since Figure 7.4b and Figure 7.4c show only four and two data sets, respectively. It may be concluded, however, that more variability would be expected between the distributions in Figure 7.4a since these

microstructures contain the least number of grains. Thus, some microstructures will contain one or multiple grains that manifest high FIPs more so than others. Larger microstructures have increased probability of manifesting high FIPs because more grains are sampled. Figure 7.4c is striking because the two FIP EVD appear almost indistinguishable. Two experimental specimen sets with different critically stressed volumes under identical applied stress or strain conditions would be expected to display different variability in fatigue response (e.g., fatigue life measured by number of cycles to fracture). The specimen set with the smaller critically stressed volume would unquestionably exhibit higher fatigue life due to a decreased probability of a critical hot spot for fatigue crack formation [240]. Moreover, it would also be expected to display higher variability in fatigue life because a relatively limited number of grains are sampled.

In Figure 7.4d, the 100 highest FIPs from each of the previous three microstructure sets are fit to the Gumbel EVD alongside the FIPs from the largest 160,000 grains microstructure. There is remarkable overlap between all four data sets in the high probability regime towards the left, suggesting that any of the four microstructure sets can be individually pursued to generate a reliable FIP EVD, i.e., each set collectively establishes a reliable RVE for fatigue related applications. There is, however, a distinct discrepancy in the low probability regime associated with the highest FIPs for each microstructure and SVE ensemble. The seven highest FIPs from the ~160,000 grain microstructure (purple star markers) deviate from the other three data sets. The grains that manifest these highest FIPs are thoroughly investigated next. To the best of the author's knowledge, the analysis of extreme value FIPs in the ~160,000 grain microstructure here

utilizes the largest microstructure-sensitive CPFEM simulation to date, not considering other simulation schemes such as FFT crystal plasticity [238, 239], for example.

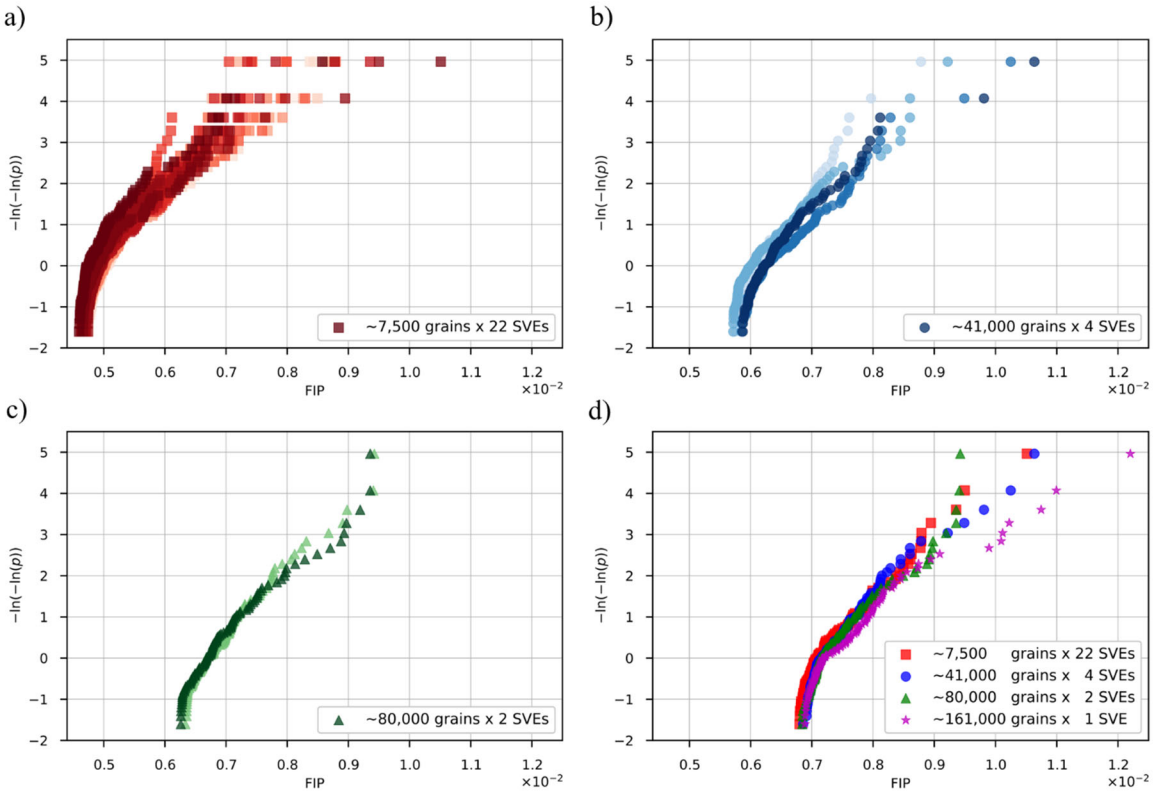

Figure 7.4. The highest 100 FIPs compiled and fit to the Gumbel extreme value distribution for the microstructures shown in Figure 7.3: a) ~7,500 grains x 22 SVEs, b) ~41,000 grains x 4 SVEs, and c) ~80,000 grains x 2 SVEs. In d), the highest 100 FIPs from each of the previous ensembles are compiled and plotted alongside the 100 highest FIPs from the ~160,000 grain microstructure.

7.5 FIP-structure correlations

To exploit the massive scale of this simulation, structural features in the neighborhoods of the distinctly high FIPs observed in Figure 7.4d are further investigated here. The SF and equivalent grain diameters of the grains that manifest the highest FIPs

are analyzed. Afterwards, more complex formulations for structural correlations are examined, including different neighborhood effects.

7.5.1 Grains with the highest FIPs

The apparent SFs of the slip systems that manifest the highest 50 FIPs are shown in Figure 7.5a, where the color bar represents the sub-band volume averaged FIP value. As expected, all 50 points are close to the maximum value of SF = 0.5 but there is no correlation to the highest ~5-10 FIPs, i.e., the SF alone does not explain why these certain grains manifest the highest FIPs. This accords with experimental observations: although cracks initiate mainly in grains with a rather high Schmid factor, other grains with similar characteristics do not develop damage [244]. As a note, the apparent SF is based solely on geometry and orientation of applied load. In contrast, the local SF considers the ratio of the maximum resolved shear stress divided by the global applied stress averaged over some volume and reflects the local stress state affected by intergranular interactions and microplasticity [65]. While the apparent SF is bounded by 0.5, the local SF can vary broadly between 0 and 1 due to load shielding or load shedding from neighboring grains [65].

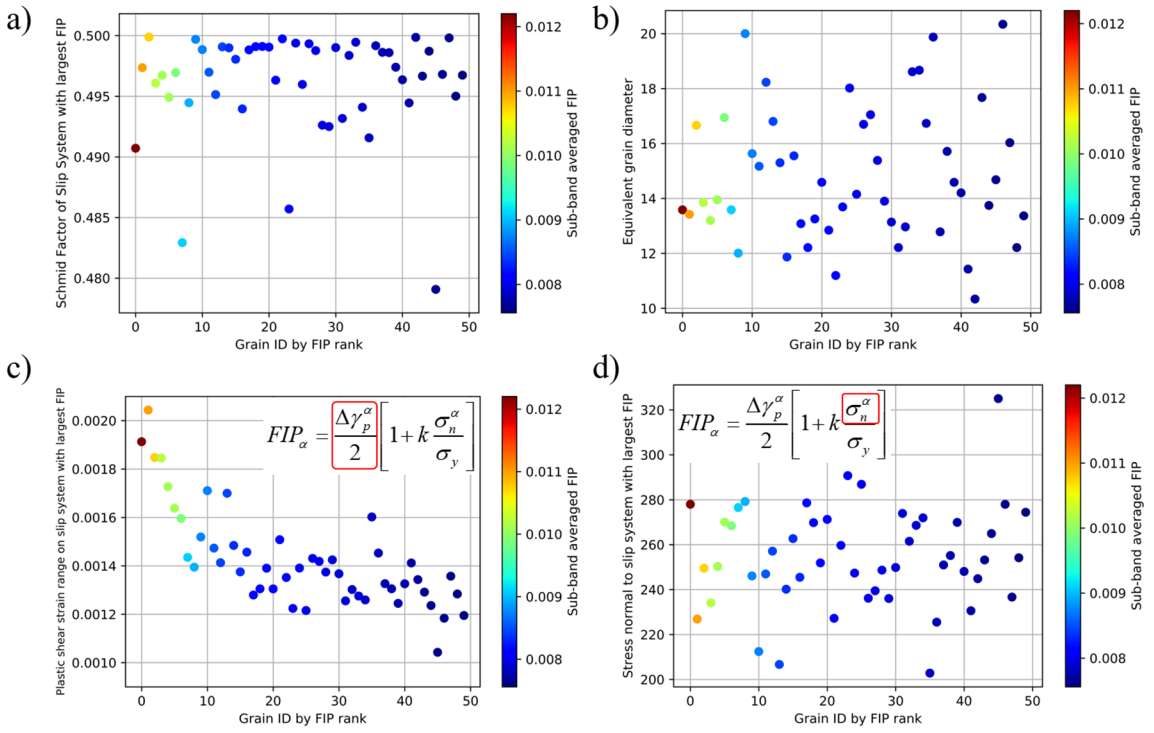

Figure 7.5. Correlations of the highest 50 FIPs from the ~160,000 grain microstructure. The a) apparent Schmid Factor (SF) of the slip systems with the highest FIPs and b) equivalent grain diameter as reported by DREAM.3D for the grains with the highest FIPs. In c) and d), the plastic shear strain range on the slip system with the highest FIPs and the stress normal to the slip plane of the highest FIPs, respectively, are shown for the highest 50 FIPs. The color bar represents the sub-band averaged FIP value.

The equivalent grain diameters of the grains that manifest the highest 50 FIPs are portrayed in Figure 7.5b and show that the highest FIPs are unrelated to grain size. Although the CPFEM model does not consider grain size effects, the increased mean free slip path in larger grains could result in the increased plastic shear strain range to manifest high FIPs. Figure 7.5c and Figure 7.5d show the two components of the highest 50 sub-band volume averaged FIPs, namely the plastic shear strain range on the slip system and the peak stress normal to the slip plane, respectively. There is a strong correlation between the plastic shear strain range and the highest FIPs. However, the variation of FIPs and peak

stress normal to slip planes exhibits no clear correlation. In the next step, the goal is to identify neighborhood structural characteristics that can explain the particularly high FIPs in the ~160,000 grain microstructure.

7.5.2 Nearest neighbor correlations

Uniaxial loading along the [100] direction in a fcc crystal activates slip on 8 of the 12 available slip systems [243]. Each of the eight slip systems have a SF of 0.41, while the remaining four are at SF = 0. Another important fcc single crystal loading direction is along the [111] direction, i.e., normal to one of the slip planes. In this case, six slip systems have SFs of 0.27 and the other six SFs are 0. This type of "hard" deformation mode would induce high stresses in a grain if the surrounding neighbors are oriented for easier slip, i.e., neighboring grains strained along the [100] direction or another orientation where one or multiple slip systems have SFs close to the maximum value of 0.5. Several NN grain structural characteristics are examined here to find the underlying mechanisms of grains with high FIPs.

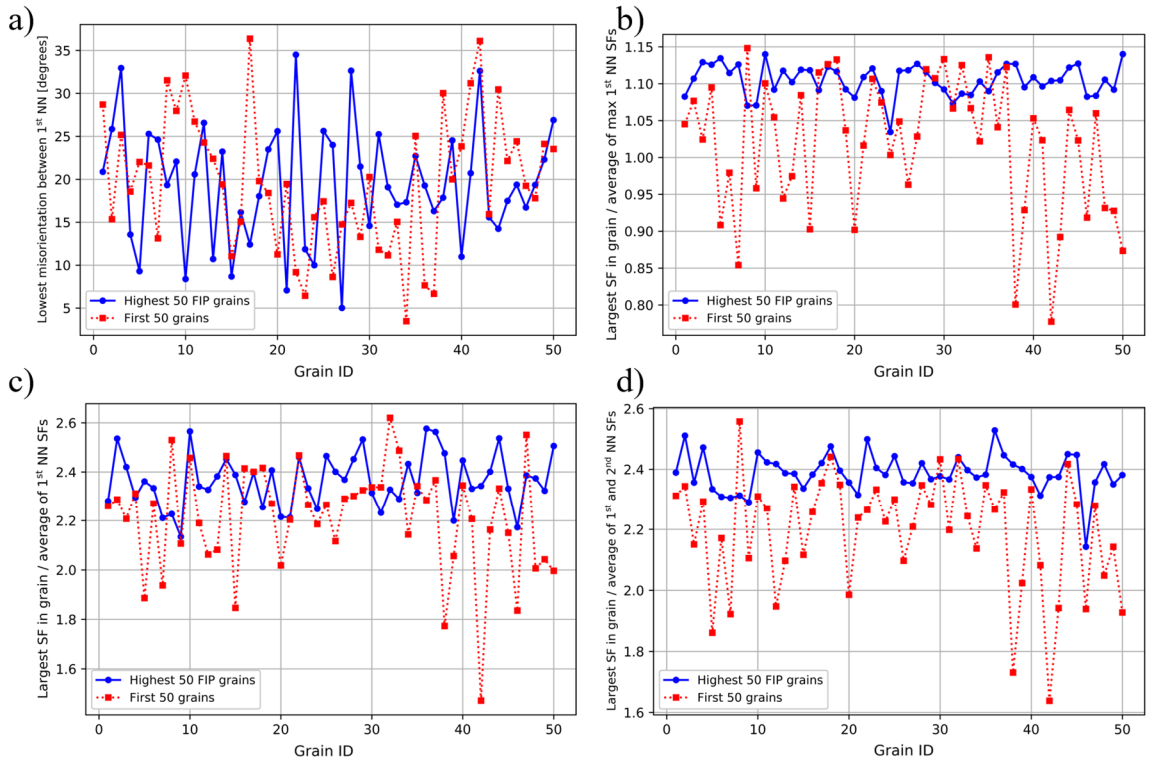

Figure 7.6. Spatial correlations for the grains that manifest the 50 highest FIPs from the ~160,000 grain microstructure. Each plot also contains the same correlations for the first 50 grains (i.e., chosen randomly as a comparison). A correlation that holds true for only the first ~5-10 highest FIP grains may explain the particularly high FIP values in the ~160,000 grain microstructure. (a) shows the lowest misorientation between a grain and its 1st nearest neighbors. In (b), the ratio of the Schmid Factor (SF) on the slip systems that manifest the highest FIPs to the average of the maximum SF in all 1st nearest neighbor grains is shown. For the first 50 grains, the highest SF in the grain is chosen. (c) and (d) depict the ratio of the highest SFs of the slip systems that manifest the highest FIPs to the average of all SFs in the 1st, or all 1st and 2nd nearest neighbor grains, respectively. None of these correlations appear to explain the highest ~5-10 FIPs observed in the ~160,000 grain microstructure.

The CPFEM model does not explicitly account for slip transfer between grains; grain boundaries are treated as impenetrable to slip. However, neighboring grains with a low misorientation may act as a "super grain" with a significantly longer mean free slip path [31, 245]. In Figure 7.6a, the blue circle markers connected with a solid line show the

lowest misorientation between the grains that manifest the 50 highest sub-band averaged FIPs and their first NN grains. In other words, the misorientations between each grain and its first NN grains are determined and the lowest is selected. First NN grains are defined by grains that share at least one element face. The goal is to find a structural correlation that holds true for the first ~5-10 highest FIPs and gradually diminishes. Alongside the lowest misorientations in Figure 7.6a for the grains with the highest FIPs, the red square markers connected with a dotted line represent the lowest misorientations between the first 50 grains out of the entire set of ~160,000 from the 250^3 microstructure as a comparison, which do not necessarily manifest high FIPs; this latter data set represents grains chosen at random. Figure 7.6a shows that first NN grain misorientation does not correlate to the highest FIPs.

Figure 7.6(b-d) consider multiple criteria for the first and second NN grains simultaneously to quantify grains oriented for the "soft" and "hard" deformation modes described earlier. Figure 7.6b shows the ratio R_1 defined as the maximum SF in a grain divided by the average value of the maximum SF in all 1st NN grains, for the grains which manifest the 50 highest sub-band averaged FIPs and for the first 50 grains (i.e., chosen at random in the microstructure) in blue circle markers and red square markers, respectively. R_1 is thus defined as follows:

$$R_1 = \frac{max\left[cos\left(\phi^i\right) cos\left(\lambda^i\right), i = 1 \dots n\right]}{\text{mean}\left\{max\left[cos\left(\phi^i\right) cos\left(\lambda^i\right), i = 1 \dots n\right]_j, j = 1 \dots N_f\right\}} \tag{7.1}$$

where ϕ^i is the angle between the i^{th} slip plane normal and loading direction, λ^i the angle between the i^{th} slip direction and loading direction, n is the number of slip systems, and N_f

is the number of first NN grains. A large R_1 value indicates that a grain is favorably oriented for significant slip along some slip system while the first NN grains are oriented in "hard" deformation modes with relatively smaller maximum SFs. The ratio R_1 does not reveal any correlations that might explain the particularly high FIP values since there is minimal variation in both the highest 50 FIP grains and 50 grains chosen at random. However, this criteria works better than the misorientation (Figure 7.6a), in general, such that grains with higher FIPs have higher values of R_1 in most of the 50 highest FIPs.

The next correlation shown in Figure 7.6c is R_2 which is defined as the ratio of the SF on the slip system that manifests the highest FIP divided by the average value of all SFs in all 1st NN grains, i.e.,

$$R_2 = \frac{max\left[cos\left(\phi^i\right) cos\left(\lambda^i\right), i = 1 \dots n\right]}{\text{mean}\left\{\left[cos(\phi^i)\, cos(\lambda^i), i = 1 \dots n\right]_j, j = 1 \dots N_f\right\}} \tag{7.2}$$

For the first 50 grains in red square markers, the highest SF of each grain is chosen for the numerator. These values are expectedly higher but cannot account for the significantly higher ~5-10 FIPs observed in the ~160,000 grain microstructure. R_2 is modified to also include the second NN grains, i.e.,

$$R_3 = \frac{max\left[cos\left(\phi^i\right) cos\left(\lambda^i\right), i = 1 \dots n\right]}{\text{mean}\left\{\left[cos(\phi^i)\, cos(\lambda^i), i = 1 \dots n\right]_j, j = 1 \dots N_{f+s}\right\}} \tag{7.3}$$

where N_{f+s} is the total number of first and second NN grains. Comparing Figure 7.6b and Figure 7.6d shows that including the second layer of NN grains improves the correlation, in that Figure 7.6d more frequently displays higher R_3 values for the highest FIP grains.

The nuance in these correlations is that a certain grain may be surrounded "above and below" by first NN grains in "hard" deformation modes and surrounded "to the left and right" by other first NN grains in "soft" deformation modes. Thus, the relatively simple structural correlation attempts made here inadvertently smear the effects of individual first and second NN grains. Clearly, more complex and higher-order statistics are required to investigate the structural features that manifest the large FIPs shown in Figure 7.4d. The results show that simple structural correlations may not suffice to determine what causes a certain grain to act as a hot spot for fatigue crack formation. We can, however, attempt to quantify these effects by varying certain NN grain orientations to better understand the sensitivity of NN grain effects. Advanced data science and machine learning techniques are required to investigate the FIP hot spots and to determine the critical structural characteristics that yield high FIPs.

7.6 Quantifying nearest neighbor influence

The results presented in Figure 7.6 demonstrate that correlations between microstructure and sites of extreme FIPs are nontrivial. As an alternative, the influence of the NN grains on the response of the hot spot grains, which manifest the highest FIPs, are systematically investigated here. The focus of the current analysis is on the extreme value local response.

7.6.1 Cropped microstructures

The grains that manifest the three highest FIPs in the ~160,000 grain microstructure are shown in Figure 7.7. The first and third highest are relatively far from the boundary of the microstructure and are considered in this section. Two new microstructures are cropped

from the ~160,000 grain microstructure centered about these two grains. The grain that displayed the second highest FIP is not considered in this manner because it is much closer to the boundary of the microstructure. The cropped regions contain ~4,600 grains discretized using a 72^3 FE mesh. They are subjected to the same cyclic straining conditions as the other microstructures.

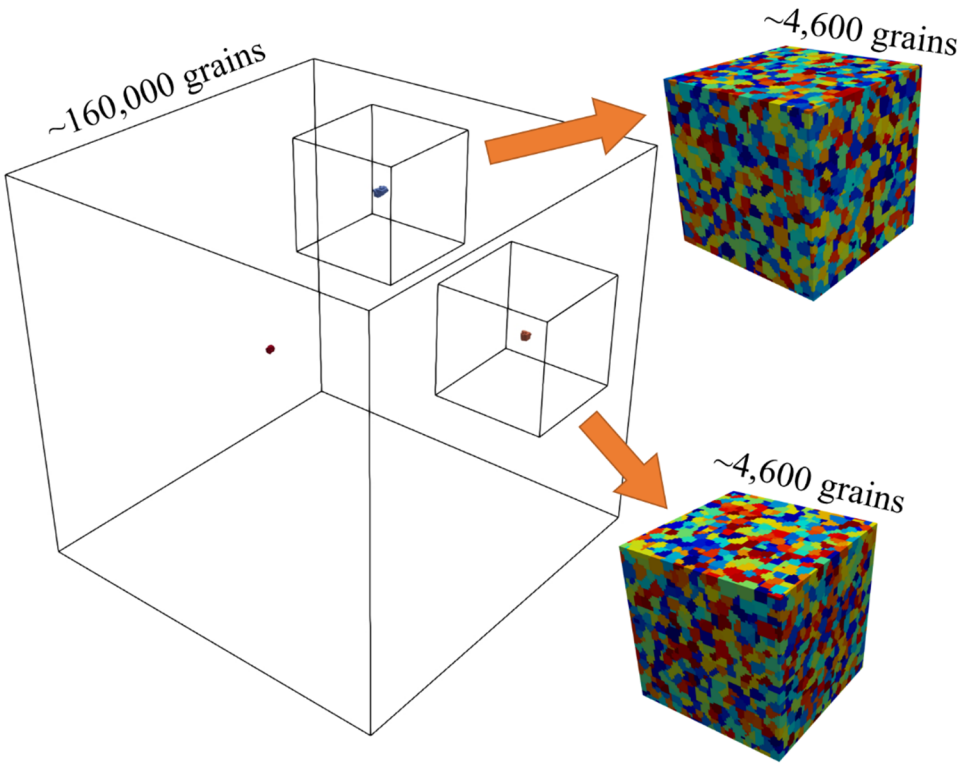

Figure 7.7. Location of the three highest FIPs in the ~160,000 grain microstructure discretized by 250^3 voxels. New microstructures with ~4,600 grains discretized by a 72^3 FE mesh are cropped about the grains that manifest the first and third highest FIPs. These microstructures then undergo the same cyclic straining conditions to quantify the influence of nearest neighbor grains on the FIP response in the center grain of interest. The second highest FIP grain is not considered because it is too close to the microstructure boundary.

To quantify the influence of NN grains on the response of the GOI about which the cropped regions are centered, the grain orientations of certain NN grains are systematically

changed. The cropped microstructure then undergoes the same straining conditions as the previous microstructures. Periodic boundary conditions are prescribed to retain bulk, subsurface material response. The first and third highest FIPs have values of 1.22×10^{-2} and 1.07×10^{-2}, respectively, in the ~160,000 grain microstructure. After the two ~4,600 grain microstructures are cropped and undergo cyclic straining, the highest FIPs still occur in the same grain about which the microstructures are centered (and on the same slip bands), but the values change to 1.20×10^{-2} and 1.10×10^{-2}, respectively. This speaks to the influence of distant grain neighbors on the response of the GOI at the center of the cropped regions. In the subsequent analysis, the responses of the ~4,600 grain microstructures are considered as the baseline for comparison.

Several NN grain orientations are systematically altered by sampling from grain orientations in the uncropped region of the ~160,000 grain microstructure. The NN grains are first assigned to different layers as demonstrated in Figure 7.8. The GOI that manifested the highest FIP in the ~160,000 grain microstructure and about which the first ~4,600 grain microstructure is centered is shown in Figure 7.8a. Figure 7.8b shows a clipped half view of the first NN grains. The remaining subplots in this figure display clipped views of the second, third, fourth, and fifth NN grain layers.

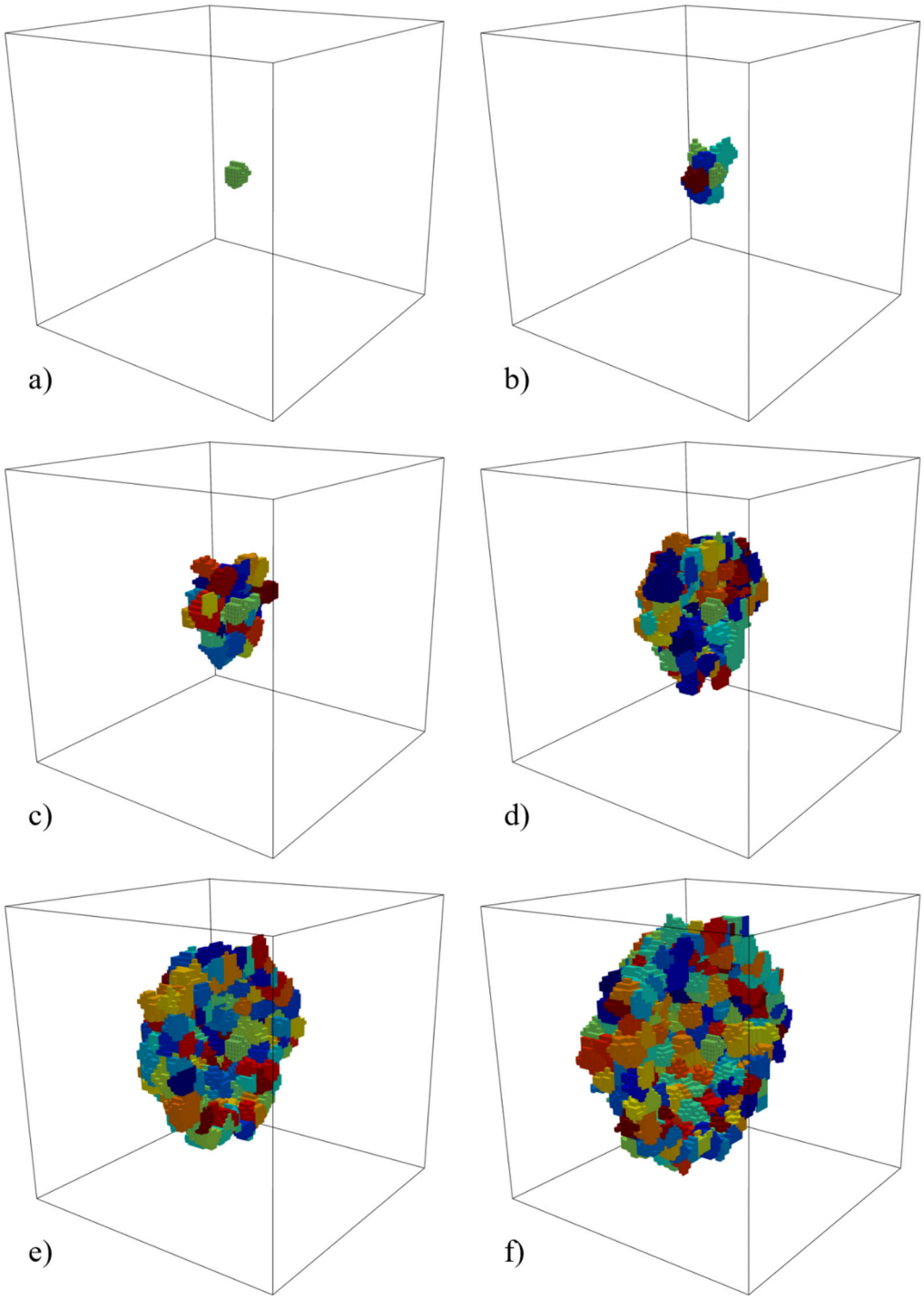

Figure 7.8. a) The grain with the highest FIP in the original ~160,000 grain microstructure cropped to a smaller domain with ~4,600 total grains discretized by 72^3 elements. Layers with the first, second, third, fourth, and fifth nearest neighbors are shown in b), c), d), e), and f), respectively. Nearest neighbor grains are defined as those that share at least one element face.

Grain orientations are systematically altered, and several scenarios are investigated. In the first scenario, the grain orientation of the single largest grain in one of the NN grain layers is altered. This is repeated for all five NN grain layers. In another scenario, all orientations in a NN grain layer are altered and this is once again repeated for all five layers. Additionally, for the first NN grain layer, the orientation of the grain that shares the most surface area with the GOI is also altered. Although this is not the largest grain in the first NN grain layer, it may have a more pronounced effect on the response of the GOI. Additional scenarios are studied for the 3rd, 4th, and 5th NN grain layers. These include altering the grain orientations of the five largest grains, the 5% largest grains, and the 20% largest grains. Table 7.1 and Table 7.2 contain statistics for the five NN grain layers in the ~4,600 grain microstructures.

Table 7.1. Nearest neighbor grain layer statistics for the first ~4,600 grain microstructure cropped about the 1st largest FIP.

Layer Number	Number of total grains	5% of total grains	20% of total grains	Number of elements in largest grain
1	13	-	-	209
2	68	-	-	226
3	159	8	32	319
4	303	15	61	291
5	517	26	103	305

Table 7.2. Nearest neighbor grain layer statistics for the second ~4,600 grain microstructure cropped about the 3rd largest FIP.

Layer Number	Number of total grains	5% of total grains	20% of total grains	Number of elements in largest grain
1	20	-	-	251
2	68	-	-	222
3	173	9	35	287
4	353	18	71	285
5	597	30	119	285

For each scenario describe above, new grain orientations are sampled five times to capture variability in NN grain effects. In the case where a single orientation is altered in the first NN grain layer, the sampling is performed ten times. The altered microstructures then undergo the same FIP calculation and volume averaging as before. For both cropped microstructures, two additional 1st NN grain modifications include setting the grain orientations of the largest grain and the grain that shares the most surface area (SA) with the GOI to the orientation of the GOI. In addition to the FIP defined in Equation (2.18), the maximum sub-band volume averaged plastic shear strain range (PSSR) calculated across the final straining cycle and the peak stress normal to a slip plane (σ_n) are also considered as two other response variables. The macroscopic cyclic stress strain response of the two ~4,600 grain cropped microstructures is shown in Figure 7.9. They are individually compared to the macroscopic responses when all 305 or 285 grain orientations in the 5th NN grain layer are altered, respectively. As expected, the curves are indistinguishable since

only a small portion of total grain orientations are changed (~6.5% of grains) and they are changed at random.

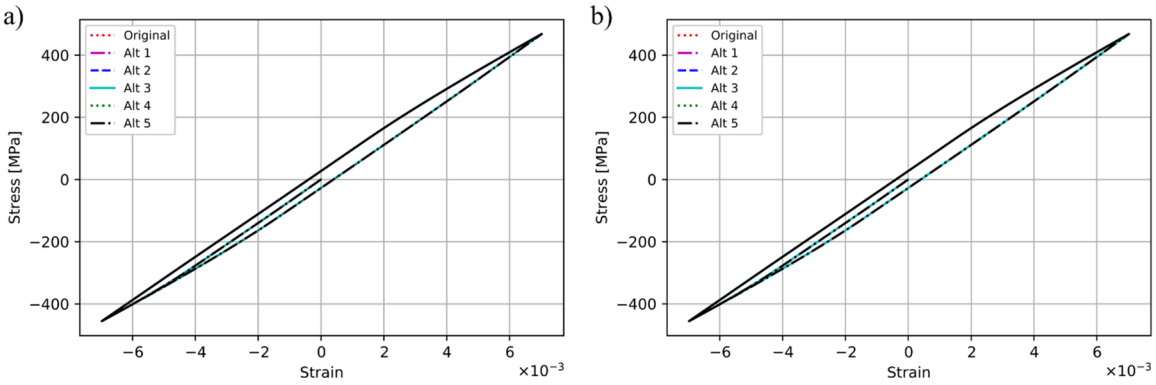

Figure 7.9. Macroscopic cyclic stress-strain response of the a) first and b) second ~4,600 grain cropped microstructures alongside the macroscopic response when all 305 or 285 grain orientations in the 5th NN grain layer are altered, respectively. In both cases, the macroscopic responses are indistinguishable.

7.6.2 Cropped region about the largest FIP

Figure 7.10a and Figure 7.10b show the highest sub-band volume averaged PSSR and FIP, respectively, for the first ~4,600 grain microstructure. More specifically, this figure depicts the highest volume averaged response variables in the GOI after one or multiple NN grain orientations are changed. The first two columns in both Figure 7.10a and Figure 7.10b contain data from 10 individual simulations (since sampling was performed 10 times in the case of a single grain orientation altered in the 1st NN grain layer), whereas the following 9 columns each contain data from 5 unique simulations. The last two data points are each extracted from a single simulation and thus, the data in Figure 7.10 is extracted from a total of 67 simulations. In a few cases, the highest damage parameter no longer occurs within the GOI. For instance, when the orientations of all 13

NN grains in the 1st layer or all 68 NN grains in the 2nd layer are altered (7th and 8th data sets in Figure 7.10), the red triangle markers indicate that the highest response variables now occur elsewhere. The PSSRs and FIPs in Figure 7.10 shows similar trends and different magnitudes. The maximum value of σ_n in the entire ~4,600 grain microstructure ranged between 535.5 MPa and 539.0 MPa for all 67 simulations. Further investigation revealed small variations to σ_n in the GOI. The maximum values of σ_n in the GOI for all 67 simulations ranged between 346.5 MPa and 370.9 MPa, which were the extremes and occurred in the case where all 2nd NN grain orientations and all 1st NN grain orientations were altered, respectively. σ_n in the GOI was 358.1 MPa with no altered grain orientations.

Figure 7.10 quantifies the extent to which NN grains influence the extreme value response of the original ~160,000 grain microstructure. The first data sets in Figure 7.10a and Figure 7.10b (magenta diamond markers) show the response variability of the GOI (grain #2424) after the orientation of the 1st NN grain that shares the most surface area with the GOI is altered. In one of these 10 simulations, the maximum value of the damage parameter remains the same as compared to the cropped region with no altered grain orientations (black dashed line). The other nine simulations reduce the maximum value. The lowest PSSR and FIP is reduced by 23.5% and 24.9%, respectively, as compared to the unaltered microstructure simulation. This shows the importance of 1st NN grain interactions, whose change in orientation can reduce the response of a hot spot grain by nearly 25%.

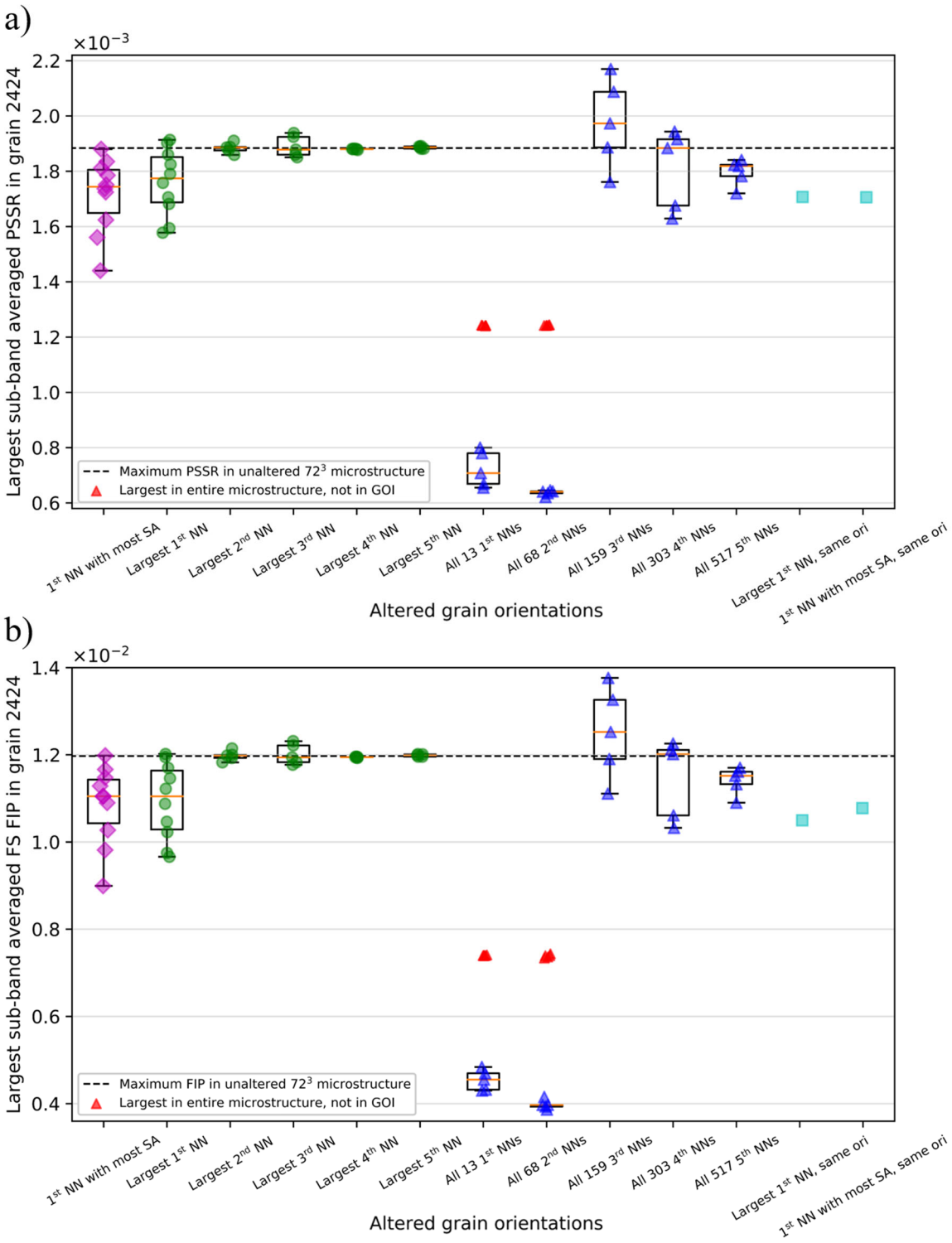

Figure 7.10. The highest sub-band volume averaged a) PSSR and b) FIP in the grain (#2424) about which the first ~4,600 grain microstructure was cropped from the ~160,000 grain microstructure. The black dashed line indicates the highest PSSR or FIP in this grain without changing any grain orientations. Red triangle markers indicate the highest PSSR or FIP that did not occur within grain #2424.

The next five data sets (green circle markers) show the response variability after the single largest NN grain orientation in each of the five layers is changed. This effect is most significant for the 1st NN grain layer and quickly decays. Surprisingly, the maximum response variable is in some cases larger than the unaltered microstructure simulation. Five random changes to the orientation of the largest NN grain in the 4th and 5th layers do not influence the GOI. Therefore, the effect is limited to the first three layers of NN grains. Altering the orientation of the largest 1st NN grain appears to influence the response variables less than altering the 1st NN grain that shares the most surface area with the GOI. This is further examined later. The subsequent five data sets (blue triangle markers) show the response variability after all grain orientations in each of the five layers are altered. A change to all grain orientations in the first two layers sufficiently perturbs the micromechanical response to drive the highest response variable to a different grain, as indicated by the red triangle markers. When all 3rd NN grain orientations are altered, however, the highest damage parameter once again occurs within the GOI, and in three out of the five cases the response is now larger than the response of the unaltered microstructure (black dashed line). Altering several hundred grain orientations in layers progressively farther from the GOI slows the decayed response as compared to the green circle markers. Finally, the two cyan square markers in Figure 7.10a and Figure 7.10b depict the response when the orientations of the largest 1st NN grain and the 1st NN grain that shares the most surface area with the GOI are equal the orientation of the GOI. The response is reduced in both cases and these two scenarios are investigated in more detail later. The Coefficient of Variation (COV, defined as the standard deviation of a data set divided by the mean) for the three response variables is shown in Figure 7.11. This

quantifies the variability of the three response variables and emphasizes that σ_n is weakly perturbed by changes to orientations of NN grains.

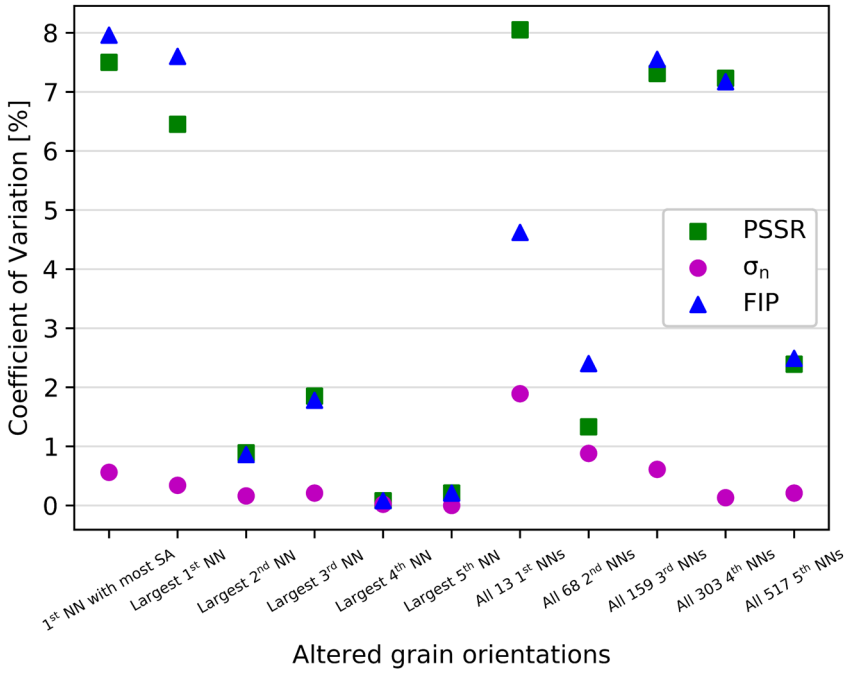

Figure 7.11. Coefficient of variation for the response variables of the first ~4,600 grain cropped microstructure, using data shown in Figure 7.10.

Figure 7.12 depicts the FIP response variability when different numbers of grain orientations are altered in the 3rd, 4th, and 5th NN grain layers. Grain orientations are extracted from the earlier scenario in which all NN grain orientations in a layer were altered. Therefore, altering the grain orientations of the 5, 5%, and 20% largest grains in a layer are intermediate scenarios between the extremes of changing all or none of the grain orientations, i.e., the scenarios here represent a gradual change to the GOI's neighborhood. Whereas Figure 7.10b indicated no influence past the 3rd NN grain layer when altering the orientation of the largest grain (green circle markers), the first three data sets in Figure 7.12 show that changes to multiple grain orientations in progressively farther NN grain layers

perturb the GOI, with a diminishing effect. Interestingly, changing the orientations of the 20% largest grains in each of the three layers results in similar variability (last three data sets in Figure 7.12).

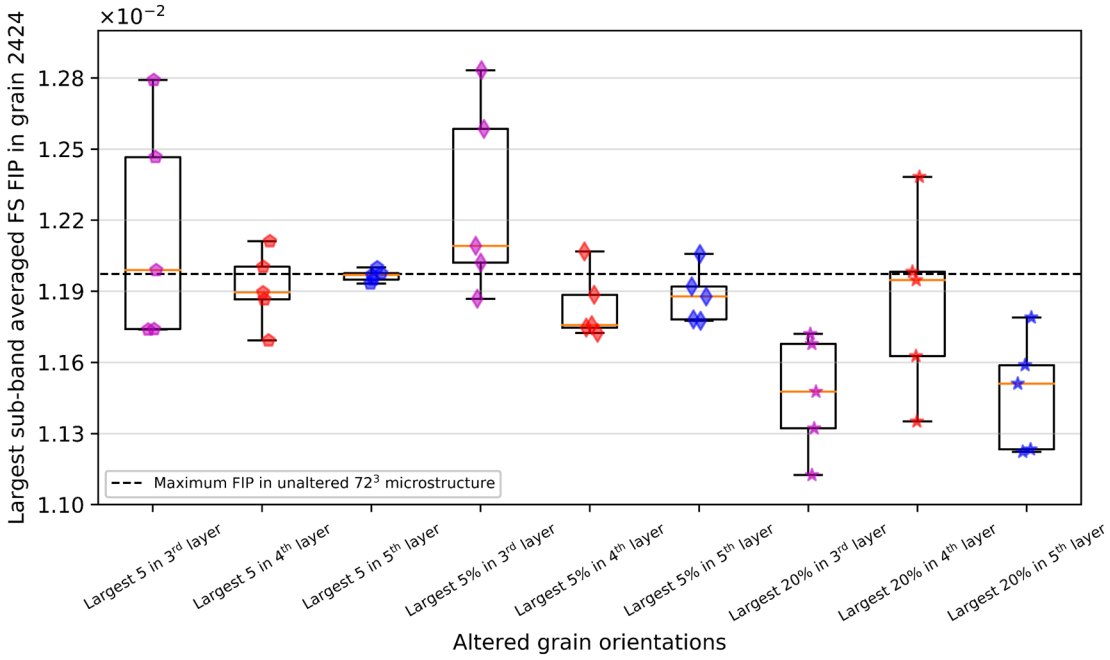

Figure 7.12. The highest sub-band volume averaged FIP in the grain (#2424) about which the first ~4,600 grain microstructure was cropped from the ~160,000 grain microstructure. The black dashed line indicates the highest FIP in this grain without changing any grain orientations. Table 7.1 indicates the number of altered grain orientations in each data set.

7.6.3 Cropped region about 3rd largest FIP

The analysis in the previous section is repeated for the second ~4,600 grain cropped microstructure. Only the response variability of the maximum sub-band volume averaged FIP is shown due to the similarities between the FIP and PSSR observed in Figure 7.10. Figure 7.13 shows similar trends to the data presented in Figure 7.10. For instance, altering the largest NN grain in each layer only perturbs the GOI up to the third layer. Similarly,

the effect of altering all NN grains in progressively distanced layers appears to decay, but not as quickly as altering the single largest NN grain in each layer, because in the former scenario, several hundreds of grain orientations are altered. There are interesting contrasts in this second ~4,600 microstructure. First, there is greater response variability when the largest 1st NN grain orientation is altered versus the 1st NN that shares the most surface area with the GOI. Furthermore, the two final cyan square markers indicate that changing the two 1st NN grains has little influence on the GOI. These trends will be explored in further detail.

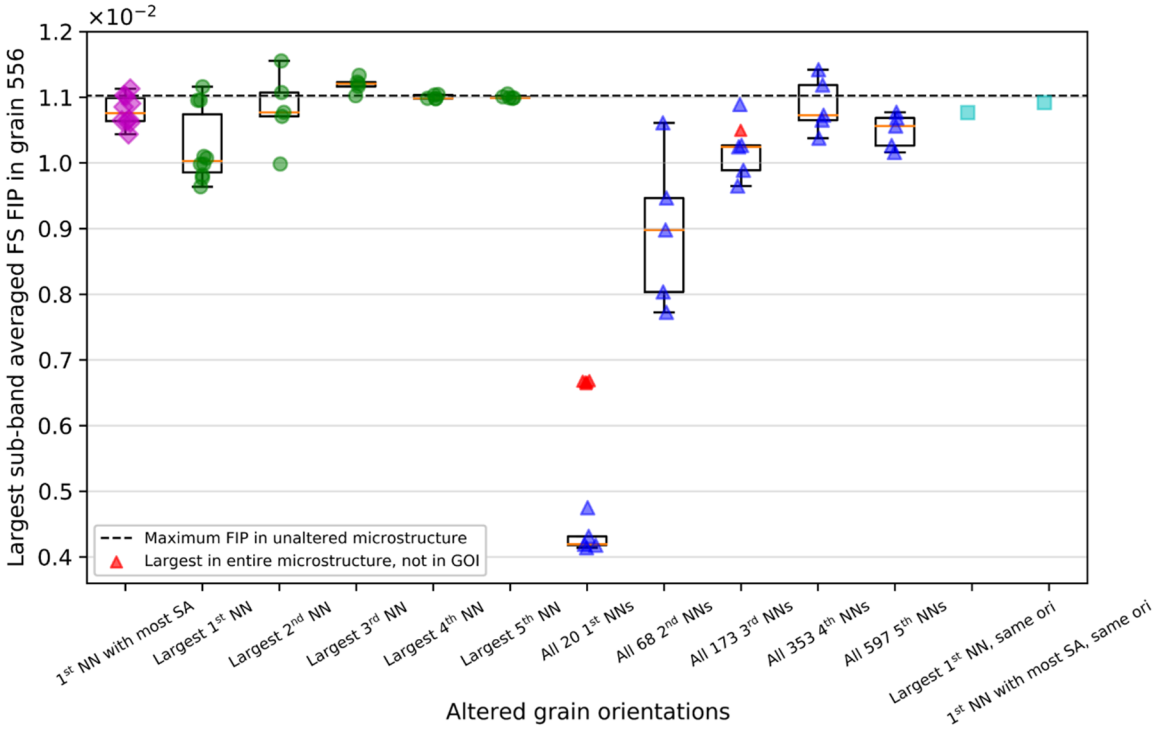

Figure 7.13. The highest sub-band volume averaged FIP in the grain (#556) about which the second ~4,600 grain microstructure was cropped from the ~160,000 grain microstructure. The black dashed line indicates the highest FIP in this grain without changing any grain orientations. Red triangle markers indicate the highest FIP that did not occur within grain #556.

The effects of altering certain grain orientations in the 3rd, 4th, and 5th NN grain layers for the second ~4,600 microstructure are shown in Figure 7.14. These are comparable to the same analysis presented in Figure 7.12 with the notable exception that altering the grain orientations of the 20% largest grains in the 3rd and 4th NN grain layers manifests the highest variability. In fact, the variability in these last three data sets resembles the data sets in Figure 7.13 in which all grain orientations were changed in the 3rd, 4th, and 5th NN grain layers.

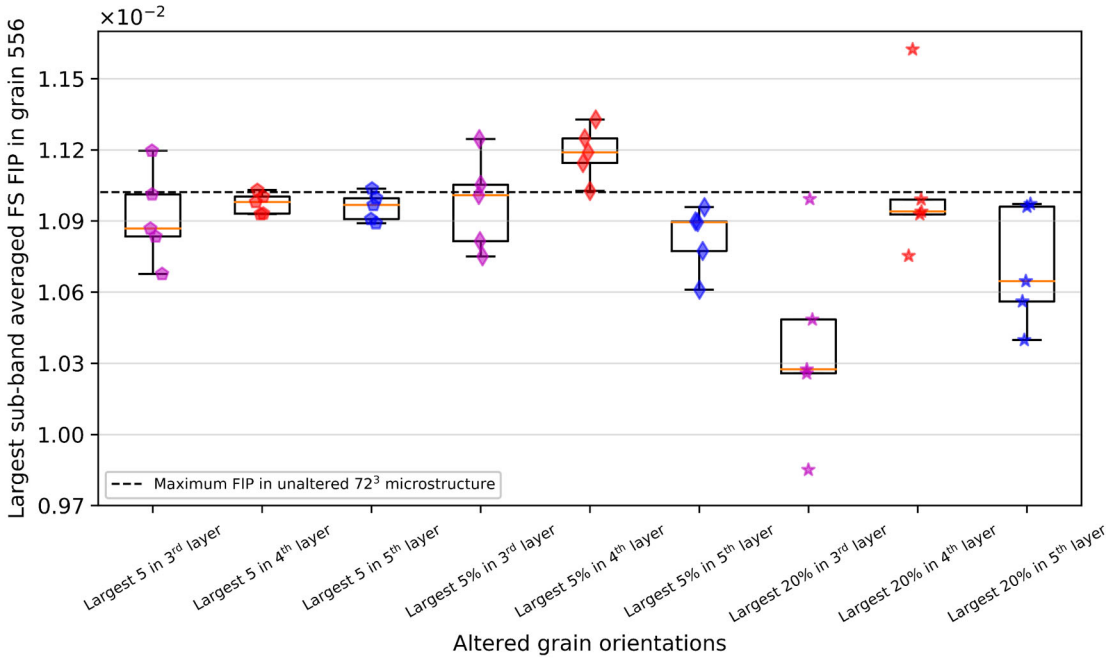

Figure 7.14. The highest sub-band volume averaged FIP in the grain (#556) about which the second ~4,600 grain microstructure was cropped from the ~160,000 grain microstructure. The black dashed line indicates the highest FIP in this grain without changing any grain orientations. Table 7.2 indicates the number of altered grain orientations in each data set.

7.6.4 Discussion of nearest neighbor influence

To further investigate the response variability in the GOI when a single grain in the first layer is altered, Figure 7.15 depicts the grains that manifest the 1st and 3rd highest FIPs (about which the two ~4,600 grain microstructure were cropped), along with the grains whose orientations were altered to produce the first two data sets in Figure 7.10 and Figure 7.13, respectively. Table 7.3 contains the apparent SFs of each grain and includes SFs for an FCC crystal loaded along the [100] and [111] directions.

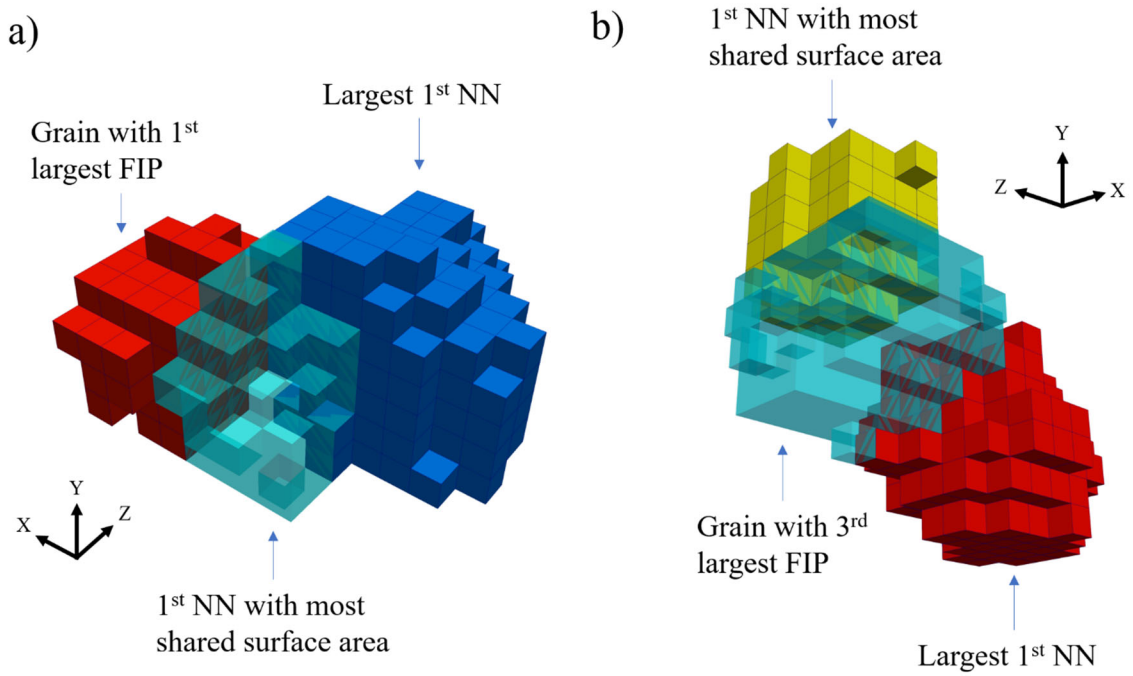

Figure 7.15. The grains that manifest the a) 1st (grain #2424) and b) 3rd (grain #556) highest FIPs in the ~160,000 grain microstructure. The 1st NN grains that share the most surface area with the grains of interest and the largest 1st NN grains are shown. Microstructures were strained in the X direction. Some grains are shown as opaque to improve visualization.

Table 7.3. Apparent Schmid Factors (SF) for the six grains depicted in Figure 7.15. The last two rows show SFs for an fcc crystal loaded in the [100] and [111] directions.

Slip planes	(1,1,1)			(-1,1,1)			(1,1,-1)			(1,-1,1)		
Slip directions	[0,1,-1]	[-1,0,1]	[1,-1,0]	[0,-1,1]	[-1,0,-1]	[1,1,0]	[0,-1,-1]	[1,0,1]	[-1,1,0]	[0,1,1]	[1,0,-1]	[-1,-1,0]
1st highest FIP grain												
Grain of interest (#2424)	0.32	0.49	0.17	0.10	0.13	0.23	0.26	0.45	0.20	0.04	0.09	0.14
Largest 1st NN	0.07	0.23	0.30	0.20	0.09	0.11	0.12	0.01	0.13	0.40	0.34	0.06
Most shared area	0.06	0.20	0.26	0.20	0.13	0.06	0.14	0.02	0.16	0.40	0.36	0.03
3rd highest FIP grain												
Grain of interest (#556)	0.50	0.24	0.26	0.17	0.05	0.23	0.47	0.17	0.30	0.20	0.12	0.33
Largest 1st NN	0.35	0.44	0.09	0.43	0.43	0.00	0.44	0.36	0.09	0.35	0.35	0.00
Most shared area	0.00	0.24	0.24	0.00	0.41	0.41	0.17	0.13	0.05	0.17	0.05	0.13
Along [100]	0.00	0.41	0.41	0.00	0.41	0.41	0.00	0.41	0.41	0.00	0.41	0.41
Along [111]	0.00	0.00	0.00	0.00	0.27	0.27	0.27	0.27	0.00	0.27	0.00	0.27

The microstructures were strained in the X direction and Figure 7.15 reveals that the position of these 1st NN grains may explain the difference in response variability observed in Figure 7.10 and Figure 7.13. The 1st NN grain that shares the most surface area with grain #2424 (Figure 7.15a) is positioned directly along the straining direction. The largest 1st NN grain is offset in the straining direction but also in the Z direction. In contrast, the two 1st NN grains of grain #556 (Figure 7.15b) are offset in the Y and Z directions with roughly the same center of mass in the X direction. Variability in the grain response may therefore be affected by whether the altered grains are positioned along the straining direction with respect to the GOIs. More specifically, the first two data sets in Figure 7.10a

and Figure 7.10b, in which the orientations of a grain in the 1st NN grain layer were altered, vary much more significantly than the first two data sets in Figure 7.13. This suggests that local response is more sensitive to changes in the orientations of NN grains along the global straining direction.

Setting the orientations of the 1st NN grains in Figure 7.15 to the orientations of grain #2424 and grain #556 perturbs the response of the GOI differently, and these effects are difficult to predict. The last two data sets in Figure 7.10a and Figure 7.10b showed a substantial decrease in response variables, whereas the last two data sets in Figure 7.13 showed nearly negligible change. Both grain #2424 and grain #556 have maximum SFs of 0.49 and 0.50, respectively, as shown in Table 7.3. The final data markers in Figure 7.10b and Figure 7.13 show the change in FIP response inside the GOI when the 1st NN grain that shares the most surface area with the GOI has the same grain orientation as the GOI. Table 7.3 shows that the maximum apparent SF for these two grains is similar and close to 0.40-0.41. Altering these grain orientations raises the maximum SFs to either ~0.49-0.50. The next important factor is the position of the grain, which in one case is positioned directly along the straining direction and in the other, positioned along the Y direction of the GOI. In the latter case (Figure 7.15b), the difference in GOI response is almost negligible, as indicated by the last data marker in Figure 7.13. In contrast, the last data marker in Figure 7.10b indicates that the position of the 1st NN grain that shares the most surface area with grain #2424 (Figure 7.15a) strongly reduces the plastic deformation in grain #2424. This argument is complicated for the scenario in which the orientation of the largest 1st NN grain is changed to the orientation of the GOI because the change in maximum SF for the two largest 1st NN grains is different. Such spatial considerations are

particularly important for low symmetry alloys in which soft-hard rough grain combinations have been suggested to contribute to dwell fatigue failure [246, 247]. This once again indicates that more complex data science/machine learning and spatial statistics are required that consider both the extreme value response and structural characteristics of many NN grain layers. One promising avenue is the Materials Knowledge System (MKS) which has not yet been applied to such large microstructure data sets [77-80], combined with machine learning methods.

7.7 Conclusions

This chapter examined the extreme value local response of progressively larger microstructures with different crystallographic textures and grain morphologies to explore trends in FIP EVDs as a function of maximum SVE size, comparing to ensembles comprising the same cumulative volume of microstructure. The trends of the FIP EVDs from different microstructures sets, the largest of which contained over 160,000 grains discretized by a ~15.6 million finite element mesh, shows a progressive increase in the maximum computed extreme value FIPs. While the establishment of RVE size has not been resolved with these simulations, the monotonicity of the increase of FIP EVDs with increase of size, along with preservation of relative rank ordering of several microstructures based on FIP EVDs, indicates that the process of convergence towards a RVE will be smooth and continuous, and that SVE ensembles indeed are useful for ranking microstructures in terms of relative resistance to fatigue crack formation. While convergence of the macroscopic stress-strain response has been previously shown to require only on the order of hundreds of grains, convergence of the FIP EVDs requires significantly more grains. The cubic crystallographic texture may require tens of thousands

of grains for convergence of FIP EVDs. In contrast, the increased probability of individual grains oriented favorably for significant plastic slip in microstructures with random or rolled crystallographic textures requires substantially more grains for convergence. Crystallographic texture is significantly more influential in this regard than grain morphology.

Four different microstructure sets, each with over ~160,000 grains, demonstrated that an ensemble of smaller statistical volume elements may be simulated to accumulate a near equivalent distribution of extreme value FIPs as compared to a single massive microstructure. The seven distinctly high FIPs from the ~160,000 grain microstructure were further investigated to elucidate the structural mechanisms of the largest fatigue hot spots. The tested criteria incorporated the orientation of the GOI with highest FIP and the 1st and 2nd NN grains, in addition to the misorientation between the GOI and its neighbors. Nontrivial structural correlations at the most extreme fatigue hot spots revealed the need for more advanced formulations (e.g., n-point statistics [77-80]) to better understand the connection between structure and extreme value response. Finally, a unique study in which individual grain orientations were systematically altered investigated the variability in extreme value FIPs. Changes to a single grain orientation only affected the response of the GOI up to the third layer of NN grains, in accordance with the work of Diehl et al. [183]. Altering several grain orientations in layers progressively farther from the GOI shows a decayed response. Further investigation suggested that the spatial location of the 1st NN grains with respect to the global straining direction may also influence response variability in the GOI. This is especially true for low symmetry HCP alloys where soft-hard rough grain combinations have been suggested to contribute to dwell fatigue failure [246, 247].

This study in this chapter leverages very large simulations to explore the complex structural characteristics and interactions responsible for the extreme value response at hot spot grains. It is complicated by virtue of grain orientation and morphology, loading direction, and long-range spatial interactions. Although the results demonstrate the extent to which nearest neighbor grains influence the extreme value response at fatigue hot spots, more advanced data science and machine learning techniques are required to better understand and quantify these trends. It lies beyond human intuition and simple approaches to reduce dimensionality. The effects of grain nearest neighbor interactions are also expected to strongly depend on the material system and constitutive model employed. For instance, previous work demonstrated that the influence of a free surface in polycrystalline simulations of HCP Ti alloy Ti-6Al-4V decayed more rapidly as compared to the FCC Al 7075-T6 alloy explored in this work [128]. Furthermore, the two term Ohno-Wang type hardening law in this constitutive model, which was essential during model calibration to match experimentally measured plastic strain at low levels of applied stress, undoubtably influences the extent of NN grain interactions differently than other hardening models (e.g., Armstrong-Frederick hardening model). The simulation of massive microstructures enabled by the PRISMS-Fatigue framework is necessary to simulate sufficient grain/phase heterogeneity that leads to the extreme value responses investigated here. It is emphasized that out of the ~160,000 simulated grain in the largest microstructure, only seven manifested distinctly high FIPs. Thus, attempts to leverage data science and machine learning techniques in these problems will rely on the availability of massive data sets that PRISMS-Fatigue can provide.

CHAPTER 8. CONCLUSIONS AND RECOMMENDATIONS

8.1 Overview of contributions

The digital workflows developed and exercised in this thesis demonstrate their importance in providing decision support to ICME in the materials selection and design processes. CPFEM simulations of several candidate microstructures under various boundary conditions, strain states, and strain amplitudes allow for the rank ordering of relative fatigue resistance. Furthermore, the implementation of the developed Python-scripted digital workflows along with the open-source PRISMS-Plasticity solver as a standalone framework available to the research community will increase the rate at which new and existing materials are evaluated for fatigue critical applications. Chapters 6 and 7 demonstrated the versatility of the PRISMS-Fatigue framework. Each chapter is briefly reviewed below.

8.1.1 Surface versus bulk effects in fatigue

Chapter 3 demonstrated the unique differences in the driving force for fatigue crack formation in the two alloys of interest, particularly how this driving force is perturbed in the presence of a free surface. Additionally, the sensitivity of this driving force to crystallographic texture, grain morphology, and loading direction was evaluated. The increased symmetry of the fcc Al 7075-T6 alloy resulted in strong interactions between surface and near surface grains, whereas for hcp Ti-6Al-4V, individual grain/phase interactions dominated, and no preference was indicated for surface-correlated activity. It is important to note that these surface and bulk simulations agree with experimental trends, which showed that fatigue cracks in 7000 series Al alloys were found to form either at or

within 10 μm of the free surface for various surface conditions and stress amplitudes [149, 150]. In contrast, the location of fatigue crack formation in high strength titanium alloys such as Ti-6Al-4V is more sensitive to the surface condition and fatigue regime [151-153]. Executing the same simulation strategy on vastly different alloys and constitutive models revealed insights extracted only when results for both alloys are compared.

8.1.2 Effects of multiaxial strain states on the driving force for fatigue crack formation

Chapter 4 examined the fatigue response of the two alloys of interest under different multiaxial strain states and strain magnitudes. As described in Section 4.1, engineering components seldom undergo simple uniaxial states of strain. However, most fatigue tests are performed in this simple experimental configuration. Thus, it is crucial to evaluate the fatigue performance of alloys under a variety of strain states and magnitudes. Chapter 4 examined FIP EVDs for both alloys under uniaxial, equibiaxial, pure shear, and simple shear states of strain and generally aligned with experimental literature, i.e., pure and simple shear straining results in lower FIP magnitudes as compared to uniaxial straining. A methodology to generate computational Γ Planes that span various strain states and strain magnitudes was outlined which can aid in the design of engineering components. The Al 7075-T6 Γ Plane closely resembles trends compiled by Brown and Miller [16]. Finally, the elastic strains normal to the slip planes of the highest FIPs were correlated to the four strain states. An unexpected result was that shear straining shifted the sites of the highest sub-band volume averaged FIPs to the prismatic slip systems, whereas the sites of highest FIPs remained on basal slip systems under uniaxial and equibiaxial straining. These results can thus inform future experiments to maximize information gain or assist in assessing massive data sets such as those gathered from HEDM experiments.

8.1.3 PRISMS-Fatigue: an open-source crystal plasticity fatigue analysis tool

In Chapter 5, a novel open-source ICME framework capable of large-scale fatigue analysis was introduced. PRISMS-Fatigue is a highly efficient, scalable, flexible, and easy-to-use community platform. Several applications demonstrated the versatility of PRISMS-Fatigue, including the simulations from Chapters 3 and 4 but also one in which progressively larger microstructures were simulated. The largest microstructure contained ~160,000 grains discretized by 250^3 = 15,625,000 elements, which is the largest microstructure-sensitive CPFEM simulation currently available in the literature, not considering simulation schemes other than FE methods such as FFT crystal plasticity [238, 239], for example. A microstructure with ~7,500 grains discretized by 90^3 = 729,000 elements simulated in PRISM-Fatigue and the commercial solver ABAQUS demonstrated that the former is nearly 26 times faster than ABAQUS. Furthermore, PRISMS-Fatigue continued to scale well even with as many as 480 CPUs, whereas ABAQUS scalability saturated at 240 CPUs. The strong-scaling of PRISMS-Fatigue was demonstrated using a microstructure with ~41,000 grains discretized by 160^3 = 4,096,000 elements.

PRISMS-Fatigue is envisioned to be constantly under development so that researchers can maximize benefit from the framework and build on community best practices. In addition to a written tutorial available on GitHub, nearly three hours of video tutorials are available on YouTube to fully guide new users (see Section 5.2.10). The PRISMS-Fatigue publications associated with this thesis (Chapters 5, 6, and 7) include all the raw microstructure and simulation data to recreate all the results and figures presented in those chapters.

8.1.4 Effects of boundary conditions on microstructure-sensitive fatigue crystal plasticity analysis

With the advent of PRISMS-Fatigue, microstructure-sensitive modeling of fatigue is not only available to the entire research community but also allows for very large simulations previous thought untenable. This may eventually rid the need for periodic boundary conditions as simulation sizes will approach laboratory test specimens.

Chapter 6 explores the different boundary conditions available in PRISMS-Fatigue and that are commonly used in CPFEM simulations. The efficacy of periodic boundary conditions imposed using multi-point constraints is demonstrated and the effects of three non-periodic boundary conditions are assessed using the macroscopic stress-strain response, measures of local plastic slip, and corresponding FIPs. The two non-periodic boundary conditions referred to as “symmetry” and “minimal” are most appropriate for fatigue related analyses, whereas the “grip” boundary condition was determined to be too artificially constraining. Furthermore, the combined effects of different boundary conditions, crystallographic textures, and surface area-to-volume ratios on extreme value FIPs were assessed. This chapter provides vital guidance to future studies aimed at assessing the driving force for fatigue crack formation in polycrystalline metals and alloys, using either the SVE ensemble scheme with periodic boundary conditions or very large microstructures with one of the non-periodic boundary conditions mentioned above.

8.1.5 Very large-scale crystal plasticity finite element method simulations

The final chapter leverages the powerful capabilities of PRISMS-Fatigue to investigate the extreme value fatigue response of progressively larger polycrystalline

microstructures. Although the RVE size for fatigue related application is difficult to assess, it is nonetheless important to study the convergence rate of EVDs of FIPs with increase of highly stressed volume. The ~160,000 grain microstructure simulated in Chapter 5, along with three other SVE ensembles each with ~160,000-165,000 total grains, demonstrated that an ensemble of smaller SVEs may be simulated to accumulate a near equivalent distribution of extreme value FIPs as a single large microstructure. The distinctly high FIPs from the largest microstructure were further investigated to elucidate the structural mechanisms of the largest fatigue hot spots. Nontrivial structural correlations revealed the need for more advanced formulations and data science/machine learning techniques. Nonetheless, the sensitivity of local micromechanical response at these hot spot grains was quantitatively investigated by systematically altering the orientations of nearest neighbor grains.

8.2 Recommendations for future work

This section details recommendations for future work and most promising avenues to further advance microstructure-sensitive fatigue modeling efforts.

8.2.1 Complex microstructures

The high scalability of PRISMS-Fatigue permits simulations of microstructures with tens of millions of elements. Although the polycrystalline microstructures evaluated in this thesis were cuboid in shape, different geometries may be simulated for novel fatigue related studies. A finer mesh can be employed in areas of high interest while rendering acceptable simulation run times.

One future area of interest is the simulation of notched microstructures to examine the effects of surface roughness on the extreme value fatigue response. Previous work that explored the effects of surface roughness using simulations of crystal plasticity constitutive models suffered from poor scalability and were in some cases restricted to relative smooth geometries in 2.5D simulations [33-35]. PRISMS-Fatigue allows for more complex notch microstructures with a notch size on the order of grain size, all while retaining a fine enough mesh but large enough domain for a meaningful CPFEM simulation and subsequent analysis. This is currently under investigation by the author in collaboration with the PRISMS Center at the University of Michigan.

A crucial aspect of such a study is the comparison between the fatigue response of a microstructure with a smooth notch geometry (i.e., meshed with conforming hexahedral elements) compared to a notch represented entirely by cubic voxels of the same size (i.e., producing a "staircase" effect at the notch). Such analysis might demonstrate that the more refined and computationally expensive smooth notch geometry varies insignificantly from the latter, relatively inexpensive mesh. Simulating notched microstructures with crystal plasticity models that explicitly account for crystallographic grain orientation can also be compared to simpler models such as isotropic plasticity and J_2 models [248]. Subsequent analysis may then reveal whether explicitly considering grain orientation in a more advanced constitutive model such as crystal plasticity decreases the extent to which a notch affects material response, thereby indicating that simpler models may overestimate the detrimental effects of surface roughness. This will be strongly influenced by the orientation of grains near and at the notch root. However, a series of notched microstructures may first be generated with grain orientations assigned later, to hold structure fixed while altering

only grain orientations and therefore examining interactions amongst nearest neighbor grains. Finally, executing such pipelines with multiple material systems will reveal insights analogous to the findings of Chapters 3 and 4, which observed considerable differences of the two alloys as affected by different boundary conditions.

8.2.2 High fidelity experiments coupled with simulations

The recent use of HEDM experiments coupled with crystal plasticity simulations has ushered in a new era of combined computational and experimental fatigue analysis and modeling. Some of the most notable recent advances include crystal plasticity constitutive model parameter calibration [85], assessment of different slip system back stress formulations [87], and direct observation of crack closure during microstructurally small fatigue crack growth [88]. Several HEDM techniques in unison (e.g., NF and FF HEDM, along with micro-computed tomography) can provide a high-fidelity mesh with experimentally derived grain-averaged strain tensors [82, 83]. Very recently, these techniques have begun to resolve sub-grain orientation fields [249, 250]. Further advancements in these techniques, as well as upcoming upgrades to high energy synchrotron sources (e.g., APS upgrade at ANL), will allow for experimental investigation of lower length scale phenomena such as dislocation motion in polycrystalline alloys. Consequently, the unison of lower length-scale computational and experimental fatigue modeling will aid in the selection of appropriate crystal plasticity model forms and help calibrate constitutive model parameters [111, 112].

8.2.3 Machine learning techniques for large data sets

Chapter 7 analyzed a massive data set made possible using PRISMS-Fatigue. It was demonstrated that out of the largest microstructure with ~160,000 grains, only seven grains manifested distinctly high FIPs. Simple attempts to correlate these highest FIPs to structural characteristics were nontrivial. Machine learning techniques, such as the MKS imbued with Gaussian Process Regression, are promising avenues to elucidate these structural mechanisms. However, successful machine learning endeavors depend on the availability of massive data sets. Paulson and colleagues [77-80] demonstrated that SP linkages for the extreme value fatigue response required significantly more data than SP linkages for homogenized response such as elastic stiffness or yield strength. Unsupervised machine learning and data science techniques alone may not suffice for these materials science problems and may instead require a trained materials scientist for guidance.

It would be particularly interesting and nontrivial to examine the differences in these large data sets with different material systems and constitutive models. The most fruitful insight from these types of studies often arises when different material systems are examined given the same microstructure sizes and boundary and loading conditions (e.g., the study performed in Chapters 3 and 4 on Al 7075-T6 and Ti-6Al-4V), or perhaps with different constitutive model forms (e.g., different formulations of back stress, or a Power Law Flow Rule versus a Kocks Activation Enthalpy Flow Rule).

REFERENCES

[1] I. Milne, "The importance of the management of structural integrity," *Engineering Failure Analysis,* 1, 171 (1994)

[2] D. L. McDowell, "Basic issues in the mechanics of high cycle metal fatigue," *International Journal of Fracture,* 80, 103 (1996)

[3] J. H. Panchal, S. R. Kalidindi, and D. L. Mcdowell, "Key computational modeling issues in integrated computational materials engineering," *Computer Aided Design,* 45, 4 (2013)

[4] Simulia, ABAQUS, 6.16, Providence, RI, USA.

[5] M. Yaghoobi *et al.*, "Prisms-plasticity: An open-source crystal plasticity finite element software," *Computational Materials Science,* 169, 109078 (2019)

[6] J. A. Bannantine, J. J. Comer, and J. L. Handrock, *Fundamentals of metal fatigue analysis*. Prentice Hall, 1990.

[7] O. H. Basquin, in *Proc Am Soc Test Mater*, 1910, vol. 10, pp. 625-630.

[8] L. F. Coffin Jr, "A study of the effects of cyclic thermal stresses on a ductile metal," *Transactions of the American Society of Mechanical Engineers, New York,* 76, 931 (1954)

[9] S. Manson, "Behavior of materials under conditions of thermal stress," *Heat Transfer Symposium,* 9 (1953)

[10] A. A. Griffith and G. I. Taylor, "Vi. The phenomena of rupture and flow in solids," *Philosophical Transactions of the Royal Society of London. Series A, Containing Papers of a Mathematical or Physical Character,* 221, 163 (1921)

[11] G. R. Irwin, "Fracturing of metals," *American Society for Metals,* 147 (1949)

[12] G. R. Irwin, "Analysis of stresses and strains near the end of a crack traversing a plate," *Trans. ASME, Journal of Applied Mechanics,* E24, 361 (1957)

[13] P. Paris and F. Erdogan, "A critical analysis of crack propagation laws," *Journal of Basic Engineering,* 85, 528 (1963)

[14] P. J. E. Forsyth, "A two stage process of fatigue crack growth," *Proceedings of the Crack Propagation Symposium,* 1, 76 (1961)

[15] W. N. Findley, "A theory for the effect of mean stress on fatigue of metals under combined torsion and axial load or bending," *Journal of Engineering for Industry,* 81, 301 (1959)

[16] M. W. Brown and K. J. Miller, "A theory for fatigue failure under multiaxial stress-strain conditions," *Proceedings of the Institution of Mechanical Engineers,* 187, 745 (1973)

[17] A. Fatemi and P. Kurath, "Multiaxial fatigue life predictions under the influence of mean-stresses," *Journal of Engineering Materials and Technology,* 110, 380 (1988)

[18] A. Fatemi and D. F. Socie, "A critical plane approach to multiaxial fatigue damage including out-of-phase loading," *Fatigue & Fracture of Engineering Materials & Structures,* 11, 149 (1988)

[19] D. L. McDowell and J.-Y. Berard, "A δj-based approach to biaxial fatigue," *Fatigue & Fracture of Engineering Materials & Structures,* 15, 719 (1992)

[20] V. P. Bennett and D. McDowell, "Polycrystal orientation effects on microslip and mixed-mode behavior of microstructurally small cracks," *American Society for Testing and Materials,* 203 (1999)

[21] V. P. Bennett and D. L. McDowell, "Cyclic crystal plasticity analyses of stationary, microstructurally small surface cracks in ductile single phase polycrystals," *Fatigue & Fracture of Engineering Materials & Structures,* 25, 677 (2002)

[22] V. P. Bennett and D. L. McDowell, "Crack tip displacements of microstructurally small surface cracks in single phase ductile polycrystals," *Engineering Fracture Mechanics,* 70, 185 (2003)

[23] V. P. Bennett and D. L. McDowell, "Polycrystal orientation distribution effects on microslip in high cycle fatigue," *International Journal of Fatigue,* 25, 27 (2003)

[24] D. L. McDowell, K. Gall, M. F. Horstemeyer, and J. Fan, "Microstructure-based fatigue modeling of cast a356-t6 alloy," *Engineering Fracture Mechanics,* 70, 49 (2003)

[25] C.-H. Goh, R. W. Neu, and D. L. McDowell, "Crystallographic plasticity in fretting of ti–6al–4v," *International Journal of Plasticity,* 19, 1627 (2003)

[26] D. L. McDowell, "Viscoplasticity of heterogeneous metallic materials," *Materials Science and Engineering: R: Reports,* 62, 67 (2008)

[27] D. L. McDowell, "Simulation-based strategies for microstructure-sensitive fatigue modeling," *Materials Science and Engineering: A,* 468-470, 4 (2007)

[28] D. L. McDowell,"Microstructure-sensitive modeling and simulation of fatigue," *Fundamentals of modeling for metals processing*, vol. 22A: ASM International, 2009, IBSN 13:978-1-61503-001-0.

[29] D. L. McDowell and F. P. E. Dunne, "Microstructure-sensitive computational modeling of fatigue crack formation," *International Journal of Fatigue,* 32, 1521 (2010)

[30] C. P. Przybyla and D. L. McDowell, "Simulated microstructure-sensitive extreme value probabilities for high cycle fatigue of duplex ti–6al–4v," *International Journal of Plasticity,* 27, 1871 (2011)

[31] G. M. Castelluccio and D. L. McDowell, "Mesoscale modeling of microstructurally small fatigue cracks in metallic polycrystals," *Materials Science and Engineering: A,* 598, 34 (2014)

[32] S. K. Ås, B. Skallerud, and B. W. Tveiten, "Surface roughness characterization for fatigue life predictions using finite element analysis," *International Journal of Fatigue,* 30, 2200 (2008)

[33] Y. Guilhem, S. Basseville, F. Curtit, J.-M. Stéphan, and G. Cailletaud, "Numerical analysis of the effect of surface roughness on mechanical fields in polycrystalline aggregates," *Modelling and Simulation in Materials Science and Engineering,* 26, 045004 (2018)

[34] H. Hallberg, S. K. Ås, and B. Skallerud, "Crystal plasticity modeling of microstructure influence on fatigue crack initiation in extruded al6082-t6 with surface irregularities," *International Journal of Fatigue,* 111, 16 (2018)

[35] A. Le Pécheur, F. Curtit, M. Clavel, J. M. Stephan, C. Rey, and P. Bompard, "Polycrystal modelling of fatigue: Pre-hardening and surface roughness effects on damage initiation for 304l stainless steel," *International Journal of Fatigue,* 45, 48 (2012)

[36] M. D. Sangid, P. Ravi, V. Prithivirajan, N. A. Miller, P. Kenesei, and J.-S. Park, "Icme approach to determining critical pore size of in718 produced by selective laser melting," *JOM,* 72, 465 (2020)

[37] G. M. Castelluccio and D. L. McDowell, "Effect of annealing twins on crack initiation under high cycle fatigue conditions," *Journal of Materials Science,* 48, 2376 (2012)

[38] W. D. Musinski, PhD Thesis, George W. Woodruff School of Mechanical Engineering, Georgia Institute of Technology, (2014).

[39] N. Salajegheh and D. L. McDowell, "Microstructure-sensitive weighted probability approach for modeling surface to bulk transition of high cycle fatigue failures dominated by primary inclusions," *International Journal of Fatigue,* 59, 188 (2014)

[40] W. D. Musinski, Masters Thesis, George W. Woodruff School of Mechanical Engineering, Georgia Institute of Technology, (2010).

[41] W. D. Musinski and D. L. McDowell, "On the eigenstrain application of shot-peened residual stresses within a crystal plasticity framework: Application to ni-base superalloy specimens," *International Journal of Mechanical Sciences,* 100, 195 (2015)

[42] G. Owolabi, B. Egboiyi, L. Shi, and H. Whitworth, "Microstructure-dependent fatigue damage process zone and notch sensitivity index," *International Journal of Fracture,* 170, 159 (2011)

[43] G. M. Owolabi, R. Prasannavenkatesan, and D. L. McDowell, "Probabilistic framework for a microstructure-sensitive fatigue notch factor," *International Journal of Fatigue,* 32, 1378 (2010)

[44] G. Owolabi, O. Okeyoyin, A. Olasumboye, and H. Whitworth, "A new approach to estimating the fatigue notch factor of ti-6al-4v components," *International Journal of Fatigue,* 82, 29 (2016)

[45] G. Owolabi, O. Okeyoyin, O. Bamiduro, A. Olasumboye, and H. Whitworth, "The effects of notch size and material microstructure on the notch sensitivity factor for notched components," *Engineering Fracture Mechanics,* 145, 181 (2015)

[46] G. M. Owolabi and H. A. Whitworth, "Modeling and simulation of microstructurally small crack formation and growth in notched nickel-base superalloy component," *Journal of Materials Science & Technology,* 30, 203 (2014)

[47] W. D. Musinski and D. L. McDowell, "Microstructure-sensitive probabilistic modeling of hcf crack initiation and early crack growth in ni-base superalloy in100 notched components," *International Journal of Fatigue,* 37, 41 (2012)

[48] J. E. Bozek *et al.*, "A geometric approach to modeling microstructurally small fatigue crack formation: I. Probabilistic simulation of constituent particle cracking in aa 7075-t651," *Modelling and Simulation in Materials Science and Engineering,* 16, 065007 (2008)

[49] J. D. Hochhalter *et al.*, "A geometric approach to modeling microstructurally small fatigue crack formation: Ii. Physically based modeling of microstructure-dependent slip localization and actuation of the crack nucleation mechanism in aa 7075-t651," *Modelling and Simulation in Materials Science and Engineering,* 18, 045004 (2010)

[50] J. D. Hochhalter *et al.*, "A geometric approach to modeling microstructurally small fatigue crack formation: Iii. Development of a semi-empirical model for nucleation," *Modelling and Simulation in Materials Science and Engineering,* 19, 035008 (2011)

[51] G. Venkataramani, D. Deka, and S. Ghosh, "Crystal plasticity based fe model for understanding microstructural effects on creep and dwell fatigue in ti-6242," *Journal of Engineering Materials and Technology,* 128, 356 (2006)

[52] D. Ozturk, A. Shahba, and S. Ghosh, "Crystal plasticity fe study of the effect of thermo-mechanical loading on fatigue crack nucleation in titanium alloys," *Fatigue & Fracture of Engineering Materials & Structures,* 39, 752 (2016)

[53] M. Anahid, M. K. Samal, and S. Ghosh, "Dwell fatigue crack nucleation model based on crystal plasticity finite element simulations of polycrystalline titanium alloys," *Journal of the Mechanics and Physics of Solids,* 59, 2157 (2011)

[54] Y. Liu and F. P. E. Dunne, "The mechanistic link between macrozones and dwell fatigue in titanium alloys," *International Journal of Fatigue,* 142, 105971 (2021)

[55] F. P. E. Dunne, D. Rugg, and A. Walker, "Lengthscale-dependent, elastically anisotropic, physically-based hcp crystal plasticity: Application to cold-dwell fatigue in ti alloys," *International Journal of Plasticity,* 23, 1061 (2007)

[56] M. A. Cuddihy, A. Stapleton, S. Williams, and F. P. E. Dunne, "On cold dwell facet fatigue in titanium alloy aero-engine components," *International Journal of Fatigue,* 97, 177 (2017)

[57] D. Deka, D. S. Joseph, S. Ghosh, and M. J. Mills, "Crystal plasticity modeling of deformation and creep in polycrystalline ti-6242," *Metallurgical and Materials Transactions A,* 37, 1371 (2006)

[58] V. Hasija, S. Ghosh, M. J. Mills, and D. S. Joseph, "Deformation and creep modeling in polycrystalline ti–6al alloys," *Acta Materialia,* 51, 4533 (2003)

[59] G. Venkatramani, S. Ghosh, and M. Mills, "A size-dependent crystal plasticity finite-element model for creep and load shedding in polycrystalline titanium alloys," *Acta Materialia,* 55, 3971 (2007)

[60] D. Wilson, W. Wan, and F. P. E. Dunne, "Microstructurally-sensitive fatigue crack growth in hcp, bcc and fcc polycrystals," *Journal of the Mechanics and Physics of Solids,* 126, 204 (2019)

[61] F. Bridier, D. L. McDowell, P. Villechaise, and J. Mendez, "Crystal plasticity modeling of slip activity in ti–6al–4v under high cycle fatigue loading," *International Journal of Plasticity,* 25, 1066 (2009)

[62] M. Zhang, F. Bridier, P. Villechaise, J. Mendez, and D. L. McDowell, "Simulation of slip band evolution in duplex ti–6al–4v," *Acta Materialia,* 58, 1087 (2010)

[63] E. Kakandar, A. Barrios, J. Michler, X. Maeder, O. N. Pierron, and G. M. Castelluccio, "A computational and experimental comparison on the nucleation of

fatigue cracks in statistical volume elements," *International Journal of Fatigue,* 137, 105633 (2020)

[64] C. P. Przybyla and D. L. McDowell, "Microstructure-sensitive extreme-value probabilities of high-cycle fatigue for surface vs. Subsurface crack formation in duplex ti–6al–4v," *Acta Materialia,* 60, 293 (2012)

[65] C. P. Przybyla and D. L. McDowell, "Microstructure-sensitive extreme value probabilities for high cycle fatigue of ni-base superalloy in100," *International Journal of Plasticity,* 26, 372 (2010)

[66] B. D. Smith, D. S. Shih, and D. L. McDowell, "Fatigue hot spot simulation for two widmanstätten titanium microstructures," *International Journal of Fatigue,* 92, 116 (2016)

[67] G. M. Castelluccio and D. L. McDowell, "A mesoscale approach for growth of 3d microstructurally small fatigue cracks in polycrystals," *International Journal of Damage Mechanics,* 23, 791 (2014)

[68] F. P. E. Dunne, "Fatigue crack nucleation: Mechanistic modelling across the length scales," *Current Opinion in Solid State and Materials Science,* 18, 170 (2014)

[69] C. P. Przybyla, W. D. Musinski, G. M. Castelluccio, and D. L. McDowell, "Microstructure-sensitive hcf and vhcf simulations," *International Journal of Fatigue,* 57, 9 (2013)

[70] C. P. Przybyla, R. Prasannavenkatesan, N. Salajegheh, and D. L. McDowell, "Microstructure-sensitive modeling of high cycle fatigue," *International Journal of Fatigue,* 32, 512 (2010)

[71] G. M. Castelluccio, W. D. Musinski, and D. L. McDowell, "Computational micromechanics of fatigue of microstructures in the hcf–vhcf regimes," *International Journal of Fatigue,* 93, 387 (2016)

[72] G. M. Castelluccio, W. D. Musinski, and D. L. McDowell, "Recent developments in assessing microstructure-sensitive early stage fatigue of polycrystals," *Current Opinion in Solid State and Materials Science,* 18, 180 (2014)

[73] S. Kotha, D. Ozturk, and S. Ghosh, "Uncertainty-quantified parametrically homogenized constitutive models (uq-phcms) for dual-phase α/β titanium alloys," *npj Computational Materials,* 6, 117 (2020)

[74] D. Ozturk, S. Kotha, A. L. Pilchak, and S. Ghosh, "Two-way multi-scaling for predicting fatigue crack nucleation in titanium alloys using parametrically homogenized constitutive models," *Journal of the Mechanics and Physics of Solids,* 128, 181 (2019)

[75] D. Ozturk, S. Kotha, A. L. Pilchak, and S. Ghosh, "Parametrically homogenized constitutive models (phcms) for multi-scale predictions of fatigue crack nucleation in titanium alloys," *JOM,* 71, 2657 (2019)

[76] T. Maloth, D. Ozturk, G. M. Hommer, A. L. Pilchak, A. P. Stebner, and S. Ghosh, "Multiscale modeling of cruciform dwell tests with the uncertainty-quantified parametrically homogenized constitutive model," *Acta Materialia,* 200, 893 (2020)

[77] N. H. Paulson, M. W. Priddy, D. L. McDowell, and S. R. Kalidindi, "Data-driven reduced-order models for rank-ordering the high cycle fatigue performance of polycrystalline microstructures," *Materials & Design,* 154, 170 (2018)

[78] N. H. Paulson, M. W. Priddy, D. L. McDowell, and S. R. Kalidindi, "Reduced-order microstructure-sensitive protocols to rank-order the transition fatigue resistance of polycrystalline microstructures," *International Journal of Fatigue,* 119, 1 (2019)

[79] M. W. Priddy, N. H. Paulson, S. R. Kalidindi, and D. L. McDowell, "Strategies for rapid parametric assessment of microstructure-sensitive fatigue for hcp polycrystals," *International Journal of Fatigue,* 104, 231 (2017)

[80] N. H. Paulson, M. W. Priddy, D. L. McDowell, and S. R. Kalidindi, "Reduced-order structure-property linkages for polycrystalline microstructures based on 2-point statistics," *Acta Materialia,* 129, 428 (2017)

[81] S. Gustafson *et al.*, "Quantifying microscale drivers for fatigue failure via coupled synchrotron x-ray characterization and simulations," *Nature Communications,* 11, 3189 (2020)

[82] D. Naragani *et al.*, "Investigation of fatigue crack initiation from a non-metallic inclusion via high energy x-ray diffraction microscopy," *Acta Materialia,* 137, 71 (2017)

[83] D. P. Naragani, P. A. Shade, P. Kenesei, H. Sharma, and M. D. Sangid, "X-ray characterization of the micromechanical response ahead of a propagating small fatigue crack in a ni-based superalloy," *Acta Materialia,* 179, 342 (2019)

[84] P. R. Dawson, D. E. Boyce, J.-S. Park, E. Wielewski, and M. P. Miller, "Determining the strengths of hcp slip systems using harmonic analyses of lattice strain distributions," *Acta Materialia,* 144, 92 (2018)

[85] D. C. Pagan *et al.*, "Modeling slip system strength evolution in ti-7al informed by in-situ grain stress measurements," *Acta Materialia,* 128, 406 (2017)

[86] T. J. Turner *et al.*, "Crystal plasticity model validation using combined high-energy diffraction microscopy data for a ti-7al specimen," *Metallurgical and Materials Transactions A,* 48, 627 (2017)

[87] R. Bandyopadhyay, S. E. Gustafson, K. Kapoor, D. Naragani, D. C. Pagan, and M. D. Sangid, "Comparative assessment of backstress models using high-energy x-ray diffraction microscopy experiments and crystal plasticity finite element simulations," *International Journal of Plasticity,* 136, 102887 (2021)

[88] P. Ravi, D. Naragani, P. Kenesei, J.-S. Park, and M. D. Sangid, "Direct observations and characterization of crack closure during microstructurally small fatigue crack growth via in-situ high-energy x-ray characterization," *Acta Materialia,* 205, 116564 (2021)

[89] L. Chen, T. E. James Edwards, F. Di Gioacchino, W. J. Clegg, F. P. E. Dunne, and M.-S. Pham, "Crystal plasticity analysis of deformation anisotropy of lamellar tial alloy: 3d microstructure-based modelling and in-situ micro-compression," *International Journal of Plasticity,* 119, 344 (2019)

[90] Z. Zhang, T.-S. Jun, T. B. Britton, and F. P. E. Dunne, "Determination of ti-6242 α and β slip properties using micro-pillar test and computational crystal plasticity," *Journal of the Mechanics and Physics of Solids,* 95, 393 (2016)

[91] J. S. Weaver, M. W. Priddy, D. L. McDowell, and S. R. Kalidindi, "On capturing the grain-scale elastic and plastic anisotropy of alpha-ti with spherical nanoindentation and electron back-scattered diffraction," *Acta Materialia,* 117, 23 (2016)

[92] T.-S. Jun, Z. Zhang, G. Sernicola, F. P. E. Dunne, and T. B. Britton, "Local strain rate sensitivity of single α phase within a dual-phase ti alloy," *Acta Materialia,* 107, 298 (2016)

[93] L. K. Aagesen *et al.*, "Prisms: An integrated, open-source framework for accelerating predictive structural materials science," *JOM,* 70, 2298 (2018)

[94] S. DeWitt, S. Rudraraju, D. Montiel, W. B. Andrews, and K. Thornton, "Prisms-pf: A general framework for phase-field modeling with a matrix-free finite element method," *npj Computational Materials,* 6, 29 (2020)

[95] R. J. Asaro, "Crystal plasticity," *Journal of Applied Mechanics,* 50, 921 (1983)

[96] R. J. Asaro and J. R. Rice, "Strain localization in ductile single crystals," *Journal of the Mechanics and Physics of Solids,* 25, 309 (1977)

[97] M. W. Priddy, PhD Thesis, George W. Woodruff School of Mechanical Engineering, Georgia Institute of Technology, (2016).

[98] C. Hennessey, G. M. Castelluccio, and D. L. McDowell, "Sensitivity of polycrystal plasticity to slip system kinematic hardening laws for al 7075-t6," *Materials Science and Engineering: A,* 687, 241 (2017)

[99] A. Renard, A. S. Cheng, R. De La Veaux, and C. Laird, "The cyclic stress-strain response of polycrystalline al-zn-mg alloy and commercial alloys based on this system," *Materials Science and Engineering,* 60, 113 (1983)

[100] R. D. McGinty, PhD Thesis, George W. Woodruff School of Mechanical Engineering, Georgia Institute of Technology, (2001).

[101] M. Yaghoobi, K. S. Stopka, A. Lakshmanan, V. Sundararaghavan, J. E. Allison, and D. L. McDowell, "Prisms-fatigue computational framework for fatigue analysis in polycrystalline metals and alloys," *npj Computational Materials,* 7, 38 (2021)

[102] J. R. Mayeur and D. L. McDowell, "A three-dimensional crystal plasticity model for duplex ti–6al–4v," *International Journal of Plasticity,* 23, 1457 (2007)

[103] R. Morrissey, C.-H. Goh, and D. L. McDowell, "Microstructure-scale modeling of hcf deformation," *Mechanics of Materials,* 35, 295 (2003)

[104] M. Zhang, J. Zhang, and D. L. McDowell, "Microstructure-based crystal plasticity modeling of cyclic deformation of ti–6al–4v," *International Journal of Plasticity,* 23, 1328 (2007)

[105] B. D. Smith, D. S. Shih, and D. L. McDowell, "Cyclic plasticity experiments and polycrystal plasticity modeling of three distinct ti alloy microstructures," *International Journal of Plasticity,* 101, 1 (2018)

[106] K. Zhang, K. V. Yang, A. Huang, X. Wu, and C. H. J. Davies, "Fatigue crack initiation in as forged ti–6al–4v bars with macrozones present," *International Journal of Fatigue,* 80, 288 (2015)

[107] G. F. Whelan, PhD Thesis, School of Material Science and Engineering, Georgia Institute of Technology, (2020).

[108] T. Gu, K. S. Stopka, C. Xu, and D. L. McDowell, "Prediction of maximum fatigue indicator parameters for duplex ti–6al–4v using extreme value theory," *Acta Materialia,* 188, 504 (2020)

[109] L. Li, L. Shen, G. Proust, C. K. S. Moy, and G. Ranzi, "Three-dimensional crystal plasticity finite element simulation of nanoindentation on aluminium alloy 2024," *Materials Science and Engineering: A,* 579, 41 (2013)

[110] J. S. Weaver and S. R. Kalidindi, "Mechanical characterization of ti-6al-4v titanium alloy at multiple length scales using spherical indentation stress-strain measurements," *Materials & Design,* 111, 463 (2016)

[111] A. E. Tallman, L. P. Swiler, Y. Wang, and D. L. McDowell, "Hierarchical top-down bottom-up calibration with consideration for uncertainty and inter-scale

discrepancy of peierls stress of bcc fe," *Modelling and Simulation in Materials Science and Engineering,* 27, 064004 (2019)

[112] A. E. Tallman, L. P. Swiler, Y. Wang, and D. L. McDowell, "Reconciled top-down and bottom-up hierarchical multiscale calibration of bcc fe crystal plasticity," *International Journal for Multiscale Computational Engineering,* 15, 505 (2017)

[113] M. A. Groeber and M. A. Jackson, "Dream.3d: A digital representation environment for the analysis of microstructure in 3d," *Integrating Materials and Manufacturing Innovation,* 3, 56 (2014)

[114] C. P. Przybyla, PhD dissertation, School of Materials Science and Engineering, Georgia Institute of Technology, (2010).

[115] S. P. Donegan, J. C. Tucker, A. D. Rollett, K. Barmak, and M. Groeber, "Extreme value analysis of tail departure from log-normality in experimental and simulated grain size distributions," *Acta Materialia,* 61, 5595 (2013)

[116] D. T. Fullwood, S. R. Niezgoda, and S. R. Kalidindi, "Microstructure reconstructions from 2-point statistics using phase-recovery algorithms," *Acta Materialia,* 56, 942 (2008)

[117] D. M. Turner and S. R. Kalidindi, "Statistical construction of 3-d microstructures from 2-d exemplars collected on oblique sections," *Acta Materialia,* 102, 136 (2016)

[118] C. Zhang *et al.*, "Effect of realistic 3d microstructure in crystal plasticity finite element analysis of polycrystalline ti-5al-2.5sn," *International Journal of Plasticity,* 69, 21 (2015)

[119] T. J. Turner *et al.*, "Combined near- and far-field high-energy diffraction microscopy dataset for ti-7al tensile specimen elastically loaded in situ," *Integrating Materials and Manufacturing Innovation,* 5, 94 (2016)

[120] B. Chen, J. Jiang, and F. P. E. Dunne, "Is stored energy density the primary meso-scale mechanistic driver for fatigue crack nucleation?," *International Journal of Plasticity,* 101, 213 (2018)

[121] X. Tu, A. Shahba, J. Shen, and S. Ghosh, "Microstructure and property based statistically equivalent rves for polycrystalline-polyphase aluminum alloys," *International Journal of Plasticity,* 115, 268 (2019)

[122] T. J. Barrett, D. J. Savage, M. Ardeljan, and M. Knezevic, "An automated procedure for geometry creation and finite element mesh generation: Application to explicit grain structure models and machining distortion," *Computational Materials Science,* 141, 269 (2018)

[123] T. Hsu *et al.*, "Microstructure generation via generative adversarial network for heterogeneous, topologically complex 3d materials," *JOM,* 73, 90 (2021)

[124] S. Bargmann *et al.*, "Generation of 3d representative volume elements for heterogeneous materials: A review," *Progress in Materials Science,* 96, 322 (2018)

[125] M. Groeber, S. Ghosh, M. D. Uchic, and D. M. Dimiduk, "A framework for automated analysis and simulation of 3d polycrystalline microstructures.: Part 1: Statistical characterization," *Acta Materialia,* 56, 1257 (2008)

[126] M. Groeber, S. Ghosh, M. D. Uchic, and D. M. Dimiduk, "A framework for automated analysis and simulation of 3d polycrystalline microstructures. Part 2: Synthetic structure generation," *Acta Materialia,* 56, 1274 (2008)

[127] K. S. Stopka, G. Whelan, and D. L. McDowell, in *Society of the Advancement of Material and Process Engineering (SAMPE, 2019)*, Charlotte, NC, 2019.

[128] K. S. Stopka and D. L. McDowell, "Microstructure-sensitive computational estimates of driving forces for surface versus subsurface fatigue crack formation in duplex ti-6al-4v and al 7075-t6," *JOM,* 72, 28 (2020)

[129] K. S. Stopka and D. L. McDowell, "Microstructure-sensitive computational multiaxial fatigue of al 7075-t6 and duplex ti-6al-4v," *International Journal of Fatigue,* 133, 105460 (2020)

[130] K. S. Stopka, T. Gu, and D. L. McDowell, "Effects of algorithmic simulation parameters on the prediction of extreme value fatigue indicator parameters in duplex ti-6al-4v," *International Journal of Fatigue,* 141, 105865 (2020)

[131] F. Roters *et al.*, "Damask – the düsseldorf advanced material simulation kit for modeling multi-physics crystal plasticity, thermal, and damage phenomena from the single crystal up to the component scale," *Computational Materials Science,* 158, 420 (2019)

[132] S. R. Yeratapally, M. G. Glavicic, M. Hardy, and M. D. Sangid, "Microstructure based fatigue life prediction framework for polycrystalline nickel-base superalloys with emphasis on the role played by twin boundaries in crack initiation," *Acta Materialia,* 107, 152 (2016)

[133] T. Ozturk *et al.*, "Simulation domain size requirements for elastic response of 3d polycrystalline materials," *Modelling and Simulation in Materials Science and Engineering,* 24, 015006 (2015)

[134] T. Ozturk and A. D. Rollett, "Effect of microstructure on the elasto-viscoplastic deformation of dual phase titanium structures," *Computational Mechanics,* 61, 55 (2018)

[135] S. Mandal, J. Lao, S. Donegan, and A. D. Rollett, "Generation of statistically representative synthetic three-dimensional microstructures," *Scripta Materialia,* 146, 128 (2018)

[136] S. P. Donegan and A. D. Rollett, "Simulation of residual stress and elastic energy density in thermal barrier coatings using fast fourier transforms," *Acta Materialia,* 96, 212 (2015)

[137] A. E. Tallman, K. S. Stopka, L. P. Swiler, Y. Wang, S. R. Kalidindi, and D. L. McDowell, "Gaussian-process-driven adaptive sampling for reduced-order modeling of texture effects in polycrystalline alpha-ti," *JOM,* 71, 2646 (2019)

[138] M. Kasemer, M. P. Echlin, J. C. Stinville, T. M. Pollock, and P. Dawson, "On slip initiation in equiaxed α/β ti-6al-4v," *Acta Materialia,* 136, 288 (2017)

[139] K. Chatterjee, M. P. Echlin, M. Kasemer, P. G. Callahan, T. M. Pollock, and P. Dawson, "Prediction of tensile stiffness and strength of ti-6al-4v using instantiated volume elements and crystal plasticity," *Acta Materialia,* 157, 21 (2018)

[140] R. Quey, P. R. Dawson, and F. Barbe, "Large-scale 3d random polycrystals for the finite element method: Generation, meshing and remeshing," *Computer Methods in Applied Mechanics and Engineering,* 200, 1729 (2011)

[141] R. Quey and L. Renversade, "Optimal polyhedral description of 3d polycrystals: Method and application to statistical and synchrotron x-ray diffraction data," *Computer Methods in Applied Mechanics and Engineering,* 330, 308 (2018)

[142] M. Kasemer, R. Quey, and P. Dawson, "The influence of mechanical constraints introduced by β annealed microstructures on the yield strength and ductility of ti-6al-4v," *Journal of the Mechanics and Physics of Solids,* 103, 179 (2017)

[143] K. A. Hart and J. J. Rimoli, "Generation of statistically representative microstructures with direct grain geometry control," *Computer Methods in Applied Mechanics and Engineering,* 370, 113242 (2020)

[144] K. A. Hart and J. J. Rimoli, "Microstructpy: A statistical microstructure mesh generator in python," *SoftwareX,* 12, 100595 (2020)

[145] F. J. Humphreys and M. Hatherly,"Chapter 7 - recrystallization of single-phase alloys," *Recrystallization and related annealing phenomena (second edition)*, (Oxford: Elsevier, 2004, IBSN 978-0-08-044164-1.

[146] P. Ramesh Narayanan, S. Suwas, K. Sreekumar, P. P. Sinha, and S. Ranganathan, "Evolution of crystallographic texture in cold rolled al-zn-mg alloys used in space applications," *Materials Science Forum,* 702-703, 315 (2012)

[147] M. Peters, A. Gysler, and G. LÜtjering, "Influence of texture on fatigue properties of ti-6al-4v," *Metallurgical and Materials Transactions A,* 15, 1597 (1984)

[148] G. Lütjering, "Influence of processing on microstructure and mechanical properties of (α+β) titanium alloys," *Materials Science and Engineering: A,* 243, 32 (1998)

[149] S. Fintová, I. Kuběna, L. Trško, V. Horník, and L. Kunz, "Fatigue behavior of aw7075 aluminum alloy in ultra-high cycle fatigue region," *Materials Science and Engineering: A,* 774, 138922 (2020)

[150] M. Shahzad, M. Chaussumier, R. Chieragatti, C. Mabru, and F. Rezai Aria, "Influence of surface treatments on fatigue life of al 7010 alloy," *Journal of Materials Processing Technology,* 210, 1821 (2010)

[151] J. H. Zuo, Z. G. Wang, and E. Han, "Effect of microstructure on ultra-high cycle fatigue behavior of ti–6al–4v," *Materials Science and Engineering: A,* 473, 147 (2008)

[152] K. S. Ravi Chandran and S. K. Jha, "Duality of the s–n fatigue curve caused by competing failure modes in a titanium alloy and the role of poisson defect statistics," *Acta Materialia,* 53, 1867 (2005)

[153] C. J. Szczepanski, S. K. Jha, J. M. Larsen, and J. W. Jones, "Microstructural influences on very-high-cycle fatigue-crack initiation in ti-6246," *Metallurgical and Materials Transactions A: Physical Metallurgy and Materials Science,* 39, 2841 (2008)

[154] V. Prithivirajan and M. D. Sangid, "Examining metrics for fatigue life predictions of additively manufactured in718 via crystal plasticity modeling including the role of simulation volume and microstructural constraints," *Materials Science and Engineering: A,* 783, 139312 (2020)

[155] R. Prasannavenkatesan, J. Zhang, D. L. McDowell, G. B. Olson, and H.-J. Jou, "3d modeling of subsurface fatigue crack nucleation potency of primary inclusions in heat treated and shot peened martensitic gear steels," *International Journal of Fatigue,* 31, 1176 (2009)

[156] G. M. Castelluccio and D. L. McDowell, "Microstructure-sensitive small fatigue crack growth assessment: Effect of strain ratio, multiaxial strain state, and geometric discontinuities," *International Journal of Fatigue,* 82, 521 (2016)

[157] S.-P. Zhu, Z.-Y. Yu, J. Correia, A. De Jesus, and F. Berto, "Evaluation and comparison of critical plane criteria for multiaxial fatigue analysis of ductile and brittle materials," *International Journal of Fatigue,* 112, 279 (2018)

[158] A. Hor, N. Saintier, C. Robert, T. Palin-Luc, and F. Morel, "Statistical assessment of multiaxial hcf criteria at the grain scale," *International Journal of Fatigue,* 67, 151 (2014)

[159] C. Robert, N. Saintier, T. Palin-Luc, and F. Morel, "Micro-mechanical modelling of high cycle fatigue behaviour of metals under multiaxial loads," *Mechanics of Materials,* 55, 112 (2012)

[160] M. Poncelet, C. Doudard, S. Calloch, B. Weber, and F. Hild, "Probabilistic multiscale models and measurements of self-heating under multiaxial high cycle fatigue," *Journal of the Mechanics and Physics of Solids,* 58, 578 (2010)

[161] J. V. Sahadi, R. J. H. Paynter, D. Nowell, S. J. Pattison, and N. Fox, "Comparison of multiaxial fatigue parameters using biaxial tests of waspaloy," *International Journal of Fatigue,* 100, 477 (2017)

[162] B. Crossland, in *Proc. Int. Conf. on Fatigue of Metals*, 1956, vol. 138, pp. 12-12: Institution of Mechanical Engineers London.

[163] T. Matake, "An explanation on fatigue limit under combined stress," *Bulletin of JSME,* 20, 257 (1977)

[164] A. R. Kallmeyer, A. Krgo, and P. Kurath, "Evaluation of multiaxial fatigue life prediction methodologies for ti-6al-4v," *Journal of Engineering Materials and Technology,* 124, 229 (2002)

[165] D. Skibicki and Ł. Pejkowski, "The relationship between additional non-proportional hardening coefficient and fatigue life," *International Journal of Fatigue,* 123, 66 (2019)

[166] G. M. Castelluccio and D. L. McDowell, "Assessment of small fatigue crack growth driving forces in single crystals with and without slip bands," *International Journal of Fracture,* 176, 49 (2012)

[167] W. D. Musinski and D. L. McDowell, "Simulating the effect of grain boundaries on microstructurally small fatigue crack growth from a focused ion beam notch through a three-dimensional array of grains," *Acta Materialia,* 112, 20 (2016)

[168] C. D. Hennessey, Masters Thesis, George W. Woodruff School of Mechanical Engineering, Georgia Institute of Technology, (2015).

[169] P. C. Kern, Masters Thesis, George W. Woodruff School of Mechanical Engineering, Georgia Institute of Technology, Atlanta, GA, (2016).

[170] G. M. Castelluccio and D. L. McDowell, "Microstructure and mesh sensitivities of mesoscale surrogate driving force measures for transgranular fatigue cracks in polycrystals," *Materials Science and Engineering: A,* 639, 626 (2015)

[171] I. Bantounas, D. Dye, and T. C. Lindley, "The effect of grain orientation on fracture morphology during high-cycle fatigue of ti–6al–4v," *Acta Materialia,* 57, 3584 (2009)

[172] F. Bridier, P. Villechaise, and J. Mendez, "Slip and fatigue crack formation processes in an α/β titanium alloy in relation to crystallographic texture on different scales," *Acta Materialia,* 56, 3951 (2008)

[173] A. Muth, R. John, A. Pilchak, S. R. Kalidindi, and D. L. McDowell, "Analysis of fatigue indicator parameters for ti-6al-4v microstructures using extreme value statistics in the hcf regime," *International Journal of Fatigue,* 106096 (2020)

[174] R. Hill, "Elastic properties of reinforced solids: Some theoretical principles," *Journal of the Mechanics and Physics of Solids,* 11, 357 (1963)

[175] T. Kanit, S. Forest, I. Galliet, V. Mounoury, and D. Jeulin, "Determination of the size of the representative volume element for random composites: Statistical and numerical approach," *International Journal of Solids and Structures,* 40, 3647 (2003)

[176] F. Qayyum, A. A. Chaudhry, S. Guk, M. Schmidtchen, R. Kawalla, and U. Prahl, "Effect of 3d representative volume element (rve) thickness on stress and strain partitioning in crystal plasticity simulations of multi-phase materials," *Crystals,* 10, 944 (2020)

[177] F. Qayyum, M. Umar, S. Guk, M. Schmidtchen, R. Kawalla, and U. Prahl, "Effect of the 3rd dimension within the representative volume element (rve) on damage initiation and propagation during full-phase numerical simulations of single and multi-phase steels," *Materials,* 14, 42 (2021)

[178] H. J. Bong, H. Lim, M.-G. Lee, D. T. Fullwood, E. R. Homer, and R. H. Wagoner, "An rve procedure for micromechanical prediction of mechanical behavior of dual-phase steel," *Materials Science and Engineering: A,* 695, 101 (2017)

[179] M. Bouchedjra, T. Kanit, C. Boulemia, A. Amrouche, and M. E. A. Belouchrani, "Determination of the rve size for polycrystal metals to predict monotonic and cyclic elastoplastic behavior: Statistical and numerical approach with new criteria," *European Journal of Mechanics - A/Solids,* 72, 1 (2018)

[180] H. Lim, C. C. Battaile, J. E. Bishop, and J. W. Foulk, "Investigating mesh sensitivity and polycrystalline rves in crystal plasticity finite element simulations," *International Journal of Plasticity,* 121, 101 (2019)

[181] M. D. Sangid, J. Rotella, D. Naragani, J.-S. Park, P. Kenesei, and P. A. Shade, "A complete grain-level assessment of the stress-strain evolution and associated deformation response in polycrystalline alloys," *Acta Materialia,* 201, 36 (2020)

[182] K. Boyle and W. Curtin, in *AIP Conference Proceedings*, 2005, vol. 778, no. 1, pp. 433-438: American Institute of Physics.

[183] M. Diehl, P. Shanthraj, P. Eisenlohr, and F. Roters, "Neighborhood influences on stress and strain partitioning in dual-phase microstructures," *Meccanica,* 51, 429 (2016)

[184] E. Castillo, *Extreme value theory in engineering*. Elsevier Science, 2012.

[185] I. Marines, X. Bin, and C. Bathias, "An understanding of very high cycle fatigue of metals," *International Journal of Fatigue,* 25, 1101 (2003)

[186] P. S. De, R. S. Mishra, and C. B. Smith, "Effect of microstructure on fatigue life and fracture morphology in an aluminum alloy," *Scripta Materialia,* 60, 500 (2009)

[187] T. Zhao and Y. Jiang, "Fatigue of 7075-t651 aluminum alloy," *International Journal of Fatigue,* 30, 834 (2008)

[188] T. Itoh, H. Nakamura, M. Takanashi, and M. Wu, "Multiaxial low cycle fatigue life of ti-6al-4v under non-proportional loading with mean strain," *Theoretical and Applied Fracture Mechanics,* 90, 165 (2017)

[189] A. Fatemi, R. Molaei, S. Sharifimehr, N. Phan, and N. Shamsaei, "Multiaxial fatigue behavior of wrought and additive manufactured ti-6al-4v including surface finish effect," *International Journal of Fatigue,* 100, 347 (2017)

[190] T. Hoshide, E. Kakiuchi, and T. Hirota, "Microstructural effect on low cycle fatigue behaviour in ti-alloys under biaxial loading," *Fatigue & Fracture of Engineering Materials & Structures,* 20, 941 (1997)

[191] Z.-R. Wu, X.-T. Hu, and Y.-D. Song, "Multiaxial fatigue life prediction for titanium alloy tc4 under proportional and nonproportional loading," *International Journal of Fatigue,* 59, 170 (2014)

[192] N. Shamsaei, M. Gladskyi, K. Panasovskyi, S. Shukaev, and A. Fatemi, "Multiaxial fatigue of titanium including step loading and load path alteration and sequence effects," *International Journal of Fatigue,* 32, 1862 (2010)

[193] F. Berto, A. Campagnolo, and P. Lazzarin, "Fatigue strength of severely notched specimens made of ti–6al–4v under multiaxial loading," *Fatigue & Fracture of Engineering Materials & Structures,* 38, 503 (2015)

[194] G. Meneghetti, A. Campagnolo, F. Berto, and K. Tanaka, "Notched ti-6al-4v titanium bars under multiaxial fatigue: Synthesis of crack initiation life based on the averaged strain energy density," *Theoretical and Applied Fracture Mechanics,* 96, 509 (2018)

[195] N. Gates and A. Fatemi, "Notched fatigue behavior and stress analysis under multiaxial states of stress," *International Journal of Fatigue,* 67, 2 (2014)

[196] E. U. Lee and R. E. Taylor, "Fatigue behavior of aluminum alloys under biaxial loading," *Engineering Fracture Mechanics,* 78, 1555 (2011)

[197] P. J. E. Forsyth, "Fatigue damage and crack growth in aluminium alloys," *Acta Metallurgica,* 11, 703 (1963)

[198] D. L. McDowell and V. P. Bennett, "A microcrack growth law for multiaxial fatigue," *Fatigue & Fracture of Engineering Materials & Structures,* 19, 821 (1996)

[199] N. R. Gates and A. Fatemi, "On the consideration of normal and shear stress interaction in multiaxial fatigue damage analysis," *International Journal of Fatigue,* 100, 322 (2017)

[200] A. Fatemi, R. Molaei, S. Sharifimehr, N. Shamsaei, and N. Phan, "Torsional fatigue behavior of wrought and additive manufactured ti-6al-4v by powder bed fusion including surface finish effect," *International Journal of Fatigue,* 99, 187 (2017)

[201] J. Park and D. Nelson, "Evaluation of an energy-based approach and a critical plane approach for predicting constant amplitude multiaxial fatigue life," *International Journal of Fatigue,* 22, 23 (2000)

[202] M. Shenoy, J. Zhang, and D. L. McDowell, "Estimating fatigue sensitivity to polycrystalline ni-base superalloy microstructures using a computational approach," *Fatigue & Fracture of Engineering Materials & Structures,* 30, 889 (2007)

[203] N. Salajegheh, R. Prasannavenkatesan, D. L. McDowell, G. B. Olson, and H.-J. Jou, "Finite element simulation of shielding/intensification effects of primary inclusion clusters in high strength steels under fatigue loading," 136, 031003 (2014)

[204] V. Segal, "Review: Modes and processes of severe plastic deformation (spd)," *Materials,* 11, 1175 (2018)

[205] F. Pedregosa *et al.*, "Scikit-learn: Machine learning in python," *Journal of machine learning research,* 12, 2825 (2011)

[206] J. Zhang and A. Fatemi, "Surface roughness effect on multiaxial fatigue behavior of additive manufactured metals and its modeling," *Theoretical and Applied Fracture Mechanics,* 103, 102260 (2019)

[207] Q. Wang, C. Xin, Q. Sun, L. Xiao, and J. Sun, "Biaxial fatigue behavior of gradient structural purity titanium under in-phase and out-of-phase loading," *International Journal of Fatigue,* 116, 602 (2018)

[208] V. Doquet and V. De Greef, "Dwell-fatigue of a titanium alloy at room temperature under uniaxial or biaxial tension," *International Journal of Fatigue,* 38, 118 (2012)

[209] H. S. Turkmen, R. E. Loge, P. R. Dawson, and M. P. Miller, "On the mechanical behaviour of aa 7075-t6 during cyclic loading," *International Journal of Fatigue,* 25, 267 (2003)

[210] J. V. Bernier, J.-S. Park, A. L. Pilchak, M. G. Glavicic, and M. P. Miller, "Measuring stress distributions in ti-6al-4v using synchrotron x-ray diffraction," *Metallurgical and Materials Transactions A,* 39, 3120 (2008)

[211] M. Valiev *et al.*, "Nwchem: A comprehensive and scalable open-source solution for large scale molecular simulations," *Computer Physics Communications,* 181, 1477 (2010)

[212] P. Motamarri, S. Das, S. Rudraraju, K. Ghosh, D. Davydov, and V. Gavini, "Dft-fe – a massively parallel adaptive finite-element code for large-scale density functional theory calculations," *Computer Physics Communications,* 246, 106853 (2020)

[213] CASM GITHUB REPOSITORY, V0.1.0, AVAILABLE FROM HTTPS://GITHUB.COM/PRISMS-CENTER/CASMCODE. DOI: 10.5281/ZENODO.546148,

[214] S. Plimpton, "Fast parallel algorithms for short-range molecular dynamics," *Journal of Computational Physics,* 117, 1 (1995)

[215] J. C. Phillips *et al.*, "Scalable molecular dynamics with namd," *Journal of Computational Chemistry,* 26, 1781 (2005)

[216] D. Gaston, C. Newman, G. Hansen, and D. Lebrun-Grandié, "Moose: A parallel computational framework for coupled systems of nonlinear equations," *Nuclear Engineering and Design,* 239, 1768 (2009)

[217] M. Tegeler, O. Shchyglo, R. D. Kamachali, A. Monas, I. Steinbach, and G. Sutmann, "Parallel multiphase field simulations with openphase," *Computer Physics Communications,* 215, 173 (2017)

[218] B. Puchala, G. Tarcea, E. A. Marquis, M. Hedstrom, H. V. Jagadish, and J. E. Allison, "The materials commons: A collaboration platform and information repository for the global materials community," *JOM,* 68, 2035 (2016)

[219] M. Yaghoobi, J. E. Allison, and V. Sundararaghavan, "Multiscale modeling of twinning and detwinning behavior of hcp polycrystals," *International Journal of Plasticity,* 127, 102653 (2020)

[220] S. Ganesan *et al.*, "The effects of heat treatment on the response of we43 mg alloy: Crystal plasticity finite element simulation and sem-dic experiment," *International Journal of Plasticity,* 137, 102917 (2021)

[221] W. Bangerth, R. Hartmann, and G. Kanschat, "Deal.Ii-a general-purpose object-oriented finite element library," *ACM Trans. Math. Softw.,* 33, 24 (2007)

[222] L. Anand and M. Kothari, "A computational procedure for rate-independent crystal plasticity," *Journal of the Mechanics and Physics of Solids,* 44, 525 (1996)

[223] A. Staroselsky and B. N. Cassenti, "Combined rate-independent plasticity and creep model for single crystal," *Mechanics of Materials,* 42, 945 (2010)

[224] A. Staroselsky and B. N. Cassenti, "Creep, plasticity, and fatigue of single crystal superalloy," *International Journal of Solids and Structures,* 48, 2060 (2011)

[225] S. R. Kalidindi, C. A. Bronkhorst, and L. Anand, "Crystallographic texture evolution in bulk deformation processing of fcc metals," *Journal of the Mechanics and Physics of Solids,* 40, 537 (1992)

[226] S. R. Kalidindi, "Incorporation of deformation twinning in crystal plasticity models," *Journal of the Mechanics and Physics of Solids,* 46, 267 (1998)

[227] J. R. Rice, "Inelastic constitutive relations for solids: An internal-variable theory and its application to metal plasticity," *Journal of the Mechanics and Physics of Solids,* 19, 433 (1971)

[228] G. Z. Voyiadjis and M. Yaghoobi,"Chapter 3 - nonlocal crystal plasticity," *Size effects in plasticity*: Academic Press, 2019, IBSN 978-0-12-812236-5.

[229] S. Abhyankar, J. Brown, E. M. Constantinescu, D. Ghosh, B. F. Smith, and H. Zhang, "Petsc/ts: A modern scalable ode/dae solver library," *arXiv preprint arXiv:1806.01437,* (2018)

[230] S. Balay *et al.*, "Petsc users manual," (2019)

[231] N. Ohno and J. D. Wang, "Kinematic hardening rules with critical state of dynamic recovery, part i: Formulation and basic features for ratchetting behavior," *International Journal of Plasticity,* 9, 375 (1993)

[232] N. Ohno and J. D. Wang, "Kinematic hardening rules with critical state of dynamic recovery, part ii: Application to experiments of ratchetting behavior," *International Journal of Plasticity,* 9, 391 (1993)

[233] D. L. McDowell, "Stress state dependence of cyclic ratchetting behavior of two rail steels," *International Journal of Plasticity,* 11, 397 (1995)

[234] W. Wu *et al.*, "Goss texture intensity effect on fatigue crack propagation resistance in an al-cu-mg alloy," *Journal of Alloys and Compounds,* 730, 318 (2018)

[235] T. J. Stannard, J. J. Williams, S. S. Singh, A. S. Sundaram Singaravelu, X. Xiao, and N. Chawla, "3d time-resolved observations of corrosion and corrosion-fatigue crack initiation and growth in peak-aged al 7075 using synchrotron x-ray tomography," *Corrosion Science,* 138, 340 (2018)

[236] Y. Y. Sun *et al.*, "Fatigue performance of additively manufactured ti-6al-4v: Surface condition vs. Internal defects," *JOM,* 72, 1022 (2020)

[237] H. Yu, F. Li, Z. Wang, and X. Zeng, "Fatigue performances of selective laser melted ti-6al-4v alloy: Influence of surface finishing, hot isostatic pressing and heat treatments," *International Journal of Fatigue,* 120, 175 (2019)

[238] S. Lucarini and J. Segurado, "An upscaling approach for micromechanics based fatigue: From rves to specimens and component life prediction," *International Journal of Fracture,* 223, 93 (2020)

[239] S. Lucarini and J. Segurado, "On the accuracy of spectral solvers for micromechanics based fatigue modeling," *Computational Mechanics,* 63, 365 (2019)

[240] C. R. Mischke, "Prediction of stochastic endurance strength," *Journal of Vibration, Acoustics, Stress, and Reliability in Design,* 109, 113 (1987)

[241] K. Kapoor and M. D. Sangid, "Initializing type-2 residual stresses in crystal plasticity finite element simulations utilizing high-energy diffraction microscopy data," *Materials Science and Engineering: A,* 729, 53 (2018)

[242] P. R. Dawson and D. E. Boyce, "Fepx--finite element polycrystals: Theory, finite element formulation, numerical implementation and illustrative examples," *arXiv preprint arXiv:1504.03296,* (2015)

[243] Q. Liu and N. Hansen, "Deformation microstructure and orientation of f.C.C. Crystals," *physica status solidi (a),* 149, 187 (1995)

[244] L. Signor, P. Villechaise, T. Ghidossi, E. Lacoste, M. Gueguen, and S. Courtin, "Influence of local crystallographic configuration on microcrack initiation in fatigued 316ln stainless steel: Experiments and crystal plasticity finite elements simulations," *Materials Science and Engineering: A,* 649, 239 (2016)

[245] M. Oja, K. S. Ravi Chandran, and R. G. Tryon, "Orientation imaging microscopy of fatigue crack formation in waspaloy: Crystallographic conditions for crack nucleation," *International Journal of Fatigue,* 32, 551 (2010)

[246] S. Waheed, Z. Zheng, D. S. Balint, and F. P. E. Dunne, "Microstructural effects on strain rate and dwell sensitivity in dual-phase titanium alloys," *Acta Materialia,* 162, 136 (2019)

[247] D. Wilson, Z. Zheng, and F. P. E. Dunne, "A microstructure-sensitive driving force for crack growth," *Journal of the Mechanics and Physics of Solids,* 121, 147 (2018)

[248] H. M. Sajjad, S. Hanke, S. Güler, H. Ul Hassan, A. Fischer, and A. Hartmaier, "Modelling cyclic behaviour of martensitic steel with j2 plasticity and crystal plasticity," (in eng), *Materials,* 12, 1767 (2019)

[249] K. E. Nygren, D. C. Pagan, J. V. Bernier, and M. P. Miller, "An algorithm for resolving intragranular orientation fields using coupled far-field and near-field high energy x-ray diffraction microscopy," *Materials Characterization,* 165, (2020)

[250] K. E. Nygren, D. C. Pagan, and M. P. Miller, "Sub-grain orientation resolution during continuous loading using only far-field hedm," *IOP Conference Series: Materials Science and Engineering,* 580, (2019)

VITA

Krzysztof (Kris) S. Stopka was born in the city of Zakopane in Southern Poland in 1992. He is the son of Stanisław Stopka and Maria Stopka of Stare Bystre, Poland. Along with his sisters Beata and Joanna, his family emigrated to the United States in 1998 with the help of his grandparents who lived in Chicago. He was awarded the degree of Bachelor of Science in Mechanical Engineering, magna cum laude, from the Rose-Hulman Institute of Technology in 2015. Kris was awarded the Georgia Institute of Technology President's Fellowship from 2016-2020. His long-term goal is to pursue a career in academia.